# Characterizing and Mitigating Scattering Effects in Terahertz Time Domain Spectroscopy Measurements

by

**Mayank Kaushik**

Bachelor of Electronics and Telecommunication Engineering (Honours),
NRI Institute of Science and Technology, Bhopal, India, 2005
Master of Electronics and Telecommunication Engineering (Advanced),
The University of Adelaide, 2007

Thesis submitted for the degree of

**Doctor of Philosophy**

in

Electrical and Electronic Engineering
University of Adelaide

2013

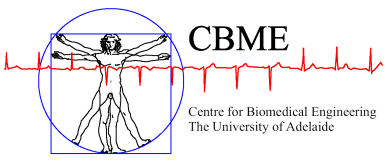




# Contents

# Abstract

Terahertz research has came a long way since its inception in the mid 1980s when the first pulsed THz emission was reported using electro-optic sampling. With rapid advent in THz generation and detection techniques, research in terahertz time-domain spectroscopy (THz-TDS) has progressed to such a great extent that terahertz is finding potential use in real world applications such as biomedical sensing, security screening and defence related applications. While many researchers and commercial organizations have successfully demonstrated efficacy of terahertz, various challenges still exist before THz technology transitions from the realm of research into everyday life.

This thesis focuses on the topical area of characterization and mitigation of scattering in terahertz time-domain spectroscopy measurements. Motivated by the lack of theoretical models and signal processing techniques, this thesis, presents several pieces of novel work that include theoretical models, numerical methods, signal processing techniques and experimental procedures to estimate and mitigate the scattering contribution in THz-TDS measurements of dielectric materials. The thesis is divided in to three main sections:

**Section I**

Section I describes the various theoretical models developed for estimating and approximating the scattering cross-section, when an electromagnetic wave interacts with a random medium with characteristic particle dimensions comparable to the wavelength of the incident radiation. The section is divided in two main sub-sections, (i) scattering through a sparse distribution of particles, and (ii) scattering from dense media.

**Section II**

Section II presents several signal processing based approaches for estimating and mitigating scattering effects in THz-TDS measurements for samples that exhibit sharp and sparse absorption features, without requiring *a priori* information such as its granularity, refractive index, and density.

**Section III**

Section III discusses some common experimental techniques such as milling the material of interest into fine powder and time domain averaging spatially disjoint or multiple sample measurements, in order to reduce the presence of scattering features and effects in the THz-TDS measurements. Recognizing the invasive access and/or specialized measurement apparatus requirement for these techniques, we present our preliminary investigation in analysing multiple Fresnel echoes for estimating and mitigating scattering contribution in THz-TDS measurements.

In addition to this, the thesis offers an introductory background to THz-TDS, in areas of hardware, applications, signal processing, and terahertz interaction with matter.

# Statement of Originality

This work contains no material that has been accepted for the award of any other degree or diploma in any university or other tertiary institution to Mayank Kaushik and, to the best of my knowledge and belief, contains no material previously published or written by another person, except where due reference has been made in the text.

I give consent to this copy of the thesis, when deposited in the University Library, being available for loan, photocopying, and dissemination through the library digital thesis collection, subject to the provisions of the Copyright Act 1968.

I also give permission for the digital version of my thesis to be made available on the web, via the University's digital research repository, the Library catalogue, the Australasian Digital Thesis Program (ADTP) and also through web search engines, unless permission has been granted by the University to restrict access for a period of time.

*25 January 2013*

Signed

Date

# Acknowledgments

I would like to express my deep gratitude to my supervisors—Dr Brian W.-H. Ng, Dr Bernd M. Fischer, and Prof. Derek Abbott. Their guidance, enthusiasm, and support has made my PhD journey memorable, rewarding and satisfying. Dr Brian W.-H. Ng, my principal supervisor, expressed the promptness and concern since our first discussion and that has been unchanged throughout the period under his supervision. His long experience in signal processing has been of great help and importance towards my research. He has always given me critical comments upon the drafts. I am also strongly indebted to my co-supervisor, Dr Bernd M. Fischer. His long experience in T-rays and THz-TDS has been of great importance towards my research. He defined the word 'quality' for the research. I wish to thank my co-supervisor, Prof. Derek Abbott, for introducing me to the field of terahertz, and for teaching me to think and write like a researcher. His encouraging attitude and critical suggestions have been very helpful throughout my research.

My appreciation extends to other great scholars at the University of Adelaide, Dr Withawat Withayachumnankul, Mr Matthew Trinkle, Dr Muammar Kabir, Prof. Christophe Fumeaux, Dr Gretel M. Png, and Dr Tamath Rainsford, who have occasionally provided useful discussions and critical comments to my research. Thanks are also due to all my colleagues in the Adelaide T-ray group in particular, Benjamin S.-Y. Ung, Dr Hungyen Lin, Si Tran Nugyen, Shaoming Zhu, Henry Ho, Dr Shaghik Atakaramians, and Dr Jegathisvaran Balakrishnan for their fruitful discussions and help in everything. I would also like to thank Aoife McFadden and Angus Netting of Adelaide Microscopy for assistance with the scanning electron microscope images and the 3D X-ray tomography.

During my candidature, administrative work has been assisted by Rose-Marie Descalzi, Ivana Rebellato, Colleen Greenwood, Danny Di Giacomo, and Stephen Guest. Other supporting people include IT support officers, David Bowler, Ryan King, and Mark J. Innes, and technical officers, Ian Linke, and Alban O'Brien are also acknowledged.

Major financial support has been provided by the University of Adelaide Divisional Scholarship. Additional support was received from the Walter & Dorothy Duncan Trust Grant, 2011. Travel grants were from IEEE South Australia Section, 2010–2011.

The Adelaide T-ray program has been supported by the Australian Research Council, the Sir Ross and Sir Keith Smith Fund, the Defence Science and Technology Organisation (DSTO), and NHEW P/L.

Last but not the least, my appreciation goes towards my loving wife Divya Kaushik, whose love, support, and belief helped me sustain my PhD journey, and my parents who always endow me with infinite encouragement and support. No words are enough to express my gratefulness to them.

Mayank Kaushik

# Conventions

**Typesetting** This thesis is type set using LaTeX2e software using the TeXnicCenter interface.

**Referencing** The Harvard style is used for referencing and citations in this thesis.

**Spelling** Australian English is adopted as spelling convention in this thesis.

**System of units** The units used in this thesis comply with the international system of units recommended in an Australian standard: AS ISO 1000-1998 (Standards Australia Committee ME/71, Quantities, Units and Conversations 1998).

**Physical constants** The physical constants comply with the recommendation by the Committee on Data of Science and Technology: CODATA (Mohr and Taylor 2005).

**Definition** In this Thesis, the terahertz band is defined as being from 0.1–10 THz (1 THz = $10^{12}$ Hz).

# Publications

## Journal Publications

**Kaushik-M.**, Ng-B. W.-H., Fischer-B. M. & Abbott-D., (2012). Reduction of scattering effects in THz-TDS signals, *IEEE Photonics Technology Letters*, **24**(2), pp. 155−157.

**Kaushik-M.**, Ng-B. W.-H., Fischer-B. M. & Abbott-D., (2012). Terahertz scattering by granular composite materials: An effective medium theory, *Applied Physics Letters*, **100**(1), art. no. 011107.

**Kaushik-M.**, Ng-B. W.-H., Fischer-B. M. & Abbott-D., (2012). Terahertz fingerprinting in presence of quasi-ballistic scattering, *Applied Physics Letters*, **101**(6), art. no. 061108.

**Kaushik-M.**, Ng-B. W.-H., Fischer-B. M. & Abbott-D., (2012). Terahertz scattering by dense media, *Applied Physics Letters*, **100**(24), art. no. 241110.

**Kaushik-M.**, Ng-B. W.-H., Fischer-B. M. & Abbott-D., (2012). Terahertz scattering by two phased media with optically soft scatterers, *Journal of Applied Physics*, **112**(11), art. no. 113112.

## Conference Publications

**Kaushik-M.**, Ng-B. W.-H., Fischer-B. M. & Abbott-D., (2010). Mitigating scattering effects in THz-TDS measurements, *35th International Conference on Infrared Millimeter and Terahertz Waves (IRMMW-THz)*. DOI: 10.1109/ICIMW.2010.5612470.

**Kaushik-M.**, Ng-B. W.-H., Fischer-B. M. & Abbott-D., (2011). Scattering estimation from spectral moments of THz-TDS signals, *36th International Conference on Infrared Millimeter and Terahertz Waves (IRMMW-THz)*. DOI: 10.1109/irmmw-THz.2011.6104872.

**Kaushik-M.**, Ng-B. W.-H., Fischer-B. M. & Abbott-D., (2011). Scattering robust features for classification of materials using terahertz, *Seventh International Conference on Intelligent Sensors, Sensor Networks and Information Processing (ISSNIP)*. DOI: 10.1109/ISSNIP.2011.6146581.

# List of Figures

---

# List of Tables

# Chapter 1

# Introduction

THE terahertz band is a frequency region of the electromagnetic spectrum that has only become widely accessible over the past decades. It lies between the infrared and millimetre wave regions and occupies the gap between the traditional worlds of electronics and photonics, popularly known as the 'terahertz gap'. Since the introduction of terahertz time-domain spectroscopy (THz-TDS) in the late 1980s, the technique, based on the generation and detection of sub-picosecond terahertz pulses, has found widespread use as a simple and versatile experimental technique for characterizing and classifying various gases, solids and liquids. This introductory chapter offers brief background descriptions and literature review of T-rays and THz-TDS.

## 1.1 Introduction

In this chapter, an introduction to terahertz technology is first provided, followed by an overview of terahertz technological and scientific achievements where several terahertz applications and prospects are discussed. The motivation for work presented in this thesis is then presented, followed by outline of the chapters in this thesis. This chapter then concludes with a brief summary of the original contributions made to the field of material classification and identification by terahertz time domain spectroscopy.

## 1.2 What is terahertz?

Terahertz radiation (THz or T-rays, 1 THz = $10^{12}$ Hz) is a type of electromagnetic radiation that spans the gap between millimetre wave and infrared radiation. T-ray radiation is loosely defined as the range between 0.1 (100 GHz) to 10 THz (Abbott and Zhang 2007), bridging the gap between the electronic and the photonic worlds. As shown in the Fig. 1.1, the terahertz band has its upper and lower limits overlapping the millimetre wave and infrared spectra respectively. Therefore, THz range is also referred to as sub-millimetre waves, whilst the higher end of the frequency range is also referred to as far-infrared (FIR). Overlapping definitions of frequency bands is not unusual, as the precedence already exists, for example, the bands of gamma rays and X-rays (Abbott and Zhang 2007).

Prior to existing technologies, the terahertz frequency band had only limited access. Electronics devices are hampered by parasitic capacitances, which cause such systems to behave like low pass filters. A rarity of media possessing unthermalized energy level transitions in terahertz frequencies deters the realization of stimulated emission at room temperature, where $k_B T/h = 5.6$ THz, which indicates the energy levels are undesirably thermalized in the THz frequency range. Furthermore, propagation of T-rays in the ambient environment suffers the problem of high atmospheric absorption (Barnes *et al.* 1935, Exter *et al.* 1989). However, apart from these limitations, terahertz has some benefits over the other frequency ranges in the electromagnetic spectrum. For example, pulsed THz signals have good temporal resolution like microwaves, but pulsed THz have better a better spatial resolution than microwave radiation. In addition the photon energy of THz ($\approx 10^{-3}$ eV) is almost six orders lower than that of

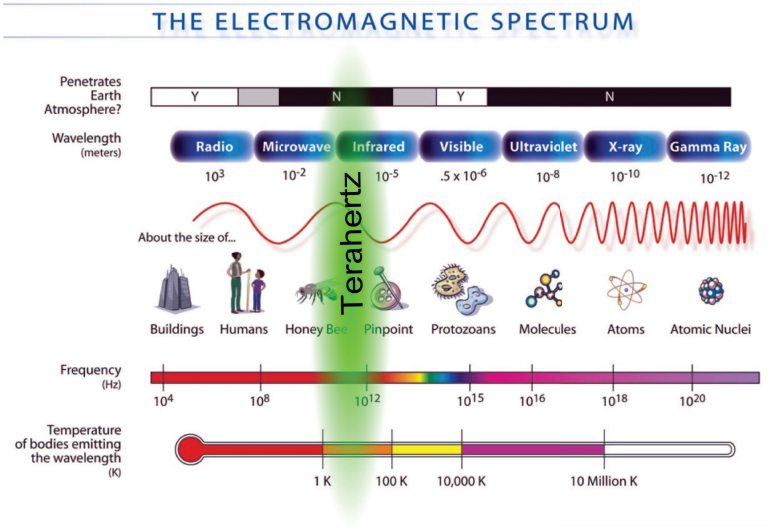


**Figure 1.1. The electromagnetic spectrum.** Electromagnetic spectrum showing a pictorial view of the relative size of the various wavelengths. Adapted from *http://mynasadata.larc.nasa.gov*

X-rays, and at such low power levels (below the level that causes heating), THz is considered safe for prolonged exposure to living bio-tissues. Transmission or reflection of THz from a sample impresses the coherent spectroscopic information (at THz frequencies) of the sample on the emerging radiation (Siegel 2004). In other words, the THz radiation can capture the sample's characteristic THz resonance features (*fingerprints*) attributed to the sample's macroscopic molecular structure (Fischer *et al.* 2005).

## 1.3 An overview of terahertz technological and scientific achievements

Recent years have seen a plethora of significant advances in terahertz technology. Terahertz radiation has found application in various fields such as spectroscopy, astrophysics, and imaging techniques namely for biomedical applications. Its low interference and non-ionising characteristics, have made it a good candidate for use in safe *in vivo* medical imaging. Terahertz has interested astrophysicists since the mid 1920s. One of the first uses of the term *terahertz* was made by Senitzky and Oliner (1970) in review on application of sub-millimetre waves for analyzing the composition of interstellar bodies such as dust clouds.

Before 1971, there were only a few established methods for generating and detecting THz radiation and atmospheric attenuation (primarily due to water vapour) limited the THz research to propagation over short distances only (Chan *et al.* 2009). An important breakthrough came in 1971, when Yang *et al.* (1971) reported the generation of THz radiation by nonlinear frequency conversion with an ultrafast laser. Soon after this, in 1976, Shen (1976) reported another method for generating THz from rectification of optical pulses. With the advent of ultrafast lasers with femtosecond laser pulses by the late 1980s, implementation of these groundbreaking THz generation techniques became more common. It was only in 1985, when Auston and Cheung (1985) developed the first terahertz time domain spectroscopy (THz-TDS) system at the AT&T Bell Laboratories. This was followed by Smith *et al.* (1988), who first reported the capability of photoconductive antennas to generate and detect THz radiation up to 2 THz. Over the next decade, a series of breakthroughs were made in the generation and detection of THz radiation. In 1993, Brown *et al.* (1993) demonstrated the generation of widely tunable THz radiation from the photomixing of two lasers at different frequencies. Soon after this, in 1995, Wu and Zhang (1995) reported the use of free-space electro-optic sampling for the measurement of freely propagating electromagnetic radiation with sub-picosecond resolution. Also in 1995, Hu and Nuss (1995) reported the first imaging system based on optoelectronic terahertz time-domain spectroscopy. They are also credited with coining the term 'T-rays' to describe terahertz radiation.

In recent years, terahertz research has evolved beyond standard spectroscopy to include 3-dimensional imaging (Mittleman *et al.* 1996, Zhang 2004, Crawley *et al.* 2003, Wallace *et al.* 2002, Fitzgerald *et al.* 2002, Nguyen *et al.* 2005, Zeitler *et al.* 2007a), tomography (Wang and Zhang 2004, Mittleman and Nuss 2000, Takashi *et al.* 2006, Ferguson *et al.* 2002, Wang *et al.* 2002b, Sunaguchi *et al.* 2009), interferometric and synthetic phase array imaging (O'Hara and Grischkowsky 2002, O'Hara and Grischkowsky 2004, Walsh *et al.* 2004, Federici *et al.* 2003, Pearce *et al.* 2005), and near-field microscopy (Planken *et al.* 2005, Kersting *et al.* 2008, Mitrofanov *et al.* 2000, Lin *et al.* 2011).

### 1.3.1 Terahertz applications and prospects

Owing to their unique properties, terahertz radiation provide a variety of applications and opportunities in different fields. The following is a brief introduction to some of these aspects.

### Space

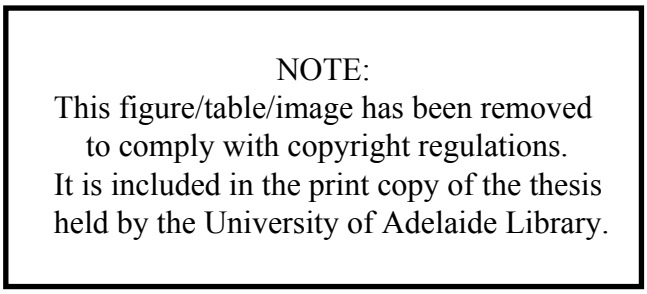


**Figure 1.2. Spectral signatures of interstellar dust clouds.** Radiated energy versus wavelength showing 30-K blackbody, typical interstellar dust, and key molecular line emissions in the sub-millimetre regime. After Phillips and Keene (1992).

Sub-millimetre wavelengths have interested astrophysicists since the mid 1920s. As can be seen in Fig. 1.2, interstellar dust clouds have spectral signatures in the range of 1 mm to 100 $\mu$m, which explains the interest of astronomers in the terahertz frequency range. Although interstellar dust clouds exhibit many individual spectral signatures, only a few have been identified so far. To eliminate affects of spectral clutter and atmospheric absorption (primarily water), high resolution mapping of the terahertz band is required. Almost 98% of the photon emitted since the Big Bang fall in the sub-millimetre and far-IR spectral range (Leisawitz *et al.* 2000), thus terahertz detectors offer us an unique opportunity to tap into the early universe and discover more about its origin and evolution (Siegel 2002). However, this would require detectors with high resolving power and high spectral resolution.

Sub-millimetre waves have found applications in studying important atmospheric phenomena by using high resolution heterodyne receivers for monitoring thermal emission lines for the stratosphere and upper tropospheric gases (Waters 1992). However,

as a consequence of strong attenuation of terahertz due to the presence of water and oxygen, longer millimetre waves are required for chemical probing of lower stratosphere.

### Spectroscopy

Spectroscopy is one of the many interesting applications where terahertz has seen rapid advances over the last decade. In general, non-polar and non-metallic materials, such as paper, plastic, wood, fabric, are transparent or translucent to terahertz radiation because of their low photon energies and non-ionizing nature. Due to these specifications, many chemical substances, pharmaceuticals and explosive materials exhibit characteristic spectral responses in this frequency range. As a result, broadband terahertz radiation permits the identification and discrimination of a number of substances, including explosives and biochemicals (Choi *et al.* 2004). This has motivated the use of spectroscopic analysis using T-rays in security screening, pharmaceutical and food quality control (Wang *et al.* 2002a, Zandonella 2003, Morita *et al.* 2005, Jördens and Koch 2008). Examples of terahertz spectroscopy for common explosives, drugs, substances and clothing materials is presented in Fig. 1.3.

Non-invasive, non-destructive detection and classification of drugs, explosives and biochemicals and agents, pharmaceutical and food products quality control, and medical diagnostics are among the various applications related to terahertz spectroscopy. With the increasing number of terahertz spectra being collected in databases, this range of applications is likely to grow in the future.

### Industrial applications

The ability to penetrate cardboard, paper, dry wood, various paints, many plastics, many ceramic materials, and many semiconductor materials, makes terahertz spectroscopy an promising tool for industrial applications such as inspection of silicon solar cells, nanocomposites, polymer and dielectric films (Tonouchi 2007). Furthermore, owing to the strong absorption of terahertz from water, an industrial application for characterizing water content of newspaper prints has also been reported (Izatt *et al.* 1988). Like far-IR, terahertz can also be used to detect small voids and recognize their size and position inside the sample under study. However, the high cost of the current terahertz

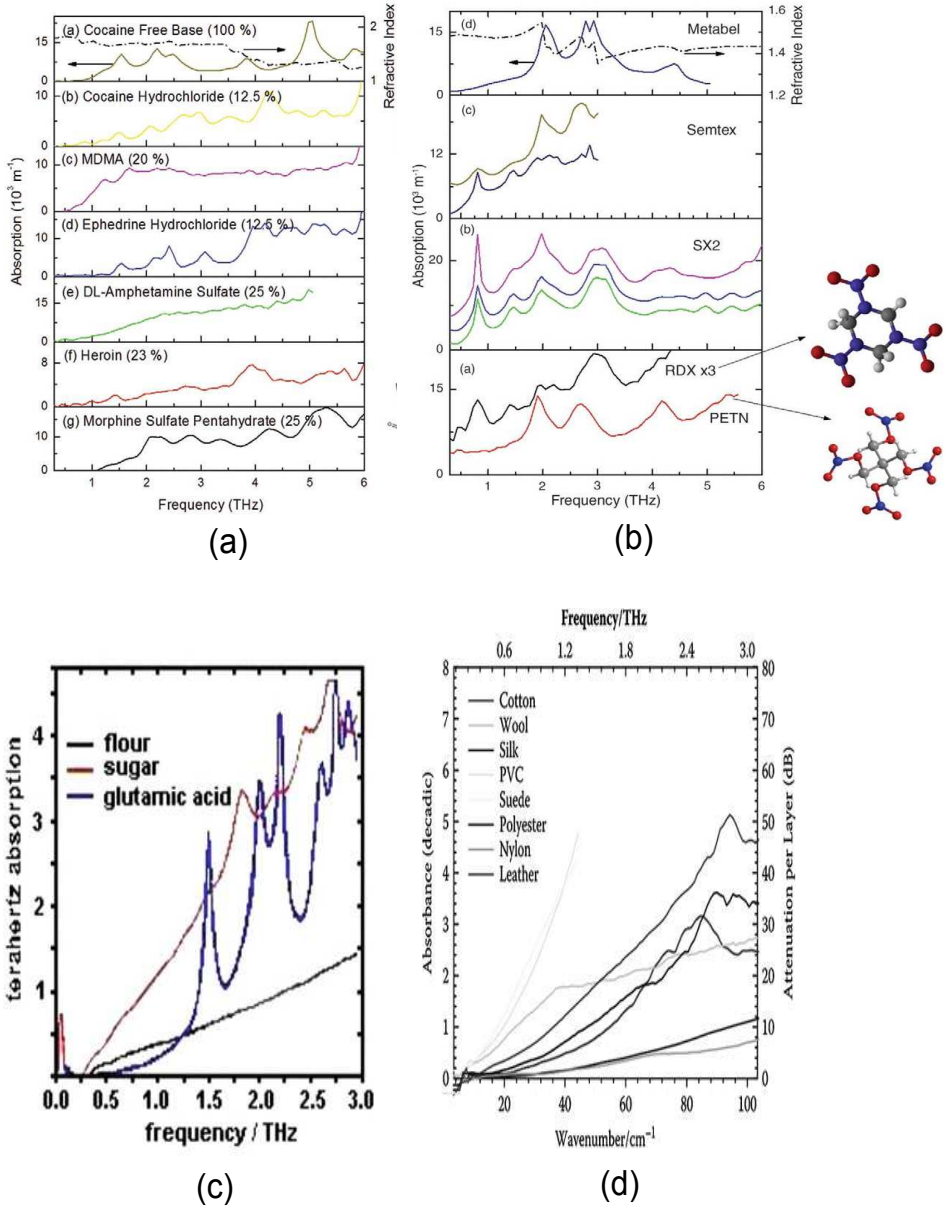


**Figure 1.3. Terahertz absorption by various materials.** (a) THz absorption for common explosives, (b) THz absorption of common drugs, after Davies *et al.* (2008), (c) THz absorption for common daily use substances, after Rostami *et al.* (2010), and (d) THz spectrum of common clothing materials, after Dexheimer (2007).

technology is the main obstacle for industrial uptake of the terahertz measurement instruments. However, with the increase in the number of reports on low cost alternatives for key THz spectroscopy components (Ung *et al.* 2012, Scherger *et al.* 2011), it should not be long before low-cost THz spectrometers will be commercially available.

### Communication

Generally, "terahertz communication" means communication with a terahertz carrier wave. Apart from small antenna sizes and greater bandwidths, several other factors make THz an attractive option for communication. To begin with, frequencies above 300 GHz are currently unallocated by the Federal Communications Commission Fig. 1.4. THz would offer lower scattering with greater penetration through aerosols and clouds as compared with IR and optical wavelengths for communication in the stratosphere. However, the biggest factor limiting the implementation of THz communication network arises from the strong absorption through the atmosphere due to the presence of water vapour (Fig. 1.5). This limitation might possibly be overcome with improvements in the power and efficiency of THz sources, and by careful choice of narrow band THz atmospheric windows although this would be a major challenge.

Another limitation comes from the unavailability of the required compact components for realizing a THz communication system such as amplifiers, planar integrated circuits, and antenna arrays, which do not exist above 125 GHz currently. However, recently, compound semiconductor and Si-CMOS devices, which were previously considered unsuitable for operations at THz frequency due to the lossy substrate, operating at up to 1 THz have been reported (Piesiewicz *et al.* 2005, Hirata *et al.* 2003, Piesiewicz *et al.* 2007, Hirata *et al.* 2007).

In spite of strong atmospheric attenuation and inefficient sources, THz may find possible application in satellite to satellite communication. For links that do not interact with the Earth's atmosphere, terahertz technology can provide higher data rates (large bandwidth) in comparison to microwaves. THz also offer the advantage of smaller antenna sizes when compared with microwaves, which helps in reducing the size of the satellite systems (Fitch and Osiander 2004, Tonouchi 2007). In essence, THz communication is in the very early stages of development, but with increasingly high efficiency THz communication components being reported in the literature, it cannot be too far in the future when we will be able to take advantage of high bandwidth THz communication systems.

**Figure 1.4. Frequency allocation chart.** The regulated spectrum as designated by the U.S. Federal Communications Commission. Frequency above 300 GHz are currently unallocated. (Source: *http://www.ntia.doc.gov/osmhome/allochrt.pdf*.).

### Imaging

Terahertz radiation has received great attention in the area of imaging and sensing. As mentioned earlier, the inherent properties of terahertz such as the ability to penetrate a wide variety of non-conducting materials, to trigger only the vibrational and rotational state of a molecule without altering its electronic state and its non-ionizing nature, which makes it safer for interaction with living tissues as compared to X-rays, make terahertz a very attractive candidate for a number of sensing and imaging applications. One of the technical advantages for using terahertz for imaging is that its short wavelength offers a better spatial resolution in comparison to microwaves, which is sufficient for many imaging applications. Many recent publications have reported details of a variety of THz imaging techniques and systems (Hu and Nuss 1995, Wu *et al.* 1996, Jiang and Zhang 1998, Hunsche *et al.* 1998, Chen *et al.* 2000, Jiang *et al.* 2000, Rudd *et al.* 2000, Kawase *et al.* 2003, Dobroiu *et al.* 2004, Siebert *et al.* 2002, Usami *et al.* 2002, Chen *et al.* 2003). However, a basic imaging system can be described as a system that brings the collimated THz beam to an intermediate focus using a pair of

**Figure 1.5. Terahertz attenuation by atmosphere.** Atmospheric attenuation of THz as compared to other communication frequency bands. (Source: http://www.st-andrews.ac.uk)

lenses or parabolic reflectors (Mittleman *et al.* 1999). As shown in Fig. 1.6, by placing an object at the focus of the THz beam, one can measure the waveform that has transmitted through the object. The measurement can be repeated over various locations on the object to build a pixel by pixel image of the object. The list of possible applications of such a system is quite extensive. Detection of concealed weapons, hidden explosives and land mines, medical imaging, real-time fingerprinting of chemical and biological terror materials, packages or air (security inspection) and characterization of semiconductors (quality control) are some prominent examples (Rostami *et al.* 2010). Fig. 1.7 and Fig. 1.8 show a few examples of application of THz imaging. Thus THz imaging proves to be a versatile tool for a wide variety of applications.

### Medicine and biology

Both THz spectroscopy and imaging have found a variety of applications for medicine and biology. The broadband nature of THz pulses make spectroscopic analysis an attractive tool for a pharmaceutical analysis and quality control. Several authors have

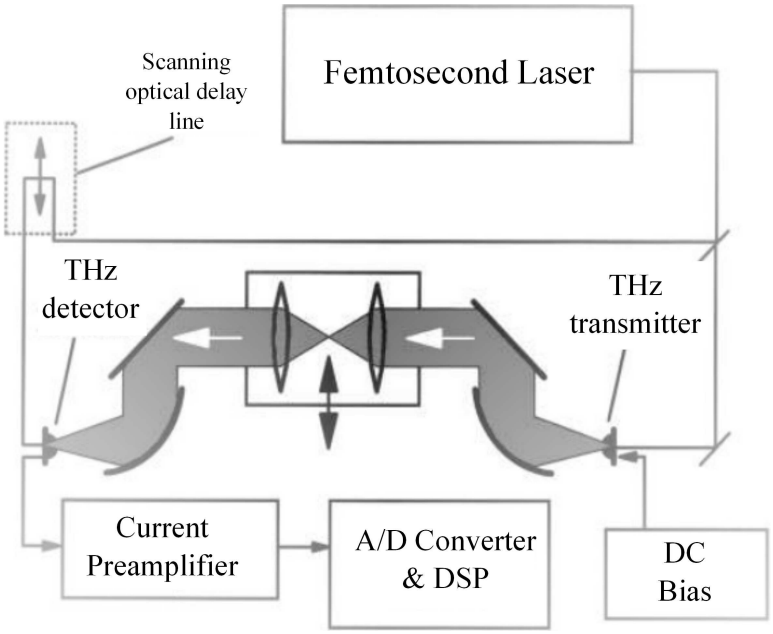


**Figure 1.6. A basic THz-TDS system.** A schematic of a basic THz-TDS system, consisting of the femtosecond laser, scanning delay line, THz transmitter and detector, and associated optics and electronics. For a transmission mode imaging system with an intermediate focus, a pair lenses separated by $2f$ (focal length) is inserted between the collimated region of the THz beam. After Mittleman *et al.* (1999).

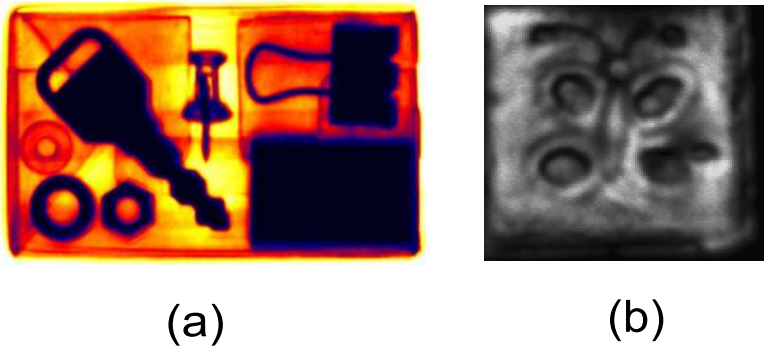


**Figure 1.7. Examples of imaging by terahertz.** (a) THz imaging application to hidden object detection. After Dobroiu *et al.* (2006), (b) THz imaging applied to mural paintings, graphite image of a butterfly, extracted from between plaster layers. After Jackson *et al.* (2008).

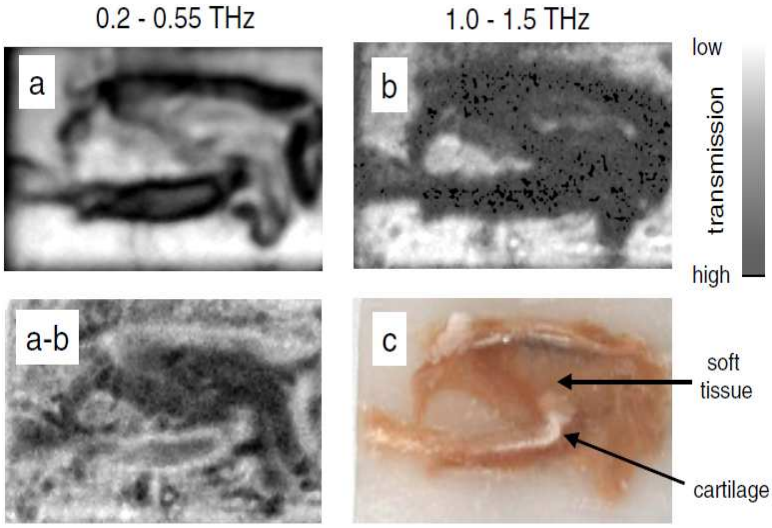


**Figure 1.8. Example of medical imaging using terahertz.** Pulsed THz imaging of histopathological sample of pig larynx (c) with two different integration windows (a and b) and their differential output (a-b). After Knobloch *et al.* (2002).

reported application of THz spectroscopy for a variety of applications in pharmaceutical settings. In an initial study, Taday *et al.* (2003) demonstrated the ability to distinguish between two different polymorphic forms of ranitidine hydrochloride using THz pulsed spectroscopy. In their analysis Taday *et al.* (2003) were able to differentiate between the polymorphic forms of pure specimens as well as of formulated commercial tablets. Further work into characterization of crystalline properties of drugs was carried out by Strachan *et al.* (2004) for Carbamazepine (CBZ), enalapril maleate (EM), indomethacin (IM) and fenoprofen calcium (FC). Several other THz spectroscopic analysis of crystalline pharmaceutical materials that have been reported in the literature include acetylsalicylic acid, benzoic acid (Walther *et al.* 2002), D-glucose (Upadhya *et al.* 2003), D-mannose, D-galactose, D-fructose, D-maltose, $\beta$-lactose (Upadhya *et al.* 2004), cocaine, morphine, lactose $\alpha$-monohydrate (Fischer *et al.* 2005), and methamphetamine (Ning *et al.* 2005). Fig. 1.9 shows an example of the ability of THz spectroscopy to distinguish between the polymorphic forms of a given substance.

Terahertz imaging on the other hand reveals spatially resolved information of the sample under study, which enables it to examine the physical properties of the sample such as density variations (Zeitler *et al.* 2007b). Terahertz imaging has been applied to a variety of pharmaceutical and chemical analysis such as tablet coating analysis (Zeitler *et al.* 2007a, Fitzgerald *et al.* 2005, Ho *et al.* 2007, Shen and Taday 2008, Maurer and Leuenberger 2009, Ho *et al.* 2008, Spencer *et al.* 2008, Cogdill *et al.* 2007), interface

**Figure 1.9. An example of characterization of polymorphic forms using terahertz.** Terahertz spectra of the five polymorphic forms of sulfathiazole. After Zeitler *et al.* (2007b).

and buried structure detection (Zeitler *et al.* 2007a), and 2D and 3D non-destructive chemical imaging (Shen *et al.* 2005b, Shen *et al.* 2005a, Fischer *et al.* 2005). Fig. 1.10 shows a few examples of THz imaging applied to pharmaceutical and chemical analysis.

Recently, terahertz has also been employed as a tool for early detection of cancer. Terahertz provides means for dielectric contrast imaging without being ionizing. Several analyses deploying terahertz spectroscopy and imaging for detecting cancerous tissues have been reported in the literature (Woodward *et al.* 2003, Oh *et al.* 2009, Ashworth *et al.* 2009). Woodward *et al.* (2003) presented the first frequency-domain analysis of basal cell carcinoma *in vitro*. However, unlike time domain analysis, their reflection mode analysis was only able to identify surface features in skin and information retrieval from depth was not achieved. Ashworth *et al.* (2009), on the other hand, used

**Figure 1.10. Pharmaceutical tablet coating analysis using terahertz imaging.** (a) Tablet coating analysis using THz imaging: cross-section depth profile of the tablet structure, (b) false-colour terahertz chemical mapping image showing the spatial distributions of (A) lactose, (B) sucrose, and (C) reconstructed chemical map of the sample where blue shows lactose, red shows sucrose, pink shows both lactose and sucrose, and green shows neither lactose nor sucrose. After Zeitler *et al.* (2007b).

both terahertz spectroscopy and imaging to measure and compare the complex refractive index of freshly excised and cancerous breast tissues from 20 patients. They reported higher refractive index and absorption coefficient for the tissues affected by cancer. However, the root cause of the increases in these fundamental properties is yet to be determined. Recently, Oh *et al.* (2009) demonstrated the nanoparticle-contrast-agent enabled terahertz imaging (CATHI) technique for cancer detection. They reported that the THz reflection amplitude from the cancer cells with gold nano-rods (GNRs) increased by 20% upon IR laser irradiation compared to cancer cells without GNRs. In the differential mode, the THz signal from the cancer cells with GNRs was 30 times higher than that from cancer cells without GNRs. Such studies have proven that terahertz analyis could facilitate the diagnosis and study of cancers at a very early stage. Further research is yet neccesary in order to confirm these results.

Furthermore, terahertz promises the ability of collecting rich spectroscopic information of biological tissues since the vibrational and rotational transition energies of the biomolecular constituents of tissue fall in the THz frequency range; e.g. DNA (Fischer *et al.* 2002) and proteins (Markelz *et al.* 2000, Smye *et al.* 2001). Since water absorbs THz waves strongly, *in vivo* THz imaging has been primarily used for skin,

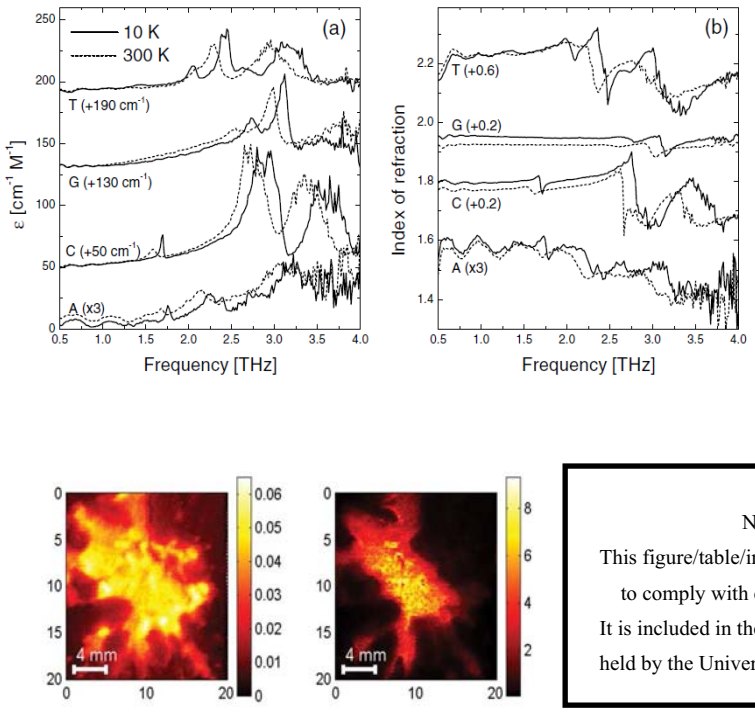


NOTE:
This figure/table/image has been removed to comply with copyright regulations.
It is included in the print copy of the thesis held by the University of Adelaide Library.

**Figure 1.11. Cancer detection using terahertz.** (a) Absorption coefficient and (b) index of refraction of the nucleobases A, C, G and T, recorded at 10 K (solid curves) and 300 K (dashed curves). After Fischer *et al.* (2002). (c) Two terahertz images generated using the maximum of the reflected pulse (leftmost figure) and the ratio between maximum and minimum of the reflected pulse (middle). In the $E_{\max}$ image all the tissue is shown, tumor with surrounding adipose tissue. In $E_{\max}/E_{\min}$ only the tumor is visible and correlated well with the tumor shown in the histology image. After Ashworth *et al.* (2009).

dentistry and breast cancer analysis. Fig. 1.11 shows example of terahertz radiation applied for analyzing DNA and cancerous tissues.

### Metamaterials at terahertz frequencies

Increasing focus has been applied on research of artificial materials with engineered electric and magnetic response. Several artificial structures with electrical and magnetic resonances in terahertz frequency range have been reported in the recent years (Padilla *et al.* 2007, Zhang *et al.* 2009, Chen *et al.* 2006, Padilla *et al.* 2006, Grzegorczyk and Kong 2006, Singh *et al.* 2009, Koschny *et al.* 2005). These artificial materials, also known as metamaterials, exhibit negative permittivity and permeability, which result

in specific optical properties that can be of interest for several purposes such as developing a spatial light modulator of terahertz frequency (Chan *et al.* 2009) and measuring high-strain mechanical deformations (Pryce *et al.* 2010).

One of the most common elements for obtaining a magnetic response is a pair of concentric split rings, often referred to as a split ring resonator (SRR). The structure also displays an electric response under normal incidence radiation with the electric field component perpendicular to the SRR gap and the magnetic field lying in the SRR plane. As a result the incident electric field causes an inductive-capacitive resonance. The magnetic field component causes a current flow in the inner and outer rings due to the high capacitance between the rings. While, in theory, split ring resonators can be used as electrically resonant elements, coupling between the electrical and magnetic resonance can cause complicated bianistropic electromagnetic response (Withayachumnankul and Abbott 2009). In the case where only electrical response is required, the SRR structure can be modified to introduce symmetry in the SRRs with respect to the electric field direction thus suppressing the magnetic response while retaining the electrical response (Schurig *et al.* 2006). This structure is also known as electric SRR structure or eSRR. Some common SRR structures studied at terahertz frequencies are depicted in Fig. 1.12.



**Figure 1.12. Common SRR structures.** Some common SRR structure variants studied at terahertz frequencies: (a) double SRR, (b) single SRR, (c) eSRR, (d) four-fold rotational-symmetry eSRR, (e) rectangular eSRR, and (f) complementary eSRR. Field orientation is shown for all structures, except for the complementary eSRR which requires the in-plane 90 field rotation. After Withayachumnankul and Abbott (2009).

The ability to freely tune the electric and magnetic responses in metamaterials makes it possible to realize negative-index materials (NIMs). Such structures have both permittivity and permeability less than zero (negative) at the same frequency. The first ever NIMs were realized using a combination of wires and SRRs, excited at microwave frequencies to produce overlapping negative permeability and permittivity bands (Pendry and Smith 2004). As a result of this interesting behavior, NIMs have become the the center of metamaterial research in the optical frequency regime (Shalaev 2007, Soukoulis *et al.* 2007, Klar *et al.* 2006). With the ability to obtain a tunable electromagnetic response, metamaterials offer immense opportunities in developing new and improving existing optical systems. Given the existing deficiency of materials having a suitable THz electronic response which is present for microwave and lower frequencies, or photonic response which is present for infrared and higher frequencies, metamaterials present a new opportunity that is otherwise not available in the naturally occurring materials (Chen *et al.* 2011a).

## 1.4 Motivation for this thesis

When a terahertz pulse propagates through a dielectric medium, it suffers from various losses. There are reflection losses at medium boundaries, absorption losses and scattering losses. Scattering is caused by variations in the refractive index that are smaller than the wavelength of the scattered radiation (Zhang 2002). These variations may be present due to impurities, imperfections, inhomogeneity, particle size variations and irregular or rough surfaces in the sample and can lead to multiple scattering. Many of these causes are a result of improper sample preparation. When the particle size of the sample material is of the order of the wavelength of the incident radiation, scattering can lead to significant losses in power. Scattering can occur over a broad range of frequencies and its effects are more pronounced at high frequencies. It can change the shape of the measured absorption spectrum of the sample under test, making it difficult to determine specific dielectric properties of the sample.

When the scatterers (radius = $r$) are much smaller than the wavelength ($\lambda$) of the incident radiation ($x = 2\pi r/\lambda \ll 1$), the measured scattering cross-section can be explained using Rayleigh approximation (Fox and Bertsch 2002). For the Rayleigh approximation, the scattering cross-section is given by:

$$\sigma_{\text{ray}} = \frac{8\pi}{3}\left(\frac{2\pi n_{\text{med}}}{\lambda}\right)^4 r^6 \left(\frac{m^2-1}{m^2+2}\right)^2, \tag{1.1}$$

where $n_{\text{med}}$ is the refractive index of the medium, and $m = n_{\text{sph}}/n_{\text{med}}$ where $n_{\text{sph}}$ is the refractive index of the particles or scatterers. In the above equation scattering cross-section $\sigma_{\text{ray}}$ is inversely proportional to the fourth power of the incident wavelength, which implies that smaller wavelengths are scattered more strongly.

On the other hand, in polycrystalline samples, scattering is primarily caused by inhomogeneities that are often estimated to have characteristic dimensions in tens of microns. In that case the size of the scattering centers are of the order of the THz wavelengths and therefore, the scattering cross-section can no longer be described by the Rayleigh approximation given in Eq. 1.1, but needs to be modeled by a more complex process (Born and Wolf 1999). Several researchers have reported that THz extinction for finely ground solids does not vary as the fourth power of frequency and have suggested that Rayleigh scattering can be ruled out (Bandyopadhyay *et al.* 2007, Nam *et al.* 2012). Only a few researchers have reported theoretical models or quantitative estimations of the extinction of granular materials.

In 2007, Bandyopadhyay *et al.* (2007) applied Mie theory (Mie 1908) of spherical particles under the assumption of weak scattering limit to estimate the scattering contribution in the experimentally obtained extinction spectra of granular salt, flour and ammonium nitrate. While Bandyopadhyay *et al.* (2007) demonstrated that Mie theory can be used in the weak scattering limit at THz region, their analysis was not applicable for media with high particle densities and/or with large non-spherical particle size such as pharmaceutical tablets and explosives. In the same year, Zurk *et al.* (2007) showed good agreement between the experimentally obtained extinction spectra for granular polyethylene (PE) pellets with the theoretical results produced by applying the Quasi Crystalline Approximation (QCA) under the assumption of a dense media model. While their model, unlike the model of Bandyopadhyay *et al.* (2007), was much more general and applicable to a variety of dielectric samples, their method not only required precise knowledge of the sample particle sizes, bulk dielectric constant, and volume fraction of constituents, but also assumed spherical particles and a probabilistic Percus-Yevick (PY) pair distribution for particle locations within the sample. Recently, Nam *et al.* (2012) applied the radiative transfer theory for studying the terahertz scattering from layered granular media. Similar to the QCA model given by Zurk *et al.* (2007), this model also relied on precise information of parameters such as grain size,

fractional volume of grains, and thickness of scattering layer. As radiative transfer theory is suitable for low fractional volume, Nam *et al.* (2012) used the QCA model given by Zurk *et al.* (2007) for studying samples with high fractional volume of scatterers.

Another approach that various researchers used to address the issues around THz scattering in dielectric media was to develop experimental and numerical techniques for sample preparation and data analysis that help in reducing the effects of scattering in the THz-TDS measurements. One common approach is to grind the sample material to a fine powder and then mix it with fine powder of materials that do not have absorption features in the THz frequency range such as polyethylene (PE) or high-density polyethylene (HDPE). This reduces the number of coarse grains in the sample and thus limits the scattering. In 2008, Shen *et al.* (2008) averaged a large number of disjoint transmission measurements taken over multiple points on a sample to mitigate the random scattering contribution. On the other hand, Franz *et al.* (2008) used Raman's theoretical description of the Christiansen Effect (Raman 1949) and the experimentally measured frequency dependent refractive indices of the sample and host materials, to numerically eliminate the effects of scattering from the terahertz extinction spectrum. In their model, Franz *et al.* (2008) assumed a layered internal structure to represent a media with essentially a random internal structure. All these approaches either rely on specific information and assumptions about the sample under study or often require a complex and time consuming sample preparation and measurement process. However, in real-world applications such as stand-off measurements, *a priori* information of the the sample is not always known and therefore limits the applicability of these techniques.

Motivated by the lack of theoretical models and signal processing techniques, this thesis, presents several pieces of novel work which includes theoretical models, numerical methods, signal processing techniques and experimental procedures to estimate and mitigate the scattering contribution in THz-TDS measurements of dielectric materials. These techniques not only enable non-invasive estimation and mitigation of scattering effects in the THz-TDS measurements but also offer the advantage of being computationally more efficient and demand less *a priori* information, in comparison to the techniques described in the existing literature.

## 1.5 Thesis outline

The overarching theme of this thesis is to characterize and mitigate the effects of scattering in terahertz time domain spectroscopy measurements. As outlined in Fig. 1.13, the thesis is divided into three main sections: scattering estimation and mitigation, (i) theoretical modeling, (ii) signal processing techniques, and (iii) experimental techniques. Sections consist of one chapter each. In addition to this, an introduction chapter and two background chapters encompassing THz and THz-TDS are given to provide context. The following is a detailed description of each part of the thesis:

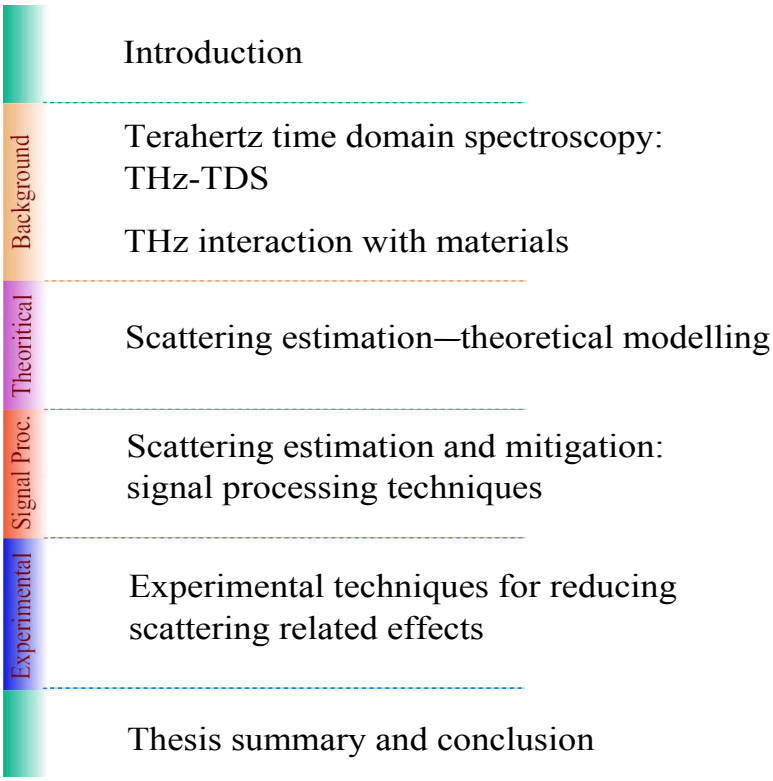


**Figure 1.13. Thesis outline.** This thesis is composed of 7 chapters and is divided in to four sections. The original contributions are distributed over three main sections as shown above. An introduction chapter and two background chapters are also included to provide ample context on the current state of THz and THz-TDS research. The thesis is concluded by a chapter providing overall thesis summary, conclusion and future work suggestions.

Background: This section consists of two chapters. Chapter 2 describes the underlying mechanisms behind the generation and detection of T-rays, basic principles, operation and variants of THz-TDS, data acquisition and material characterization theory for a typical THz time domain spectrometer and also discusses various post measurement

signal processing techniques for THz-TDS data. Chapter 3 discusses the basic concepts and theories of terahertz interaction with materials and propagation in dielectric material. First, it describes the THz wave propagation in matter and across interfaces, followed by a discussion on origin of spectral fingerprints in the THz region and is concluded with a detailed discussion on the various challenges and hurdles that constrain plausible scenarios for the application of terahertz technology for material classification and identification.

Section I—Theoretical Modeling: This chapter reviews various theoretical models developed for estimating and approximating the scattering cross-section, when an electromagnetic wave interacts with a random medium with characteristic particle dimensions comparable to the wavelength of the incident radiation. The chapter is divided in two main sub-sections, (i) scattering through a sparse distribution of particles, and (ii) scattering from dense media. Several existing theories are discussed, a new iterative algorithm based on the effective field approximation proposed by Waterman and Truell (1961) for estimating the frequency dependent scattering loss for THz transmission through a random media is presented. Finally a numerical approach based on the modified Rayleigh-Gans-Debye approximation to reduce the scattering contribution in transmission mode THz-TDS measurements of two phased media with absorbing constituents is also presented. The discussed theories and models are compared with transmission mode THz-TDS measurements of various material samples to validate their accuracy and applicability.

Section II—Signal Processing Techniques: Here we present several signal processing based approaches for estimating and mitigating scattering effects in THz-TDS measurements for samples that exhibit sharp and sparse absorption features, without requiring *a priori* information of its granularity, refractive index, and density. Techniques are introduced in an orderly fashion such that each technique improves, in terms of accuracy or computational efficiency, on the preceding technique. Analysis was carried out on THz-TDS measurements of two materials: $\alpha$-monohydrate lactose and $\alpha$-D-glucose. Both materials are commonly found in many pharmaceutical tablets and food products and show distinctive and sharp absorption features in the THz spectral range, making them suitable for this study.

Section III—Experimental techniques: Here we review experimental techniques for mitigating scattering effects. This chapter discusses some common experimental techniques such as milling the material of interest into fine powder and time domain averaging spatially disjoint or multiple sample measurements, in order to reduce the presence of scattering features and effects in the THz-TDS measurements. In order to develop an experimental method that does not require special measurement apparatus or invasive access to the sample, we present our initial exploration in analysing multiple Fresnel echoes for estimating and mitigating scattering contribution in THz-TDS measurements.

## 1.6 Summary of original contributions

This thesis involves a number of original contributions in the field of material analysis using THz-TDS, as declared in this section.

- In Section I, we applied the effective medium theory proposed by Chýlek *et al.* (1988) to yield a parameterized model to estimate the frequency dependent scattering loss from three different granularities of polyethylene and air samples and compare the theoretical analysis with the transmission THz-TDS measurements of these samples. Unlike previous approaches our method does not rely on assumptions regarding position of particles within the sample, the sample internal structure or on experimental observations to fit unknown theoretical parameters. We supported our analysis and results using information extracted from high resolution Scanning Electron Microscope (SEM) images and 3D models generated using X-ray tomography of our samples. The research is published in *Applied Physics Letters*, volume-101, 2012 under the title 'Terahertz scattering by granular composite materials: An effective medium theory' (Kaushik *et al.* 2012a).

- In Section I, we present an iterative algorithm using the multiple scattering theory of Waterman and Truell (1961) and the self consistency condition of Chýlek and Srivastava (1983) for calculating the effective propagation constant. From the comparison of simulated and experimental results, it is found that the algorithm accurately estimated the optical properties of high density (>10%) samples made of non-absorbing granular PE particles of dimensions comparable to the incident wavelength. The proposed technique offers a rather simple and computationally efficient method for estimating the multiple scattering response of a dense

medium. The research is published in *Applied Physics Letters*, volume-100, 2012 under the title 'Terahertz scattering by dense media' (Kaushik *et al.* 2012d).

- In Section I, we also present a numerical approach based on the modified Rayleigh-Gans-Debye approximation to reduce the scattering contribution in transmission mode THz-TDS measurements of two phased media with absorbing constituents. The resulting expression relates the scattering attenuation in terms of the refractive indices of the sample constituents. The proposed technique not only eliminates the increased baseline, but also corrects the extinction spectrum for asymmetrically distorted absorption bands, often observed as consequence of multiple scattering in the sample. The method was tested on experimentally obtained extinction spectrum of a sample made of $\alpha$-monohydrate lactose and PE powder and was found to reasonably eliminate the scattering contribution for the measured extinction, using only the THz-TDS measurements of samples refractive index, to reveal the true absorption spectra for a given sample. The research is published in *Journal of Applied Physics*, volume-112, 2012 under the title 'Terahertz scattering by two phased media with optically soft scatterers' (Kaushik *et al.* 2012e).

- In Section II, we report a signal processing technique to estimate scattering contribution in THz-TDS measurements by exploring the relation between the change in spectral moments and time domain features of a THz pulse when it passes through a dielectric material and the frequency dependent scattering attenuation that occurs as a result of the interaction of the THz radiation with the internal structure of the sample material. The proposed technique is an extension of the centroid shift technique, initially proposed by Dines and Kak (1979), and relied on the analytical description of the THz signal proposed by Xu *et al.* (2003). The estimates from the technique were compared with the THz-TDS measurements of two $\alpha$-monohydrate lactose and polyethylene (PE) samples. It was found that the technique reasonably estimates scattering loss profile for both the cases without using *a priori* information of the physical characteristics of the sample or the material, which makes it very useful for mitigating scattering effects in real world applications such as standoff measurements. The research is published in *IEEE Photonics Technology Letters*, Volume-24 under the title 'Reduction of Scattering Effects in THz-TDS Signals' (Kaushik *et al.* 2012b).

- In Section II, we report a signal processing technique that does not rely on any analytical expression to describe the THz signal and produces features that are robust against various scattering conditions, without requiring *a priori* information of the sample's internal structure. Using the relation between the log magnitude spectrum of the reference and the sample measurements and an arbitrary frequency dependence of the scattering attenuation, a system of equations were formed that can be iteratively solved to result in a spectral function that is independent of the scattering attenuation and depends only on the reference signal and absorption from the sample. The technique was tested on THz-TDS measurements of two $\alpha$-monohydrate lactose and polyethylene (PE) samples and was found to be providing reasonable mitigation to the scattering contribution. The research is presented at the *Seventh International Conference on Intelligent Sensors, Sensor Networks and Information Processing (ISSNIP)*, 2011 and the proceeding was published under the title 'Scattering robust features for classification of materials using terahertz' (Kaushik *et al.* 2011).

- In Section II, we also present an iterative multilevel discrete wavelet transform based technique for estimating frequency dependent scattering baseline for transmission mode THz-TDS measurements. The method is tested on four sample pellets, two comprising $\alpha$-monohydrate lactose and PE (with different granularity), while the other two comprising $\alpha$-D-glucose (with different granularity) and PE. From the comparison of the scattering reduced spectrum with the scattering free/limited spectrum obtained from well prepared samples it was clear that the technique reasonably estimates most of the general scattering attenuation profile. The proposed method also helps in cleaning the measurements for other background contributions such as systematic errors due to laser drift to enable direct comparison with spectra of pure samples in a spectral data base for automated recognition. The research is published in *Applied Physics Letters*, Volume-101, 2012, under the title 'Terahertz fingerprinting in presence of quasi-ballistic scattering' (Kaushik *et al.* 2012c).

# Chapter 2

# Terahertz time domain spectroscopy: THz-TDS

THE introduction of terahertz time domain spectroscopy in the late 1980's offered a new and effective technique to explore the THz region. In the time domain, the broadband THz radiation takes the shape of a very short, single cycle pulse. The underlying mechanism behind the generation and detection of these extremely short pulses is based on the creation and gated detection of electromagnetic transients by using femtosecond laser pulses. This can be achieved either by: optical rectification of non-linear crystals, or transient photo-conductivity. This chapter first introduces the ultrafast and nonlinear methods to generate broadband THz pulses before comprehensively describing terahertz-TDS data analysis techniques.

## 2.1 Introduction

A THz system which generates, propagates and detects transient electromagnetic pulses is commonly referred as a pulsed THz system. In order to have a broadband energy spectrum in the THz frequency range, the time duration of the generated electromagnetic radiation must be of the order of picoseconds. The two most common approaches for generation and detection of pulsed THz radiation from femtosecond laser pulses are based on either photoconductive switches or second order non-linear optical crystals. The first THz emitter and detector prototypes were realized by Fattinger and Grischkowsky (1988) and Fattinger and Grischkowsky (1989), using a photoconductive antenna. The commercial unavailability of the photoconductive antennas in the late 1990's caused many THz research groups around the world to prefer non-linear crystals like for example ZnTe for generation of THz pulses based on optical-rectification. This technique was first demonstrated for generating far-infrared radiation using ZnTe and $LiNbO_3$, by Yang *et al.* (1971).

There are many methods for performing terahertz spectroscopy. The first and one of the earliest techniques is the Fourier Transform Spectroscopy (FTS) (Ferguson and Zhang 2002). In FTS, the sample under study is placed in an optical interferometer system and is illuminated with a thermal source with broad spectral range. It is scanned for a length of one interferometer arm; while a detector such as helium cooled bolometer (Ferguson and Zhang 2002) is used to detect the resulting signal. The Fourier transform of the measured data leads to the determination of the sample's radiated power spectral density. Although FTS has the advantage of being able to characterize a material over a wide bandwidth, its performance is fundamentally limited by its spectral resolution.

For high resolution spectral measurements, narrowband spectroscopy is an appropriate method (Ferguson and Zhang 2002). In narrowband spectroscopy the terahertz source as well as detector can be tuned across a desired frequency range for determining the optical properties of the sample under study within this bandwidth. However, tuning of source and detector is a time consuming and costly process that limits the applicability of this method.

The most recent technique is known as terahertz time domain spectroscopy (THz-TDS). In this technique the sample is irradiated with very short duration broadband

terahertz pulses generated using ultrafast laser pulses. Typically, a standard THz-TDS system has bandwidth up to 4 THz. However, recently a few new photoconductive antennas reporting bandwidths up to 8 THz (Shen *et al.* 2004) and optical rectification systems with bandwidths up to 40 THz have been demonstrated (Wu and Zhang 1997, Sinyukov and Hayden 2002). A THz-TDS system has a number of other advantages, such as the ability to make coherent measurements of the transmitted THz electric field, thus providing highly sensitive and time resolved amplitude and phase information. The frequency range of a pulsed THz system is equal to the classical vibrational frequency range of polar molecules, enabling them to study rotational and vibrational modes of molecules. This makes pulsed THz systems suitable for carrying out spectroscopic studies of biomolecules (Withayachumnankul *et al.* 2007).

In this Chapter, we will review the fundamental physics behind THz generation and detection using both non-linear crystals and photoconductive switches and outline the basic principles of terahertz time-domain spectroscopy (THz-TDS).

## 2.2 Generation and detection of THz waves

A typical pulsed THz wave generation and detection system is a pump and probe setup as depicted in Fig. 2.1. The femtosecond (fs) laser pulses are split into separate pump and probe beams using a beam splitter. The pump beam is incident on a photoconductive or an electrooptical emitter to generate THz radiation. The radiation is then collimated and focused on the sample under study by using a set of parabolic mirrors.

A similar set of parabolic mirrors are used to refocus and collimate the sample transmitted THz pulse on the detector. A mechanical delay line is typically used to change the time delay between THz pulse and the probe pulse. The delayed probe beam is used to optically gate the photoconductive THz detector, modulating the THz field and thus allowing measurement of the instantaneous THz electric field at instants controlled by the relative delay between the pump and probe beams. To increase the sensitivity, the pump beam is modulated by an optical chopper, and the THz-induced modulation on the probe beam is extracted by a lock-in amplifier. This pulsed information acquired in the time domain is transformed to the frequency domain with a Fourier transform from which spectral information can be obtained.

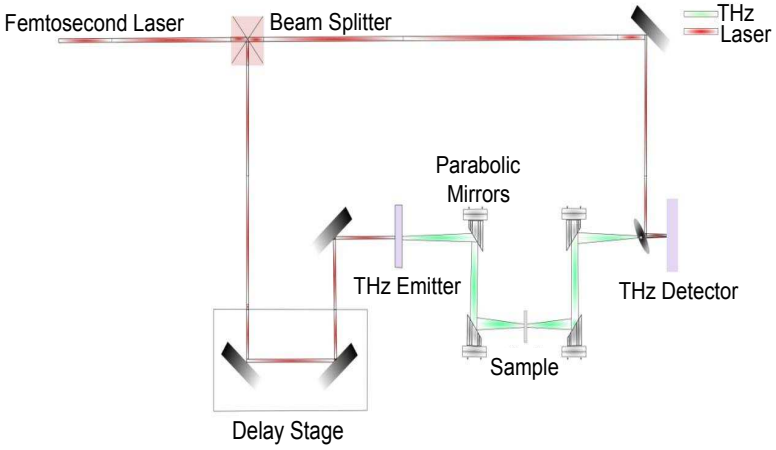


**Figure 2.1. A basic THz-TDS setup.** Illustration of a basic THz-TDS setup showing the femtosecond laser source, beam splitter, delay stage, THz emitter, detector, parabolic mirrors and sample under study.

### 2.2.1 Photoconductive antennas

The photoconductive antenna (PCA) is one of the most commonly used components in the generation and detection of THz radiation. A PCA is essentially an electrical switch that becomes conductive when exposed to light. When the energy of the incident photon is sufficiently greater than the band gap energy of the PCA material, free carriers (electrons and holes) are generated which makes the switch conducting. A PCA based source chip for pulsed THz radiation is shown schematically in Fig. 2.2. A PCA emitter consists of a semiconducting substrate with two metal electrodes. To generate the THz signal, a DC bias is applied across the emitter electrodes and an ultrafast laser pulse is focused near the anode of the antenna. The ultrafast laser pulse acts as transient switch and causes rapid generation of free carriers. The free carriers are then driven, under the influence of the DC bias, across the gap and produce a photocurrent. This time-varying current produces electromagnetic radiation in the form of a THz pulse. Since the mobility of holes is much smaller than the electrons, their contribution can be ignored in most cases. Under this assumption, the current density can be expressed as:

$$J(t) = N(t)e\mu E_{\mathrm{b}}, \tag{2.1}$$

where $N$ is density of photocarriers, $e$ denotes the elementary charge, $\mu$ is the mobility of electron, and $E_{\mathrm{b}}$ is the bias electric field. The photocarrier density $N(t)$ is determined by the incident laser pulse shape and the carrier lifetimes. The photocurrent thus produced is also time varying and therefore generates an electromagnetic pulse

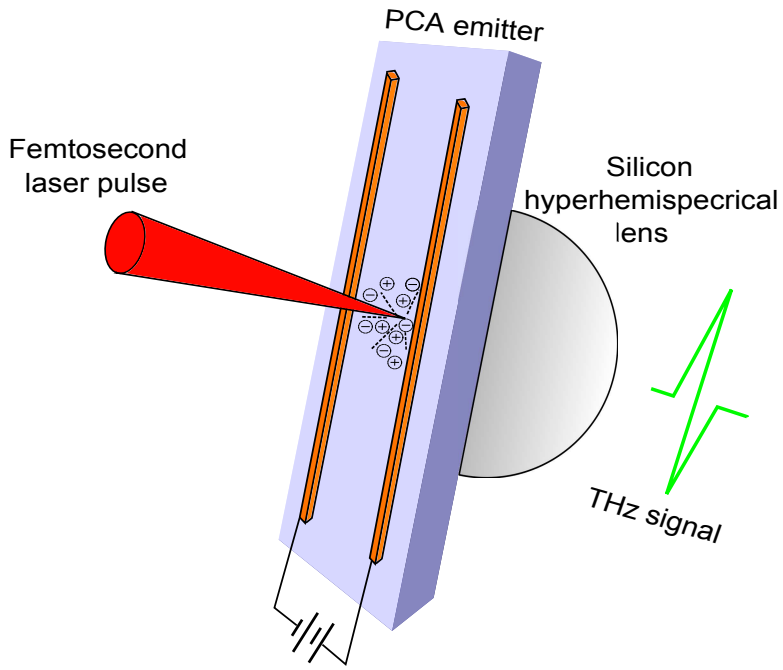


**Figure 2.2. Schematic illustration of a photoconductive switch.** Two biased parallel metal strip lines with a typical separation of some tens of micrometer are embedded in a semiconductor substrate. The THz pulse is generated when a fs-laser pulse is focused near the anode of the antenna thereby creating free charge carriers, which are accelerated in the electric field between the striplines. These are radiated into the substrate (and in opposite direction) and collimated by a hyper-hemispherical silicon lens.

with far-field electric field given by:

$$\begin{aligned} E_{\mathrm{THz}} &= \frac{A}{4\pi\epsilon_0 c^2 z}\frac{\delta J(t)}{\delta t}, \\ &= \frac{Ae}{4\pi\epsilon_0 c^2 z}\frac{\delta N(t)}{\delta t}\mu E_{\mathrm{b}}, \end{aligned} \tag{2.2}$$

where $A$ is the area in the gap illuminated by the laser light, $\epsilon_0$ is the vacuum permittivity, $c$ is the speed in vacuum, and $z$ is the distance between the field point and the THz source. When the PCA substrate is excited with the ultrafast laser pulse, it becomes a conducting medium and therefore the induced field screens the biased field. Taking this into account, the expression for photocurrent becomes (Darrow *et al.* 1992):

$$J(t) = \frac{\sigma(t)E_{\mathrm{b}}}{\frac{\sigma(t)\eta_0}{1+n}+1}, \tag{2.3}$$

where $\sigma$ denotes the conductivity of the substrate, $\eta_0$ represents the impedance of air, and $n$ represents the refractive index of the substrate. As the conductivity of the substrate is induced by the exciting laser, it is proportional to the excitation laser intensity

($T_0$). The resulting THz electric field can now be expressed as:

$$\begin{aligned} E_{\mathrm{THz}} &\propto \frac{d\sigma(t)}{dt}\frac{1}{\left[\frac{\sigma(t)\eta_0}{1+n}+1\right]^2}, \\ &\propto \frac{I_0}{(1+kI_0)^2}, \end{aligned} \tag{2.4}$$

where $k = \sigma(t)\eta_0/I_0(1+n)$.

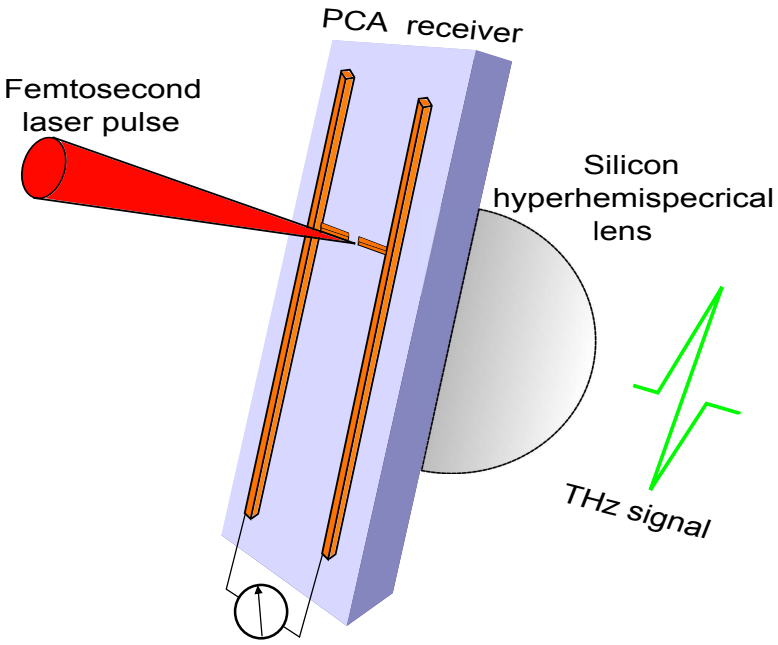


**Figure 2.3. A photoconductive antenna based THz receiver.** The THz receiver is gated by focusing a pulsed laser in the 5 $\mu$m wide gap between the electrodes. The injected carriers are driven by the received THz field and a current is measured.

On the receiver side, a PCA based THz detector is very similar to the PCA based THz emitter, the major difference being, that a detector has H-shaped electrodes connected to a current sensor, instead of a power supply. As shown in Fig. 2.3, when the optical probe beam is focused between protruding parts of the electrodes, it generates free carriers in the substrate which causes resistance in the switch to drop to about a hundred Ohms. On the other hand, the electric field of the focused incoming THz radiation induces a transient bias voltage across the 5 $\mu$m gap between the protruding arms of the electrodes of the receiving antenna. In the PCA based THz generation and detection setup depicted in Fig. 2.1, the electric field across the electrodes of the photoconductive switch at any given point in time can be sampled by the optical probe pulse, by delaying the optical probe pulse relative to the incoming THz pulse. This time delay allows the measurement of the time-dependence of the photocurrent. The THz field induced

current can be expressed as:

$$\bar{J} = \bar{N} e \mu E_{\tau}, \tag{2.5}$$

where $\bar{N}$ is the average electron density, and $\tau$ denotes the time delay between the optical probe pulse and the incoming THz pulse.

In order to generate or detect THz radiation, the switching time of the PCA should be within sub-picosecond range. The overall switching time can be divided into two parts: (i) switch on, and (ii) switch off time. Switch on time is basically a function of the laser pulse duration, while the switch off time is governed by the carrier lifetime of the semiconductor substrate. Thus, the desirable properties for a photoconductive material for generation and detection of THz are: short carrier lifetime, high carrier mobility and a high breakdown voltage. Several photoconductive materials have been tested, but the most common materials used for generating and detecting THz radiation are RD-SOS and LT-GaAs. More detailed descriptions and characterizations of photoconductive antennas can be found in Jepsen *et al.* (1996), Jepsen and Keiding (1995), and Gürtler *et al.* (2000).

### 2.2.2 Nonlinear crystals—non-linear optical processes

#### Optical rectification

THz pulse generation using photoconductive antennas utilizes real photoinduced carriers, while optical rectification is a method that uses non-linear optical process, which can be considered as virtual photoinduced carriers. The key component for THz generation and detection using non-linear optical processes is a non-linear crystal. The linearity of a dielectric medium is characterized by the relation between its polarization density ($P$) and the incident electric field ($E$). For a medium to be linear, the relation between its $P$ and $E$ needs to be linear, while for a non-linear medium, this relation is non-linear, as illustrated in Fig. 2.4.

When an ultrafast optical pulse interacts with a non-linear crystal, it induces a time varying polarization of dipoles within the crystal. The time dependence of the induced polarization follows the intensity envelope of the incident optical pulse. Optical rectification is process that requires a second-order nonlinear optical effect. Let $E(t)$ represent the electric field of the incident optical pulse, the second-order time varying polarization in the non-linear crystal is given by:

$$P_{\mathrm{NL}}^{(2)}(t) = \chi^{(2)} E^2(t), \tag{2.6}$$

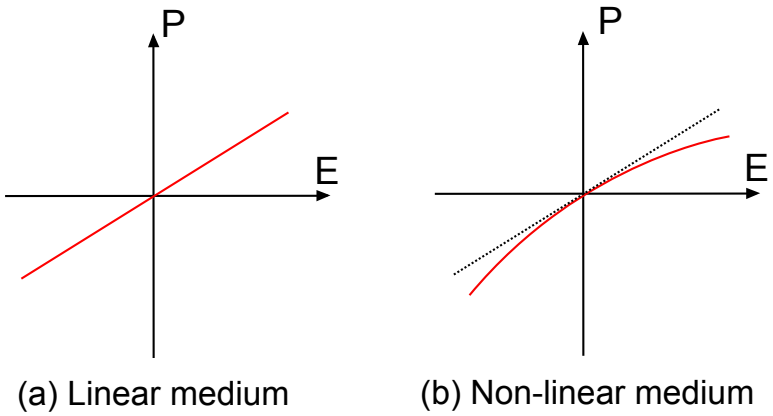


**Figure 2.4. The P-E relation.** The PE relation for (a) a linear dielectric medium, and (b) a nonlinear medium.

where $\chi^{(2)}$ represents the second order susceptibility of the crystal, and NL denotes the non-linearity. When the incident light is a plane wave, $E(t)$ can be expressed as:

$$E(t) = \int_0^\infty E(\omega)\exp(-i\omega t)d\omega + \text{c.c.}, \tag{2.7}$$

where c.c. represents the complex conjugate of all terms to its left. By substituting Eq. 2.7 in to Eq. 2.6, the polarization for optical rectification is given by:

$$P_{\text{NL}}^{(2)}(t) = 2\chi^{(2)}\int_0^\infty\int_0^\infty E(\omega_1)E^*(\omega_2)\exp\left[-i(\omega_1-\omega_2)t\right]d\omega_1 d\omega_2. \tag{2.8}$$

Because an ultrashort optical pulse $E(t)$ contains a great number of frequency components, the optical rectification process results in a oscillating polarization with a number of difference frequencies ranging from near zero to a few terahertz. In the far-field, the radiated THz electric field $E_{\text{THz}}(t)$ is proportional to the second time derivative of $P_{\text{NL}}^{(2)}(t)$:

$$E_{\text{THz}}(t) \propto \frac{\partial^2 P_{\text{NL}}^{(2)}(t)}{\partial t^2}. \tag{2.9}$$

The susceptibility term $\chi^{(2)}$ depends on the structure of the crystal. Therefore, if the crystal structure and incident optical electric field are known, Eq. 2.9 can be used to determine the far-field waveform of the THz radiation. However, many other factors such as crystal orientation, dimension, absorption and dispersion, diffraction, phase matching and saturation, can affect the pulse shape, and frequency distribution (Zhang and Xu 2009). A suitable non-linear crystal for THz generation and detection must be highly transparent to both optical and THz frequencies to minimize energy dissipation and have a large electro-optic coefficient to achieve high conversion efficiency. Dielectric crystals such as, $LiNbO_3$, and $LiTaO_3$ and semiconductors such as, GaAs, and ZnTe

satisfy these requirements and are commonly used in THz time domain spectroscopy setups.

### Elecrooptical sampling

Electrooptical (EO) sampling can be considered as the inverse process of optical rectification. The THz field is measured by modulating the optical probe beam inside the crystal. This is carried out by copropagating a linearly polarized optical probe beam with the THz beam in the crystal. The electric field of the THz beam induces a change in the refractive index of the lens, which in turn modulates the phase and thus changes the polarization of the probe beam. This polarization change is then converted to intensity change by an Wollaston prism, followed by a pair of balanced photodiodes, to suppress the common laser noise while doubling the signal.

A typical EO detection setup is illustrated in Fig. 2.5. The pellicle beamsplitter reflects the optical probe beam to copropagate it with the THz beam through the ZnTe crystal. The ZnTe crystal phase modulates the optical beam according to the instantaneous amplitude of the THz field. For a ZnTe crystal with thickness $d$, the phase delay of the optical beam can be calulated by:

$$\Gamma = \frac{\pi d n_o^3 \gamma_{41} E_{\mathrm{THz}}}{\lambda} (\cos\ \alpha\ \sin\ 2\phi + 2 \sin \alpha\ \cos\ 2\phi), \tag{2.10}$$

where $\lambda$ is the optical wavelength; $n_o$ is the optical refractive index of the ZnTe crystal; $\gamma_{41}$ is the electro-optical coefficient of the crystal; $\alpha$ and $\phi$ are the polarization angles of the THz beam and the optical probe beam with respect to the $\langle 001 \rangle$ direction, respectively (Gorenflo 2006). Maximum phase retardation is achieved at $\alpha = \phi = 90^\circ$ (Gorenflo 2006). In the absence of the copropagating THz beam, the optical beam passes through the crystal without phase modulation. Then, the optical beam which is still linearly polarized, enters the quarter-wave plate at a polarization angle of $45^\circ$ with respect to the optical axis of the wave plate. The quarter-wave plate retards one component of the optical beam by $90^\circ$ with respect to its orthogonal component, thus making it circularly polarized. The Wollaston prism then splits the optical beam into its two orthogonal components. The intensity difference between the two components is now measured using balanced photodiodes. In the absence of the copropagating THz beam, this difference is zero. When the copropagating THz beam is present, the optical beam gets phase modulated and changes its polarization from linear to strongly elliptical after passing through the non-linear crystal. The quarter-wave plate retards

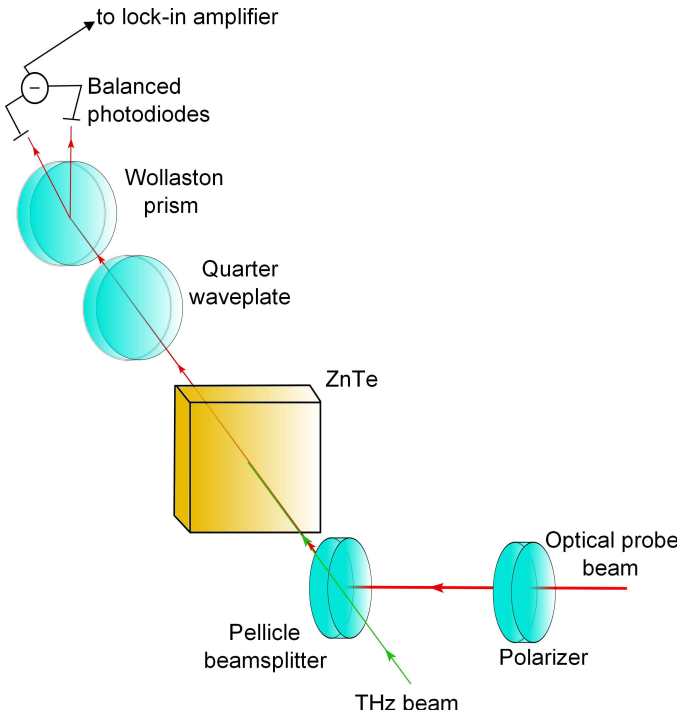


**Figure 2.5. A typical EO detection setup.** The pellicle beamsplitter reflects the optical probe beam to copropagate it with the THz beam through the ZnTe crystal. The ZnTe crystal phase modulates the optical beam according to the instantaneous amplitude of the THz field. The quarter-wave plate retards the phase of one component by 90° with respect to the other, changing the polarization of the optical beam to weakly elliptical. The Wollaston prism then separates the optical beam into its two orthogonal components. These two components that now have different intensities are fed to a balanced photodetector. The photodetector then produces the difference signal that is directly proportional to the THz beam amplitude.

the phase of one component by 90° with respect to the other, changing the polarization of the optical beam to weakly elliptical. The Wollaston prism then separates the optical beam into its two orthogonal components. These two components that now have different intensities are fed to a balanced photodetector. The photodetector then produces the difference signal that is directly proportional to the THz beam amplitude. To obtain the maximum temporal resolution and detection bandwidth, the optical probe beam and the THz beam should be phase matched. More detailed descriptions and characterizations of non-linear crystals, optical rectification and electrooptic sampling can be found in Gorenflo (2006) and Zhang and Xu (2009).

## 2.3 THz time domain spectroscopy

In Section 2.2, we discussed the important THz generation and detection techniques in detail. There are two configurations in which pulsed THz systems are usually operated: transmission mode and reflection. Most commercial pulse THz system are designed to operate in one mode only, however it is possible to build customized systems which support both the modes. Although both modes have their advantages, transmission mode systems tend to be more popular as it is easier to align. In this section we provide a detailed description of the transmission mode THz-TDS systems. Here, we will describe two transmission mode systems, one employing PCAs for THz generation and detection, while the other using non-linear crystals. Then we will discuss the data acquisition and analysis techniques for THz-TDS systems.

### 2.3.1 THz-TDS using PCAs

Fig. 2.6 shows a typical transmission mode THz-TDS setup using PCAs as emitter and detector. A MiraSeed (Coherent) Ti:sapphire femtosecond mode-locked laser pumped by a Verdi (Coherent) V6 is used as the source of the optical pulses. The output pulses from the femtosecond (fs) laser have duration less than 50 fs at a repetition rate of 76 MHz. The output power of the laser is 0.75 W with a center wavelength of 800 nm. The femtosecond laser beam then is split into two beams, the probe beam and the pump beam, using a beam splitter. The pump beam laser is modulated by an optical chopper and thereafter is focused onto a photoconductive emitter that is biased at 95 V dc by a 6 mm diameter plano-convex optical lens. The generated THz pulse is emitted into the GaAs substrate in a cone normal to the interface. The THz radiation is then collimated by a crystalline hyperhemispherical silicon lens attached to the back side of the PCA emitter chip. The silicon lens also helps in limiting the multiples reflections from the semiconductor material (Jepsen and Keiding 1995, Rudd and Mittleman 2002). The THz pulse from the silicon lens is then focused on the sample under study using off-axis gold plated paraboloidal mirrors with an effective focal length 100 mm. In this geometry we use a f-2f arrangement of the mirrors to produce a focus on the sample position. A similar set of parabolic mirrors (with 2f-f) arrangement is used to refocus and collimate the sample transmitted THz pulse on the detector. On the receiving end, the probe beam is focused using a plano-convex lens onto the photoconductive detector. The averaged THz pulse can be sampled and measured by the

probe beam at instants controlled by the relative delay between the pump and probe beams. The received signal is then passed to a lock-in amplifier (model SR830).

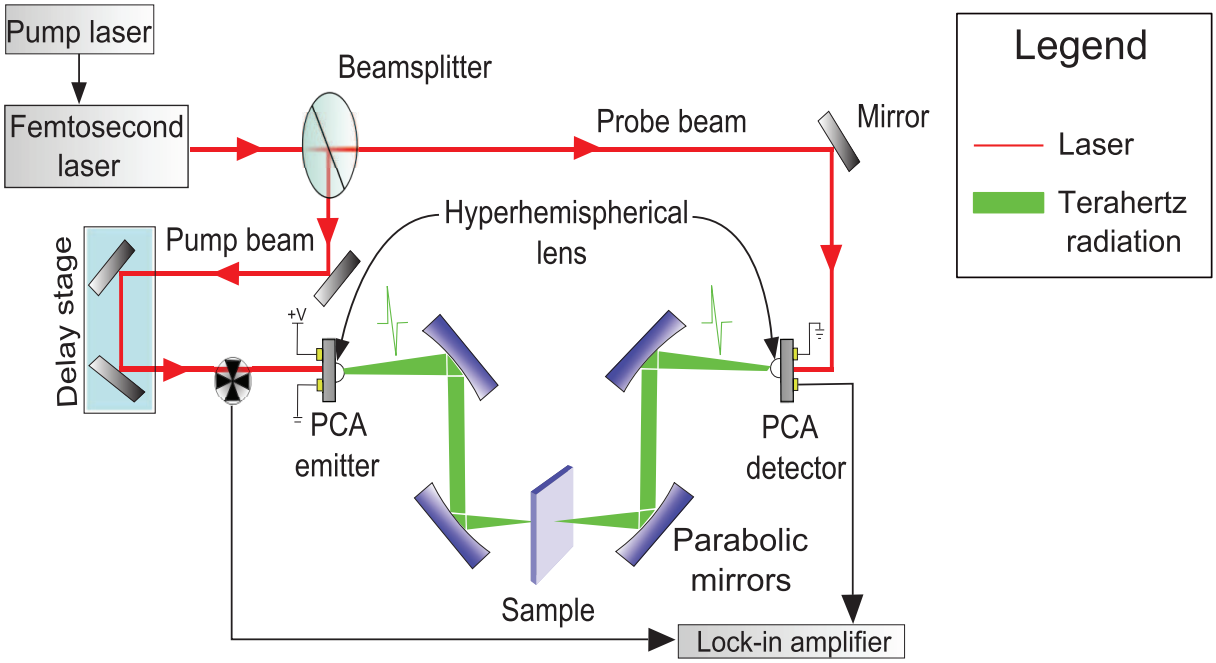


**Figure 2.6. A typical PCA based THz-TDS setup.** Schematic diagram of a complete photoconductive antenna (PCA) based THz-TDS system.

### 2.3.2 THz-TDS using non-linear crystals

Fig. 2.7 shows a typical transmission mode THz-TDS setup using non-linear crystals as emitter and detector. This setup is quite similar to the one that uses PCAs, albeit with major differences at the detection end. On the emitter side, when the ultrafast pump beam interacts with the crystal, it induces time varying polarization dipoles in the crystal. As a result of optical rectification due to the second order frequency mixing in the crystal, THz radiation is generated. While, on the detector end, a pellicle beamsplitter is used to copropagate the THz beam with the optical probe pulse through the crystal to phase modulate the optical beam according to the THz amplitude. The optical beam is then split into its two orthogonal components by using a quarter-wave plate and a Wollaston prism. The balanced photodetector then measures the intensity difference between the two components of the optical beam, which is directly proportional to the THz beam amplitude. Further details on THz generation and detection using non-linear crystals can be found in Section 2.2.2.

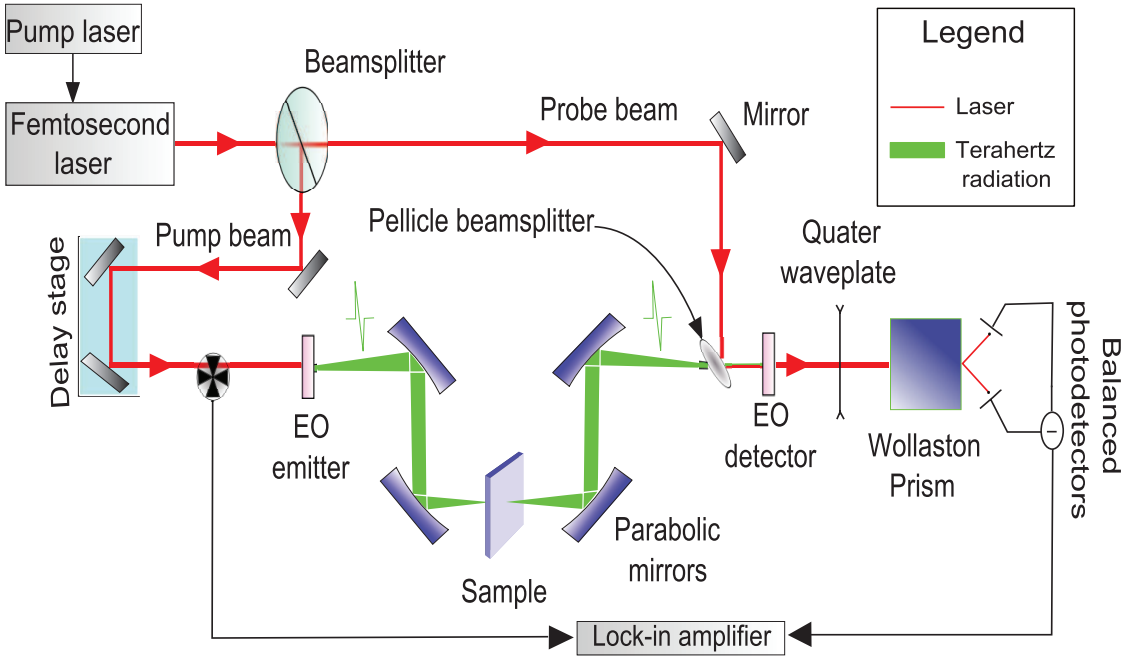


**Figure 2.7. A typical EO based THz-TDS setup.** Schematic diagram of a complete electrooptic based THz-TDS system using non-linear crystals for THz generation and detection.

### Component list for THz-TDS spectrometer

In this Thesis, we have used a PCA based transmission mode THz-TDS system as illustrated in Fig. 2.6. The components used in this spectrometer are listed as follows:

- MiraSeed (Coherent) Femtosecond Modelocked Ti: Sapphire laser
- Diode-Pumped laser (Coherent) Verdi V6 (not shown)
- XPS motion controller
- ILS linear stage (Newport)
- SR540 chopper controller with 30 slots chopper blade
- SR830 lock-in amplifier
- Stripline GaAs photoconductive antennas for emitter and detector - (Zomega)
- Standard biasing power supply

- Paraboloidal mirrors (Edmund Optics)
- Retroreflector (Edmund Optics)
- Plano-convex lens 6 mm diameter with a focal length of 12 mm
- Custom-built plano convex lens holder
- IR filters (Newport)
- XYZ stages (Newport)
- Non-polarised beamsplitter (Thorlabs)
- Custom-built antenna mount modules
- Valumax mirrors (Newport)

### 2.3.3 Data acquisition and analysis for transmission mode THz-TDS

The temporal electric field is obtained by measuring the shape of the field strengths of the short electromagnetic pulse in time domain obtained using the THz-TDS spectrometer illustrated in Fig. 2.6. When a terahertz pulse passes through a sample material, its temporal shape changes and the extent of change depends on the linear response of the material (Fischer 2005). This linear response of a material is governed by its optical properties. Thus we can say that the temporal shape of the sample pulse contains the complete information of the dielectric function of the sample material, for example the attenuation of the pulse is an estimate of the absorption by the material and the time delay is indicative of the refractive index of the material. The detailed frequency dependence of the dielectric function can only be determined in the frequency domain. Thus in order to access this information, Fourier transformation of the THz pulse is carried out, and a comparison of this pulse with a reference pulse (assumed to

have traveled through vacuum) can lead to a determination of the average dielectric properties of the sample material (Fischer 2005).

Consider a monochromatic plane wave of angular frequency $\omega$ propagating through a material with complex dielectric constant $\hat{n} = n + i\kappa$ in +z direction. The time dependent electric field can be expressed as:

$$\begin{aligned} E(z,t) &= E_0(t)\exp\left\{i(\omega t + \frac{\hat{n}\omega}{c}z)\right\} \\ &= E_0(t)\exp\left\{i\frac{n\omega}{c}z\right\}\exp\left\{-\frac{\kappa\omega}{c}z\right\}, \end{aligned} \tag{2.11}$$

where $E_0(t) = E_0 e^{i\omega t}$ is the time-varying component of the incident electric field. Eq. 2.11 consists of an oscillating time-dependent term that represents the wave propagation and an exponential decay due to the absorption. In order to explain the frequency dependence of the dielectric functions, we will consider a THz pulse that has propagated through a sample of thickness $d$. As we want to study the dielectric function in the frequency domain, we take Fourier transform of Eq. 2.11:

$$E(\omega) = E_0(\omega)\exp\left\{i\frac{n(\omega)\omega}{c}z\right\}\exp\left\{-\frac{\kappa(\omega)\omega}{c}z\right\}. \tag{2.12}$$

Now, when a beam propagates from one medium with refractive index $n_1$ to another with refractive index $n_2$, there are some reflections losses at the medium boundaries. In order to compensate for these losses, we need to determine the transmission amplitude coefficient $T$ of this system, which is given by Fresnel's equations as follows:

$$T_{1\to 2} = \frac{2n_2}{n_1 + n_2}. \tag{2.13}$$

In a transmission mode THz-TDS setup, the THz beam has to propagate through two medium boundaries (air→sample→air) before reaching the detector. This further attenuates the signal and the total transmission amplitude coefficient $T$ for transmission mode THz-TDS system is given by:

$$\begin{aligned} T &= T_{\text{air}\to\text{sample}} \cdot T_{\text{sample}\to\text{air}}, \\ &= 4\frac{n(\omega)}{\{n(\omega)+1\}^2}, \end{aligned} \tag{2.14}$$

and thus the THz electric field, after propagation through a sample of thickness $d$ and considering the transmission attenuation at the medium boundaries, is given by:

$$E_{\text{sample}}(\omega) = E_0(\omega)T\exp\left\{i\frac{n(\omega)\omega}{c}d\right\}\exp\left\{-\frac{\kappa(\omega)\omega}{c}d\right\}, \tag{2.15}$$

while the field of the reference pulse, that has propagated the same distance in vacuum ($n = 1, \kappa = 0$) is given by:

$$E_{\text{reference}}(\omega) = E_0(\omega) \exp\left\{ i\frac{\omega d}{c} \right\}. \tag{2.16}$$

By dividing Eq. 2.15 with Eq. 2.16, we can determine the complete transmission coefficient of the system. This is given by:

$$\begin{aligned} T_c(\omega) &= Ae^{i\phi} = \frac{E_{\text{sample}}(\omega)}{E_{\text{reference}}(\omega)}, \\ &= \frac{4n(\omega)}{\{n(\omega)+1\}^2} \exp\left\{ i\frac{(n(\omega)-1)\omega}{c} d \right\} \exp\left\{ -\frac{\kappa(\omega)\omega}{c} d \right\}. \end{aligned} \tag{2.17}$$

The index of refraction can directly be extracted from the phase $\phi$ in Eq. 2.17 as:

$$n(\omega) = 1 + \frac{\phi c}{\omega d}, \tag{2.18}$$

and the complex index $\kappa$ can be determined by from the complex amplitude $A$ as follows

$$\kappa(\omega) = -\frac{c}{\omega d} \left\{ \frac{(n(\omega)+1)^2}{4n(\omega)} A \right\}. \tag{2.19}$$

The absorption coefficient $\alpha$ is commonly expressed as:

$$\begin{aligned} \alpha(\omega) &= 2\frac{\kappa(\omega)\omega}{c}, \\ &= -\frac{2}{d} \ln\left\{ \frac{(n(\omega)+1)^2}{4n(\omega)} A \right\}. \end{aligned} \tag{2.20}$$

In Fig. 2.8 we show the acquisition and analysis process of a 3 mm thick polyvinyl chloride (PVC) sheet by a transmission mode THz-TDS spectroscopy setup as illustrated in Fig. 2.6. This experiment is conducted in a nitrogen purged environment to eliminate the presence of water absorption lines in the measurements. The inset (a) shows the temporal profiles reference and sample THz pulses. The effects of absorption (attenuation of the main peak maximum amplitude) and refractive index change (time delay of the pulse) can be clearly seen. Inset (b) shows the spectral amplitude of the reference and sample pulses after the fast Fourier transform process. Using the Eq. 2.18, 2.19 and 2.20, we calculated the frequency dependent index of refraction $n(\omega)$ and the absorption coefficient $\alpha(\omega)$, which are shown in inset (c) and inset (d) respectively.

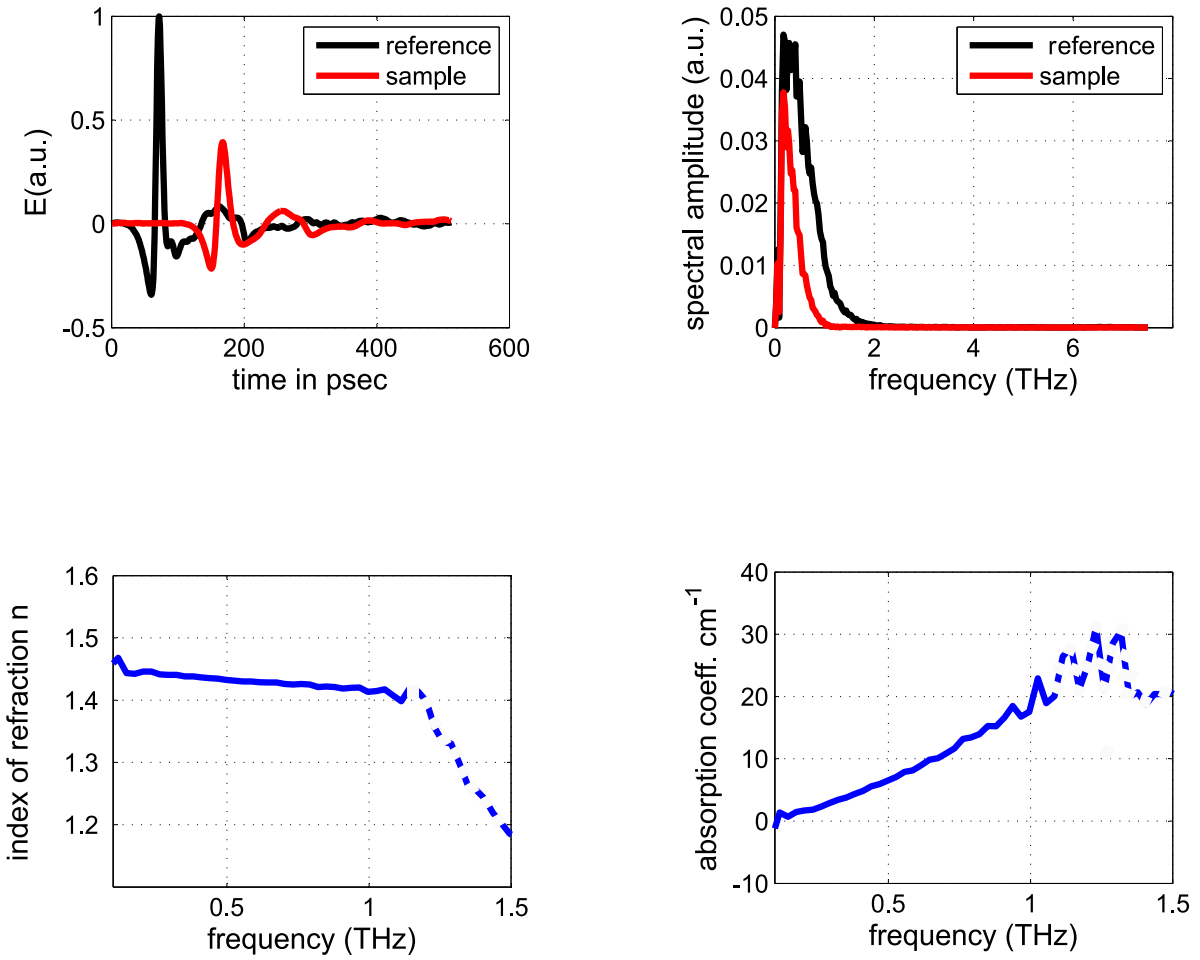


**Figure 2.8. Material parameter extraction.** An example for the determination of the dielectric function from a reference and sample (3 mm thick PVC polymer pellet) THz pulse. (a) The temporal shape of the reference pulse reflects the dielectric properties of the sample: the time delay of the pulse is due to the higher index of refraction, the attenuation of the peak amplitude is due to the absorption and the ringing after the main pulse is a characteristic for strong distinct resonance features. (b) These are clearly visible in the representation of the spectral amplitude. (c) From the frequency dependent amplitudes and phases the index of refraction and (d) the absorption coefficient is plotted as a function of frequency.

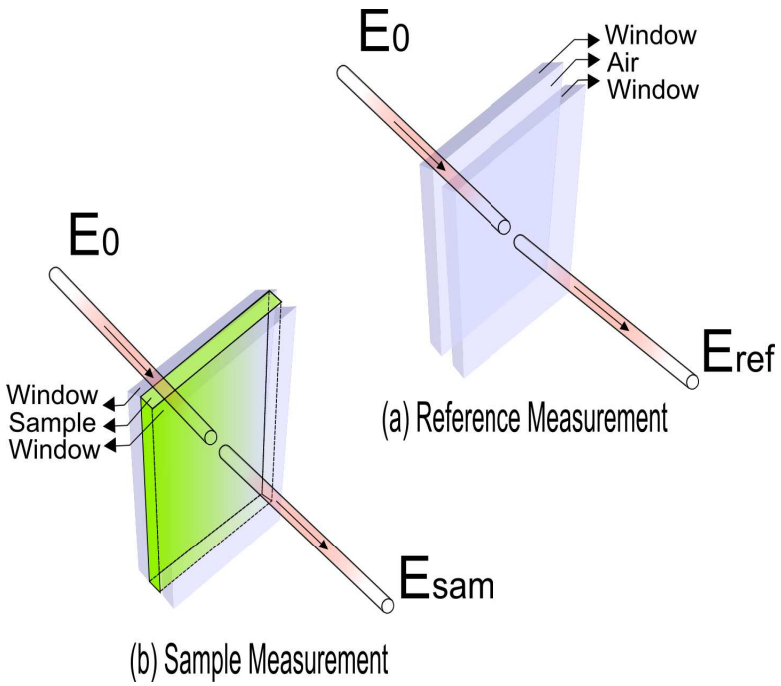


**Figure 2.9. Measurement with a sample cell.** (a) THz radiation propagates through an empty sample cell, as the reference. (b) THz radiation propagates through an identical sample cell, filled with the powder sample.

### 2.3.4 Measurement and data analysis of sample in a cell

Spectroscopy of powders, liquid or gas often requires a cell to hold or confine the sample. The cell is constructed of material that are transparent to THz, allowing the radiation to probe the sample material effectively. The cell windows must be optically thick enough, so that the Fresnel echoes generated at the cell to air and cell to sample interfaces can be separated in the temporal profile. In this section, we present the analysis of wave propagation and sample measurement in a cell.

Fig. 2.9 illustrates the propagation of T-rays through a cell during the measurements of the sample and reference data.

By analyzing the propagation geometry, we can express the reference and sample spectrum as:

$$\begin{aligned} E_{\mathrm{ref}}(\omega) &= \tau_{\mathrm{aw}}^2 \tau_{\mathrm{wa}}^2 E_0(\omega) \mathrm{FP}_{\mathrm{awa}}^2(\omega) \mathrm{FP}_{\mathrm{waw}}(\omega) \\ &\quad \exp\left[-jn_0(\omega)\frac{\omega d_{\mathrm{s}}}{c}\right] \exp\left[-j\hat{n}_{\mathrm{w}}(\omega)\frac{\omega d_{\mathrm{w}}}{c}\right], \end{aligned} \tag{2.21}$$

$$E_{\text{sam}}(\omega) = \tau_{\text{aw}}\tau_{\text{ws}}\tau_{\text{sw}}\tau_{\text{wa}}E_0(\omega)\text{FP}^2_{\text{aws}}(\omega)\text{FP}_{\text{wsw}}(\omega) \exp\left[-j\hat{n}_{\text{s}}(\omega)\frac{\omega d_{\text{s}}}{c}\right]\exp\left[-j\hat{n}_{\text{w}}(\omega)\frac{\omega d_{\text{w}}}{c}\right], \tag{2.22}$$

and the transfer function for this system is given by:

$$H(\omega) = E_{\text{sam}}(\omega)/E_{\text{ref}}(\omega) = \frac{\tau_{\text{ws}}\tau_{\text{sw}}\text{FP}^2_{\text{aws}}(\omega)\text{FP}_{\text{wsw}}(\omega)}{\tau_{\text{wa}}\tau_{\text{aw}}\text{FP}^2_{\text{awa}}(\omega)\text{FP}_{\text{waw}}(\omega)}\exp -j(\hat{n}_{\text{s}} - n_0)\frac{\omega d_{\text{s}}}{c}, \tag{2.23}$$

where the subscripts a, s and w are for air, sample, and window, respectively, and $d_{\text{s}}$ is the thickness of the sample. Therefore, $\tau_{\text{aw}}$ describes the propagation from air to window, $\tau_{\text{ws}}$ describes the propagation from window to sample and so on. Here, $\hat{n}_{\text{s}}$ is the complex refractive index of the sample and $n_0 = 1$ is the refractive index of free air. Here, $\text{FP}_{\text{aws}}$ is the Fabry-Pérot term for the reflections in the window, with air on one side and sample on the other side. Similarly, $\text{FP}_{\text{awa}}$ is the Fabry-Pérot term for the reflections in the window, with air on both the sides, while $\text{FP}_{\text{wsw}}$ and $\text{FP}_{\text{waw}}$ represents the Fabry-Pérot term for reflections in sample and air, with window on both sides, respectively. The generation and expression of the Fabry-Pérot term is discussed in detail in Section 3.2.

By assuming the reflections are removed from the sample and reference data, the transfer function can now be given by:

$$H(\omega) = \frac{\tau_{\text{ws}}\tau_{\text{sw}}}{\tau_{\text{wa}}\tau_{\text{aw}}}\exp\left[-j(\hat{n}_s - n_0)\frac{\omega d_s}{c}\right]. \tag{2.24}$$

If the refractive index of the cell windows is very close to that of air, then the transmission coefficients can be approximated as $\tau_{ws} \approx \tau_{wa}$ and $\tau_{sw} \approx \tau_{aw}$. Thus, the transfer function can be given by:

$$H(\omega) \approx \exp\left[-j(\hat{n}_s - n_0)\frac{\omega d_s}{c}\right], \tag{2.25}$$

and the optical constants be found from

$$n_s(\omega) = n_0 - \frac{c}{\omega d_s}\angle H(\omega), \qquad k_s(\omega) = -\frac{c}{\omega d_s}\ln|H(\omega)|. \tag{2.26}$$

The estimation of optical constants in the sample cell measurement setting relies heavily on approximations. Using the iterative parameter estimation technique proposed by Withayachumnankul (2009) the accuracy of the estimates can be improved.

### Dynamic range of the setup

As described in the Section 2.3.3, the dielectric function of a sample material can be determined by measuring the reference THz electric field $E_{\text{reference}}$ in an empty (or nitrogen purged) spectrometer and a sample THz pulse $E_{\text{sample}}$ propagating through a sample of thickness $d$ placed inside the spectrometer, in the THz beam path. The index of refraction $n$ and the absorption coefficient $\alpha$ are evaluated from the frequency dependent amplitudes $A$ and phase difference $\phi$ using the Eq. 2.18 and 2.20. Due to the single cycle nature of the pulse, the measured spectral amplitude exhibits a strong amplitude at low frequencies and a gradual roll-off at the high frequencies, until the detected signal level approaches the noise floor of the experiment (Jepsen and Fischer 2005). They showed that the normalized spectrum of the measured THz pulse is a good measure of the frequency dependent dynamic range of the experiment. Jepsen and Fischer (2005) introduced the following expression for the largest detectable absorption coefficient $\alpha_{\text{max}}$ that can be measured reliably for a given dynamic range ($\eta_{\text{DR}}$) and sample thickness $d$:

$$\alpha_{\text{max}}(\omega) = \frac{2}{d} \ln \left\{ \eta_{\text{DR}} \frac{4n(\omega)}{(n(\omega)+1)^2} \right\}. \tag{2.27}$$

Absorption features that exceed the value of $\alpha_{\text{max}}$ can not be detected and are saturated by the value of $\alpha_{\text{max}}$.

## 2.4 Post measurement processing for THz-TDS data

Post measurement, several signal processing techniques are applied to the THz-TDS data before it can be used for further analysis. These techniques commonly include signal averaging, denoising, and phase unwrapping. The following is a brief review of these techniques.

### 2.4.1 Signal averaging

In order to reduce the random noise in the measurement, multiple repeated measurements are averaged in time domain. Consider a noise free signal $y_0(t)$ and random noise (Gaussian distribution) $n(t)$ measured from a time invariant system. The $m^{\text{th}}$ measurement can be expressed as:

$$y_m(t) = y_0(t) + n_m(t). \tag{2.28}$$

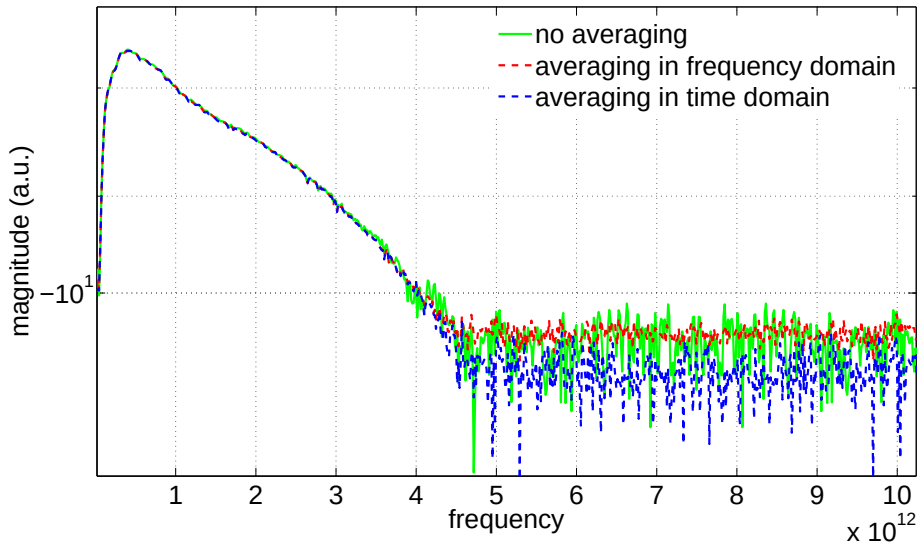


**Figure 2.10. Signal averaging.** A comparison of the measured amplitude spectrum obtained by time domain averaging, frequency domain averaging (using individual magnitude spectrum), and from a single measurement (no averaging). It is clear that time domain averaging exhibits significantly lower noise floor and thus an increase in bandwidth and dynamic range.

The expectation of the $m^{\text{th}}$ measurement can be given by:

$$E\left[y_m(t)\right] = y_0(t), \tag{2.29}$$

as the expectation of the random noise, a Gaussian process, is zero. Thus, averaging the signal in time-domain reduces the noise. This, however in not true of signal averaging in frequency domain. Consider the amplitude spectrum of the $m^{\text{th}}$ measurement:

$$\left|Y_m(\omega)\right| = \left|Y_0(\omega) + N_m(\omega)\right|. \tag{2.30}$$

The expectation of the magnitude spectrum is:

$$E\left[\left|Y_m(\omega)\right|\right] = E\left[\left|Y_0(\omega) + N_m(\omega)\right|\right]. \tag{2.31}$$

Clearly, the expectation of the magnitude spectrum of the $m^{\text{th}}$ measurement is not noise free. The difference in averaging performance between the two domains is also evident from the Fig. 2.10, where the effect of time domain averaging and frequency domain averaging is compared with a signal with no averaging.

### 2.4.2 Signal denoising

There are several sources of noise in a terahertz system. Both systematic and random noise sources contribute towards the overall noise of a measurement. As discussed in the previous section, one way of reducing the random noise is by time domain averaging of multiple repeated measurements, however, this method is not effective for systematic noise and also increases the data acquisition time. The other significant source for errors and ambiguity in THz systems is the system hardware itself. Electrical noise, optical reflections in hardware and several other hardware generated effects can interfere with the far-infrared properties of the sample under study by introducing unwanted artefacts (Mittleman *et al.* 1998). These artefacts can be removed by isolating the signal of interest from the unwanted components by performing deconvolution (Mittleman *et al.* 1998). However, deconvolution process is very sensitive to noise and can result in introduction for further errors in presence of noise.

An improved solution for the noise problem can be found in digital signal processing techniques such as wavelet denoising. Ferguson and Abbott (2001a) and Ferguson and Abbott (2001b), discussed the applicability of wavelet denoising algorithms, by testing them on THz measurements with simulated additive noise. Zhu *et al.* (2009) also applied wavelet based denoising to show an improvement in the SNR of the signals. However, wavelet based denoising has some drawbacks. The optimal wavelet choice can change from one system to another and is highly dependent on the pulse shape of the THz signal.

Another digital signal processing denoising algorithm based on moving average filtering was proposed by Pupeza *et al.* (2007). Their spatially variant moving average filtering (SVMAF) technique starts with establishing a confidence interval on the measured transfer function. This is followed by extraction of intermediate optical constants from the averaged transfer function. These optical constants were then smoothed using an average filter over the frequency range of the measurement. Using the new optical constants, the process is repeated and a new transfer function is obtained and accepted if it falls within the defined confidence interval.

### 2.4.3 Phase unwrapping

As can be seen in the Eq. 2.18, in order to calculate index of refraction, ($n$) and subsequently the absorption coefficient, ($\alpha$), phase information, ($\phi$) is required. The phase

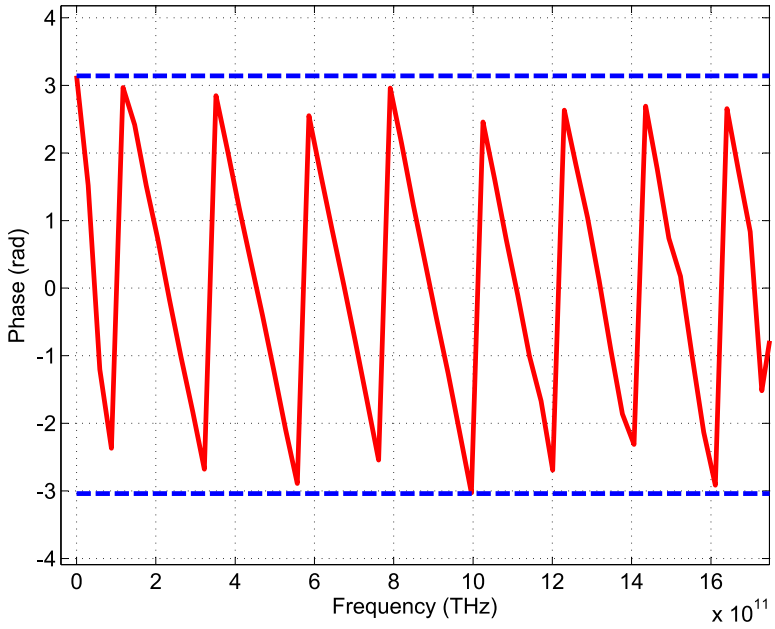


**Figure 2.11. Phase wrapping.** The phase of a transfer function, obtained from a measured PE sample is wrapped around $-\pi$ to $\pi$.

spectrum is obtained directly from the angle between the real and imaginary part of the transfer function.

However, this phase information is not continuous. Whenever the absolute value of the phase is greater that $\pi$, it jumps to opposite polarity by $2\pi$ (Hoffmann 2006). This wrapping is illustrated in the Fig. 2.11.

In order to obtain continuous phase greater than or above $2\pi$ , we need to unwrap the original phase information. This process was carried out in Matlab, using the following command:

$$\text{phase} = \text{unwrap}\left(\text{angle}\left(T_c(\omega)\right)\right), \tag{2.32}$$

where, $T_c(\omega)$ denotes the complex transmission coefficient, and angle refers to the wrapped phase information. However, at lower frequencies, noise can dominate the THz signal (Duvillaret *et al.* 1996). To avoid the propagation of unwrapping error at low frequencies to higher frequencies, the distorted phase is artificially linearly extrapolated at the low frequencies from the unwrapped phase at higher frequencies (Duvillaret *et al.* 1996). After the extrapolation the whole phase profile is then forced to start at zero. This procedure is illustrated in the Fig. 2.12.

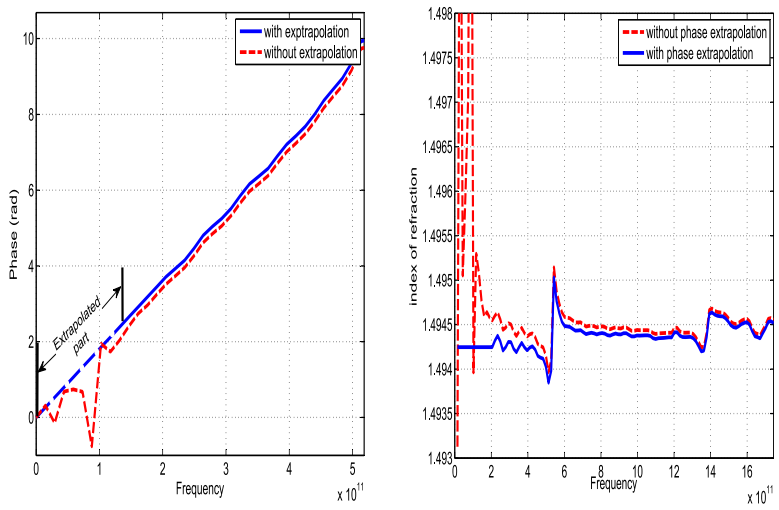


(a) unwrapped phase (b) index of refraction

**Figure 2.12. Phase extrapolation.** (a) The phase of a transfer function, obtained from the measurement of $\alpha$-monohydrate lactose and PE (mixed in 1:1 ratio and pressed into pellet) sample, unwrapped with and without phase extrapolation. The phase between 0.0 to 0.02 THz is linearly extrapolated from 0.02 THz to 0.04 THz. (b) The index of refraction determined with phase without and with phase extrapolation.

## 2.5 Chapter summary

This chapter presents an introduction to the several aspects of T-ray generation and detection techniques. Two major types of the coherent sources and detectors for T-rays discussed in this chapter are PCAs and non-linear crystals. When excited by ultrashort optical pulses, free carriers generated in PCAs play the main role in T-ray generation while in non-linear crystals induced dipoles are resposible for T-ray generation. Thus, the underlying mechanisms for T-ray generation is completely different for PCAs and non-linear crystals. Later, we introduce typical setups for THz-TDS in transmission mode followed by a list of components used in a typical THz spectrometer. To further the discussion on THz-TDS we present an introduction to material charaterisation using THz-TDS. Measurement and data analysis for single sample and sample in a cell is described by presenting analytical model for parameter extraction based on ray optics. In addition, this chapter also disccusses some post measurement signal processing techniques such as signal averaging, denoising and phase unwrapping, which are frequently implemented along with parameter extraction.

The next chapter introduces the basic concepts and theories that form the understanding platform of THz interaction with materials. The process of absorption and dispersion of THz wave when propagating through a medium with a complex refractive index is described in detail. Furthermore the discussion is extended to describe the cause of generation of the material *spectral fingerprints*.

# Chapter 3

# THz interaction with materials

COHERENT THz wave signals are detected in the time domain by mapping the transients of the electric field in amplitude and phase. This enables measurement of dielectric properties of the material sample under study. T-rays can easily penetrate most dielectric materials, which may be opaque to visible light, making T-rays a very useful tool for material characterization and identification in applications such as security screening, pharmaceutical and industrial quality control. In this chapter, we discuss the basic concepts and theories of terahertz interaction with materials and propagation in dielectric material. We then discuss, the various challenges and hurdles that constrain plausible scenarios for the application of terahertz technology for material classification and identification.

## 3.1 THz waves in matter

Just like any other frequency region, THz radiation can be described using macroscopic form of Maxwell's equations:

$$\nabla \cdot \mathbf{D} = \rho_f, \tag{3.1}$$

$$\nabla \cdot \mathbf{B} = 0, \tag{3.2}$$

$$\nabla \times \mathbf{E} = -\frac{\partial \mathbf{B}}{\partial t}, \tag{3.3}$$

$$\nabla \times \mathbf{H} = \mathbf{J}_f + \frac{\partial \mathbf{D}}{\partial t}, \tag{3.4}$$

where $\rho_f$ and $\mathbf{J}_f$ represent the free charge density and the free current density, respectively. The macroscopic fields $\mathbf{D}$ and $\mathbf{H}$ are related to the fundamental fields $\mathbf{E}$ (electric field) and $\mathbf{B}$ (magnetic field) according to the following relations:

$$\mathbf{D} = \epsilon_0 \mathbf{E} + \mathbf{P} = \epsilon \mathbf{E}, \tag{3.5}$$

$$\mathbf{H} = \frac{1}{\mu_0}\mathbf{B} - \mathbf{M} = \frac{1}{\mu}\mathbf{B}, \tag{3.6}$$

where $\epsilon_0$ and $\mu_0$ represent the permittivity and permeability of free space and $\mathbf{P}$ and $\mathbf{M}$ represent the polarization and magnetization, respectively. The last parts of the Eq. 3.5 and 3.6, where $\epsilon$ and $\mu$ are the electric permittivity and the magnetic permeability of the medium, are only valid under the assumption of an isotropic and linear medium. Using the linear relations described in Eq. 3.5 and 3.6, the electric field and the magnetic field can be disentangled from Eq. 3.3 and 3.4 as:

$$\nabla \times (\nabla \times \mathbf{E}) + \epsilon\mu \frac{\partial^2 \mathbf{E}}{\partial t^2} = -\mu \frac{\partial \mathbf{J}_f}{\partial t}, \tag{3.7}$$

$$\nabla \times (\nabla \times \mathbf{H}) + \epsilon\mu \frac{\partial^2 \mathbf{H}}{\partial t^2} = \nabla \times \mathbf{J}_f. \tag{3.8}$$

Using the vector identity $\nabla \times (\nabla \times \mathbf{A}) = \nabla(\nabla \mathbf{A}) + \nabla^2 \mathbf{A}$, the above equations can be rewritten as:

$$\nabla^2 \mathbf{E} - \epsilon\mu \frac{\partial^2 \mathbf{E}}{\partial t^2} = \mu \frac{\partial \mathbf{J}_f}{\partial t} + \frac{1}{\epsilon}\nabla \rho_f, \tag{3.9}$$

$$\nabla^2 \mathbf{H} - \epsilon\mu \frac{\partial^2 \mathbf{H}}{\partial t^2} = -\nabla \times \mathbf{J}_f. \tag{3.10}$$

Eq. 3.9 can be further simplified by assuming a linear relation between $J_f$ and $E$, given by $\mathbf{J}_f = \sigma \mathbf{E}$, where $\sigma$ represents the electrical conductivity and negligible free charge fluctuation, i.e., $\nabla \rho_f = 0$, as follows:

$$\nabla^2 \mathbf{E} = \sigma\mu \frac{\partial \mathbf{E}}{\partial t} + \epsilon\mu \frac{\partial^2 \mathbf{E}}{\partial t^2}, \tag{3.11}$$

where $\sigma$ and $\epsilon$ are real and independent. The wave equation for $\mathbf{H}$ can be simplified in a similar way. When propagating in a dielectric medium, the wave equation can be expressed as:

$$\nabla^2\mathbf{E} = \epsilon\mu\frac{\partial^2\mathbf{E}}{\partial t^2} = \frac{1}{v^2}\frac{\partial^2\mathbf{E}}{\partial t^2}, \tag{3.12}$$

where $v$ represents the velocity of propagation in the media. The general solution to the above equation is given by:

$$\mathbf{E}(\mathbf{r},t) = \mathbf{E}_0 \exp\left\{i(\mathbf{k}.\mathbf{r} - \omega t)\right\}, \tag{3.13}$$

where $\mathbf{k}$ represents the wave vector and $\omega$ denotes the angular frequency of the wave. For the wave equation in $\mathbf{H}$, the solution is similar to that of $\mathbf{E}$ and is given by:

$$\mathbf{H}(\mathbf{r},t) = \mathbf{H}_0 \exp\left\{i(\mathbf{k}.\mathbf{r} - \omega t)\right\}. \tag{3.14}$$

Substituting the Eq. 3.13 and 3.14 in the Maxwell's equations $\nabla \cdot \mathbf{E} = 0$ and $\nabla \cdot \mathbf{H} = 0$, we obtain:

$$\mathbf{k} \cdot \mathbf{E} = 0, \tag{3.15}$$

$$\mathbf{k} \cdot \mathbf{H} = 0, \tag{3.16}$$

which means that the electric field $\mathbf{E}$ and the magnetic field $\mathbf{H}$ are perpendicular to the wave vector, this can be seen in Fig. 3.1.

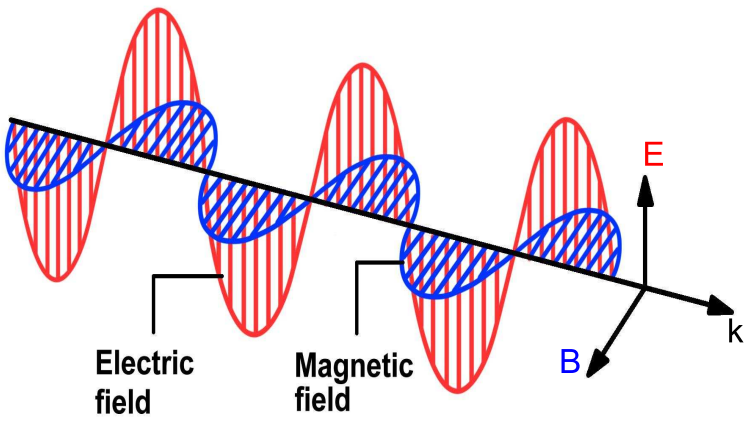


**Figure 3.1. The electromagnetic wave.** Illustration of an electromagnetic wave that consists of an electric field coupled with a magnetic field. The magnetic and electric fields of an electromagnetic wave are perpendicular to each other and to the wave vector.

The propagation of a electromagnetic wave in a medium is governed by the electromagnetic properties ($\epsilon$ and $\mu$) of the medium. Inserting Eq. 3.13 back into Eq. 3.12

yields the following expression:

$$k^2 = \epsilon\mu\omega^2. \tag{3.17}$$

This equation, known as the dispersion relation, completely describes the propagation of an electromagnetic wave in a medium. Here, $k$ represents the wavenumber of the medium, and for a non-magnetic medium is given by:

$$k = \frac{2\pi}{\lambda} = n\frac{c}{v}, \tag{3.18}$$

where, $\lambda$ represents the wavelength of the wave and $n$ represents the refractive index of the medium.

## 3.2 THz propagation across an interface

When an electromagnetic wave propagates across the interface of two media with different refractive indices, a fraction of the wave energy is refracted into the second medium while some of it is reflected back in the first medium. At the interface, both **E** and **H** follow Snell's law given by:

$$\hat{n}_a \sin\theta_i = \hat{n}_b \sin\theta_r, \tag{3.19}$$

where $\theta_i$ and $\theta_r$ are the angle of incidence and the angle of refraction, respectively, and $\hat{n}_a$ and $\hat{n}_b$ are the complex refractive indices of the two media. The complex refractive index, $\hat{n}(\omega) = n(\omega) + j\kappa(\omega)$, comprises the index of refraction, $n(\omega)$, and the extinction coefficient, $\kappa(\omega)$, which together, are referred to as the optical constants. In Fig. 3.2, when the wave propagates from medium $a$ into medium $b$, and the polarization of the electric field is perpendicular to the plane of incidence, the propagation is called $s$-polarized or Transverse Electric (TE) and when the polarization of electric field is parallel to the plane of incidence, the propagation is termed as $p$-polarized or transverse magnetic (TM).

The ratios of the refracted and reflected field amplitudes to the incident field amplitude are known as Fresnel reflection and transmission coefficients and are given in Table 3.1. When the angle of incidence is normal to the interface, the Fresnel coefficients for the two modes of propagation (TE and TM) are equal to each other:

$$\begin{aligned} \tau_{\mathrm{TE}} &= \tau_{\mathrm{TM}}, \\ \rho_{\mathrm{TE}} &= \rho_{\mathrm{TM}}. \end{aligned} \tag{3.20}$$

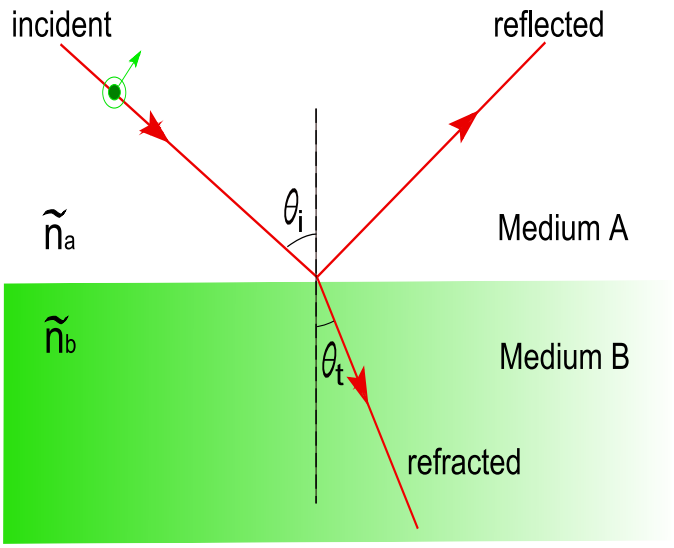


**Figure 3.2. Reflection and refraction.** Reflection and refraction of an incident wave at interface between two media.

**Table 3.1.** Fresnel coefficients for wave propagation across an interface.

| TE mode of propagation | | TM mode of propagation | |
|---|---|---|---|
| Transmission | Reflection | Transmission | Reflection |
| $\tau_{TE} = \frac{2\hat{n_a}\cos\theta_i}{\hat{n_a}\cos\theta_i+\hat{n_b}\cos\theta_t}$ | $\rho_{TE} = \frac{\hat{n_a}\cos\theta_i-\hat{n_b}\cos\theta_t}{\hat{n_a}\cos\theta_i+\hat{n_b}\cos\theta_t}$ | $\tau_{TM} = \frac{2\hat{n_a}\cos\theta_i}{\hat{n_a}\cos\theta_t+\hat{n_b}\cos\theta_i}$ | $\rho_{TM} = \frac{\hat{n_a}\cos\theta_t-\hat{n_b}\cos\theta_i}{\hat{n_a}\cos\theta_t+\hat{n_b}\cos\theta_i}$ |

Fresnel equations also predict that, a $p$-polarized wave (TM mode of propagation) propagating from medium $a$ into medium $b$ will not have any reflected component, if the angle of incidence is:

$$\theta_B = \tan^{-1}\left\{\frac{n_b}{n_a}\right\}. \tag{3.21}$$

This angle is called the *Brewster's angle*. Also, if the medium $a$ is optically denser than medium $b$, i.e., $n_a > n_b$, than for all angles greater than a critical angle given by:

$$\theta_c = \sin^{-1}\left\{\frac{n_b}{n_a}\right\}, \tag{3.22}$$

the reflectivity becomes unity and there is no transmission across the interface. This phenomenon is know as *Total Internal Reflection* $(TIR)$.

### Wave propagation in a slab

If the second medium is a slab, the traversing refractive wave will encounter the other interface where again reflection and refraction will take place. This process continues

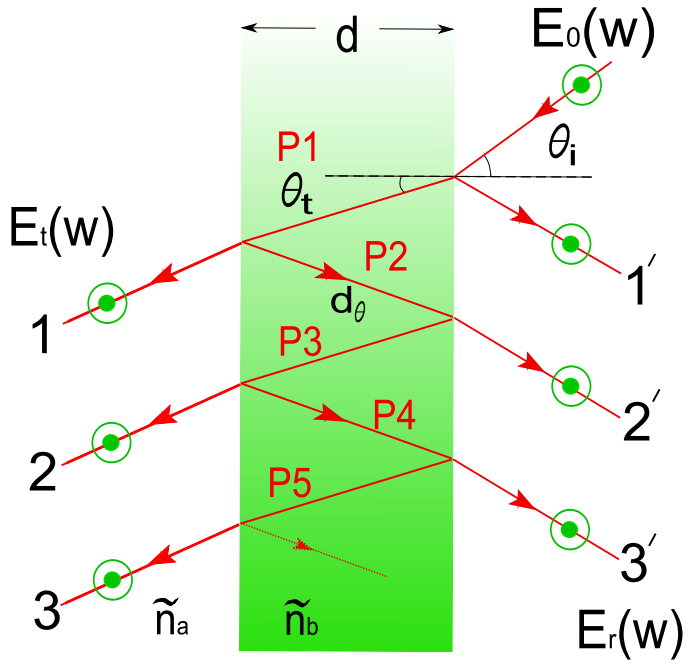


**Figure 3.3. Wave propagation through a dielectric slab.** Wave propagation through a slab of homogeneous dielectric: directly propagated pulse and Fresnel echoes.

until all of the wave energy is dissipated, thus splitting the wave into a number of intermediate paths. This process is illustrated in Fig. 3.3. In our experiments, the angle of incidence of the incoming waves is not strongly oblique and therefore, all the transmission and reflections paths overlap. The total transmitted wave is therefore the summation of these intermediate transmitted components. A general expression for that is given by:

$$\begin{aligned} E_t &= \tau\tau' E_0 \exp\left[-j\hat{n}_b \frac{\omega d_\theta}{c}\right] \\ &\quad \left\{1 + \rho^2 \exp\left[-j\hat{n}_b \frac{\omega 2 d_\theta}{c}\right] + \rho^4 \exp\left[-j\hat{n}_b \frac{\omega 4 d_\theta}{c}\right] + ...\right\} \end{aligned} \tag{3.23}$$

or

$$E_t = \tau\tau' E_0 \exp\left[-j\hat{n}_b \frac{\omega d_\theta}{c}\right] \mathrm{FP}, \tag{3.24}$$

where $E_0$ is the signal incident on the medium, and FP represents the Fabry-Pérot effect, and is given by (Withayachumnankul 2009) :

$$\mathrm{FP} = 1 + \rho^2 \exp\left[-j\hat{n}_b \frac{\omega 2 d_\theta}{c}\right] + \rho^4 \exp\left[-j\hat{n}_b \frac{\omega 4 d_\theta}{c}\right] + .... \tag{3.25}$$

## 3.3 Absorption and dispersion

In Section 3.1, we saw that an electromagnetic wave propagates with a phase velocity $v = 1/\sqrt{\epsilon\mu} = c/n$, which is slower than the velocity of light, in a conventional dielectric medium (real $\epsilon$, greater than unity). However, many commonly known dielectric medium have a complex $\epsilon$. This leads to a complex wave vector $\mathbf{k}$ and thus for a wave propagating in the $z$ direction, Eq. 3.13 can be rewritten as:

$$\mathbf{E} = \mathbf{E}_0 \exp\{i(\Re(k)z + \omega t)\} \exp\{-\Im(k)z\}. \tag{3.26}$$

Thus, when an electromagnetic wave propagates through a medium with a complex dielectric constant, it suffers attenuation (or amplification when imaginary part of $k$ is negative).

Until now, we have assumed that $\epsilon$ of medium is the same for all frequencies. In practice, this is not the case. Generally, dielectric media have a frequency dependent permittivity $\epsilon(\omega)$, this causes the different frequencies in the wave to travel at different velocities. This phenomenon is known as frequency dispersion. When a electromagnetic pulse travels through vacuum, all its frequencies travel at the same velocity ($c$) and maintain the pulse shape, but when the same pulse travels through a dielectric medium, frequency dispersion causes the pulse shape to change. Sometimes, a medium can have $\epsilon$ that changes non-linearly with the frequency and may have frequency bands that attenuate more than others (i.e. absorption). In order to show how an electromagnetic wave shape is distorted by the dispersive media, let us investigate an electromagnetic wave propagating through a transparent, isotropic, non-conducting, medium. The electric displacement inside the medium is given by Eq. 3.5. The electromagnetic field causes the electrons inside the medium to displace, giving rise to the electrical polarization $\mathbf{P}$:

$$\mathbf{P} = -Nes, \tag{3.27}$$

where $s$ is the displacement distance, $N$ is the density of the electrons and $e$ represents the electronic charge. The equation of motion of the charge displacement can be expressed by the following differential equation:

$$\frac{d^2s}{dt^2} + g\omega_0\frac{ds}{dt} + \omega_0^2 s = -\frac{e}{m}\mathbf{E}, \tag{3.28}$$

where $\omega_0$ represents the oscillation frequency of the electrons, $g$ represents the damping constant and $m$ represents the electron mass. The damping term $g\omega_0\frac{ds}{dt}$ accounts

for the electrons to eventually come to rest after oscillating for a long time under the influence of the electromagnetic field. The typical value for $g$ is this much less than unity. If the incident electromagnetic radiation is a monochromatic wave given by:

$$\mathbf{E}(t) = \mathbf{E}_0 \exp\{-i\omega t\}, \tag{3.29}$$

where $\omega$ is the angular frequency of the wave, then the solution to the Eq. 3.28 can be given by:

$$s(t) = s_0 \exp\{-i\omega t\}, \tag{3.30}$$

where $s_0$:

$$s_0 = -\frac{e}{m}\frac{\mathbf{E}}{\omega_0^2 - \omega^2 - ig\omega\omega_0}. \tag{3.31}$$

The electric polarization can now be expressed as:

$$\mathbf{P} = \frac{Ne^2}{m}\frac{\mathbf{E}}{\omega_0^2 - \omega^2 - ig\omega\omega_0}, \tag{3.32}$$

and using the second part of the Eq. 3.5, we can express $\epsilon$ as:

$$\epsilon = 1 + \frac{P}{\epsilon_0 \mathbf{E}}, \tag{3.33}$$

or

$$\epsilon(\omega) = 1 + \frac{Ne^2}{\epsilon_0 m(\omega_0^2 - \omega^2 - ig\omega\omega_0)}. \tag{3.34}$$

The complex dielectric constant $\epsilon(\omega)$ can be split into its real and imaginary parts as follows:

$$\begin{aligned} \Re\{\epsilon(\omega)\} - 1 &= \frac{Ne^2(\omega_0^2 - \omega^2)}{\epsilon_0 m((\omega_0^2 - \omega^2)^2 - g^2\omega^2\omega_0^2)}, \\ \Im\{\epsilon(\omega)\} &= \frac{Ne^2\omega g}{\epsilon_0 m((\omega_0^2 - \omega^2)^2 - g^2\omega^2\omega_0^2)}. \end{aligned} \tag{3.35}$$

Using the dispersion relation given by Eq. 3.17, the frequency dependent complex wave number can now be expressed as:

$$k(\omega) = k_{\mathrm{R}}(\omega) + ik_{\mathrm{I}}(\omega) = \sqrt{\epsilon(\omega)}\frac{\omega}{c}. \tag{3.36}$$

The imaginary part of the complex wavenumber indicates an exponential decay in the radiation intensity due to attenuation and the real part is related to the phase velocity of the wave by the relation $v = c/n(\omega) = \omega/\Re\{(k(\omega))\}$.

For simplicity, in the discussion above we considered only one oscillation frequency in the charge displacement Eq. 3.28, however, in a dielectric medium different electrons may be bound differently and may exhibit several oscillation frequencies or resonances. Let us now suppose that there are $N$ molecules per unit volume with $M$ electrons per molecule for a given dielectric medium. Instead of a single oscillation frequency for all electrons, there are $i$ oscillation frequencies denoted by $\omega_i$, and $g_i$ represents damping constants for $f_i$ electrons per molecule. Under these assumptions, the expression for complex dielectric constant can now be rewritten as:

$$\epsilon(\omega) = 1 + \frac{Ne^2}{\epsilon_0 m} \sum_i \frac{f_i}{(\omega_i^2 - \omega^2 - ig_i\omega\omega_0)}, \tag{3.37}$$

where the term $f_i$ represents the oscillator strengths and follow the rule:

$$\sum_i f_i = M. \tag{3.38}$$

If the value of damping constants $g_i$ for frequencies other than the oscillation frequencies is very small, than the term $g_i\omega\omega_0$ in the above equation can be neglected and the expression for complex dielectric constant becomes real and is expressed as:

$$\epsilon(\omega) = 1 + \frac{Ne^2}{\epsilon_0 m} \sum_i \frac{f_i}{(\omega_i^2 - \omega^2)}. \tag{3.39}$$

When expressed in terms of wavelength, the above equation is known as Sellmeier's formula and can be used to formulate empirical expressions for representing the refractive index (at certain frequency ranges) by curve fitting to the experimental measurements.

## 3.4 Origin of spectral fingerprints in the THz region

When an electric field is applied across a medium, the molecules of the medium get excited and jump to a higher energy level from their ground states. This transition depends on the photon energy and therefore the frequency of the incident radiation. When excited, the molecules vibrate and/or rotate. Here, vibration refers to the interatomic interactions that causes bonds between atoms to either stretch or bend in different directions from each other, while, rotation refers to interatomic interactions that cause the bond to rotate. In 1901, Max Planck proposed an equation that relates the energy state transition with the frequency $\nu$ of the applied electric field:

$$E_1 - E_2 = \Delta E = h\nu = \frac{hc}{\lambda}, \tag{3.40}$$

where $h$ is the Planck's constant ($6.62 \times 10^{-34}$J $\cdot$ s), $c$ is the speed of light in vacuum, and $\lambda$ is the incident wavelength.

For rotation to occur, only a small energy level transition ($\Delta E \approx 10^{-3}$ eV) is required. According to Eq. 3.40, this energy transition corresponds to a wavenumber of 1 cm$^{-1}$ or wavelengths of the order of microwave frequencies (Ingram 1967). On the other hand, for vibration to occur, significantly larger amount of energy ($\Delta$E $\approx$ 0.1 eV or 806.5 cm$^{-1}$) is required. Although, molecular rotation is also present at this energy levels, but its impact on the molecule is effectively overshadowed by the strong atomic vibrations (Ingram 1967). Thus, when excited, molecules absorb specific frequencies called *resonant frequencies* when they rotate or vibrate and produce absorption spikes (features) at these resonant frequencies in the observed attenuation spectrum. These absorption features are unique to every material and thus are called *spectral fingerprints* of the material. At THz frequencies the main cause of absorption fingerprints are either from low-frequency delocalised intramolecular vibrations of large parts of the molecule or from the intermolecular vibrations of the weakly bound molecular network (Fischer 2005), although a number of molecules in the gas phase show rotational structures at THz frequencies. Therefore, the molecule response to THz can be divided in to three categories (i) pure rotations, (ii) intramolecular vibrations and (iii) intermolecular vibrations (Gorenflo 2006).

### Intramolecular vibrations

At far-infrared frequencies the intramolecular vibration modes are very delocalised with many atoms of the molecule involved. These vibrations can have resonant frequencies down to 100 cm$^{-1}$. Intramolecular vibration may arise at low frequencies if the value of the force constant for the atomic displacement is relatively small compared with a "normal chemical" bond. An example of intramolecular vibration at THz frequency is the low-frequency stretching and bending modes in some hydrogen bonded systems provide as a result of small force constant. Another example for low-frequency intramolecular vibrations can be found in the spectra of linear polymers and polysaccharides where phonon-like vibrations of long molecular chains formed relatively large of single molecules segments (Fischer 2005).

Another kind of vibration that has characteristic resonances in the THz spectral range is the torsional vibration. These modes are primarily observed in gases and liquids and occur due to a potential barrier, which hinders the free rotation about a given bond.

#### Intermolecular vibrations

Intermolecular vibrations exhibit resonances at low frequencies and are caused when a large group of a molecule move around their collective equilibrium. Hydrogen bonds have typical energies of 10-40 kJ/mol and thus lattice or phonon-like vibrations (caused by relative motions of molecules or complex ions as a whole within the crystal lattice) of the hydrogen-bonded networks fall in the far-infrared frequency range. Besides hydrogen bonds, these high mass vibrations are also observed in weak van der Waals and dipole-dipole interactions which have energies of the order of 1-2 kJ/mol. The distinctive phonon mode observed in semiconductor crystals are an example of intermolecular vibrations at THz frequencies. Most spectra contain resonances as a result of a combination of several types of vibrations and overtones.

## 3.5 Challenges and hurdles

Material identification and classification using terahertz technology faces many challenges and hurdles. Various factors severely constrain plausible scenarios for the application of terahertz technology for real world applications. In this section, we discuss the various challenges faced by THz-TDS. These challenges include power limitations, bandwidth limitations, water absorption, etalon effect, scattering... etc. Throughout the discussion we highlight recent progress in addressing these problems.

### 3.5.1 Power limitations

A primary challenge and limitation of working with THz-TDS systems is the low power of the THz beam, with average power typically ranging between 0.1 $\mu$W and 100 $\mu$W. The reason for such low power levels is the low conversion efficiency. However, as a result of the coherent detection in THz-TDS systems, noise from many common noise sources is effectively rejected. This results in high dynamic range that allows measurement even in situations where only a fraction of the generated power reaches the detector, such as transmission through a multiple scattering medium (Pearce *et al.* 2003). However, for THz-TDS imaging setups, the existing commercially available detectors such as pyroelectric cameras required power levels up to 100 $\mu$W per illuminated pixel. As a result, raster scanning of either THz beam or the object under study is used. This poses significant limitations on the acquisition rate of the image. Low

power of THz-TDS systems can also limit the penetration capabilities of the THz beam for study of dense media with high refractive index such as explosives.

### 3.5.2 Signal to noise ratio

Terahertz time-domain spectroscopy systems are capable of very high signal-to-noise ratios (SNRs) of over 100,000. However, in biomedical imaging, a number of factors combine to dramatically reduce the SNR to the point where it is a limiting concern. Some of these factors include the need to accelerate the imaging acquisition speed and the high absorption of biological tissue. Solutions to the problem of SNR are sought in improving the T-ray hardware. Terahertz sources have very low average output powers and THz sensors have relatively low sensitivity compared to sources and sensors operating in the optical spectrum. Both of these aspects of T-ray systems are subjects of current research and continue to improve. Other problems are related to the THz generation process, which results in THz beams that are not Gaussian and cannot be collimated as well as optical beams. This results in additional noise in THz images. Potential solutions to the SNR problem may be found in free-electron lasers (FEL) or in all electronic THz systems although currently each of these alternatives has its own disadvantages.

### 3.5.3 Bandwidth limitations

Currently, standard photoconductive dipole antenna (PDA) THz sources are limited to frequencies below 3 or 4 THz with only a few new antennas reporting bandwidths up to 8 THz (Shen *et al.* 2004). Optical rectification provides a wider bandwidth and generation and detection bandwidths in excess of 40 THz have been demonstrated (Wu and Zhang 1997, Sinyukov and Hayden 2002), however this is at the expense of THz power (and therefore SNR). Ideally, a THz imaging system would allow tissue responses to be measured up into the infrared region. This would not only allow broader signatures to be observed but also allow the potential for reduced water attenuation, which falls dramatically as the frequency increases over 100 THz.

### 3.5.4 Etalon reflections

As illustrated in Fig. 3.2, when a THz beam penetrates the interface between two media of refractive indices $n_a$ and $n_b$, according to Fresnel equations (Saleh and Teich 2001) a part of it gets reflected, while the rest of it is refracted into the other medium. Similarly, when the refracted part of the beam reaches the nest interface ($n_b$ to $n_a$) it again undergoes reflection and refraction. A detailed description of this process is taken into account in the data analysis in Section 3.2. The process of multiple reflections within the sample splits the wave into a number of intermediate paths as illustrated in Fig. 3.3. Each intermediate component is phase retarded to the previous component by:

$$\Delta\phi = \frac{2d_\theta n\omega}{c}. \tag{3.41}$$

If $\Delta\phi = \pi$, negative interference occurs causing the signal to attenuate. The signal loss can be detected from the maximum absorption observed at:

$$\nu = \frac{c}{4\pi d_\theta n}, \tag{3.42}$$

and its odd multiples. This introduces an oscillatory (ringing) feature in the data and can corrupt the extracted optical constants (Withayachumnankul 2009). The amplitude of these oscillations depends on the reflectivity of the interface, in other words on the refractive index and the surface smoothness of the sample. For optically thick samples the temporal curves of the detected electric field exhibit well-separated etalon echoes. This is illustrated in Fig. 3.4.

Thus the reflections can be cut off from the main pulse, without loosing significant information, in thin samples, however, these reflections are either overlapping each other with a part of the main pulse or appear shortly after the main pulse in a region where significant information is present and therefore cannot be cut off. Fischer (2005) carried out THz-TDS of a 100 $\mu$m and a 45 $\mu$m thick sample of polynucleotides poly-C and poly-A, respectively, to show how etalon artefacts can dominate the observed spectra and therefore may even be misinterpreted as resonance features.

Several researcher have attempted and proposed algorithms to remove the effects of etalon echoes. Duvillaret *et al.* (1996) proposed an iterative algorithm to remove the etalon effects from the estimated parameters for a single sample setting. In the first iteration, they measure the transfer function of the sample, carry out material parameter extraction and calculate the Fabry-Pérot term using the Eq. 3.25. Then, the Fabry-Pérot term is deconvolved from the measured transfer function and the updated transfer

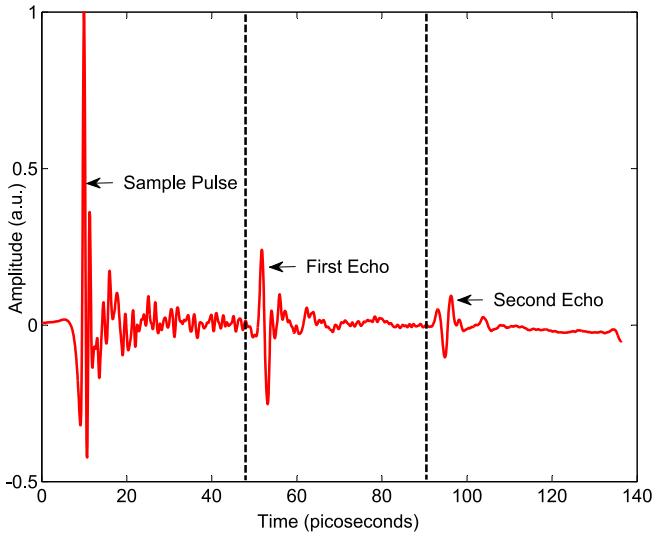


**Figure 3.4. The etalon effect.** Terahertz pulses transmitted through an optically thick sample.

function is used to update the material parameters. This process is repeated to obtain improved material parameter estimates. The main drawbacks of this algorithm are that it is computationally expensive and can fail if some reflected pulses are removed prior to the iterative process. On the other hand, Withayachumnankul *et al.* (2006) proposed a frequency domain algorithm that directly approximates the transfer function of the sample with a simple model and estimates and subtracts the reflection from the measured signal to extract the primary pulse. Similar to Duvillaret *et al.* (1996) algorithm, this method did not require information about the sample thickness. However, this method was much more efficient as it did not involve an iterative procedure. Since then several simple and direct methods have been proposed to reduce or remove the etalon artefacts (Naftaly and Miles 2007, Hirsch *et al.* 2008).

In some cases, however, the delayed reflections are of great value for the data analysis. Duvillaret *et al.* (1999) used the temporal profile of the measurements containing etalon echoes, to precisely determine the sample optical parameters and thickness. Their method is applicable to any material with low absorption, can determine sample thickness with accuracies within 1%. Naftaly *et al.* (2010), on the other hand, proposed an etalon-based method of calibrating the frequency of terahertz time-domain spectrometers. Their method used the etalon echoes produced by multiple reflections in non-absorbing wafers to provide the frequency calibration. Fischer (2005) showed that etalon echoes can be used to ensure an accurate positioning of the sample with respect to the reference surface in reflection mode THz-TDS. In Section 6.3 we present an initial

exploration in to analysing multiple Fresnel echoes for estimate scattering contribution in the THz-TDS measurements of materials with sharp absorption features.

### 3.5.5 Scattering

As described in Section 1.4, when the size of the scattering centers are of the order of the THz wavelengths and the scattering cross-section can no longer be described by a simple Rayleigh approximation, but needs to be modeled by a more complex process (Born and Wolf 1999). Scattering can occur over a broad range of frequencies and its effects are more pronounced at high frequencies. It can change the shape of the measured absorption spectrum of the sample under test, making it difficult to determine specific dielectric properties of the sample. Generally, in polycrystalline samples scattering is primarily caused by inhomogeneities that are of the order of the THz wavelengths.

In order to understand that how scattering can effect the correct determination of dielectric properties of a sample, we carry out THz-TDS on two PE samples. Two different granularities of spectroscopic grade PE powder from the same manufacturer (Inducos) were used for our experiments. The characteristic dimensions of the particles in the powders, were measured with a scanning electron microscope (SEM) and were found to be in good agreement with the range provided by the manufacturer. The first powder sample, had relatively small PE grain sizes, with approximately 60 $\mu$m (Inducos), while the second one, had considerable a larger grain size of approximately 360 $\mu$m in diameter. The details of the sample preparation and experiment can be found in Section 4.3.3. The extinction spectra for the two PE samples of same thickness, are plotted in Fig. 3.5.

In spite of being the same material (same quality), the PE sample with larger grain size, shows a much higher frequency dependent attenuation as compared to the PE sample with smaller grain size. This can often be confused as an absorption feature of the sample, but instead, this increased attenuation is caused by scattering of the THz radiation from the large size PE particles. Thus, it can be seen that scattering can change or contaminate the THz *spectra fingerprint* of a sample.

In order to understand how scattering can affect the spectrum of a sample that contains distinct absorption peaks, we carry out THz-TDS on two glucose samples. Granular and coarse grained polycrystalline glucose was purchased from Sigma-Aldrich. One of

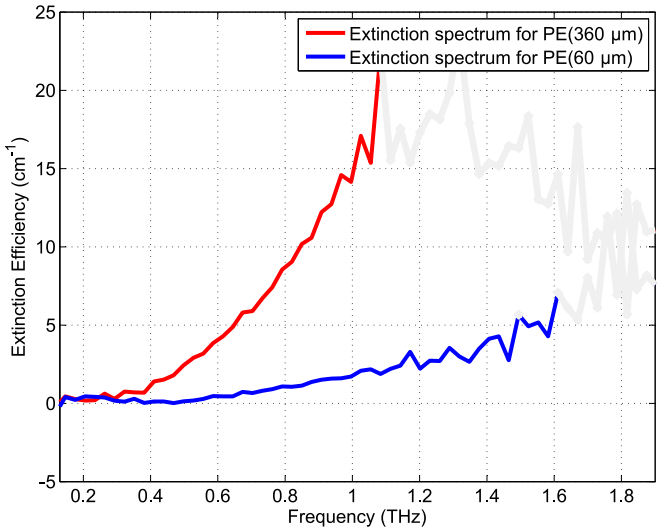


**Figure 3.5. Terahertz scattering—effect of grain size.** Effects of scattering on the spectra of polycrystalline PE (polyethylene) samples. Two samples with different grain sizes were measured, and an increased baseline slope, owing to scattering of THz, was observed for the sample with bigger grains. The whitened-out region represents data that is outside the dynamic range of the measurement setup and hence does not provide any useful information.

the samples was directly mixed with fine polyethylene powder and pressed to a coplanar pellet, while for the other sample, the coarse glucose grain were first ground to a fine powder and then mixed with polyethylene powder to achieve an approximately homogeneous grain size of dimensions well below the THz wavelengths. The extinction spectra for both the samples are plotted in Fig. 3.6. It can be seen that the granular sample not only has an increased baseline slope, but also has significant broadening of the absorption peaks as a result of the resonance light scattering (Collings *et al.* 1999).

As described in Section 1.4, several researcher have proposed various techniques and theoretical models to estimate and/or mitigate the scattering effects from the THz-TDS measurements (Bandyopadhyay *et al.* 2007, Shen *et al.* 2008, Zurk *et al.* 2007, Franz *et al.* 2008). However, as all these approaches either rely on specific information about the sample under study and/or require special and complex sample preparation technique and/or measurement process, they may not be suitable for real-world applications such as stand-off measurements, where *a priori* information of the the sample is not always known.

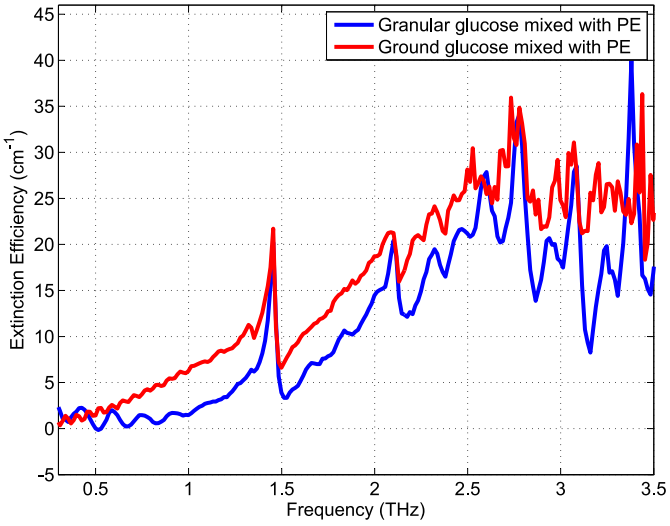


**Figure 3.6. Terahertz scattering—absorbing media.** Effects of scattering on the spectra of polycrystalline glucose sample samples. In addition to an increased baseline slope, a significant broadening of the absorption peaks cause by the phenomenon of resonance light scattering is observed for the granular sample.

In this thesis, we present several theoretical models, signal processing techniques and experimental methods/algorithms to estimate, and mitigate or reduce the effects of scattering in the transmission mode THz-TDS measurements, that are computationally more efficient and less *a priori* information demanding than the techniques described in the existing literature.

## 3.6 Chapter summary

This chapter discussed the basic concepts and theories that form the understanding platform of THz interaction with materials. Classical electromagnetic theory is used to describe the propagation and interaction of THz wave through macroscopically uniform media. First, we described the THz waves using Maxwell's equations and their reflection and transmission at a dielectric interface. We then describe the process of absorption and dispersion of THz wave when propagating through a medium with a complex refractive index. Furthermore we extend our discussion to describe what causes the generation of the material *spectral fingerprints*. We conclude this chapter by discussing the various challenges and hurdles that have stunted the application

of terahertz technology for material classification and identification in real world applications. In particular, we studied the effects of scattering on the THz spectra of polycrystalline material samples and how scattering can alter the THz spectra of these samples.

In line with the scattering related issues presented in this chapter, the next chapter, reviews various theoretical models for estimating and approximating the scattering cross-section for THz transmission through sparse and dense distribution of particles. Theoretical calculations are compared with THz-TDS measurements and a new numerical approach to eliminate scattering contributions from the THz-TDS measurements is also presented.

# Chapter 4

# Scattering estimation—theoretical modeling

RECENT years have seen significant advances in material diagnostics and analysis using THz-TDS and imaging. Frequency dependent absorption of materials at distinct frequencies in the THz range are commonly used as *spectral fingerprints* for identification and classification of materials. However, as we saw in the last chapter, scattering of THz radiation due to the granular and structural nature of various material samples, can often distort or obscure these *spectral fingerprints*. Thus, understanding scattering is crucial in many existing and potential THz applications, which rely on detection transmitted/reflected THz signals, such as security screening, pharmaceutical/food quality control, and biosensing.

In this chapter, we review various theoretical models developed for estimating and approximating the scattering cross-section, when an electromagnetic wave interacts with a random medium with characteristic particle dimensions comparable to the wavelength of the incident radiation. The chapter is divided in two main sections, (i) scattering through a sparse distribution of particles, and (ii) scattering from dense media. We compare the discussed theories with transmission mode THz-TDS measurements of various material samples to validate their applicability.

## 4.1 Introduction

The transport of electromagnetic radiation through a random medium can be classified in three regimes: ballistic, quasi-ballistic and diffusive transport (Pearce and Mittleman 2002). The ballistic transport corresponds to the radiation that did not encounter any scattering centers in the medium and hence passes unscattered through the medium. This condition is usually met only in samples that are very thin or sparse. The second region, quasi-ballistic transport, is observed when the radiation suffers a few scattering events and most of the scattering is in a narrow cone in the forward direction. This condition is usually met in moderately thick and dense samples with individual particle sizes being comparable or larger than the incident wavelength (Jonasz and Fournier 2007). The third and the final scattering regime is the diffusive transport, which occurs in very dense and thick samples, where the scattered radiations completely loses its initial polarization. Diffusive scattered radiation have minimum contribution in the forward direction narrow cone and can sometimes lead to interesting phenomenon such as photon localization (Pearce and Mittleman 2002). In applications such as pharmaceutical, explosive and biological material characterization using transmission mode THz time domain spectroscopy (TDS), the commonly encountered scattering regime is the quasi-ballistic transport as only the signal collected in the forward narrow cone is detected. Under this scattering regime the detected radiation contains contributions from both absorption and scattering, it becomes essential to separate scattering from the detected response in order to reveal the true *fingerprint* of the material under study.

In a discrete random medium, the propagation constant and hence the attenuation constant of the coherent wave depends on the frequency, fractional volume density (particle concentration), and particle characteristics (Ding and Tsang 1991, Mandt *et al.* 1992, Ishimaru and Kuga 1982). For a sparse concentration of particles (particle concentration $< 10\%$), the particle positions are usually uncorrelated and the independent scattering assumption is applicable. In this case, the scattering cross-section is directly proportional to the volume density of the scatterer in the media. However, media such as, pharmaceutical tablets, closely packed powders, and snow have high scatterer densities (particle concentration $> 10\%$), causing the incident radiation to multiply scatter. In this case, particle correlation becomes important and need to be taken into account in calculating the scattering cross-section.

Several theoretical and models and formulas have been proposed to estimate/approximate the scattering cross-section on both sparse and dense media. In this chapter we review these theoretical approaches and compare their estimates with transmission mode THz-TDS measurements.

## 4.2 Scattering through a sparse distribution of particles

### 4.2.1 Independent scattering approximation

When the particle concentration is sparse, an *independent scattering* approximation can be used to estimate or approximate the optical properties of the medium. In this approximation, we assume that the incident radiation from the emitter reaches the detector after encountering very few particles and all the higher orders of scattering (double and multiple) are assumed to be negligible. The propagation of the radiation through such a medium is governed by the particle concentration and the single particle scattering properties.

When an electromagnetic wave propagates through a medium, its amplitude and phase fluctuates randomly as a result of interaction with particles. Therefore, the total field propagating through the medium can be expressed as the sum of the coherent field and the fluctuating or incoherent field (Foldy 1945):

$$E_{\text{total}}(\omega, r) = E_{\text{coh}}(\omega, r) + E_{\text{incoh}}(\omega, r), \tag{4.1}$$

where $E_{\text{coh}}(\omega, r)$ represents the coherent and $E_{\text{incoh}}(\omega, r)$ represents the incoherent component. The coherent field is given by the ensemble average of the total field over the scatterer positions, while the ensemble average of the incoherent field is zero. The incoherent intensity, however, has a non zero ensemble average. The coherent field can also be expressed as:

$$E_{\text{coh}}(\omega, r) = E_0 \exp\left\{-iK_{\text{eff}}.r\right\}, \tag{4.2}$$

where $E_0$ is the incident field and $K_{\text{eff}}$ is the effective propagation constant that accounts for the overall optical properties of the medium. When the propagation medium has sparse concentration, under the independent scattering assumption, the imaginary part of $K_{\text{eff}}$ (attenuation constant) can be determined as:

$$\Im\left(K_{\text{eff}}\right) = \sum_{i=1}^{M} \eta_i \sigma_i, \tag{4.3}$$

where $i$ describes each size in the particle size distribution of $M$ sizes, $\sigma_i$ represents the single particle extinction cross-section, and $\eta_i$ is given by:

$$\eta_i = \frac{3V_i}{4\pi a_i^3}, \tag{4.4}$$

where $V_i$ is the volume fraction and $a_i$ is the radius of the particles with the $i^{\text{th}}$ size.

For particles with dimensions comparable to the incident radiation, the single particle extinction cross-section can be given by the Mie Theory. It is based on analytical theory as it involves solving Maxwell's equations with boundary conditions for its derivation (Dorney *et al.* 2001). When a single particle is illuminated by a wave, a part of the incident power is scattered out and another part is absorbed by the particle. The characteristics of the scattering and absorption, can be expressed by assuming an incident plane wave (Ishimaru and Kuga 1982). Consider a linearly polarized electromagnetic wave propagating in the $\hat{z}$ direction, with $\hat{x}$ as the unit vector in the direction of its polarization. We can express the incident wave as:

$$E_{\text{inc}}(\hat{r}, \omega) = \hat{x}_{\text{inc}} E_0 \exp\left\{ikz - i\omega t\right\}, \tag{4.5}$$

where $k$ is the wave number of the surrounding medium. Now, the scattered field from the spherical particle is related to the incident field as follows:

$$\begin{aligned} E_{\text{s},\perp}(\hat{r}, \omega) &= E_0 S_1(\theta) \left( \frac{i \exp(ikR - i\omega t)}{kR} \right) \sin\phi, \\ E_{\text{s},||}(\hat{r}, \omega) &= E_0 S_2(\theta) \left( \frac{i \exp(ikR - i\omega t)}{kR} \right) \cos\phi, \end{aligned} \tag{4.6}$$

where $||$ and $\perp$ represent the parallel and perpendicular polarization of the scattered field, respectively, $S_1(\theta)$ and $S_2(\theta)$ are the amplitude functions that relate the scattered field for the perpendicular and parallel polarizations, $\theta$ is the angle between the incident and the scattered field, $R$ is the distance between the observation point and the center of the particle, and $\phi$ is the angle between the scattered field and the polarization direction of the incident field ($\hat{x}$). The complex amplitude functions are related to the scattering amplitude function as:

$$f(\hat{0}, \hat{z}) = \frac{i}{k} S_1(\theta) \sin\phi \hat{x}_{\perp} + \frac{i}{k} S_2(\theta) \sin\phi \hat{x}_{||}, \tag{4.7}$$

where $\hat{x}_{\perp}$ and $\hat{x}_{||}$ are vectors pointing perpendicular and parallel to the scattered field plane respectively to the direction of propagation of the scattered field. Based on the

above equations, the Mie expression for the scattering amplitude functions is given as:

$$\begin{aligned} S_1(\theta) &= \sum_{n=1}^{\infty} \frac{2n+1}{n(n+1)} \left[ a_n \pi_n(\cos\theta) + b_n \tau_n(\cos\theta) \right], \\ S_2(\theta) &= \sum_{n=1}^{\infty} \frac{2n+1}{n(n+1)} \left[ b_n \pi_n(\cos\theta) + a_n \tau_n(\cos\theta) \right]. \end{aligned} \tag{4.8}$$

Now, by integrating the scattering amplitude functions over $\theta$, the scattering cross-section $\sigma_{\text{sca}}$ and by using the forward-scattering theorem or extinction theorem (Ishimaru and Kuga 1982), the extinction cross-section $\sigma_{\text{ext}}$ can be given by:

$$\begin{aligned} \sigma_{\text{sca}} &= \sum_{n=1}^{\infty} (2n+1)(|a_n|^2 + |b_n|^2), \\ \sigma_{\text{ext}} &= \sum_{n=1}^{\infty} (2n+1)\Re(a_n + b_n), \end{aligned} \tag{4.9}$$

where $a_n$ and $b_n$ are the are complex coefficients of Riccati-Bessel functions, given by:

$$\begin{aligned} a_n &= \frac{\mu m^2 j_n(mx) \left[ x j_n(x) \right]' - \mu_1 j_n(x) \left[ mx j_n(mx) \right]'}{\mu m^2 j_n(mx) \left[ x h_n^{(1)}(x) \right]' - \mu_1 h_n^{(1)}(x) \left[ mx j_n(mx) \right]'}, \\ b_n &= \frac{\mu_1 m^2 j_n(mx) \left[ x j_n(x) \right]' - \mu j_n(x) \left[ mx j_n(mx) \right]'}{\mu_1 m^2 j_n(mx) \left[ x h_n^{(1)}(x) \right]' - \mu h_n^{(1)}(x) \left[ mx j_n(mx) \right]'}, \end{aligned} \tag{4.10}$$

where, the size parameter is given by $x = ka$, $a$ is the radius of the sphere and $k = 2\pi/\lambda$ is the wave number, $\lambda$ is the wavelength in the ambient medium, $m$ is the refractive index with respect to the ambient (surrounding) medium. The functions $j_n(z)$ and $h_n^{(1)} = j_n(z) + iy_n(z)$ are spherical Bessel functions of order $n$ and of the given arguments, $z = x$ or $mx$, respectively.

Now, using the Mie formulation for single particle scattering and assuming that all the particles in the sparse medium are identical, the effective attenuation constant given by Eq. 4.3, can be rewritten as:

$$\Im\left(K_{\text{eff}}\right) = \frac{3V}{4\pi a^3} \sum_{n=1}^{\infty} (2n+1) Re(a_n + b_n), \tag{4.11}$$

where, $V$ and $a$ are the fractional volume and radius of the particles in the sparse medium, respectively.

### 4.2.2 Effective field approximation

In 1945, Foldy introduced the concept of *configurational* averaging, which used joint probability distribution for the occurrence of a given position configuration of isotropic

scatterers to produce an average of the resulting wave over all configurations (Foldy 1945). Later, his procedure was generalized by Lax (1951) to include point scatterers with quite general scattering properties. Twersky (1978), used the same procedure studying scattering of sound waves by a rough surface. The concept behind the method was an assumption that we can replace the effect due to individual scatterers in region with a homogeneous *effective field* caused by the interaction between the individual scatterers. The multiple scattering solution can then be obtained by calculating the effect of a single scatterer on the effective field. In the framework of the Twersky approximation, the propagation of the coherent field through a distribution of particles is described by the Foldy-Twersky equation:

$$\langle \psi_a \rangle = \phi_I^a + \int u_s^a \langle \psi_s \rangle \rho(r_s) dr_s, \tag{4.12}$$

where $\rho(r_s)$ is the number density of the particles, $\langle \psi_a \rangle$ is the coherent field at position $r_a$, $\phi_I^a$ is the primary incident field, $\langle \psi_s \rangle$ is the coherent field impinging on the particle at $r_s$, and $u_s^a$ is an operator that, when acting on $\langle \psi_s \rangle$, gives the field at $r_a$.

Now, according to Twersky's approximation (Giusto *et al.* 2003), the above equation accounts for all the multiple scattering process such that the path of the light does not go through the same particle any more than once. Consider a plane wave propagating in the $z$ direction incident on a medium with identical particles present in each others' wave zone or where $u_s^a$ can be approximated by:

$$u_s^a \langle \psi_a \rangle = f(\hat{k}_s, \hat{k}_i) \frac{\exp(in_0 k |r_a - r_s|)}{|r_a - r_s|} \langle \psi_s \rangle, \tag{4.13}$$

where $\hat{k}_s$ and $\hat{k}_i$ represent the direction of observation and incidence, respectively; $f$ is the scattering amplitude of the particles; and $n_0$ represents the refractive index of the host medium. Then, the solution to the Eq. 4.12 is found to be a plane wave given by:

$$\langle \psi(z) \rangle = \exp(iK_{\text{eff}} z), \tag{4.14}$$

where $K_{\text{eff}}$, representing the effective wave number of the medium, is given by:

$$K_{\text{eff}} = \sqrt{k^2 + 4\pi\eta f(0)}, \tag{4.15}$$

where, $\eta$ represents the number of particles per unit volume given by $\eta = 3V/4\pi a^3$, $k$ is the wave number of the surrounding medium, and $f(0)$ is the forward scattering amplitude of a single particle which can be calculated using the Mie formalism of single scattering. The Eq. 4.15 is often referred to as the *Foldy's effective field approximation*

or EFA. While independent scattering approximation 4.2.1 is valid only for very low concentration (<1%), Foldy's EFA is found to produce resonable approximations upto 10.1% volume concentration (Kuga *et al.* 1996, Giusto *et al.* 2003).

### 4.2.3 Comparison of weak scattering theories with THz-TDS

In order to quantitatively verify the approximations of the above mentioned weak scattering thoeries, we carry out transmission mode THz-TDS for a granular polyethylene (PE) sample.

#### Experiment setup and sample preparation

A polyethylene sample (grain size: 300-400 $\mu$m diameter, refractive index = 1.46) was prepared from spectrometric grade PE powder (supplier: Inducos). In order to confirm the particle size, we took several scanning electron microscope (SEM) images of the PE powder and found the average particle diameter to be $\approx$ 360 $\mu$m. One of the SEM images is shown in Fig. 4.1. Common packaging tape (refractive index = 1.5) with thickness $\approx$ 500 $\mu$m was used as the sample holder. For the sample measurements, a few particles of the PE powder were carefully and evenly spread over the packaging tape and a single tape with no sample material on it was used as the reference measurement. Using the average diameter of the PE particles, number of particles, and the measured sample dimensions we estimated the PE particle volume fraction to be $\approx$ 8%. The measurement of the particle diameter was used as the sample thickness. The sample and reference measurement arrangement is depicted in Fig. 4.2. It must be noted that in this analysis we have assumed the particles to be spherical in shape. Also note that the particle sizes considered here are of the order of the incident wavelength, however the independent scattering approximation and Foldy's EFA represent these wavelength sized particles as point scatterers. Strictly speaking for such finite sized particles phase retardation inside the particles cannot be neglected. However, as the particles considered in our experiments have relatively low refractive index (relative to the host medium) phase retardation inside the particle has been neglected and finite sized particles are thus assumed to be point scatterers (Bandyopadhyay *et al.* 2007).

#### Parameter extraction

The measurement was carried out using apparatus shown in Fig. 2.6. By analyzing the propagation geometry as shown in Fig. 4.2, the sample and reference spectrum can be

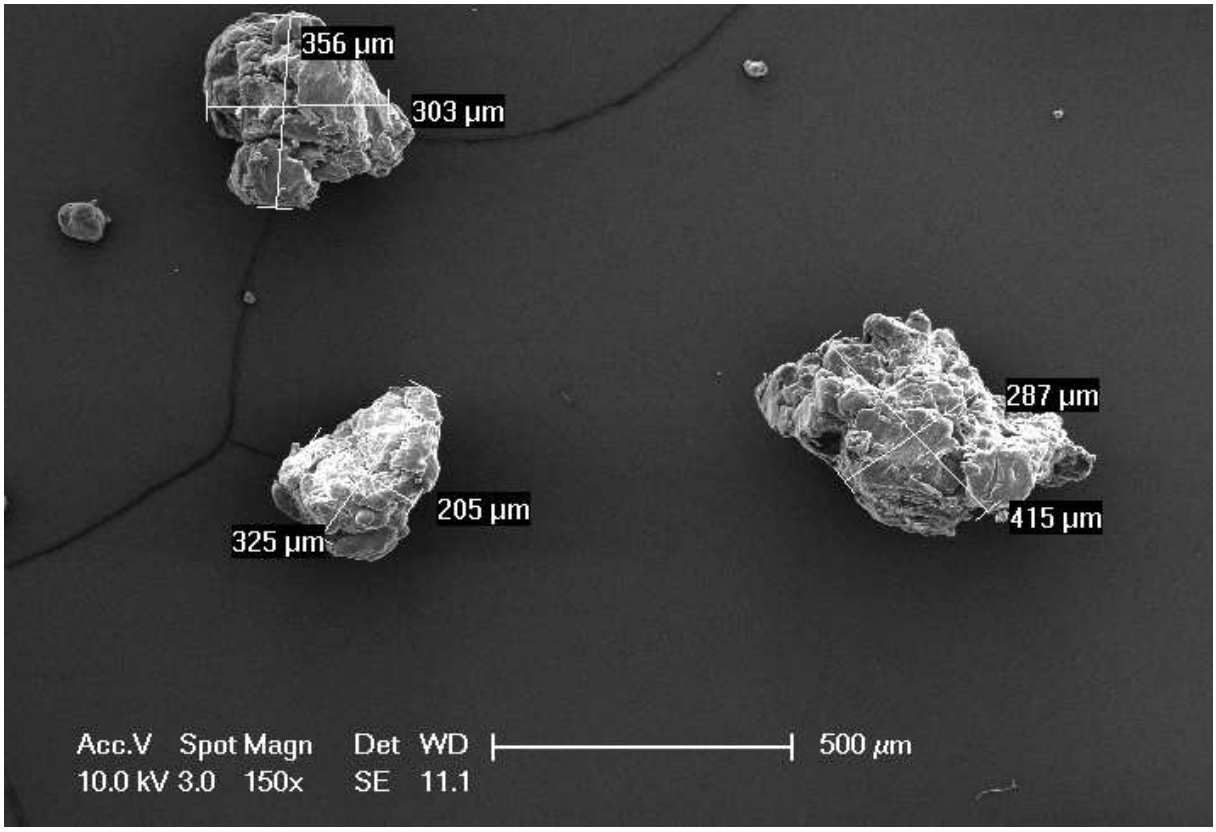


**Figure 4.1. Scanning electron microscope image of PE powder.** One of the SEM images of the PE powder particles. The average particle diameter was found from measurements of a large number of particles from several SEM images.

represented by:

$$E_{\text{sam}}(\omega) = \tau_{\text{as}}\tau_{\text{sw}}\tau_{\text{wa}}\text{FP}_{\text{asw}}\text{FP}_{\text{swa}}\exp\left[-j\hat{n}_{\text{s}}\frac{\omega d_{\text{s}}}{c}\right]\exp\left[-jn_{\text{w}}\frac{\omega d_{\text{w}}}{c}\right]E_0(\omega), \tag{4.16}$$

$$E_{\text{ref}}(\omega) = \tau_{\text{aw}}\tau_{\text{wa}}\text{FP}_{\text{awa}}\exp\left[-jn_{\text{w}}\frac{\omega d_{\text{w}}}{c}\right]E_0(\omega), \tag{4.17}$$

where the subscripts a, s and w are for air, sample, and window, respectively, and $d_{\text{s}}$ is the thickness of the sample ($\approx 360\ \mu$m) and $d_{\text{w}}$ is the thickness of the window ($\approx 500\ \mu$m). Therefore, $\tau_{\text{aw}}$ propagation from air to window, $\tau_{\text{sw}}$ propagation from sample to window and so on. $\hat{n}_{\text{s}}$ is the complex refractive index of the sample and $n_{\text{w}}$ is the refractive index of the window. Note that, $\text{FP}_{\text{asw}}$ is the Fabry-Pérot term for the reflections in the sample, with air on one side and window on the other side. Similarly, $\text{FP}_{\text{awa}}$ is the Fabry-Pérot term for the reflections in the window, with air on both the sides.

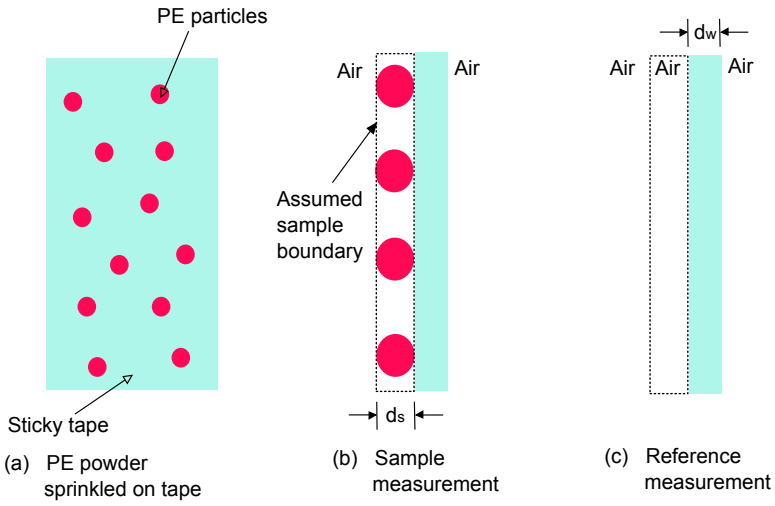


**Figure 4.2. Reference and sample measurement arangement.** (a) PE powder sprinkled on tape, (b) sample measurement arrangement, and (c) reference measurement arrangement.

Fig. 4.3 shows the temporal profile and the Fourier transform of the reference and sample THz signal. The transfer function for the measurement can now be given by:

$$\begin{aligned} T(\omega) &= \frac{E_{\text{sam}}}{E_{\text{ref}}}, \\ &= \frac{\tau_{\text{as}}\tau_{\text{sw}}\text{FP}_{\text{asw}}\text{FP}_{\text{swa}}}{\tau_{\text{aw}}\text{FP}_{\text{awa}}} \exp\left[-j\hat{n}_{\text{s}}\frac{\omega d_{\text{s}}}{c}\right], \end{aligned} \tag{4.18}$$

and thus, the extinction spectrum can be expressed as:

$$\alpha_{\text{sam}}(\omega) = \frac{2}{d_{\text{s}}}\left[\log\left(|T|\right) - \log\left(\frac{\tau_{\text{as}}\tau_{\text{sw}}\text{FP}_{\text{asw}}\text{FP}_{\text{swa}}}{\tau_{\text{aw}}\text{FP}_{\text{awa}}}\right)\right]. \tag{4.19}$$

### Comparison between independent scattering approximation and Foldy's approximation

Following the material parameter extraction procedure described in Section 4.2.3, the frequency dependent extinction coefficient for the PE sample was extracted and compared with the extinction curves calculated using the independent scattering approximation and Foldy's approximation, respectively. This is shown in Fig. 4.4.

As expected, the independent scattering approximation strongly disagrees with the measurements, as it is only valid for very low concentrations ($<$ 1%). On the other hand, Foldy's aprroximation which takes into account the first order multiple scattering process, shows a good agreement with the measurements. A similar study was carried out by Bandyopadhyay *et al.* (2007). They used the Mie theory based independent scattering approximation to compare the theoretical approximations with the

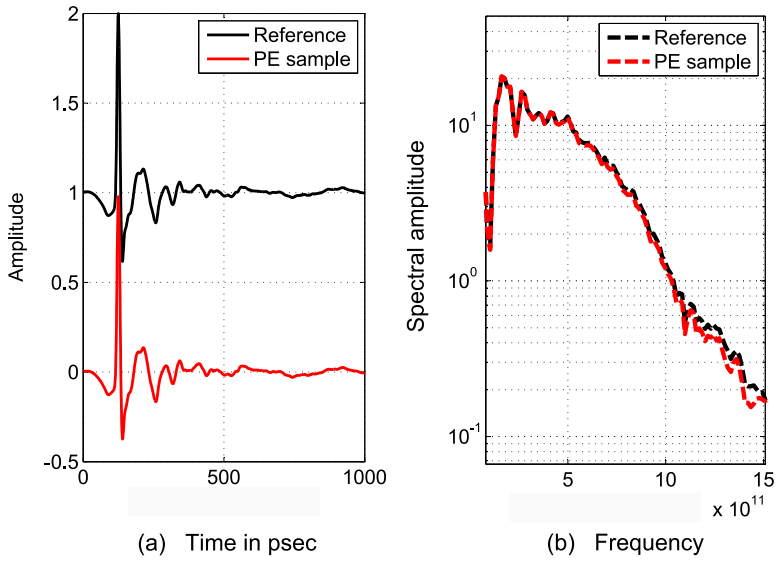


**Figure 4.3. Reference and sample measurements.** THz fields for PE sample (360 $\mu$m grain size) and reference measurement and (b) THz amplitudes of the same. The reference measurement was almost (96%) transparent and completely featureless between 0.2 and 1.4 THz.

expermentally obtained extinction spectrum of ammonium nitrate, salt, and flour samples. However, there were some potential discrepancies in their study. Firstly, they did not measure or estimate the volume concentration of the samples, which is critical for validating the applicability of the independent scattering approximation. Secondly, they also used a sticky tape as sample holder, but unlike our samples, they used sticky tape on both sides of the sample powder, which can cause introduction air bubbles in the sample, especially around the sample material particles, potentially increasing the scatterer dimensions. They did not mention any method to account for the effects of the air bubbles in the parameter extraction process. Thus, in this study, we have shown that Foldy's effective field approximation (EFA) successfully explains the observed scattering from a PE powder sample with grain diameter $\approx$ 360 $\mu$m, volume concentration $\approx$ 8 % with air (refractive index $\approx$ 1) on one side and a sticky tape (refractive index $\approx$ 1.5) on the other side, while, Mie theory based independent scattering approximation over estimates the measurements. It must be noted that with the particle sizes, and concentration of the samples considered in this experiment, near-field effects among the particles may become important - in other words higher order of multiple scattering become dominant and must be considered. However, as the refractive index mismatch between the particles and the host medium (assuming a average refractive index of $\approx (1.5 + 1)/2 = 1.25$) is very small, higher order multiple scattering

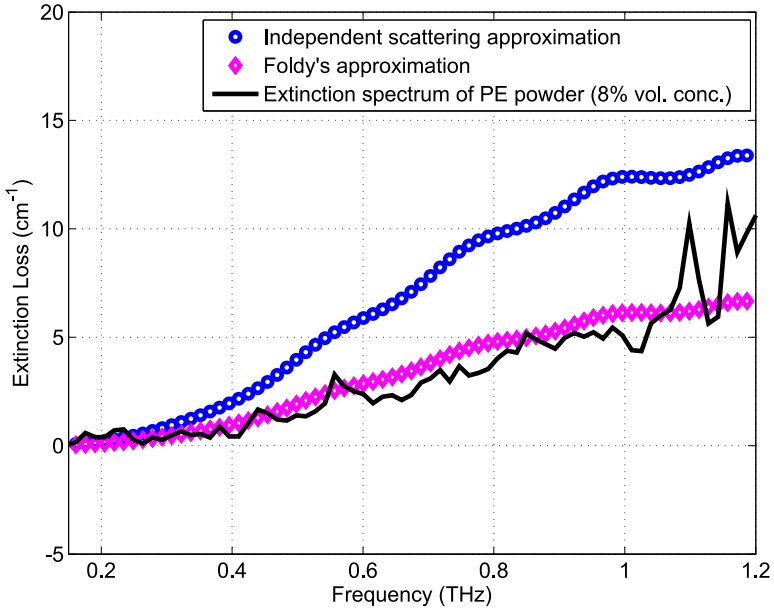


**Figure 4.4. Comparison of theory with measurements.** Comparison of the experimentally obtained extinction spectrum (black curve) of PE powder (8% volume concentration) with the approximations obtained from the independent scattering approximation (blue curve) and Foldy's approximation (magenta curve).

effects are negligible. In fact the results of the analysis presented in this section prove that as the measurement results match nicely with the predictions of the Foldy's EFA.

## 4.3 Dense medium scattering

Understanding wave propagation in medium with discrete, particulate scatterers is of fundamental importance for a wide variety of THz-TDS applications. Very often in optics, one is faced with a situation where the dimensions of the scatterers are comparable in size to the radiation wavelength, and occupies more than a few percent of the volume. Under these conditions, cyclic paths within the medium cannot be neglected and higher-order multiple scattering between the particles becomes significant. Thus, higher-order approximation of the Foldy-Twersky equation (Ishimaru 1999) is required to calculate the effective propagation constant of the medium.

### 4.3.1 Quasi-Crystalline Approximation (QCA)

The Quasi-Crystalline Approximation (QCA) is a higher-order approximation than the effective field approximation. Truncation is made at the second stage of the hierarchy

of equations. The quasi-crystalline approximation using Mie scattering coefficients and the Percus-Yevick approximation for the pair distribution function has been used for dense media, with densities up to 45% (Leung Tsang 2002). The following is a brief review of the QCA, further details can be found in Leung Tsang (2002).

Consider a system of $N$ identical dielectric spheres at positions, with relative permittivity $\epsilon_s$, embedded in a background medium of relative permittivity $\epsilon_a$, at locations $\bar{r}_p$, $p = 1, 2, 3, ...N$. An electric field $E_{inc}(\bar{r})$ with frequency $\omega$ is incident on this system, it can be expressed in terms of the regular vector spherical wave functions $\bar{M}^1_{mn}$ and $\bar{N}^1_{mn}$, where the superscript denotes the choice of wave functions that are regular at the origin (Zurk *et al.* 2007):

$$E_{inc}(\bar{r}) = \sum_{m,n} \left[ a^{(M)}_{mn} \bar{M}^1_{mn}(kr, \theta, \phi) + a^{(N)}_{mn} \bar{N}^1_{mn}(kr, \theta, \phi) \right], \tag{4.20}$$

where $k$ is the background wave number, given by $k = \sqrt{\epsilon_a}(\omega/c)$ with $c$ representing the speed of light in vacuum, and $a^{(M)}_{mn}$ and $a^{(N)}_{mn}$ represent the coefficients of the spherical wave functions. The total field incident on the $p^{\text{th}}$ particle is the sum of the incident field and the field scattered from the other particles in the medium and can be given by:

$$E_p(\bar{r}) = \sum_{m,n} \left[ w^{(M)}_{mn} \bar{M}^1_{mn}(kr, \theta, \phi) + w^{(N)}_{mn} \bar{N}^1_{mn}(kr, \theta, \phi) \right], \tag{4.21}$$

where $w^{(M)}_{mn}$ and $w^{(M)}_{mn}$ are the unknown coefficients that describe the scatterers response to the incident field. Using the $T$-Matrix formulation, these coefficients ($w^{(M)}_{mn}$ and $w^{(M)}_{mn}$) can be expressed as:

$$\bar{w}_p = \sum_{j=1\,,\, j\neq p}^{N} \bar{\bar{\sigma}}(k\bar{r}_{pj}) \bar{\bar{T}} \bar{w}_j + e^{i\bar{k}_i \cdot \bar{r}_p} \bar{a}_{inc}, \tag{4.22}$$

where, $\bar{w}_p$ is a vector of coefficients $w^{(M)}_{mn}$ and $w^{(M)}_{mn}$ grouped together, with a length of $2L_{max}$=$2n_{max}(n_{max}+2)$ (where $n_{max}$ is the order of the multipole expansion), $\bar{\bar{\sigma}}(k\bar{r}_{pj})$ is a matrix accounting for the coordinate transformation such that $\bar{r}_{pj}$ denotes a vector pointing from the center of the $p_{th}$ scatterer to the center of the $j^{\text{th}}$ scatterer, $\bar{\bar{T}}$ is the $T$-Matrix for the scatterers, and $\bar{a}_{inc}$ represents the vector of incident field coefficients ($a^{(M)}_{mn}$ and $a^{(N)}_{mn}$).

The scattered field coefficients $\bar{a}^S_p$, for a particle at the $p^{\text{th}}$ position can be now be expressed as:

$$\bar{a}^S_p = \bar{\bar{T}} \bar{w}_p. \tag{4.23}$$

In the above formulation, it must be noted that the solution for Eq. 4.20 and Eq. 4.21 needs precise information for the particle positions, shape, orientation etc. For most practical applications, it is impossible to determine these parameters. Often, numerical (such as Monte-Carlo simulation) or analytical approaches (configurational averaging) are used to approximate the solution. In the analytical approach, statistical configuration averaging is performed using a conditional probability function for the random particle positions $P(\bar{r}_1, \bar{r}_2, ...\bar{r}_p^{'}, ...\bar{r}_N|\bar{r}_p)$, where $'$ represents the missing term. Using the conditional averaging, the unknown coefficients $\bar{w}_p$ for the particle at the $p^{\text{th}}$ position can be estimated as:

$$\begin{aligned} \mathrm{E}(\bar{w}_p) &= \int \mathrm{P}(\bar{r}_1, \bar{r}_2, ...\bar{r}_p^{'}, ...\bar{r}_N|\bar{r}_p)\bar{w}_p d\bar{r}_1 d\bar{r}_2 ... d\bar{r}_l^{'} ... d\bar{r}_N, \\ &= \bar{w}(\bar{r}_p). \end{aligned} \tag{4.24}$$

The conditional probability can be expanded using Bayes' rule, to generate a hierarchy of equations. However, the QCA truncates the equations to a second-order level. For a homogeneous medium with identical particles, Eq. 4.24 can be rewritten as:

$$\bar{w}(\bar{r}_p) = n_0 \int d\bar{r}_j g(|\bar{r}_j - \bar{r}_p|)\bar{\bar{\sigma}}(k\bar{r}_{pj})\bar{\bar{T}}\bar{w}(\bar{r}_j) + e^{i\bar{k}_i\cdot\bar{r}_p}\bar{a}_{\text{inc}}, \tag{4.25}$$

where $n_0$ is the particle number density (number of particles per unit volume), and $g(r)$ is the pair distribution function for two particles separated by a distance $r$. To solve the above equation, the following approximate solution is assumed for an incident field given by $\bar{E}_{\text{inc}}(\bar{r}) = \hat{y}e^{ikz}$ in terms of the spherical wave expansion of Eq. 4.20:

$$\bar{w}(\bar{r}_j) = e^{i\bar{K}_{\text{eff}}\cdot\bar{r}_p}\bar{a}_{\text{inc}}, \tag{4.26}$$

where $K_{\text{eff}}$ is the effective wave number of the homogeneous medium. The approximate solution given in Eq. 4.26 is then inserted in the Eq. 4.25. This results in two kinds of dependencies characterized by the respective phase terms. Some terms depend on the wave propagating with the wavenumber of the incident waves, and the others depend on the waves propagating with the wavenumber of the effective medium ($K_{\text{eff}}$). According to the Ewald-Oseen extinction theorem, terms propagating with wavenumber of the incident field should balance each other, thus, generating a wave that extinguishes the original incident wave (Leung Tsang 2002). The terms with the effective wavenumber $K_{\text{eff}}$ are balanced to satisfy a generalized law. This process results in the following solution for $K_{\text{eff}}$:

$$K_{\text{eff}} = k - \frac{i\pi n_0}{k^2}\sum_n (T_n^{(M)}X_n^M + T_n^{(N)}X_n^N)(2n+1), \tag{4.27}$$

where $T_n^{(M)}$ and $T_n^{(N)}$ are the scattering coefficients of the $T$-matrix, $X_n^{(M)}$ and $X_n^{(N)}$ are unknown amplitudes that satisfy a system of simultaneous equations resulting from the  law (Leung Tsang 2002).

A closed form solution for the $K_{\text{eff}}$ can be obtained in the low frequency Rayleigh limit, by considering only the first-order electric dipole terms $T_1^{(M)}$ in the solution of the LorentzLorenz law. Further, the Percus-Yevick pair-distribution function can be used to describe the two particle pair-distribution $g(r)$ (Leung Tsang 2002). The closed form solution for $K_{\text{eff}}$ can now be given by:

$$K_{\text{eff}} = \sqrt{k^2 + \frac{3Vk^2y}{1-Vy}\left[1 + i\frac{2}{3}k^3a^3y\frac{(1-V)^4}{(1-Vy)(1+2V)^2}\right]}, \tag{4.28}$$

where $V$ represents the volume fraction of the particles, $a$ is the particle radius, and $y = (\epsilon_s - \epsilon_a)/(\epsilon_s + 2\epsilon_a)$. For the higher frequencies, the solution can be determined numerically. Leung Tsang (2002) have described a solution approach by searching for the determinant roots in the complex $K_{\text{eff}}$ plane by using Muller's method. The initial guesses can be obtained from either the Foldy's approximation described in the Section 4.2.2 or the low-frequency solution given by Eq. 4.28.

### 4.3.2 Effective medium theories

Optical properties of heterogeneous materials can be described in terms of the effective dielectric constant. Numerous effective medium expressions, with varying degree of details and complexities, have been developed. However, two effective medium theories, the Maxwell Garnett (1904) theory and the Bruggeman (1935) theory are very popular and widely used. Both theories are quasi-static theories, i.e. the effective dielectric constant for both theories does not explicitly depend on particle or inclusion size of the medium, thus, restricting their applicability to media with grain or inclusion sizes much smaller than the incident wavelength. Various extensions of the Maxwell Garnett and Bruggeman theories have been reported in the literature (Rawashdeh *et al.* 1998, Chýlek and Srivastava 1983, Doyle 1989, Foss *et al.* 1994, Lakhtakia 1992, Shanker and Lakhtakia 1993, Stroud and Pan 1978). The main purpose of these extensions was to remove the quasi-static restriction by yielding the dependence of the effective dielectric constant on the size of the grains or inclusions in the medium. Most of these extensions (Rawashdeh *et al.* 1998, Doyle 1989, Foss *et al.* 1994, Lakhtakia 1992, Shanker and Lakhtakia 1993) still considered the size of the grains or inclusions inside the medium

to be electrically small ($2\pi a/\lambda \ll 1$), where $a$ is the radius of the particles and $\lambda$ is the wavelength of the incident electromagnetic radiation, assuming the particles to be radiating like dipoles in presence of external electric field.

In 1978, Stroud and Pan (1978), proposed a new theory, *Dynamic Effective Medium Approximation* or DEMA, by considering a full multipole expansion to treat scattering from particles of sizes comparable to the wavelength of the incident radiation. This theory is not restricted to particles small compared to the wavelength of radiation in the composite, but is valid even for larger particles (or higher frequencies), as long as the attenuation length ($\Im K_{\text{eff}}{}^{-1}$) is large compared to characteristic particle or inclusion dimensions. Consider an electromagnetic wave propagating through a composite medium. As a result of multiple scattering and absorption in the medium, the wave gets attenuated as it propagates through the medium. Stroud and Pan (1978) argued that, the propagation of the wave in the medium can be described by an effective propagation constant $K_{\text{eff}}$, such that the summation of the forward scattering amplitude of the scattered waves, over all the scatterers in the composite medium is zero. This condition is defined as the self-consistency condition for determining the effective propagation constant $K_{\text{eff}}$ in the DEMA. An alternative interpretation of this conditions can be described as: consider the electric field at a point $\bar{x}$ in the medium, which can be described as the sum of incident electric field ($E_{\text{inc}}$) and the sum of the scattered field ($E_{\text{scat}}$) from the various scattering centers (grains or inclusions) of the medium. This can be expressed as:

$$E(\bar{x},t) = E_{\text{inc}}(\bar{x},t) + \sum_i E^{(i)}_{\text{scat}}(\bar{x},t), \tag{4.29}$$

where $E^{(i)}_{\text{scat}}$ represents the scattered field from the $i^{\text{th}}$ scatterer. If the $i^{\text{th}}$ scatterer is sufficiently far away from the point $\bar{x}$, then according to the self-consistency condition, the sum of all the scattered fields from all the scatters in the medium must become zero, in some average sense:

$$\sum_i E^{(i)}_{\text{scat}}(\bar{x},t) = 0. \tag{4.30}$$

Following Stroud and Pan (1978), Chýlek and Srivastava (1983) proposed a generalization of the self-consistency DEMA, by considering a continuous size distribution of grains or inclusions and an arbitrary number of components in the composite material. In the following section, we provide a brief review of the *Generalized DEMA* approach.

### Generalized DEMA

The Chýlek-Srivastava model considers a medium made of random mixture of small particles with a bulk dielectric constant of $\epsilon_j$. Such a mixture can be considered as space filled with random mixture of two or more constituents, and we can term this as an aggregated structure. This aggregated structure can be modelled as a random mixture of homogeneous spheres of individual materials. Considering a mixture of $j$ components each having a size distribution of grains $\rho_j(r)$, we can express the forward scattering amplitude $S(0)$ in the following form (Chýlek and Srivastava 1983):

$$S(0) = \frac{1}{2}\sum_j\sum_n (2n+1)\int \rho_j(r)[a_n(r,\epsilon_j) + b_n(r,\epsilon_j)]dr, \tag{4.31}$$

where $r$ stands for the radius of the grain, the sum $j$ runs over all the components of the mixture, while the sum $n$ runs over all the contributing partial waves and $a_n$ and $b_n$ are the partial wave scattering amplitudes of the Mie scattering functions. First, consider the case where particles of the random mixture are smaller than the wavelength $\lambda$ of the incident radiation. This is the case where only the first partial wave contributes to the forward scattering amplitude, as the contribution of higher order partial wave is very small and can be neglected, an expression of which can be derived by expanding $a_1$and $b_1$ in a power series of the spherical particle radius $r$, and only retaining the leading terms of the expansion as follows:

$$(a_1)_j = \frac{2}{3}ix_j^3\frac{\epsilon_j - 1}{\epsilon_j + 2}, \tag{4.32}$$

$$(b_1)_j = \frac{i}{45}ix_j^5(\epsilon_j - 1), \tag{4.33}$$

where $x = 2\pi r/\lambda$, is the size parameter for a spherical particle of radius $r$. Substituting Eq. (4.32) and Eq. (4.33) in Eq. (4.31), and assuming all particles have uniform radius, we obtain:

$$S(0) = i\left[\frac{2\pi}{\lambda}\right]^3\sum_j\int r^3\rho_j(r)\left[\frac{\epsilon_j - 1}{\epsilon_j + 2} + \frac{1}{30}\left[\frac{2\pi}{\lambda}\right]^2 r^2(\epsilon_j - 1)\right]dr. \tag{4.34}$$

Now, using the condition that when scatterers are placed in an effective medium of effective dielectric constant $\epsilon_{\text{eff}}$, the forward scattering amplitude becomes zero, we obtain the following expression in terms of effective dielectric constant $\epsilon$:

$$\sum_j V_j\frac{\epsilon_j - \epsilon_{\text{eff}}}{\epsilon_j + 2\epsilon_{\text{eff}}} + \frac{2\pi}{45}\frac{\omega^2}{c}(\epsilon_j - \epsilon_{\text{eff}})\int r^5\rho_j(r)dr = 0, \tag{4.35}$$

where $\omega$ is the circular frequency, $c$ is the speed of light and $V_j$ is the volume fraction of the $j^{\text{th}}$ component of the composite material.

Now, considering the case where some of the particles in the composite are larger and have size comparable to the incident wavelength $\lambda$, under these circumstances the contribution from higher partial wave to the forward scattering amplitude becomes significant and is required to be considered in the formulation of the effective dielectric constant $\epsilon$. The new equation to obtain the effective dielectric constant $\epsilon_{\text{eff}}$ is given as:

$$i\left[\frac{\omega}{c}\right]^3 \epsilon_{\text{eff}}^{\frac{3}{2}} \sum_j \left[\frac{3}{4\pi} V_j \frac{\epsilon_j - \epsilon_{\text{eff}}}{\epsilon_j + 2\epsilon_{\text{eff}}} + \frac{1}{30}\left[\frac{\omega}{c}\right]^2 (\epsilon_j - \epsilon_{\text{eff}}) \int r^5 \rho_j(r) dr\right] + \frac{1}{2}\sum_k \sum_n (2n+1) \int \rho_j(r)[a_n(r, \frac{\epsilon_k}{\epsilon_{\text{eff}}}) + b_n(r, \frac{\epsilon_k}{\epsilon_{\text{eff}}})]dr = 0, \quad (4.36)$$

where the sum $j$ runs over all the components contributing to the scattering amplitude only through the first partial wave, the sum $k$ runs over the components contributing other higher partial waves and the sum $n$ runs over all the contributing partial waves.

Chýlek and Srivastava (1983) also gave a simple iterative scheme for calculating effective dielectric constant $\epsilon$ for the case of a composite made up of two components with bulk dielectric constant $\epsilon_1$ and $\epsilon_2$ as follows:

$$\epsilon_{\text{eff}} = \epsilon_1 \frac{A(1-V) + B(\epsilon_{\text{eff}})}{A(1-V) - 2B(\epsilon_{\text{eff}})}, \quad (4.37)$$

where

$$A(\epsilon_{\text{eff}}) = i\frac{12\pi^2 \epsilon_{\text{eff}}^{3/2}}{\lambda^3}, \quad (4.38)$$

$$B(\epsilon_{\text{eff}}) = \int \sum_n (2n+1)\left[a_n(r, \frac{\epsilon_2}{\epsilon_{\text{eff}}}) + b_n(r, \frac{\epsilon_2}{\epsilon_{\text{eff}}})\right] \rho(\text{r})\text{dr}, \quad (4.39)$$

and $V$ is the volume fraction for the component with bulk dielectric constant $\epsilon_2$. The volume fraction for the component with bulk dielectric constant $\epsilon_1$ is given as $(1-V)$. Eq. (4.37) can be solved recursively for $\epsilon_{\text{eff}}$ using Eq. (4.38) and Eq. (4.39) until the solution converges.

### 4.3.3 Comparison of generalized DEMA with THz-TDS

In this section, we apply the generalized DEMA described in Section 4.3.2 to estimate the frequency dependent scattering loss from three different granularities of polyethylene and air samples and compare the theoretical results with the transmission THz-TDS measurements of these samples.

**Table 4.1. Sample parameter extraction from the 3D model.** The porosity and average air void diameter obtained from the 3D model of the samples.

| Sample | Porosity (in %) | Avg. Air Void Radius |
|---|---|---|
| PE (60 $\mu$m) | 24 | 25 $\mu$m |
| PE (72 $\mu$m) | 25 | 28 $\mu$m |
| PE (360 $\mu$m) | 44 | 90 $\mu$m |

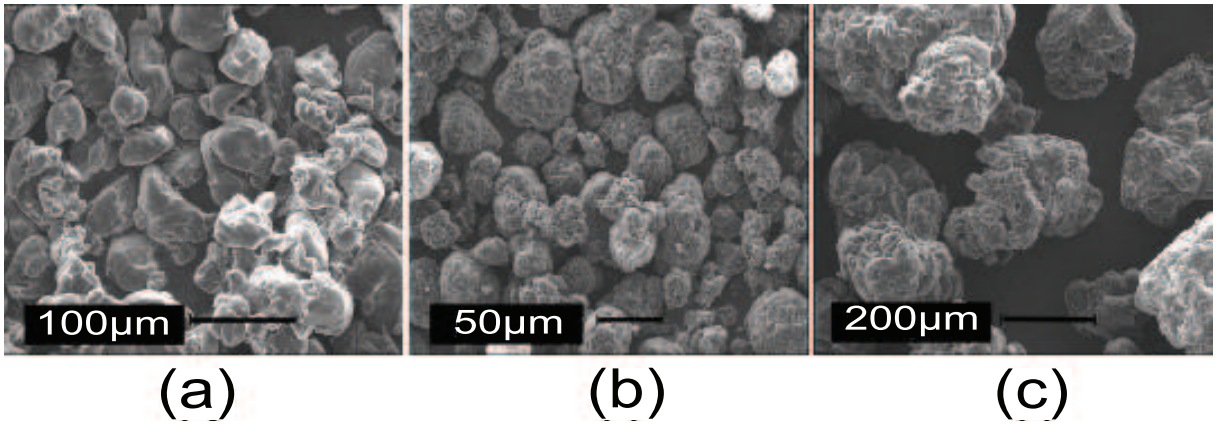


**Figure 4.5. Scanning electron microscope images of PE powders.** Three granularities are shown, with particle diameters of (a) 60 $\mu$m, (b) 72 $\mu$m and (c) 360 $\mu$m.

Three different granularities of spectroscopic grade PE powder from two different manufacturers (Sigma-Aldrich and Inducos), were used for our experiments. Two of the PE powders, one from each manufacturer, had relatively small PE grain sizes, with approximately 60 $\mu$m (Inducos) and 72 $\mu$m (Sigma-Aldrich) diameters, while the third one, again from Inducos, had a larger grain size of approximately 360 $\mu$m in diameter. These dimensions were well within the range indicated by the manufacturer, but we used scanning electron microscope (SEM) images to confirm these dimensions. These images are shown in Fig. 4.5.

In order to determine the volume fraction of PE particles and air voids for each sample, we carry out 3D X-ray tomography on each sample at every 0.68 degree rotation for a full 360 degree view. The images thus obtained are then used to construct a 3D model of the sample using software tool CTAN. From this 3D model of the samples, their respective porosity (volume fraction of air) and the average air void radius are obtained. The results are summarised in Table 4.1.

The 3D model for each sample can be seen in Fig. 4.6. In the case of our experiment we carry out transmission spectroscopy of granular PE and air samples, the background is

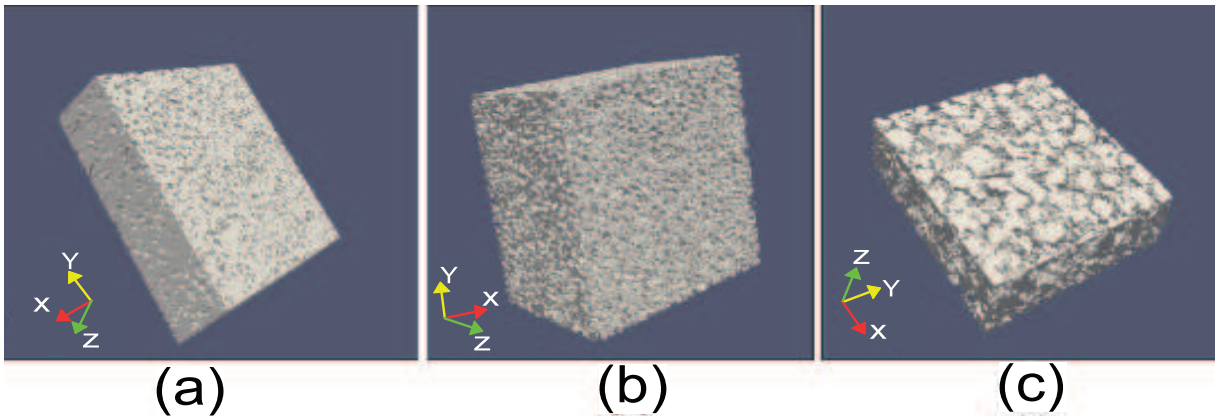


**Figure 4.6. Three dimensional model of the PE powder samples.** Here, the 3D models are constructed using software tool CTAN and Paraview, from the sample scans obtained via X-ray tomography. From the 3D models, the sample porosity (volume fraction of air) and the average air void diameter are obtained. Three granularities are shown, with particle diameters of (a) 60 $\mu$m, (b) 72 $\mu$m and (c) 360 $\mu$m.

modeled as pure PE with a relative permittivity of 2.13 and air voids occupy 25%, 27% and 44% by volume, and have a average radius of approximately 28, 30 and 86–90 $\mu$m, for 60, 72 and 360 $\mu$m (PE particle diameter) samples, respectively. Note that in the terahertz region, these spherical scatterers are in the Mie regime, which means that low frequency Rayleigh scattering does not apply, which in turn leads to the requirement for multipole expansions, even in the case of spherical scatterers. As the software used only determines the average air void radius for each sample, we assume all air voids to be of the same dimensions and therefore the size distribution function $\rho(r)$ in Eq. 4.39 takes the form of a $\delta$ function:

$$\rho(r) = N\delta(r), \tag{4.40}$$

where $N$ is the number of air voids per unit volume. Hence, Eq. 4.39 becomes:

$$B(\epsilon_{\text{eff}}) \quad = \quad N\sum_n (2n+1)\left[a_n(r, \frac{\epsilon_2}{\epsilon_{\text{eff}}}) + b_n(r, \frac{\epsilon_2}{\epsilon_{\text{eff}}})\right], \tag{4.41}$$

where $N$ is given by:

$$N = \frac{3V}{4\pi r^3}. \tag{4.42}$$

Using the setup described by Fig. 2.6, we carry out transmission measurements of the three samples comprising PE particles and air voids, prepared by sandwiching the granular PE powder between the two plates of a sample holder made of Cyclic Olefin Copolymer (COC), also known as Topas,refractive index 1.6, of dimensions 5 mm inner

thickness and 1 cm diameter. The effective dielectric constant, $\epsilon_{\text{eff}}$, is computed using the effective medium theory as described above. We make use of the relation $k_{\text{eff}} = \sqrt{\epsilon_{\text{eff}}}\omega/c$ to obtain the effective wave number, of the medium. Neglecting any intrinsic attenuation or absorption within the media, we can assume that the total attenuation here is entirely due to the scattering of the incident radiation, and can be obtained from:

$$\alpha_{\text{eff}} = \Im(k_{\text{eff}}), \tag{4.43}$$

where $\Im(\cdot)$ indicates the imaginary part. In this analysis, we assume a plane wavefront for the terahertz radiation, in the far field. Fig. 2.9 illustrates the propagation of THz radiation propagates through a sample cell during measurements of the sample and reference data. By analyzing the propagation geometry, and assuming that the reflections are removed from the sample and reference data, the transfer function is given by:

$$H(\omega) = \frac{\tau_{\text{ws}}\tau_{\text{sw}}}{\tau_{\text{wa}}\tau_{\text{aw}}} \exp(-j(\hat{n}_s - n_0)\frac{\omega l}{c}), \tag{4.44}$$

where the subscripts a, s and w are for air, sample, and window, respectively, $l$ is the thickness of the sample, and $\tau$ represents the Fresnel transmission coefficients. Therefore, $\tau_{\text{aw}}$ represents the propagation from air to window, $\tau_{\text{ws}}$ represents the propagation from window to sample, and so on. Here $n_0$ is the refractive index of free air and $\hat{n}_s$ is the complex refractive index of the sample given by the formula $\hat{n}_s = n_s + jk_s$ with $n_s$ and $k_s$ representing the measured real part of refractive index and the extinction coefficient of the sample respectively.

Thus using the above equation and the relation $\alpha_s(\omega) = 2k_s(\omega)\frac{\omega}{c}$, the optical attenuation $\alpha_s(\omega)$ can be found from:

$$\alpha_s(\omega) = \frac{2}{l}\left\{\ln\left[\frac{\tau_{\text{ws}}\tau_{\text{sw}}}{\tau_{\text{wa}}\tau_{\text{aw}}}\right] - \ln|H(\omega)|\right\}. \tag{4.45}$$

For each sample, we compare the measured attenuation loss, calculated using Eq. 4.45 with the attenuation loss given by Eq. 4.43. Fig. 4.7 show this comparison. From the visual analysis of Fig. 4.7, it can be inferred that while small details of the transmitted field and attenuation are not captured by the simulation, the overall frequency dependent trends for the three media, as calculated by the model of Chýlek *et al.* (1988), were in good agreement with the experimental measurements.

In conclusion, we examine the use of the Chýlek *et al.* (1988) effective medium model, for estimating frequency dependent scattering loss of terahertz by two component

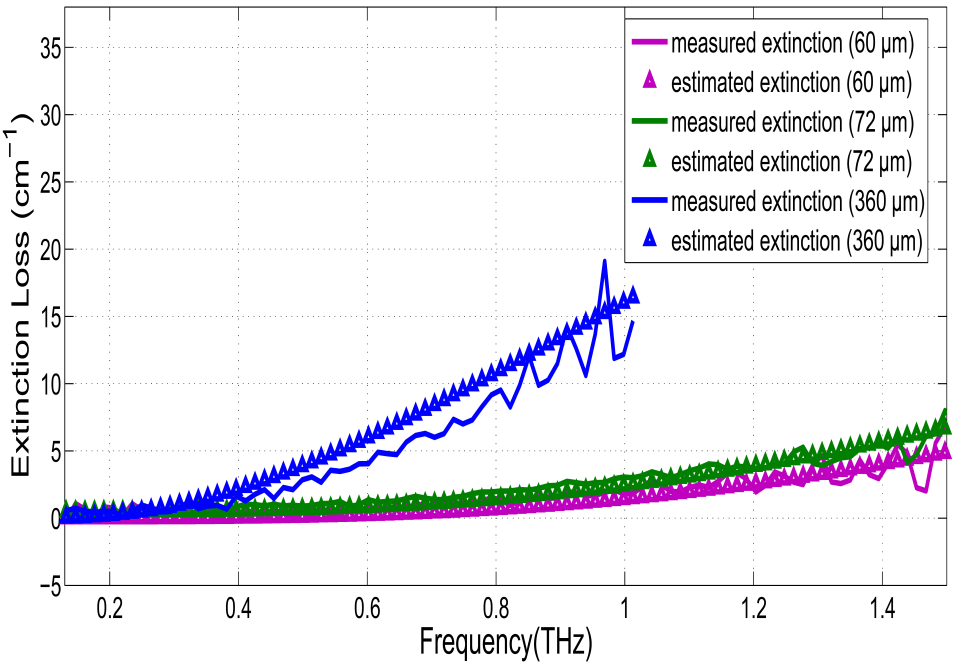


**Figure 4.7. Comparision of generalised DEMA with measurements.** Comparison of measured (solid) and theory estimated (dots) frequency dependent total attenuation (extinction) loss for the three different PE grain size samples, 60 $\mu$m (blue), 72 $\mu$m (green) and 360 $\mu$m (brown), with air void diameters 48 $\mu$m, 56 $\mu$m and 180 $\mu$m, respectively.

composite granular materials. From the comparison of simulated and experimental results, it is found that the model of Chýlek *et al.* (1988) reasonably estimates the optical properties of the samples made of granular PE particles of dimensions comparable to the incident wavelength. For estimating the effective dielectric properties of a composite medium with more than two components, the general formula given by Eq. (12) of Chýlek *et al.* (1988) must be used.

## 4.4 An iterative effective field approximation for high density composites

As discussed in Section 4.2, when the volume fraction of scattering particles in a composite medium is low, i.e., when the average inter-particle distance is greater than the incident wavelength, multiple-scattering processes are unlikely to occur. The field that impinges on each particle can be identified with the primary incident wave (Newton 2002, Mishchenko *et al.* 2002). For such cases, the macroscopic optical constants of the medium can be described in terms of the response of single particles to the incident

field. In Section 4.2, we discussed two approaches for calculating the effective propagation constant in a low density medium, namely the independent scattering approximation (ISA) and the effective field approximation (EFA). The independent scattering approximation is found to be valid only for very low concentrations (<1%), while, Foldy's effective field aproximation, which takes into account the first order multiple scattering process, is found to produce resonable results for volume densities up to ≈ 10% (Kuga *et al.* 1996, Giusto *et al.* 2003). However, when the density of the scatterers in the medium increases (>10%), the field incident on each particle is a superposition of the incident primary wave and of the field that has previously been scattered by the other particles in the medium. In other words, multiple scattering processes become dominant and independent scattering assumptions are no longer valid.

Giusto *et al.* (2003) gave a general description of the optical behavior for Intralipid solutions in terms of the characteristics of propagation of the coherent field through a random dispersion of particles, under the assumption of the Foldy-Twersky equation implying that, in general, the coherent field can be taken to satisfy the equation:

$$\left(\nabla^2 + K^2\right) \langle \psi \rangle = 0, \tag{4.46}$$

where $K$ is the effective propagation of the medium, as calculated from the Eq. 4.15, and $\langle \psi \rangle$ is the so-called coherent intensity. Giusto *et al.* (2003) argued that on consideration that Eq. 4.15 may be solved by iteration, the effective propagation constant $K$, of a medium with high scatterer density, can be calculated by a simple iteration of Eq. 4.15:

1. The first step is to start with the Foldy-Twersky equation for calculating the effective propagation constant of the medium with particles embedded in a homogeneous, non-absorbing host with propagation constant $k$:

$$K = \sqrt{k^2 + 4\pi\eta f(0)}, \tag{4.47}$$

2. In the second step, we again solve Eq. 4.47 by considering the same dispersion of the particles, however, the host medium is now represented by the complex propagation constant $K$ obtained in the first step. The scattering properties of the particles can now be calculated as if they were independent particles embedded into an effective medium with propagation constant $K$. Giusto *et al.* (2003) argued that the assumption of such a fictitious host medium should account for the multiple-scattering processes (up to second order) that occur among the particles. When calculating $f(0)$, the forward scattering amplitude, for the original dispersion, i.e., particles in a homogeneous,

non-absorbing host, the scattering cross-sections were calculated using results of Mie theory. For the second step of the iteration, when the particles are considered within the medium with the complex refractive index $K$, Giusto *et al.* (2003) followed the procedure of Sudiarta and Chylek (2001). They applied their iterative scheme (referred to as iterative EFA now onwards) to various densities of solutions of stock intralipid-10% and found their procedure to be highly effective up to 15% volume density and show limited disagreement at densities up to 22% for mesurement of scattering coeffcient carried out at a single wavelength ($\lambda$ = 632.8 nm). However, it must be noted that the Foldy's EFA, given by Eq. 4.15, assumes the particles to be point scatterers and that the medium is sparse enough, such that the scatterers positions do not influence one another. As a result, it is valid only for the cases where the backscattering from the particles can be neglected and only forward scattering is considered. This may explain the overestimation of the measurements by the theoretical results obtained by Giusto *et al.* (2003) at 22% volume density. Secondly, Giusto *et al.* (2003) did not provide any convergence criteria for their algorithm, which is essentially a two step process.

On the other hand, Waterman and Truell (1961) provided an expression for the effective propagation constant, for a medium in a concatenated slab formulation with an ensemble of finite sized scatterers, that considered the backscattering from individual particles and included terms up to the second order in $\eta$. As a result, this theory is found to produce reasonable estimates of the effective scattering attenuation for a medium with finite size particles (size parameter $a(\omega/c)$ up to 2, where $a$ is the average particle radius) and volume densities up to 30% (Chaix *et al.* 2006). Waterman and Truell (1961) gave the following expression for the effective propagation constant:

$$K = \sqrt{k^2 \left[1 + \frac{2\pi N f(0)}{k^2}\right]^2 - \left[\frac{2\pi N f(\pi)}{k^2}\right]^2}, \tag{4.48}$$

where $N$ is the number of scatterers per unit volume, $f(0)$ and $f(\pi)$ are the forward scattering and backward scattering amplitudes of a single particle, respectively. Now, because of the fact that like Eq. 4.15, Eq. 4.48 can also be solved iteratively and that the Waterman and Truell (1961) theory considers multiple scattering process for finite sized scatterers up to the second order of the scatterer density, we believe, it will be a better model for the iterative scheme suggested by Giusto *et al.* (2003).

Here, we employ the iterative scheme similar to the one suggested by Giusto *et al.* (2003), however, instead of using Foldy's EFA approximation, given by Eq. 4.15, we

have used the approximation of Waterman and Truell (1961) given by Eq. 4.48 and we also provide a convergence condition for the algorithm to determine the optimum number of iterations required. The resulting iterative scheme is illustrated in Fig. 4.8 and will be referred to as *iterative WT-EFA* from now onwards.

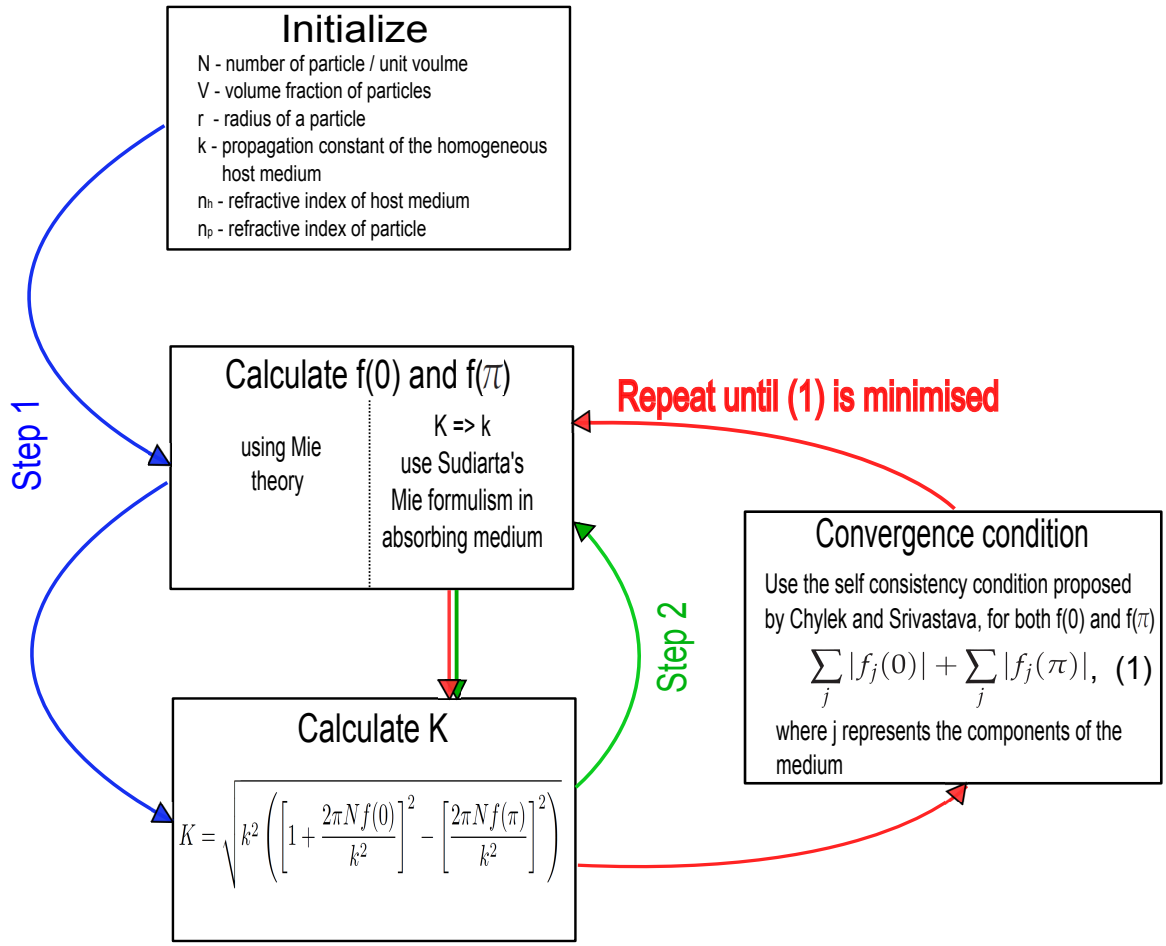


**Figure 4.8. The Waterman-Truell approximation.** Flow-chart illustrating the iterative algorithm based on Waterman-Truell approximation.

As can be seen for the Fig. 4.8, in the first step, we calculate the forward ($f(0)$) and backward ($f(\pi)$) scattering amplitudes using the Mie formalism of scattering by a single particle. Then we use the Eq. 4.48 to obtain the first estimate of the effective propagation constant of the medium. In the second step, we again calculate the ($f(0)$) and backward ($f(\pi)$) scattering amplitudes, however, this time we use the formalism of Sudiarta and Chylek (2001) for scattering by a particle in an absorbing medium, this is followed by the second evaluation of $K$ using Eq. 4.48. Up to this point, our algorithm is the same as that of Giusto *et al.* (2003), with only exception that we have used the Eq. 4.48 for calculating $K$. After the second step, we evaluate the self consistency

condition for an effective medium given by Chýlek and Srivastava (1983), which states that the forward scattering amplitude $f(0)$ vanishes if the components of the original system are placed back in the effective medium described by the effective propagation constant $K$. However, in our algorithm we also have the contribution from the backward scattering amplitude $f(\pi)$, accordingly the self consistency condition is modified such that when the components of the original system are placed back in the effective medium, both, $f(0)$ and $f(\pi)$ must be vanished. Indeed, it is impossible to conceive a real physical situation in which the forward scattering amplitude of a single object disappears while the backward scattering amplitude still exists. Thus after the second step we calculate

$$\sum_j \left|f_j(0)\right| + \sum_j \left|f_j(\pi)\right|, \tag{4.49}$$

where $j$ represents the components of the original medium, and repeat the algorithm as shown in Fig. 4.8, until Eq. 4.49 is minimized.

### 4.4.1 Comparison of the iterative EFA with THz-TDS

In this section, we apply the iterative WT-EFA algorithm, described in the previous Section 4.4, to estimate the frequency dependent scattering loss from three different granularities of polyethylene and air samples and compare the theoretical results with the transmission THz-TDS measurements of these samples.

Three different granularities of spectroscopic grade PE powder from two different manufacturers (Sigma-Aldrich and Inducos), were used for our experiments. The details of sample preparation and internal structure dimensions are the same as described in the Section 4.3.3. Using the setup described by Fig. 2.6, we carry out transmission measurements of the three samples. The background is modeled as pure PE with a relative permittivity of 2.13 and the air voids are considered as the scattering inclusions. The effective propagation constant, $K$, is computed using the iterative EFA algorithm illustrated in Fig. 4.8. Neglecting any intrinsic attenuation or absorption within the media, we can assume that the total attenuation here is entirely due to the scattering of the incident radiation, and can be obtained from:

$$\alpha_{\text{eff}} = \Im(K), \tag{4.50}$$

where $\Im(\cdot)$ indicates the imaginary part. In this analysis, we assume a plane wavefront for the terahertz radiation, in the far field. Fig. 2.9 illustrates the propagation

of THz radiation propagates through a sample cell during measurements of the sample and reference data. Using the Eq. 4.44 and Eq. 4.45 the optical attenuation can be determined.

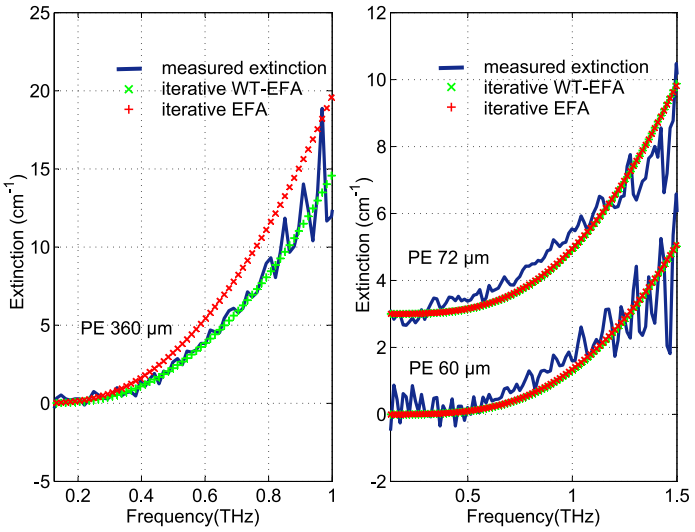


**Figure 4.9. Comparison of iterative WT-EFA with measurements.** (a) Comparison of measured (solid) and theory estimated (cross) frequency dependent total attenuation (extinction) loss for PE sample with average grain size of 360 $\mu$m, (b) Comparison of measured (solid) and theory estimated (cross) frequency dependent total attenuation (extinction) loss for PE samples with average grain size of 60 $\mu$m and 72 $\mu$m (with a vertical offset of 3 cm$^{-1}$ for clarity).

For each sample, we compare the measured attenuation loss, calculated using Eq. 4.45, with the attenuation loss given by Eq. 4.50, obtained by applying the iterative EFA algorithm. For the purpose of comparison, we also applied the iterative scheme suggested by Giusto *et al.* (2003) to obtain the estimated scattering attenuation loss for the three samples. Fig. 4.9 show this comparison. From the visual analysis of Fig. 4.9, it can be inferred that while small details of the attenuation are not captured by the simulation, the overall frequency dependent trends for the three media, as calculated by both the model algorithm, were in good agreement with the experimental measurement of the PE sample with average particle diameter 60 $\mu$m and PE sample with average particle diameter 72 $\mu$m. However, for the sample with bigger PE particles, the estimations of the iterative algorithm show much better accuracy than the iterative EFA algorithm proposed by Giusto *et al.* (2003). These results clearly indicate that when the scatterers are comparable to the incident wavelength, they can no longer be

assumed to be point sources. As this is one of the central assumptions of Foldy's approximation, the two step algorithm proposed by Giusto *et al.* (2003) fails to accurately estimate the scattering attenuation for the PE sample with the biggest scatterer dimension ($\approx$ 90 $\mu$m in radius). While, our iterative WT-EFA algorithm using the theory of Waterman and Truell (1961), accurately estimates the scattering attenuation for all the three PE samples.

In conclusion, we propose an iterative EFA algorithm using the multiple scattering theory of Waterman and Truell (1961) and the self consistency condition of Chýlek and Srivastava (1983), for calculating the effective propagation constant. From the comparison of simulated and experimental results, it is found that the iterative WT-EFA algorithm reasonably estimated the optical properties of high density (>10%) samples made of non-absorbing granular PE particles of dimensions comparable to the incident wavelength.

## 4.5 A numerical approach to scattering reduction

In this section, we present a numerical approach based on the modified Rayleigh-Gans-Debye approximation to reduce the scattering contribution in transmission mode THz-TDS measurements of two phased media with absorbing constituents. The resulting expression relates the scattering attenuation in terms of the refractive indices of the sample constituents. The proposed technique not only eliminates the increased baseline, but also corrects the extinction spectrum for asymmetrically distorted absorption bands, often observed as consequence of multiple scattering in the sample (Fischer *et al.* 2002, Walther *et al.* 2003). The method is tested on experimentally obtained extinction spectrum of a sample made of $\alpha$-monohydrate lactose and PE powder.

The basic theory of light scattering by a single particle embedded in a non absorbing medium has been thoroughly investigated and described by various researchers (Mie 1908, Ishimaru 1999, Hulst 1957). Consider a particle with refractive index $n_{\mathrm{p}}$ embedded in a homogeneous non-absorbing medium of refractive index $n_{\mathrm{m}}$. If the relative refractive index of the embedded particle is close to unity, and its size satisfies the condition $kd\,|m-1| < 1$, where $m = n_{\mathrm{p}}/n_{\mathrm{m}}$, $d$ is the particle diameter and $k$ is the propagation constant of the incident radiation, then the Rayleigh-Gans-Debye (RGD) approximation for light scattering by single particle should be valid (Elimelech *et al.*

1998). Such particles are often termed as *optically soft* scatterers. However, several researcher have reported the applicability of the RGD approximations for values of $kd\,|m-1|$ upto 3 with only limited disagreement ($\approx 10\%$) (Farias *et al.* 1996, Wang and Sorensen 2002, Sorensen 2001). Shimizu (1983) proposed a modification to the RGD approximation and compared the resulting scattering pattern with that calulated using exact Mie theory. Their results showed a good agreement, in the small-angle region, with the Mie theory, even for conditions beyond the validity of ordinary RGD approximation $kd\,|m-1| \gg 1$ (2.65 and 5.5 for their experiments). Here, we present a numerical approached based on the modified RGD approximation proposed by Shimizu (1983), to eliminate the scattering contribution in transmission mode THz-TDS measurements.

For a two phased medium composed of the homogeneous background ($n_\mathrm{m}$) and $N$ identical particles with refractive index $n_\mathrm{p}$, the transmitted intensity can be given by:

$$I_\mathrm{t} = I_0 \exp(-\alpha l), \tag{4.51}$$

where $\alpha$ represents the attenuation suffered by the radiation, and $l$ is length of the medium. Assuming the medium to be sparse, the total scattering attenuation can be obtained by multiplying the total number of scatterers ($N$) with the scattered intensity distribution ($I(\theta)$) of a single scatterer integrated over a sphere of radius $r$ and divide by $I_0$. This can be expressed by:

$$\alpha = 2\pi r^2 N \int \frac{I(\theta)}{I_0} \sin\theta d\theta. \tag{4.52}$$

The according to the RGD approximation, the transmitted intensity of a single sphere is given by:

$$I(\theta) = \frac{(1+\cos^2\theta)k^4 p^2 P^2(\theta)}{2r^2} I_0, \tag{4.53}$$

where $\theta$ is the angle of observation, $p$ is the polarizability of the sphere, $k$ is the wavenumber in the surrounding medium ($k = \frac{2\pi n_\mathrm{m}}{\lambda}$), $P(\theta) = \left[\frac{3(\sin u - u\cos u)}{u^3}\right]^2$, $u = 2kam\sin(\frac{\theta}{2})$, and $a$ is the radius of the scatterer (Shimizu 1983). The term $P(\theta)$ is known as the form factor, and represents a correction to the Rayleigh expression which accounts for the size and the shape of the scattering particle. As the scattered intensity drops rapidly as $\theta$ increases, for transmission measurements with very small detector angle of view, the term $(1+\cos^2\theta) \approx 2$ (Dunlap and Howe 1991, Elimelech *et al.* 1998). Using Eq. 4.53, and the expression for $P(\theta)$ and $u$, the integral in Eq. 4.52 can be solved by changing the variable of integration to $u$ with the lower limit of integration given by 0 and the

upper limit set to $u' = 2kam\sin(\theta'/2)$ where $\theta'$ is the detector's angle of view cutoff:

$$\alpha = \frac{4\pi N k^2 p^2}{d^2 m^2} \times \frac{9}{2}\left[\frac{-1}{u'^2} + \frac{\sin 2u'}{u'^3} + \frac{\cos 2u'}{2u'^4} - \frac{1}{2u'^4}\right], \tag{4.54}$$

where $d$ is the diameter of the particle. For a spectrometer with a detector aperture size of 10 mm, the maximum value of $u'$ for a particle of diameter 100 $\mu$m and for frequencies upto 6 THz is found to be $\approx 1$. For values of $u'$ upto 1, the last term $F(u') = \left[\frac{-1}{u'^2} + \frac{\sin 2u'}{u'^3} + \frac{\cos 2u'}{2u'^4} - \frac{1}{2u'^4}\right]$ of Eq. 4.54 can be approximated as a quadratic given by $1 - 0.025u' - 0.18u'^2$. This can be seen in Fig. 4.10.

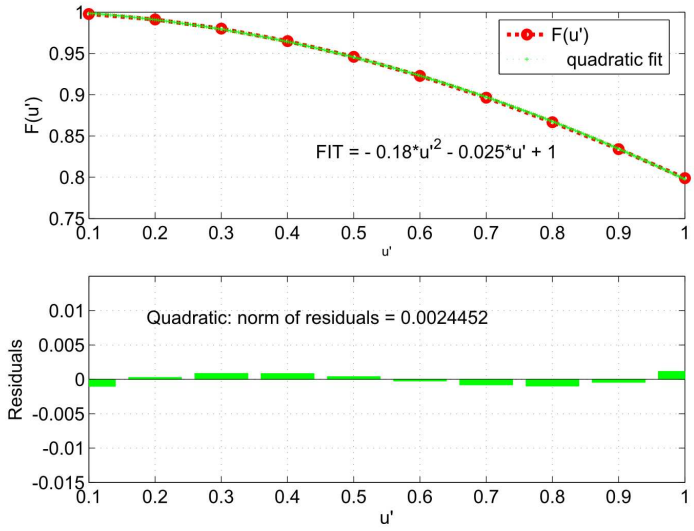


**Figure 4.10. Fitting the function $F(u')$ with a quadratic.** Fitting a quadratic to the function $F(u')$ for values of $u'$ upto 1.

The polarizability $p$ for a sphere of radius $a$ and refractive index $n_\mathrm{p}$ in a background medium $n_\mathrm{m}$ is given by the Clausius-Mossotti relation:

$$p = 4\pi a^3\left[\frac{m^2-1}{m^2+2}\right], \tag{4.55}$$

and given the condition that $|m-1| \ll 1$, the above equation can be approximated as:

$$p = \frac{8}{3}\pi a^3(m-1). \tag{4.56}$$

Substituting the above equation for $p$ and $m = n_\mathrm{p}/n_\mathrm{m}$ in Eq. 4.54 we get:

$$\alpha = 12\pi^2 k^2 dV\frac{(n_\mathrm{p}-n_\mathrm{m})^2}{n_\mathrm{p}^2} \times \left[1 - 0.025u' - 0.18u'^2\right], \tag{4.57}$$

where $V$ represents the volume fraction of the scattering particles in the medium.

The above equation provides a detailed description of the scattering attenuation characteristics of a two phased composite medium. It can be seen that the scattering attenuation is directly proportional to the propagation length $l$ and the volume fraction of the scatterers. Similarly, an increment in the refractive index mismatch between the components of the medium, will also cause the attenuation to increase. The size of the scatterer is related to the total scattering attenuation via the term $F(u') = \left[1 - 0.025u' - 0.18u'^2\right]$ which in turn depends on $u'$ or the measuring system's detector's angle of view. In our measurement setup and generally in all THz Photoconductive Antenna (PCA) detector based setups, a hyper-hemispherical silicon lens is mounted on the aperture to further focus the incoming THz beam to almost a single point on the detector. Such transmission spectrometers have a very small detector angle of view and therefore the value of $u'$ is very small and $F(u') \approx 1$, the scattering attenuation is found to be linearly dependent on the scatterer size $d$:

$$\alpha = 12\pi^2 k^2 dV \frac{(n_\mathrm{p} - n_\mathrm{m})^2}{n_\mathrm{p}^2}. \tag{4.58}$$

One of the conditions of the RGD approximation is that the scatterers of the medium are well separated and act as independent Rayleigh scatterers. The condition of being well separated corresponds to cases where the inter-particle distances are much greater than the particle dimensions, hence the sparse volume concentration. When the volume density increases, the inter-particle effects become stronger and they can not be neglected for the calculation of the transmitted intensity. Many authors have addressed the problem of accounting the inter-particle interferences by incorporating an additional structure factor ($S$) to the expression of the total scattering attenuation given by Eq. 4.52 (Belanger *et al.* 1990, Dunlap and Howe 1991, Hayter and Penfold 1981, Holoubek 1999). Dunlap and Howe (1991) reported that a structure factor accounting for the inter-particle interferences must be a function of the volume fraction, scatterer shape, and size distribution. Under the assumption of spherical particles with uniform particle size distribution, the structure factor $S(V, d, ...)$ reduces to an additional constant factor $S$ to the expression of the total attenuation. Under such conditions, the total scattering attenuation for transmission through a dense two phased medium can be given by:

$$\alpha = 12S\pi^2 \left[\frac{\omega}{c}\right]^2 dV \left(\frac{n_\mathrm{m}}{n_\mathrm{p}}\right)^2 (n_\mathrm{p} - n_\mathrm{m})^2, \tag{4.59}$$

where $k$ is substituted with $(2\pi n_m/\lambda)$, $\omega$ is the angular frequency and $c$ is the speed of incident radiation. While Dunlap and Howe (1991) applied a similar approach to study the temperature dependence of the refractive index and the effect of fillers on the thermal expansion properties of the polymer composites using ordinary RGD approximation, unlike the proposed method, their results are valid for composite materials with constituents satisfying the condition $kd(m-1) \ll 1$ and therefore are applicable to a limited number of materials.

For our measurements, two sample pellets were prepared by thoroughly mixing $\alpha$-monohydrate lactose (Sigma-Aldrich) with two PE powders (with different granularity both supplied by Inducos) with a mass ratio of about 1:2. The grain size of the samples were determined using scanning electron images (SEM) of the powders. From these images, a spherical shape was assumed for all the particles and an average particle diameter of 60 $\mu$m and 360 $\mu$m respectively for PE powders and 73 $\mu$m, for the $\alpha$-monohydrate lactose powder was measured. These dimensions were found to be well within the ranges provided by the supplier. Using a standard setup, we performed transmission mode THz-TDS of the above described sample. The optical parameters of the sample can be determined from Fourier transforms of the measurement of the sample transmitted electric field $E_t$ and the reference electric field measured in absence of the sample $E_{ref}$ as:

$$\frac{E_t(\omega)}{E_{ref}(\omega)} = \frac{4n_s(\omega)}{(n_s(\omega)+1)^2} \exp\left[i(n_s-1)\frac{\omega}{c}l_s\right] \exp\left[-\alpha_s\frac{l_s}{2}\right], \tag{4.60}$$

where $n_s$ represents the refractive index of the sample, $\alpha_s$ represents the total attenuation or extinction coefficient of the sample, and $l_s$ represents the thickness of the sample. The extinction coefficient contains contributions from both absorption and scattering (Shen *et al.* 2008). Using Eq. 4.59 to represent the total scattering attenuation $\alpha$, the extinction coefficient can be expressed as:

$$\alpha_s = \alpha_{abs} + 12S\pi^2\left[\frac{\omega}{c}\right]^2 dV\left(\frac{n_m}{n_p}\right)^2 (n_p - n_m)^2, \tag{4.61}$$

where $\alpha_{abs}$ represents the absorption coefficient of the sample, $n_p$ represents the refractive index of $\alpha$-monohydrate lactose and $n_m$ represents the refractive index of PE. To calculate the refractive index of pure lactose, we use the method suggested by Franz *et al.* (2008), $n_p = (n_s - n_m V_m)/V_p$, where $V_m$ and $V_p$ represent the volume fractions of the host medium (PE) and the embedded particles (lactose), respectively. It must be noted that $V_m + V_p = 1$. The volume fraction of the host medium (PE), $V_m$, can

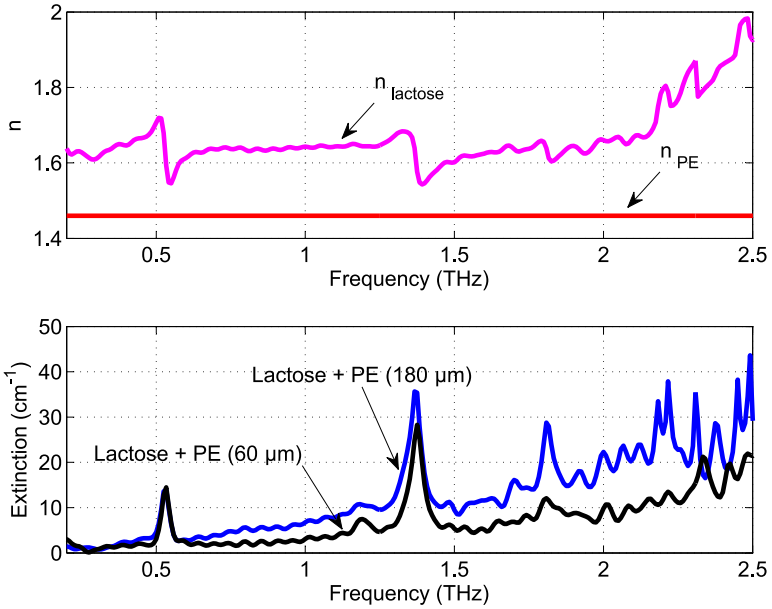


**Figure 4.11. $\alpha$-monohydrate lactose parameter extraction.** Extinction spectrum of the $\alpha$-monohydrate lactose and PE sample (blue), scattering estimate (dotted red), and scattering corrected extinction spectrum (dashed black).

be calculated from the ratio of the mass of PE (in grams) and the density of PE (0.926–0.940 g/cm$^3$ as specified by the supplier—Inducose). Hence, with the knowledge of the measured sample refractive index and the host medium, the unknown refractive index $n_\mathrm{p}$ can be calculated. The extracted parameters for both the samples are plotted in Fig. 4.11. It must be noted that the condition required for the validity of the modified RGD approximation proposed Shimizu (1983) is met, even for the maximum value of $n_\mathrm{p}$ ($\approx 1.7$ at 0.53 THz) as $|n_\mathrm{p}/n_\mathrm{m} - 1| = |1.7/1.46 - 1| = 0.165 \ll 1$.

According to Eq. 4.61, the true absorption spectra of the given samples can be obtained by simple subtracting total scattering attenuation $\alpha$ from the measured extinction $\alpha_\mathrm{s}$. The unknown parameters $S$, $V$, and $d$ are adjusted to best fit (least square) the measurements. The results are plotted in Fig. 4.12.

In conclusion, we present a method to numerically mitigate the scattering contribution in THz-TDS measurements for a two phased composite media. The final expression of the scattering attenuation given by Eq. 4.59, look very similar to the one derived by Franz *et al.* (2008), who argued the applicability of Raman's theoretical model for describing the Christiansen effect (Raman 1949). Similar to the technique proposed by Franz *et al.* (2008), the proposed method not only eliminates the scattering baseline but

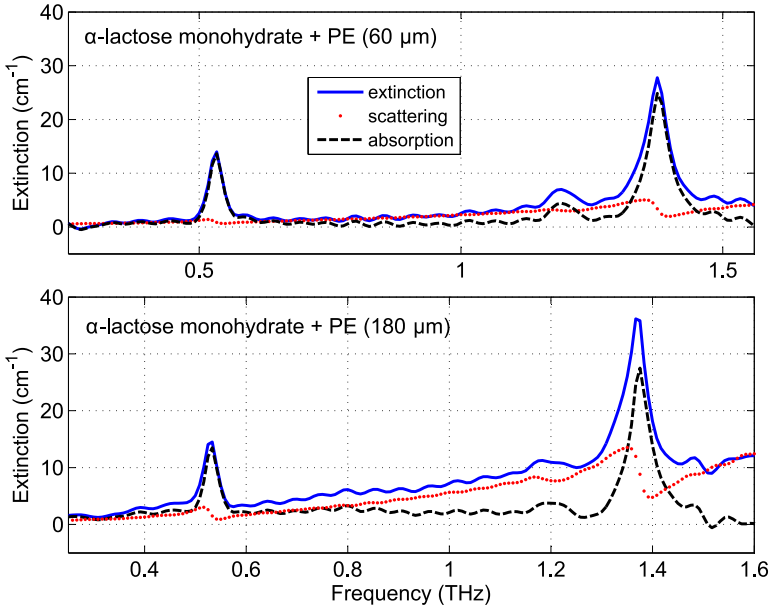


**Figure 4.12. Scattering correction—RGD based method (lactose).** Extinction coefficient and refractive index of the $\alpha$-monohydrate lactose and PE sample.

also corrects for the asymmetrical band distortions by using the knowledge of the refractive index, which is directly measured in THz-TDS. However, it must be noted that unlike the model of Franz *et al.* (2008) the proposed model does not assume a layered structure for modeling an inhomogeneous sample with a random structure, instead it relies on widely accepted RGD approximation of the Mie's theoretical description of single particle scattering (Mie 1908). The technique was tested on two samples of $\alpha$-monohydrate lactose and PE powder (with different granularities). As can be seen in Fig. 4.12, the method reasonably eliminates the scattering contribution for the measured extinction, using the THz-TDS measurements of sample's refractive index, to reveal the scattering mitigated absorption spectra for a given sample.

## 4.6 Chapter summary

In this chapter, we reviewed various theoretical models for estimating and approximating the scattering cross-section for THz transmission through a dielectric medium. We first discussed the case of media with sparse particle distribution where we applied the widely used independent scattering approximation and Foldy's approximation to calculate the scattering cross-section for a sample made of PE particles with a volume concentration of approximately 8%. It was found that the results of independent scattering approximation strongly disagree with the measurements, as it is only valid for

very low concentrations ($<$ 1%). On the other hand, Foldy's approximation which takes into account the first order multiple scattering process, showed a good agreement with the measurements.

Further to this we considered the case of THz transmission through dense media where higher orders of multiple scattering are dominant. We first provide a brief review of the Quasi-Crystalline Approximation (QCA) which accounts for the multiple scattering between densely packed dielectric particles. The QCA solution not only requires knowledge of parameters such as particle size, bulk dielectric constant, and volume fraction of constituents but also relies on assumptions such as a spherical shape for particles, dense packing, and known positions within the sample, more precisely, a probabilistic Percus-Yevick (PY) pair distribution of particle locations. Following this, we applied the effective medium theory proposed by Chýlek and Srivastava (1983) to estimate the frequency dependent scattering loss from three different granularities of polyethylene and air samples and compare the theoretical analysis with the transmission THz-TDS measurements of these samples. The technique was found to reasonably estimate the measurements and unlike the QCA solution, this method does not rely on assumptions regarding position of particles within the sample. Thereafter, we proposed an iterative algorithm based on the effective field approximation proposed by Waterman and Truell (1961) to estimate the frequency dependent scattering loss from the previously described three polyethylene and air samples and compare the theoretical analysis with the transmission THz-TDS measurements of these samples. The results were found to be in very good agreement with the measurements. The proposed technique offers a rather simple and computationally efficient method for estimating the multiple scattering response of a dense medium.

Finally, we conclude this chapter by presenting a numerical approach based on the modified Rayleigh-Gans-Debye approximation to reduce the scattering contribution in transmission mode THz-TDS measurements of two phased media with absorbing constituents. The resulting expression relates the scattering attenuation in terms of the refractive indices of the sample constituents. The proposed technique not only eliminates the increased baseline, but also corrects the extinction spectrum for asymmetrically distorted absorption bands, often observed as consequence of multiple scattering in the sample (Fischer *et al.* 2002, Walther *et al.* 2003, Kaushik *et al.* 2012b). The method was tested on experimentally obtained extinction spectrum of a sample made of $\alpha$-monohydrate lactose and PE powder and was found to reasonably eliminate the

scattering contribution for the measured extinction, using only the THz-TDS measurements of samples refractive index, to reveal the true absorption spectra for a given sample.

Due to the limited dynamic range of the THz measurement device only a few substances were studied in this chapter. However, the collective set of samples used in this chapter was carefully selected for their specific properties. The transparent (no absorption feature in THz range considered) nature of PE made it a suitable candidate for analysing various scattering theories. The sharp absorption features present in $\alpha$-monohydrate lactose made it an ideal candidate for the numerical scattering mitigation method.

# Chapter 5

# Scattering estimation and mitigation—signal processing techniques

IN the previous chapter we reviewed various theoretical models developed for calculating the frequency dependent attenuation due to the scattering of THz radiation by granular sample material and compared them with THz-TDS measurements. For samples exhibiting specific absorption features in the THz spectral range, the theoretical scattering estimate can be used for separating the scattering effects from the absorption spectrum of the sample. However, these theoretical models require precise knowledge of parameters such as particle or inclusion size, volume fraction, bulk refractive index. In real-world applications such levels of *a priori* information of the sample are not always known, limiting the applicability of these models to laboratory testing and analysis.

Here, we present signal processing based approaches for estimating and mitigating scattering effects in THz-TDS measurements for samples that exhibit sharp and sparse absorption features, without requiring *a priori* information of their granularity, refractive index, and density. We selected two materials for this study: $\alpha$-monohydrate lactose and $\alpha$-D-glucose. Both materials are commonly found in many pharmaceutical tablets and food products and show distinctive and sharp absorption features in the THz spectral range, at room temperature, making them suitable for this study.

## 5.1 Introduction

When electromagnetic radiation with frequency  propagates through a material with a complex dielectric constant, it suffers from frequency dependent attenuation mainly due to the absorption and scattering of the signal from the material. Many researchers have modeled scattering as a low order polynomial (generally linear or quadratic, depending on the medium) over the measurement frequency range (Narayana and Ophir 1983, Bao *et al.* 2000, Martens and Stark 1991). On the other hand, absorption loss is a consequence of molecular rotations or vibrations in the media (Gorenflo 2006). For materials that exhibit sharp absorption features, such as -monohydrate lactose, the absorption features are confined to distinct frequency bins specific to the constituents of the media, and are often modeled as higher order polynomials over the frequency range such as Gaussian, Lorentzian (Lorentz 1905), Weisskopf (Van Vleck and Weisskopf 1945), and Gross (Gross 1955) profiles (Withayachumnankul 2009).

In this chapter, we exploit the difference in frequency dependence of scattering and absorption loss, in order to propose several signal processing based techniques for estimating and mitigating or reducing the scattering effects in THz-TDS measurements for samples that exhibit sharp and sparse absorption features. Note that the main idea of the techniques proposed in this chapter is to separate these sharp resonant features from the scattering background to enable direct comparison with spectra of pure samples in a spectral data base for automated recognition. Generally at terahertz frequencies, absorption, phonon modes or collective molecular motion resonances are often present as narrow and sharp features in the measured extinction spectrum allowing the possibility of spectral fingerprint for material identification and classification (Leahy-Hoppa *et al.* 2010, Wheatcroft 2012). If, for a given material, these features are weak and very slowly varying with respect to the incident frequencies, the proposed algorithms will disregard them by treating them as the scattering background. However, it must be noted that such weak features do not form the basis for robust spectral fingerprint and hence are often not useful for material identification and characterisation.

## 5.2 Scattering mitigation using temporal and spectral moments

In the proposed approach, we consider a set of plane waves with angular frequency variable $\omega$ propagating through a sample of material with complex dielectric constant

**Table 5.1. Goodness of fit parameters.** Goodness of fit parameters—Mean Squared Error (MSE) and Correlation Coefficient (CC) for the fit between the measured THz reference spectrum and the Rayleigh distribution probability density function.

| Parameter | Rayleigh distribution |
|---|---|
| MSE | 3% |
| CC | 90% |

$n + ik$, with thickness $d$. The Fourier transform of the transmitted signal is given by:

$$Y(\omega) = X(\omega) \exp\left[in(\omega)\omega\frac{d}{c}\right] \exp\left\{-k(\omega)\frac{d}{c}\right\} \tag{5.1}$$

where $X(\omega)$ is the Fourier transform of the signal before propagating through the sample, $n(\omega)$ represents the frequency dependent refractive index and $k(\omega)$ represents the frequency dependent extinction coefficient of the sample, which contains contributions from both absorption and scattering (Shen *et al.* 2008). The total frequency dependent attenuation $\alpha(\omega)$ suffered by the signal during transmission through the sample is given by:

$$\alpha(\omega) = 2k(\omega)\frac{\omega}{c}. \tag{5.2}$$

As mentioned earlier, $\alpha(\omega)$, the total frequency dependent attenuation can be considered to consist of two contributing terms: the frequency dependent absorption loss $\alpha_a(\omega)$ and the frequency dependent scattering $\alpha_s(\omega)$. This relationship can be expressed as:

$$\alpha(\omega) = \alpha_a(\omega) + \alpha_s(\omega). \tag{5.3}$$

Here, we explore the relation between the change in spectral moments and time domain features of a THz pulse when it passes through a sample material and the frequency dependent scattering $\alpha_s(\omega)$ that occurs as a result of the interaction of the THz radiation with the internal structure of the sample material. In order to do this, we have to assume a standard representation of the measured THz spectrum that has a closed form solution for the calculation of spectral moments. We initially tried fitting various well known distributions to the measured spectrum and found Rayleigh distribution to be a very good match. The result of the fit can be seen in Fig. 5.1, and the goodness of fit parameters—mean square error (MSE) and Correlation Coefficient (CC)—are tabulated in Table 5.1.

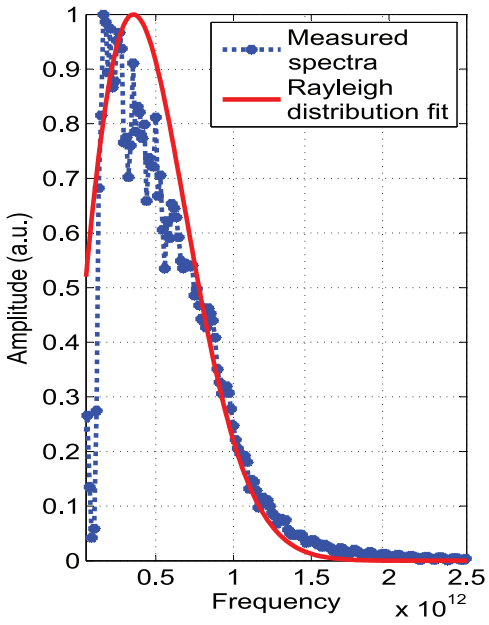


**Figure 5.1. Rayleigh distribution fit.** Various well known distributions were fitted to the measured spectrum and the Rayleigh distribution was found to be a very good match. This figure shows the fitted Rayleigh distribution (red) overlaying the measured THz reference spectrum (blue).

Thus, $|X(\omega)|$, the amplitude spectrum of the reference signal can be modeled as follows:

$$X_{\mathrm{r}}(\omega) = A\frac{\omega}{\sigma_{\mathrm{r}}^2}\exp\left(\frac{\omega^2}{2\sigma_{\mathrm{r}}^2}\right), \tag{5.4}$$

where where, $A$ represents the maximum amplitude of the T-ray field, $\omega$ represents the angular frequency and $\sigma_{\mathrm{r}}$ is the characteristic distribution parameter. Once we have established a standard representation for the measured spectrum, we can calculate the moments using the following general formula:

$$m_{\mathrm{n}} = \frac{\int_0^\infty \omega^n S(\omega)\mathrm{d}\omega}{\int_0^\infty S(\omega)\mathrm{d}\omega}, \tag{5.5}$$

where $n$ is the order of the moment. Therefore, the first order moment for the measured reference spectrum given by Eq. 5.4 is given by:

$$\begin{aligned} \mu_{\mathrm{r}} &= \sigma_{\mathrm{r}}\sqrt{\frac{\pi}{2}}, \\ &= 1.253\sigma_{\mathrm{r}}. \end{aligned} \tag{5.6}$$

When we introduce the sample to this system, the THz signal is attenuated due to the scattering and absorption of the signal by the sample. If the frequency dependent absorption features of the sample are sharp and sparse, they do not greatly influence the center frequency of the sample spectrum and the center frequency mostly depends on the frequency dependent scattering from the sample. Modeling the scattering as a linear function of propagation length $d$ and a quadratic over the given range of angular frequency $\omega$, the expression for the scattering response of the sample, $Y_s(\omega)$, can be expressed as:

$$\begin{aligned} Y_s(\omega) &= A\frac{\omega}{\sigma_r^2}\exp\left(\frac{\omega^2}{2\sigma_r^2}\right)\exp\left(-\alpha_s d\omega^2\right), \\ &= A'\frac{\omega}{\sigma_s^2}\exp\left(\frac{\omega^2}{2\sigma_s^2}\right), \end{aligned} \tag{5.7}$$

where

$$\begin{aligned} A' &= \frac{A}{1+2\alpha_s d\sigma_r^2}, \\ \sigma_s^2 &= \frac{\sigma_r^2}{1+2\alpha_s d\sigma_r^2}. \end{aligned} \tag{5.8}$$

Now, using Eq. 5.5, the first order moment of $Y_s(\omega)$ is given by:

$$\begin{aligned} \mu_s &= \sigma_s\sqrt{\frac{\pi}{2}}, \\ &= 1.253\sigma_s. \end{aligned} \tag{5.9}$$

Thus it can be seen that the spectral shape of the attenuated pulse remains unchanged. However, the attenuation for the sample has changed the mean $\mu_r$ of the reference spectrum to $\mu_s$, for the sample spectrum. Once the mean of the two measured spectra, reference and sample transmitted THz signal, are obtained from the Eq. 5.6 and 5.9, the unknown scattering attenuation coefficient $\alpha_s$ can be calculated by rearranging Eq. 5.8:

$$\alpha_s = \frac{\sigma_r^2 - \sigma_s^2}{2\sigma_r^2\sigma_s^2 d}, \tag{5.10}$$

and the frequency dependent scattering attenuation can be given by $\alpha_s\omega^2$. Similar observations were made by Dines and Kak (1979), where they estimated attenuation of soft biological tissues using ultrasound waves. They treated the attenuation as linearly dependent on the frequency and assumed a Gaussian distribution for modeling the signal spectrum; furthermore they assumed scattering to be minimal in their experiments. Flax *et al.* (1983) used a very similar formulation to Dines and Kak (1979),

but they also considered the power density spectrum to be modulated by white noise and estimated the attenuation constant from the statistics of the transmitted and the detected signal spectrum.

Thus using the first spectral moments of the measured signals, a complete scattering loss profile can be estimated for any given media under this model. Using a standard THz transmission spectroscopy setup, we carry out transmission measurements for two samples comprised of $\alpha$-monohydrate lactose powder and PE powder mixed in a 1:1 ratio and pressed to form a pellet. The PE powder used for each sample had different grain sizes. The first sample is comprised of PE powder with average grain diameter of 60 $\mu$m, while the average grain diameter for the PE powder of the second sample was 360 $\mu$m.

Assuming that the reflections are removed from the sample and reference data, the frequency dependent refractive index $n_s(\omega)$ of the sample and total attenuation $\alpha(\omega)$ is given by:

$$n_s(\omega) = n_0 - \frac{c}{\omega d}\angle H(\omega), \tag{5.11}$$

$$\alpha(\omega) = \frac{2}{d}\left\{\ln\left[\frac{4n_s(\omega)n_0}{(n_s(\omega)+n_0)^2}\right] - \ln|H(\omega)|\right\}, \tag{5.12}$$

where $n_0$ is the refractive index of free air and $H(\omega)$ is the transfer function of the sample, given by:

$$H(\omega) = \frac{E_{\text{sam}}}{E_{\text{ref}}}, \tag{5.13}$$

where $E_{\text{ref}}$ and $E_{\text{sam}}$ are the experimentally measured reference and sample spectrum respectively.

The samples clearly show characteristic absorption features of lactose at 0.53 THz, 1.19 THz and 1.39 THz. It should be noted that along with the distinct absorption features both the samples show a baseline slope owing to scattering due to the granular nature of the samples. As expected, the sample with larger PE particles shows a greater baseline slope as compared to the sample with smaller PE particles. The technique described in here estimates the baseline slope owing to the scattering of the THz signal. Thus for each sample, the reduced scattering extinction spectrum is obtained by subtracting the estimated scattering (Eq. 5.12) from the measured attenuation (Eq. 5.10). The results are shown in Fig. 5.2.

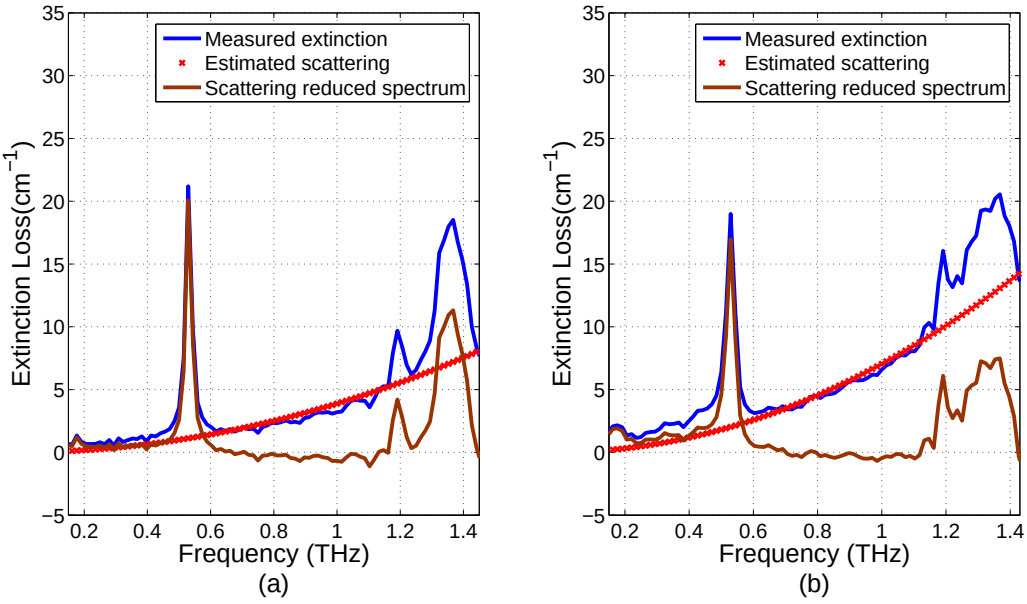


**Figure 5.2. Scattering correction using spectral moments.** Extinction loss spectra of (a) sample pellet made of $\alpha$-monohydrate lactose mixed with PE powder with avg. dia. 60 $\mu$m and (b) sample pellet made of $\alpha$-monohydrate lactose mixed with PE powder with average diameter 360 $\mu$m, with their respective estimated scattering loss profiles and scattering mitigated spectrum.

It is evident from the visual analysis of Fig. 5.2, that, while the estimated scattering captures the overall frequency trend of the extinction spectrum, it overestimates the measurements between 0.7 THz – 1.1 THz. This causes some data points in the scattering reduced spectrum to go negative, which is a physically impossible artifact. To avoid these errors and improve the reliability of the scattering reduced spectrum, instead of fitting probability distribution functions, an alternative technique is to use detailed analytical expressions to describe the THz signals.

The exact temporal waveform of the THz pulse and hence its spectral shape depends mainly on the generation and detection mechanism, which varies from one T-ray spectrometer to another. In our experiments the THz-TDS system uses photoconductive antennas (PCAs) for both the emitter and detector. One popular analytical model for the terahertz signal generated and detected using photoconductive antennas was given by Duvillaret *et al.* (2001). Their expression for the amplitude spectrum of the terahertz signal mostly depends on the carrier lifetime in the antenna's semiconductor material and on the laser pulse duration. They expressed the Fourier transform of the measured

photocurrent ($j_{\mathrm{rec}}$) as:

$$j_{\mathrm{rec}}(f) = \frac{P_{\mathrm{em}} P_{\mathrm{rec}} E_{\mathrm{DC}} \tau_{\mathrm{em}} \tau_{\mathrm{rec}} \tilde{\tau}_{\mathrm{em}} \tilde{\tau}_{\mathrm{rec}} f \exp\left(-2(\pi f \tilde{\tau}_{\mathrm{las}})^2\right)}{m_{\mathrm{em}} m_{\mathrm{rec}} (1 - 2\pi i f \tau_{\mathrm{em}})(1 - 2\pi i f \tau_{\mathrm{rec}})(1 - 2\pi i f \tilde{\tau}_{\mathrm{em}})}, \tag{5.14}$$

where $P_{\mathrm{em}}$ is the average incident laser power, $P_{\mathrm{rec}}$ is the average laser power at the receiver, $E_{\mathrm{DC}}$ is the bias DC field, $\tau_{\mathrm{em}}$ is the free-carrier recombination time in the emitter, $\tau_{\mathrm{em}}$ is the free-carrier recombination time in the detector, $\tau_{\mathrm{las}}$ is the laser pulse duration and is assumed to be same at both emitter and detector, $1/\tilde{\tau}_{\mathrm{em}} = 1/\tau_{\mathrm{em}} + 1/\delta_{\tau_{\mathrm{em}}}$, $\delta_{\tau_{\mathrm{em}}}$ is the carrier collision time in the emitter, $\tilde{\tau}_{\mathrm{las}} = \tau_{\mathrm{las}}/(2\sqrt{\ln 2})$, $f$ represents the frequency, $m_{\mathrm{em}}$ and $m_{\mathrm{rec}}$ are the carrier effective masses in the emitter and the receiver respectively.

However, for the analytical model given by Duvillaret *et al.* (2001), Eq. 5.5 does not have a closed form solution for calculating the spectral moments. Thus, this analytical model cannot be used for our purpose. Another, analytical expression for modeling the THz spectrum was given by Xu *et al.* (2003). This expression is entirely dependent on only one parameter, $\tau_r$, the FWHM (Full Width at Half Maximum) pulse duration of the THz time domain signal, and is given by:

$$X(\omega) = A \frac{\omega \tau_{\mathrm{r}}}{\sqrt{2}} \exp(-\omega^2 \tau_{\mathrm{r}}^2/4), \tag{5.15}$$

where $A$ represents the maximum amplitude of the T-ray field, and $\omega$ represents the angular frequency.

In contrast to the previous model, this analytical expression is much simpler and has a definite solution for the calculation of moments using Eq. 5.5. In order to compare the accuracy of this model with the model proposed by Duvillaret *et al.* (2001), we calculate the center frequency from the first spectral moment of experimentally observed amplitude spectrum of a reference measurement and compare it with the amplitude spectrum obtained from both the analytical expressions, one given by Duvillaret *et al.* (2001) and the other as described by Eq. 5.15. We also compare the Mean Squared Error (MSE) and correlation coefficient (CC) for each analytical model with the measured spectrum. The results are tabulated in Table 5.2 and Table 5.3.

The above results show that both models explain the experimental observations to a similar level of accuracy, with the model given by Duvillaret *et al.* (2001) showing slightly better MSE and CC parameters than the model used by Xu *et al.* (2003). Therefore, we assume the expression given in Eq. 5.15 is a reasonable approximate representation of the reference THz signal (i.e. without sample). Now using Eq. 5.15, the first moment for $X(\omega)$ is given by $\mu_{\mathrm{r}} = \sqrt{\pi}/\tau_{\mathrm{r}}$.

**Table 5.2. Comparison between the two analytical model.** Comparison of center frequency of analytical models and experiment observations.

| Model 1 (Duvillaret *et al.* 2001) | Model 2 (Xu *et al.* 2003) | Experiment |
|---|---|---|
| 0.437 THz | 0.426 THz | 0.431 THz |

**Table 5.3. Goodness of fit parameters.** Mean Squared Error (MSE) and Correlation Coefficient (CC) for fit between the analytical models and the measured THz reference spectrum.

| Parameter | Model 1 (Duvillaret *et al.* 2001) | Model 2 (Xu *et al.* 2003) |
|---|---|---|
| MSE | 0.3% | 0.4% |
| CC | 92.5% | 90.5% |

When we introduce the sample to this system, the THz signal is attenuated due to the scattering and absorption of the signal by the sample. If the frequency dependent absorption features of the sample are sharp and sparse, they do not greatly influence the center frequency of the sample spectrum and the center frequency mostly depends on the frequency dependent scattering from the sample. Modeling the scattering as a linear function of propagation length $d$ and a quadratic over the given range of angular frequency $\omega$, the expression for the scattering response of the sample, $Y_s(\omega)$, can be given by:

$$|Y_s(\omega)| = A\exp(-\alpha_s d\omega^2)\frac{\omega\tau_r}{\sqrt{2}}\exp(-\omega^2\tau_r^2/4). \tag{5.16}$$

This further reduces to

$$|Y_s(\omega)| = A\frac{\omega\tau_r}{\sqrt{2}}\exp(-\omega^2\tau_s^2/4), \tag{5.17}$$

where $\tau_s^2 = \tau_r^2 + 4\alpha_s d$, and the first moment of $Y_s(\omega)$ is given by $\mu_s = \sqrt{\pi}/\tau_s$. Thus it can be seen that the spectral shape of the attenuated pulse remains unchanged. However, the scattering from the sample has changed the distribution characteristic parameter $\tau_r$ to $\tau_s$ or it can be said that the FWHM duration of the time domain pulse has increased from $\tau_r$, for the reference THz signal to $\tau_s$, for the sample THz signal. In terms of the frequency domain, we can say that, the mean (center frequency) of the reference spectrum $\mu_r$ has changed to $\mu_s$ for the sample spectrum. Once the means of the reference signal and the transmitted sample signal are obtained from the above equations, the unknown scattering attenuation profile, $\alpha_s(\omega)$, can be calculated from the first order spectral moments of the measurements:

$$\alpha_s(\omega) = \frac{\pi}{4d}\frac{\mu_s^2 - \mu_r^2}{\mu_r^2\mu_s^2}\omega^2, \tag{5.18}$$

or from the FWHM pulse durations of the measurements:

$$\alpha_s(\omega) = \frac{1}{4d}(\tau_s^2 - \tau_r^2)\omega^2. \tag{5.19}$$

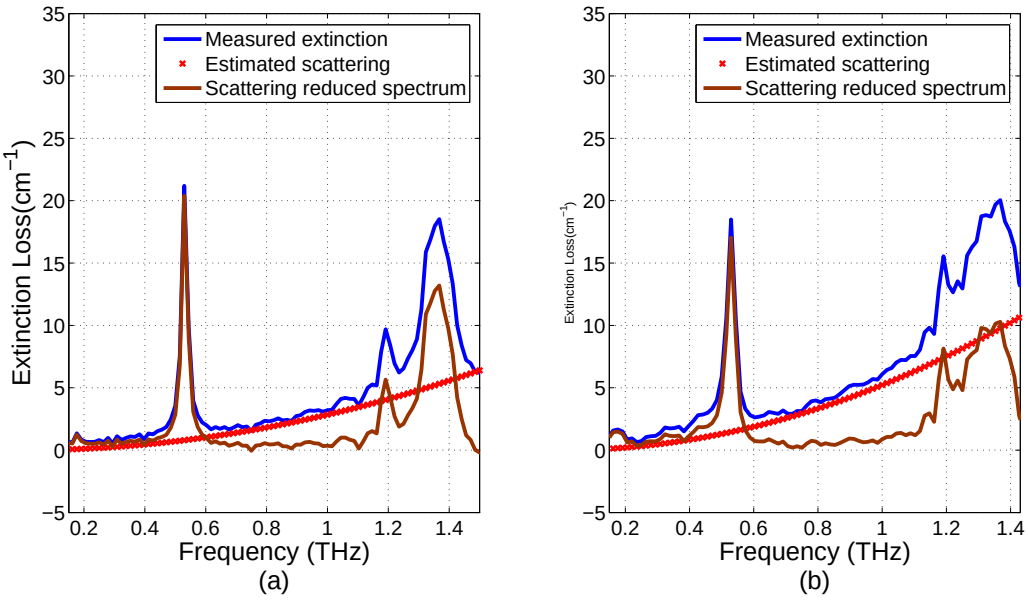


**Figure 5.3. Scattering correction using analytical model of Xu et al. (2003).** Extinction loss spectra of (a) sample pellet made of $\alpha$-monohydrate lactose mixed with PE powder with avg. dia. 60 $\mu$m and (b) sample pellet made of $\alpha$-monohydrate lactose mixed with PE powder with average diameter 360 $\mu$m, with their respective estimated scattering loss profiles and scattering mitigated spectrum.

For each sample, the reduced scattering spectrum is calculated by subtracting the estimated scattering (Eq. 5.18 or 5.19) from the measured extinction spectrum (Eq. 5.12). The results are plotted in Fig. 5.3. It can be clearly seen that the technique reasonably estimates scattering loss profile for both the cases without using *a priori* information of the physical characteristics or the internal structure of the sample or the material, which makes it very useful for mitigating scattering effects in real-world applications such as stand-off measurements. It must be noted that the scattering estimate provided by this technique assumes that the material under study has sharp and sparse absorption features, which is usually the condition required for a THz spectral fingerprint.

In conclusion, we report an extension of the centroid shift technique, initially proposed by Dines and Kak (1979), for estimating the frequency dependent scattering attenuation of THz from samples exhibiting sharp and sparse absorption features and improves on the previous technique by not over-estimating the scattering coefficient.

## 5.3 Robust scattering mitigation

The technique described in Section 5.2, provided reasonable scattering mitigation without using *a priori* information of the physical characteristics or the internal structure of the sample or the material. However, it relies on two major assumptions: (i) a quadratic frequency dependence of the scattering attenuation, and (ii) an analytical expression, valid only for PCA based systems, to represent measured THz spectrum. In this Section, we describe another signal processing technique that does not rely on any such assumptions and produces features that are robust against various scattering conditions, without requiring any *a priori* information of the sample.

We start with the Eq. 5.1 for representing the Fourier transform of the signal transmitted through a sample with complex refractive index $n + ik$. The amplitude spectrum of this signal can be given by:

$$|Y(\omega)| = |X(\omega)| \exp\left\{-\alpha(\omega)\frac{d}{2}\right\}, \tag{5.20}$$

or

$$\log(|Y(\omega)|) = \log(|X(\omega)|) - \alpha(\omega)\frac{d}{2}. \tag{5.21}$$

As mentioned earlier, $\alpha(\omega)$, the total frequency dependent attenuation consists of two contributing terms namely the frequency dependent absorption loss $\alpha_a(\omega)$ and the frequency dependent scattering $\alpha_s(\omega)$. This relationship is given by Eq. 5.3. Note that Eq. 5.21 can now be expressed as:

$$(|Y(\omega)|) = (|X(\omega)|) - \alpha_a(\omega)\frac{d}{2} - \alpha_s(\omega)\frac{d}{2}. \tag{5.22}$$

We model the scattering as a function of the angular frequency $\omega$ as

$$\alpha_s(\omega) = \alpha_0 \left[\frac{\omega}{\omega_0}\right]^A, \tag{5.23}$$

where $\omega_0$ is the angular frequency at which $\alpha_s = \alpha_0$, where $\alpha_0$ and $A$ are unknown parameters that depend on the sample granularity. A similar model was proposed by Shen *et al.* (2008) for modeling the observed extinction spectra obtained from THz-TDS of various samples made of non-absorbing granular PE particles.

Thus the expression for the magnitude response of the sample can now be expressed as:

$$(|Y(\omega)|) = (|X(\omega)|) - \alpha_a(\omega)\frac{d}{2} - \alpha_0 \left[\frac{\omega}{\omega_0}\right]^A \frac{d}{2}, \tag{5.24}$$

or

$$\begin{aligned} Z(\omega) &= \left[\frac{\omega_0}{\omega}\right]^A (|Y(\omega)|) \\ &= \left[\frac{\omega_0}{\omega}\right]^A (|X(\omega)|) - \\ &\quad \left[\frac{\omega_0}{\omega}\right]^A \alpha_a(\omega)\frac{d}{2} - \alpha_0\frac{d}{2}, \end{aligned} \tag{5.25}$$

where Eq. 5.25 shows that the spectral shape of $Z(\omega)$ does not change with the scattering coefficient $\alpha_0$, but is merely shifted in overall level by $\alpha_0\frac{d}{2}$. In order to eliminate this scattering dependent level shift, we initialize the value of A with 0 and increment it in steps of 0.01 (step size chosen arbitrarily, the smaller the step size the better is the estimation accuracy) to iteratively solve the following equation:

$$Z_0(\omega) = Z(\omega) - \overline{Z(\omega)}, \tag{5.26}$$

till, for some defined frequency region $\omega_s$ in which $|Y(\omega)|$ shows no sharp absorption resonances and the attenuation is mainly due to scattering, the value of $Z_0(\omega_s) - (\frac{\omega_0}{\omega})^A(|X(\omega_s)|)$ is minimized, where $\overline{Z(\omega)}$ represents the mean of $Z(\omega)$.

Accordingly, the spectral function $Z_0(\omega)$ does not depend on scattering, and depends only on the reference signal and absorption from the sample. One could obtain spectral features for scattering invariant material classification from $Z_0(\omega)$. Our focus here is on the absorption features, which can be obtained from $Z_0(\omega)$ by:

$$\alpha_a(\omega) = -\frac{2}{d}\frac{(\omega/\omega_0)^A Z_0(\omega)}{(|X(\omega)|)}. \tag{5.27}$$

In the above procedure an important step is to find the frequency region $\omega_s$ in which the measured spectrum shows no sharp resonant absorption features. We know that for materials such as $\alpha$-monohydrate lactose, absorption features are sharp and present in distinct frequency bins. Thus, we used a threshold based peak detection algorithm for identifying the location of the absorption features. Once the location of the absorption features are determined, the region between two consecutive absorption peaks can be identified as $\omega_s$, in which the measured spectrum shows no sharp absorption features and attenuation is mainly due to scattering (other weak background effects due to collective molecular motion such as phonon modes may be present for other materials). In our measurement setup the frequency resolution is approximately 0.1 THz, thus when determining the region $\omega_s$, based on the detected absorption peak location, we exclude the regions in the vicinity of the absorption peaks that falls within the frequency resolution limits. This is shown in Fig. 5.3.

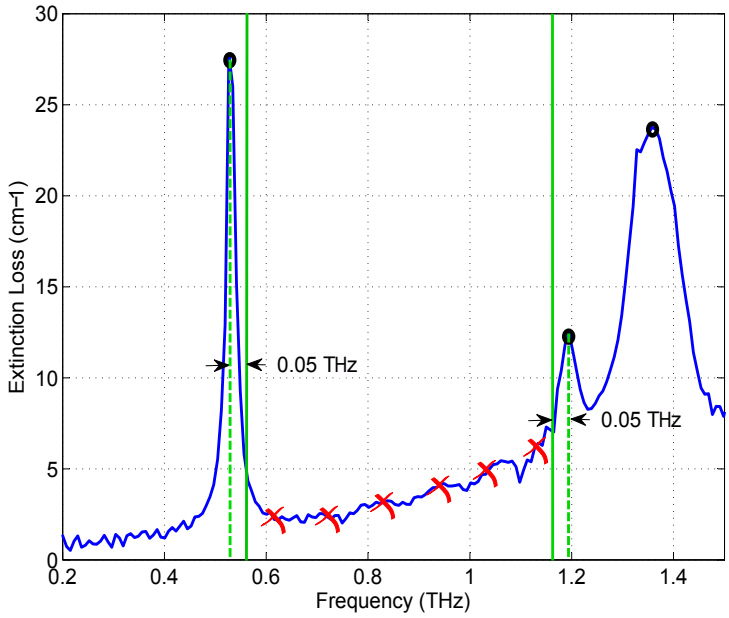


**Figure 5.4. Extracting baseline region.** Application of a peak detection algorithm to the experiment measurements to identify the absorption peak locations (marked as eclipses), the green lines (dotted and solid) represent the measurement setup frequency resolution limits, and the region $\omega_s$, where attenuation is mainly due to scattering(marked with crosses). The unknown parameter $A$ is estimated over the frequency range $\omega_s$.

We apply this techniques to obtain scattering robust/invariant spectrum $\alpha_a(\omega)$, from the THz measurement of the two $\alpha$-monohydrate lactose and PE sample, described in the previous section. Fig. 5.3 shows the comparison of the scattering removed absorption features with the measured extinction spectra. For the visual inspection of Fig. 5.3 (a) and Fig. 5.3 (b), it can be seen that the *generalized scattering mitigation* technique reasonably eliminates the samples scattering contribution from the measured extinction spectrum to reveal true absorption features of the sample, without making any prior assumptions regarding the frequency dependence of the scattering attenuation or requiring any special sample preparation technique, measurement setup and *a priori* information of the samples internal structure or physical characteristics.

## 5.4 Wavelet based scattering estimation and correction

In Section 5.3, we discussed a signal processing approach *generalized scattering mitigation* for mitigating scattering effects in the THz-TDS measurements, which did not require any *a priori* information of the sample material or structure, and the frequency

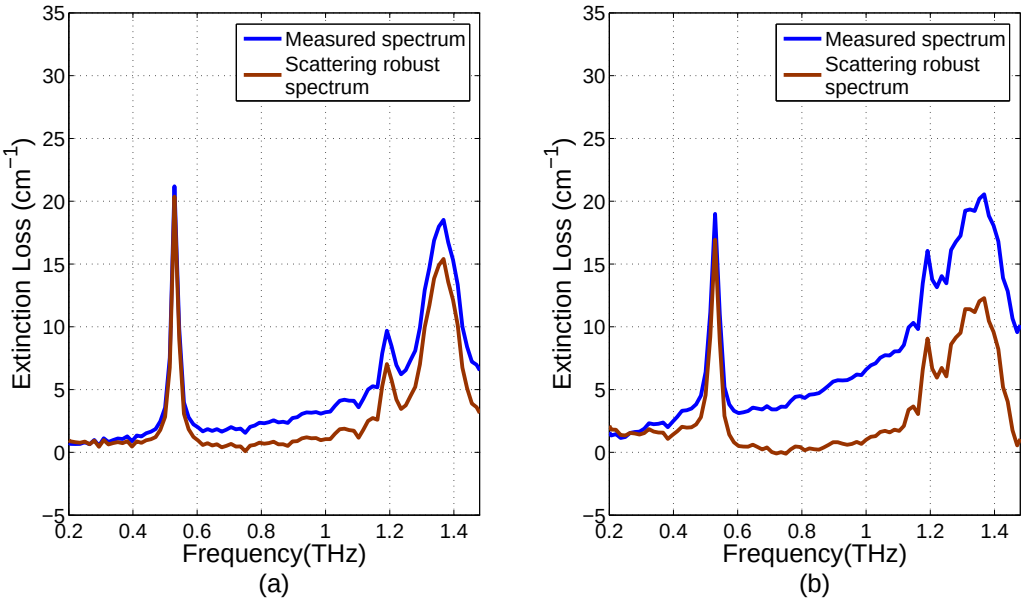


**Figure 5.5. Scattering correction using GSM technique.** (a) Measured extinction loss spectrum of sample pellet made of $\alpha$-monohydrate lactose mixed with PE powder with average diameter 60 $\mu$m vs the scattering removed absorption spectrum obtained using Eq. 5.27, (b) Measured Extinction loss spectrum of sample pellet made of $\alpha$-monohydrate lactose mixed with PE powder with average diameter 360 $\mu$m vs the scattering removed absorption spectrum obtained using Eq. 5.27.

dependence of the scattering attenuation. However, the technique heavily relies on availability of spectral regions were the measured spectrum shows no absorption features and all the attenuation is due to scattering. While many materials show sharp and sparse absorption features in the THz spectral range, some materials (such as $\alpha$-D-glucose) have absorption features quite close to each other. This makes extraction of the such regions, where all the attenuation is due to scattering only, very difficult. In this Section, we describe an iterative wavelet based technique, that does not require the sample spectrum to have sparse absorption features or *a priori* information of the sample's internal structure.

Usually in the case of the solids, the material of interest is quite dense and causes multiple scattering of THz radiation within the sample. The response of a dense medium, as a consequence of multiple scattering, can be classified into three regimes: ballistic, quasi-ballistic, and diffusive transport (Pearce and Mittleman 2002). While the THz

time domain spectroscopy (TDS) technique is sensitive to both quasi-ballistic and diffusive scattering, the criteria to determine which scattering regime is dominant, depends on the scattering ($\lambda_{sc}$) and transport mean free path lengths ($\lambda_{tr}$) in the medium, given by:

$$\lambda_{sc} = c/2n_i\omega,$$
$$\lambda_{tr} = \lambda_{sc}/(1 - \langle\cos(\theta)\rangle, \tag{5.28}$$

where $n_i$ is imaginary part of the complex refractive index of the medium, and $\langle\cos(\theta)\rangle$ is the average of cosine of the scattering angle (Kanno and Hamada 1975, Pearce and Mittleman 2001). The diffusive component is only significant and needs consideration when the medium thickness $l$ is greater than 7 to 10 times the transport mean free path length, $\lambda_{tr}$ (Pearce and Mittleman 2001, Das *et al.* 1997, Yoo and Alfano 1990). Generally in transmission mode measurements, the setup collects signal only in the forward narrow cone. The contribution of the diffusively scattered signal to the measured signal depends on the grain size, concentration, and thickness of the sample (Nam *et al.* 2012) and can be determined using the equation $\rho = \rho_B + (d\Omega/4\pi)p_D$, where $\rho$ represents the total power captured by the detector, $\rho_B$ represents the sum of contributions from the ballistic and the quasi-ballistic transport and $\rho_D$ represents the diffusive component of the transmitted signal. In our measurements, the setup collects signal only in forward narrow cone ($d\Omega \approx 6^\circ$ off the normal axis). For such narrow angles the transport mean free path lengths, given by Eq. 5.28, are several orders of magnitude larger than the scattering mean free path. Under such conditions, given that the medium thickness, $l$ is smaller than 7 to 10 times the transport mean free path length, $\lambda_{tr}$, only the information carrying ballistic and quasiballistic photons are collected by the detector and the diffuse photons that are the source of noise are mostly rejected (Mujumdar *et al.* 2005). It must be noted that, in principle, the sample thickness $l$ can be extended in which the quasi-ballistic light can be measured by reducing the angle $d\Omega$ (Chen *et al.* 2008).

As the detected radiation suffers from both absorption and scattering, it becomes essential to separate scattering from the detected response in order to reveal the true spectral fingerprint of the material under study. Recently, Arbab *et al.* (2010) showed the implementation of a wavelet based technique to retrieve the true THz spectroscopic signature in presence of surface scattering using a reflection mode THz-TDS setup. They carried out a multiresolution analysis using the maximum overlap discrete wavelet transform (MODWT) of the measured extinction spectrum of lactose samples.

Based on visual inspection of the results, they argued that the resonant feature of the lactose sample (at 0.54 THz) can be extracted from the details subband at certain levels of the decomposition. The selection was performed manually by researchers based on a visual rather a physical basis. They did not propose any reconstruction technique following their decomposition, and directly relied on the details subband for the scattering invariant material identification. This makes their technique unsuitable for automated material identification and classification in real-world applications.

We show that a simple reconstruction based only on the details subband can lead to loss or misinterpretation of significant spectral features in the extinction spectrum. Thereafter, we propose an iterative reconstruction technique using only the details subband to estimate the scattering baseline. This can be then subtracted from the original extinction spectrum to obtain a scattering reduced extinction spectrum, and avoid issues involved in the previous approach. The proposed method assists in enabling direct comparison with spectra of pure samples in a spectral database for automated recognition. It must be noted that our proposed technique and the technique proposed by Arbab *et al.* (2010) are only applicable for materials that exhibit sharp and narrow absorption features (such as $\alpha$-monohydrate lactose, $\alpha$-D-glucose, sucrose) and not to those that exhibit slowly varying and very broad absorption features (such as morphine). However, we argue that our proposed technique is useful as there is a broad range of materials that exhibit sharp and narrow absorption features in the THz range.

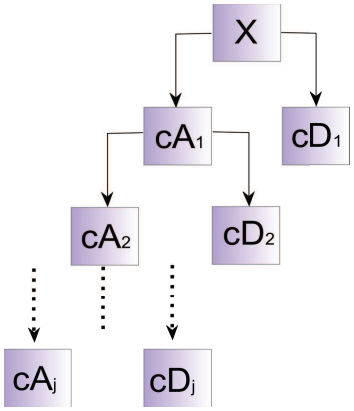


**Figure 5.6. Wavelet decomposition tree.** Signal $X$ is decomposed into several sets of approximate and details coefficients, $cA$ and $cD$ respectively. The process is repeated by decomposing the approximate coefficients $cA$ at each level, up to a desired level $j$. Each arrow feeding to a approximate coefficients $cA$ is a low-pass filter followed by a downsampler and each arrow feed to a details coefficients $cD$ is a high-pass filter followed by a downsampler.

We selected two materials namely, $\alpha$-monohydrate lactose and granular $\alpha$-D-glucose, for this study. Two sample pellets were made by mixing $\alpha$-monohydrate lactose and granular $\alpha$-D-glucose with PE powder in a ratio of 1:1 (material:PE) and pressing them using a hydraulic press at 10 tons/cm$^2$. Note that $\alpha$-monohydrate lactose has characteristic absorption fingerprint frequencies at 0.54, 1.2 and 1.39 THz, while $\alpha$-D-glucose has its characteristic absorption fingerprint frequencies at 1.25, 1.89, 2.39 and 2.57 THz.

The extinction spectra of such materials are always represented as a discrete data series in the Fourier domain. We carry out a multilevel discrete wavelet decomposition (DWT) of this data series (the extinction spectrum) in order to represent it in a set of localized contributions (details and approximations). At each level the contributions are identified by a scale and position parameter and represent the information of the different frequency contents in the original data series. A given spectrum $X(f)$ can be represented by a set of approximation $c_{j,k}$ and details $d_{j,k}$ coefficients, which correspond to a wavelet series expansion of $X(f)$:

$$X(f) = \sum_{j=0}^{J} \sum_{k=0}^{N_j} d_{j,k}\psi_{j,k}(f) + \sum_{k=0}^{N_J} c_{J,k}\phi_{J,k}(f), \tag{5.29}$$

where $\phi(f)$ and $\psi(f)$ are the chosen pair of scaling and wavelet functions, respectively. For discrete cases, the conventional technique it to consider $X(k)$ as the finest level approximation subband and the subsequent decomposition into coarser approximation and detail coefficients is known as the Discrete Wavelet Transform (DWT).

In our implementation, Mallat's multiresolution analysis (Mallat 1988) is used to decompose the discretized measured extinction spectrum $X(k)$ into several sets of approximations and details, $cA$ and $cD$, respectively. This process is depicted in Fig. 5.6. First, the signal is decomposed into $cD_1$ and $cA_1$. The sequence $cD_1$ is associated with the high frequency component of the signal, while, $cA_1$ is associated with the low frequency components. Subsequently, $cA_1$ becomes the input for the next level and the process is repeated until the desired level $j$ is reached. At each level, the signal is down sampled by 2. For materials exhibiting sharp and sparse absorption features, the extinction spectrum consists of a smooth slowly varying part (scattering contribution), some sharp, high order polynomials (absorption peaks) and other background contributions such as systematic errors due to laser drift and other non ideal behaviors.

Generally, scattering attenuation can be expressed as a linear or quadratic function over the given frequency range, depending on the medium of propagation (Narayana

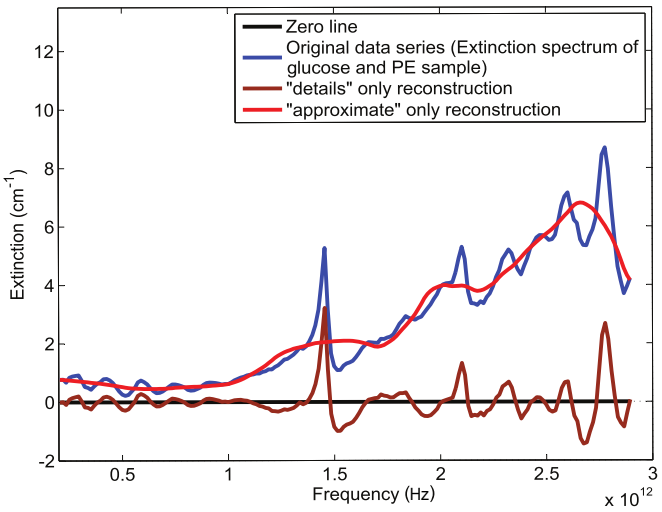


**Figure 5.7. Spectrum reconstruction using approximate and detail vectors.** Extinction spectrum of $\alpha$-D-glucose-PE sample (blue) with reconstructions based on approximation only (red) and details only (brown).

and Ophir 1983, Bao *et al.* 2000, Martens and Stark 1991, Ophir *et al.* 1984). Using the DWT decomposition we want to estimate and thereafter separate the smooth, slowly varying component (scattering contribution) from the original data series (extinction spectrum). To do so, we have selected the 'db4' wavelet of the Daubechies family as the mother wavelet for our decomposition process. Here, 'db4' is an orthogonal wavelet and has 8 taps and 4 vanishing moments, which guarantees removal of most of the scattering contributions, as the scaling functions, or just the approximation coefficients alone, can perfectly represent all polynomials up to order 3.

Fig. 5.7 illustrates a wavelet based decomposition example. Here, we consider the extinction spectrum of a $\alpha$-D-glucose and PE pellet obtained using a standard transmission mode THz-TDS setup. After the multilevel DWT based decomposition, the data series is reconstructed first from the details only and then from approximations only. It can be clearly seen in Fig. 5.7 that the reconstruction carried out from the details subband has negative values at various frequencies, which clearly is a physically impossible artifact and can cause loss or misinterpretation of the data when used for automated classification and identification. The same effect can be seen in the approximations only reconstruction, as it overdetermined the spectrum background at various frequencies, especially around the absorption peaks. In order to eliminate these errors

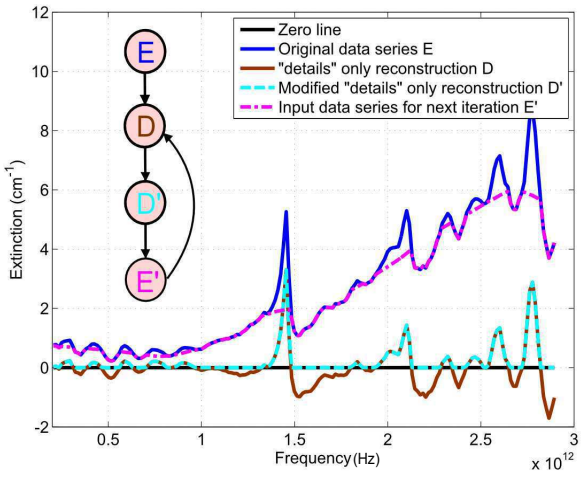


**Figure 5.8. Wavelet based method—iteration Scheme.** Original data series, extinction spectrum, of $\alpha$-D-glucose (blue) with reconstructions based on "details" only D (brown) and modified "details" only (dotted cyan) and input data series for next iteration.

and to obtain the true absorption fingerprints of the material under study, we propose the following iterative reconstruction scheme:

1. **Decompose and selective reconstruction**: Using DWT, first decompose the original data series $E$ (experimentally obtained extinction spectrum) into details and approximations and then reconstruct the data series from details only ($D$).

2. **Modify, subtract and iterate**:

$$\begin{aligned} D_i'(n) &= \max\{D_i(n), 0\} \quad \forall n, \\ E_1'(n) &= E(n) - D_1'(n), \\ E_i'(n) &= E_{i-1}'(n) - D_i'(n) \quad \forall i > 1, \end{aligned} \tag{5.30}$$

where $i$ represents the iteration number. This process is illustrated in Fig. 5.8.

3. **Convergence condition**: As we want to avoid any data in the details only reconstructed data series $D$ from going negative, we propose the following convergence criteria:
Let $N_i(m)$ represent all the negative data values in $D_i(n)$, then

$$V_i = \sum |N_i(m)|^2 \quad \forall m, \tag{5.31}$$

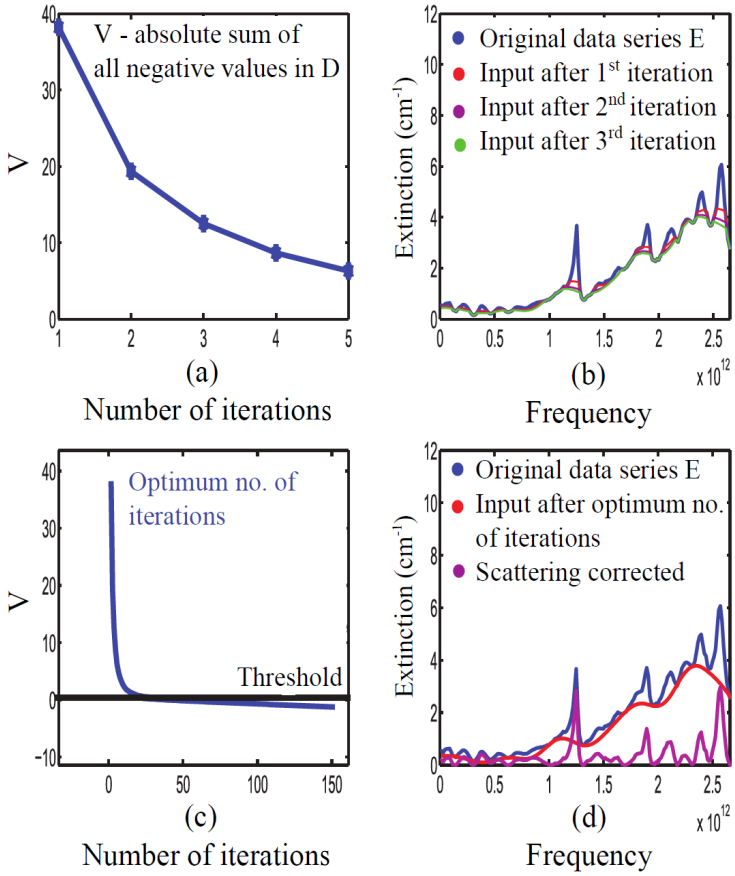


**Figure 5.9. Wavelet based method—algorithm convergence.** (a) Value of $v$ for the first five iterations, (b) Input data series for the first four iterations, (c) Convergence condition and (d) Scattering corrected spectrum after optimum number of iterations.

represents the *error energy* and convergence is met when the *error energy* becomes less than 0.01% (arbitarily chosen, the smaller the better is the accuracy) of the overall extinction spectrum energy. This can be expressed as:

$$V_i < 0.0001 \times \sum |E(n)|^2 \quad \forall n. \tag{5.32}$$

This process is illustrated in Fig. 5.9. It can be seen from the Fig. 5.9(d) that at the optimum number of iterations, the input data series $E'$, obtained by subtracting the $D'$ from $E'$, of the previous iteration, closely matches the slowly varying spectrum background and hence serves as a reasonable estimate of the frequency dependent scattering contribution in the measured spectrum.

In order to test our algorithm, we carry out THz-TDS measurements of four samples: (i) granular $\alpha$-D-glucose + PE pellet (thickness $l$ = 0.18 cm), (ii) coarsely ground $\alpha$-D-glucose + PE pellet (thickness $l$ = 0.12 cm), (iii) $\alpha$-monohydrate lactose + PE (particle

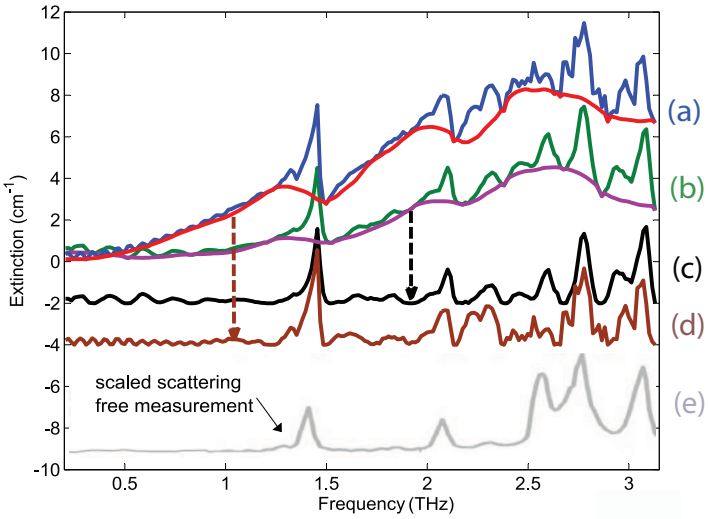


**Figure 5.10. Wavelet based method—scattering correction (glucose sample).** (a) Extinction spectrum of granular $\alpha$-D-glucose and PE sample (blue) with estimated scattering (red), (b) Extinction spectrum of coarsely ground $\alpha$-D-glucose and PE sample (green) with estimated scattering (magenta), (c) scattering corrected spectrum for granular $\alpha$-D-glucose and PE sample (brown), (d) scattering corrected spectrum for coarsely ground $\alpha$-D-glucose and PE sample (black), and (e) a scattering free/limited extinction spectrum of $\alpha$-D-glucose (scaled to 1/45).

diameter 200–400 $\mu$m) pellet (thickness $l$ = 0.45 cm), and (iv) $\alpha$-monohydrate lactose + PE (particle diameter 60-80 $\mu$m) pellet (thickness $l$ = 0.45 cm). Using the measured complex refractive index and assuming a forward narrow cone of 6°, we calculated the transport mean free path lengths for all the four samples according to the Eq. 5.28 and found them to be several orders higher than the sample thickness. Thus confirming that the measurements contain no or negligible amount of contribution from the diffusive scattered radiation. We apply the above described algorithm to the extinction spectra of these four samples to obtain an estimate of frequency dependent scattering baseline for each sample. Thereafter, to reduce the effects of scattering from the measurements, we simply subtract the estimated scattering data series from the measurements. The results are shown in Fig. 5.10 and 5.11. In order to validate our results, we compare the scattering eliminated spectrum with a scattering free/limited measurement for each sample. A completely scattering free extinction can be obtained by THz-TDS of a single crystal of the given material. However, due to the very small size of a crystal, this measurement is not possible for a number of materials. One may

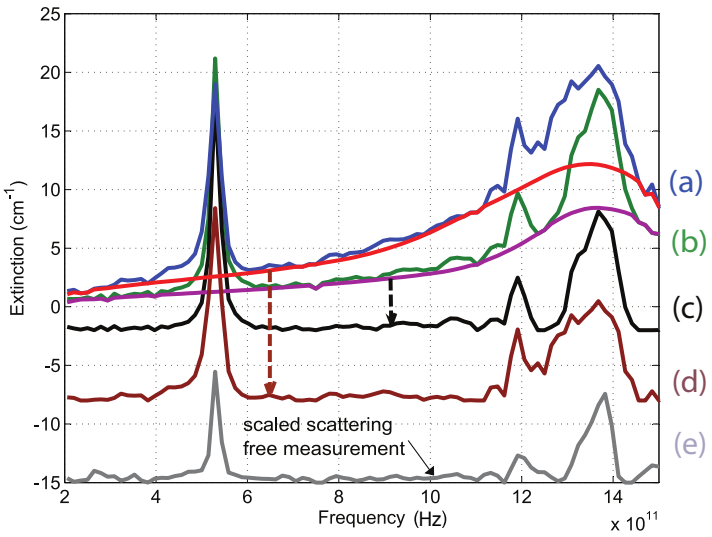


**Figure 5.11. Wavelet based method—scattering correction (lactose sample).** (a) Extinction spectrum of granular $\alpha$-monohydrate lactose and PE (diameter 200-400 $\mu$m) sample (blue) with estimated scattering (red), (b) Extinction spectrum of $\alpha$-monohydrate lactose and PE (diameter 60-80 $\mu$m)(green) with estimated scattering (magenta), (c) scattering corrected spectrum for $\alpha$-monohydrate lactose and PE (diameter 200-400 $\mu$m) sample (brown), (d) scattering corrected spectrum for $\alpha$-monohydrate lactose and PE (diameter 60-80 $\mu$m) (black), and (e) a scattering free/limited extinction spectrum of $\alpha$-D-glucose (scaled to 1/3).

attempt to grow a bigger crystal from many small crystals by dissolving in an appropriate solvent, but this process can take days and still there is a risk of introducing impurities to the crystal. Thus in the absence of a true scattering free measurement, one can resort to a measurement of a sample prepared by milling the material into a very fine powder and then pressing it into a pellet of very high density (volume fraction $\geq$ 90%). This sample preparation technique ensures very small scatterer (generally the air-voids) size and volume fraction, thus limiting the contribution of scattering in the measured extinction spectrum. Walther *et al.* (2003) carried out such a measurement for $\alpha$-D-glucose, and here we have used their measurement as the scattering free/limited reference for comparision with our results. For the scattering free/limted measurement of the lactose sample, we carry out THz-TDS of a sample prepared by pressing (pressure $\approx$ 10 ton/cm$^2$) a mixture (1:1) of very fine $\alpha$-monohydrate lactose (particle size $\approx$ 35 $\mu$m) and very fine PE powder (particle size $\approx$ 30-40 $\mu$m), to form a dense (volume fraction $>$ 90%) pellet. Note that the measurement obtained from such samples is not completely scattering free.

It must be noted that the proposed iterative reconstruction technique provides with separate scattering and absorption spectra for the sample under study as opposed to the method proposed by Arbab *et al.* (2010). For the four samples considered here, convergence was achieved after 12 iterations for the granular $\alpha$-D-glucose-PE sample, 11 iterations for the coarsely ground $\alpha$-D-glucose-PE sample, with 4-level DWT, and 15 iterations for the $\alpha$-monohydrate lactose-PE (diameter 60-80 $\mu$m) sample, and 20 iterations for the $\alpha$-monohydrate lactose-PE (diameter 200-400 $\mu$m) sample with 5-level DWT.

In conclusion, we present an iterative multilevel DWT based technique for estimating frequency dependent scattering baseline for transmission mode THZ-TDS measurements. The method is tested on four sample pellets, two comprising $\alpha$-monohydrate lactose and PE (with different granularity), while the other two comprising $\alpha$-D-glucose (with different granularity) and PE. From the comparison of the scattering corrected spectrum with the scattering free/limited spectrum obtained from well prepared samples, shown in Fig. 5.10 and 5.11, it is clear that the technique reasonably estimates most of the general scattering attenuation profile. The proposed method helps in cleaning the measurements for scattering and other background contributions such as systematic errors due to laser drift to enable direct comparison with spectra of pure samples in a spectral data base for automated recognition. It must be noted that the technique requires the material under study to exhibit sharp absorption features and uses no other *a priori* information of the physical characteristics of the sample or the material, which makes it potentially useful for material analysis in real-world applications such as in stand-off measurements and quality control.

## 5.5 Generalized Hodrick-Prescott filtering with adaptive weights

In the previous Section 5.4, we presented an iterative multilevel DWT technique for estimating frequency dependent scattering loss of terahertz by composite granular materials with absorbing constituents. We tested the algorithm for three sample pellets: $\alpha$-monohydrate lactose-PE and two $\alpha$-D-glucose-PE. The technique reasonable estimated of the overall frequency dependent scattering attenuation along with the enhanced scattering near the dispersion artifacts causing the broadening of the absorption peak. However, the accuracy and success of the technique relies on the relation between the

choice of mother wavelet and the order of the polynomial to be estimated. In this Section, we present a general approach for mitigating scattering in THz-TDS measurements. The algorithm is essentially an iterative implementation of the Hodrick-Prescott filtering technique (Hodrick and Prescott 1997). Before going in the details of the iterative scheme, we present a summary of the Hodrick-Prescott filtering technique.

The Hodrick and Prescott (1997) filter is a popular tool in the field of macroeconomics for decomposition of real business cycles. It enables the separation of the cyclical component of a time series from raw data, by obtaining a smoothed-curve representation of the time series, which is more sensitive to long-term than to short-term fluctuations. The action of Hodrick-Prescott filter can be explained as follows.

Consider a data series $y$ of length $n$, sampled at regular interval. Let $x$, represent another data series that is smooth and follows the long term trends of $y$. These two objectives can be represented by the minimization of the following regularized least squares equation.

$$F = \sum_{i=1}^{n}(y_i - x_i)^2 + \lambda \sum_{t=2}^{n-1}(x_{t-1} - 2x_t + x_{t+1})^2, \tag{5.33}$$

where $\lambda \geq 0$ is the regularization parameter used for controlling the trade-off between smoothness of $x$ and the size of the residuals $y - x$. The first term in Eq. 5.33 measures the size of the residuals, the second term, which is the second order difference of the estimated data series at sample $t$, measures the smoothness of $x$, and $\lambda$ a smoothing parameter that controls the level of smoothness of the estimated data series. As the smoothing factor grows, the Hodrick-Prescott filter converges to a linear time trend. For estimating higher order polynomials, one can vary the smoothness parameter $\lambda$. However, sometimes a data series can have several sharp variations in its long term trend and in order to estimate such trends, a generalization of the Hodrick-Prescott filter, proposed by Araujo *et al.* (2003), can be used. The minimization equation for the generalized Hodrick-Prescott filter can be given by:

$$F = \sum_{i=1}^{n}(y_i - x_i)^{t=2} + \lambda \sum_{\frac{r}{2}+1}^{n-\frac{r}{2}}(\Delta^r x_i)^2, \tag{5.34}$$

where $\Delta^r$ is the $r^{\text{th}}$ order difference matrix. As $\lambda \to \infty$, the resulting output sequence converges to a polynomial of $r-1$ degree. Thus, it can be seen that Hodrick-Prescott

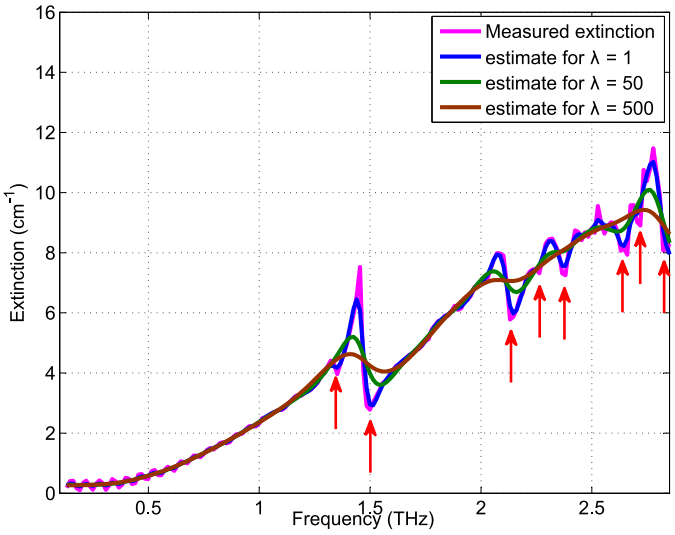


**Figure 5.12. Hodrick-Prescott filter—estimates with varying $\lambda$.** Extinction spectrum of granular $\alpha$-D-glucose-PE sample (magenta) with estimates for different values of $\lambda$. Red arrows indicating sharp features in the given data series. $\lambda$ can be varied in order to estimate sharper features of a data series.

filter given by Eq. 5.33 is a special case of the Eq. 5.34 for $r = 2$. The solution to Eq. 5.34 can be obtained by equating the partial derivative of $F$ to zero ($\delta F/\delta t = 0$). This leads to the following system of equation:

$$x = (I + \lambda D^{r\mathrm{T}} D^r)^{-1} y, \tag{5.35}$$

where, $I$ is an $n \times n$ identity matrix, $T$ is the transpose operator, and $D$ is the second order difference matrix. The solution is generally a large system with $n$ equation, each of length $n$. However, as only the main diagonal and two sub-diagonals above and below it are non-zero, the system is very sparse. While small values of the smoothing parameter $\lambda$ results in relatively light smoothing, which may be usefully for noise removal, large values for $\lambda$ causes stronger smoothing, which gives the slowly varying trend of the signal. Fig. 5.12 shows, for the extinction spectrum of a granular glucose sample, the solution of Eq. 5.35 for different values of $\lambda$. It is clear for the Fig. 5.12 that as the value of lambda increases, the estimated data series $x$, increasing represents the slow varying trend of the measured extinction. The concept here is same as that of the wavelet based technique discussed in the Section 5.4, to estimate scattering by separating the high frequency components of the measurement from the low frequency or slowly varying components. However, it can be seen from the Fig. 5.12, that the estimates overestimate the measurements at several data points (shown with red arrows) and therefore cannot be used an estimate of the scattering contribution in the

measurement. Thus, in order to reliably estimate the scattering contribution, we modify the generalized Hodrick-Prescott filter equation to include a weight vector $w$ when computing the residuals term of Eq. 5.34. The modified generalized Hodrick-Prescott filter can now be expressed as:

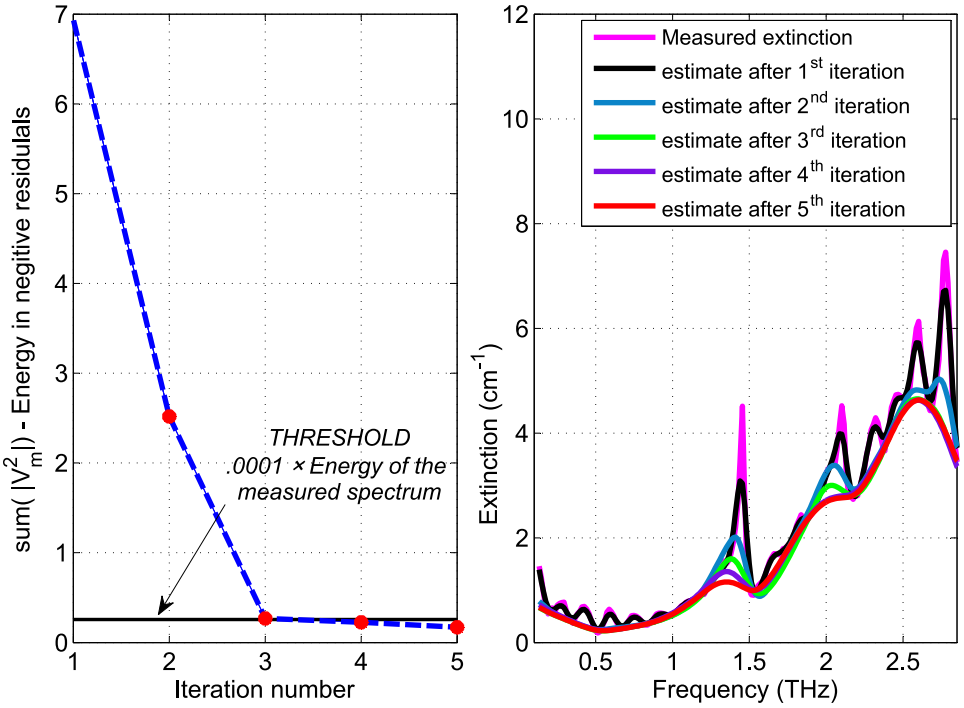


**Figure 5.13. Hodrick-Prescott filter—algorithm convergence.** Extinction spectrum of granular $\alpha$-D-glucose sample (magenta) with estimates after first five iterations.

$$F = \sum_{1}^{n} w_i (y_i - x_i)^2 + \lambda \sum_{\frac{r}{2}+1}^{n-\frac{r}{2}} (\Delta^r x_i)^2, \tag{5.36}$$

and the solution can be given by:

$$x = (W + \lambda D^{r\mathrm{T}} D^r)^{-1} W \cdot y. \tag{5.37}$$

This solution does not over-estimate the measurements at any point. Thus, we must select the weight vector $w$ such that the residuals $y$-$x$ are forced to become positive. This can be done by giving much more weight to the negative residuals as compare to the positive residuals. This can be done using the following iterative algorithm:

1. Initialize $\lambda$ and $w$:

$$\begin{aligned} \lambda &= 10, \\ w_i &= 1 \ \forall i. \end{aligned} \tag{5.38}$$

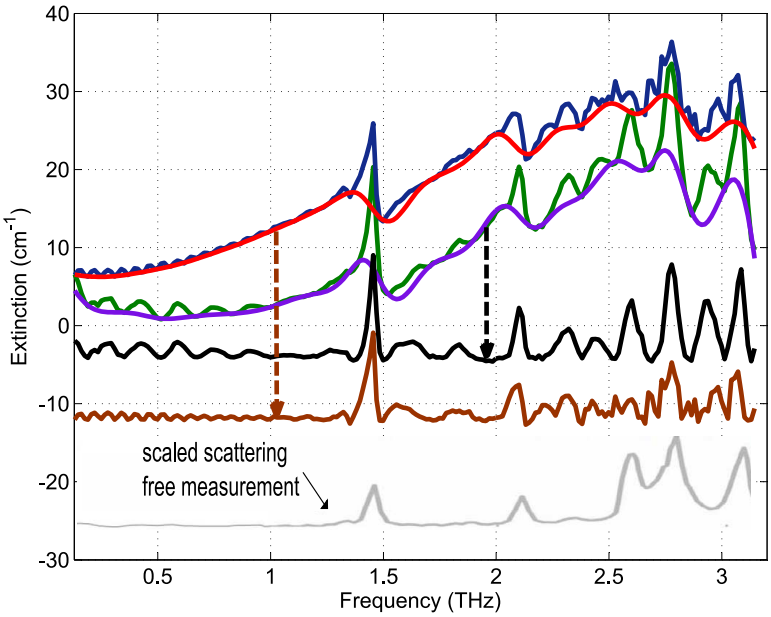


**Figure 5.14. Hodrick Prescott filter—scattering correction (glucose samples).** (a) Extinction spectrum of granular $\alpha$-D-glucose and PE sample (blue) with estimated scattering (red), (b) Extinction spectrum of coarsely ground $\alpha$-D-glucose and PE sample (green) with estimated scattering (magenta), (c) scattering corrected spectrum for granular $\alpha$-D-glucose and PE sample (brown), (d) scattering corrected spectrum for coarsely ground $\alpha$-D-glucose and PE sample (black), and (e) a scattering free/limited extinction spectrum of $\alpha$-D-glucose (grey) (scaled to 1/45).

2. Solve Eq. 5.37 and calculate the residuals vector $r$:

$$\begin{aligned} x &= (W + \lambda D^{r\mathrm{T}} D^r)^{-1} W \cdot y. \\ r_i &= y_i - x_i \ \ \forall i. \end{aligned} \tag{5.39}$$

3. Modify $w$:

$$w_i = \max(x_i - y_i, \delta) \ \ \forall i \tag{5.40}$$

It must be noted that ideally $w_i$ should be set to zero 0 for all positive residuals, but that can make the system unstable, therefore a very small arbitrary value $\delta = 0.001$ is selected.

4. Calculate $N_m$ such that it represents all the negative data values in $r_i$, then:

$$V = \sum |N_m|^2 \quad \forall m. \tag{5.41}$$

5. Repeat step 2 to 4 until:

$$V < 0.0001 \sum |y_i|^2 \quad \forall i. \tag{5.42}$$

In order to test our algorithm, we used the same four samples described in Section. 5.4. The results are shown in Fig. 5.14 and Fig. 5.15.

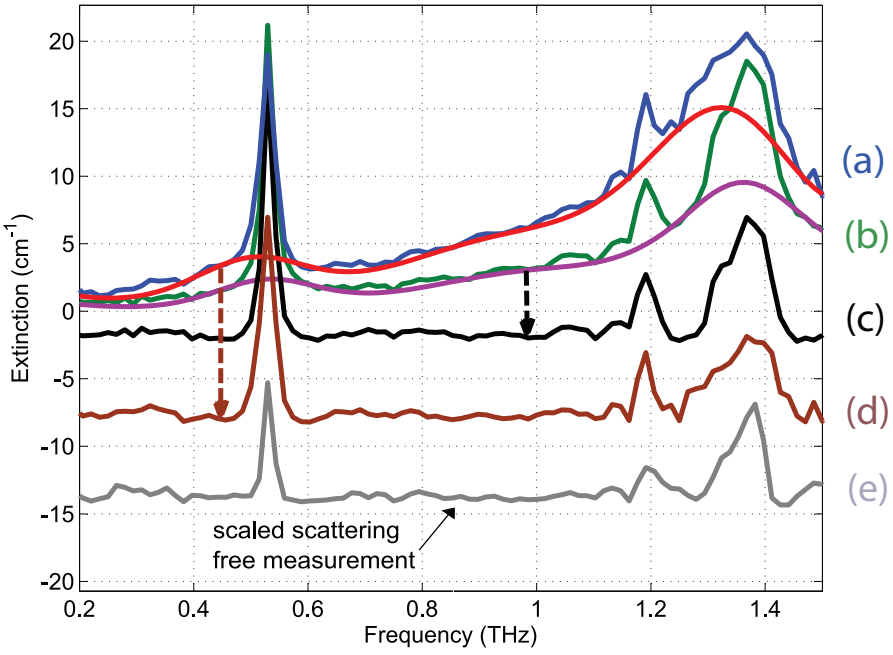


**Figure 5.15. Hodrick Prescott filter—scattering correction (lactose samples).** (a) Extinction spectrum of granular $\alpha$-monohydrate lactose and PE (diameter 200-400 $\mu$m) sample (blue) with estimated scattering (red), (b) Extinction spectrum of $\alpha$-monohydrate lactose and PE (diameter 60–80 $\mu$m)(green) with estimated scattering (magenta), (c) scattering corrected spectrum for $\alpha$-monohydrate lactose and PE (diameter 200–400 $\mu$m) sample (brown), (d) scattering corrected spectrum for $\alpha$-monohydrate lactose and PE (diameter 60-80 $\mu$m) (black), and (e) a scattering free/limited extinction spectrum of $\alpha$-D-glucose (scaled to 1/3).

Note that, we are using the same convergence condition as that of the wavelet based method described in Section 5.4. This enables us to compare the performance of the

two methods. Another suitable convergence condition can be stated as: repeat the step 2 to step 4 of the above algorithm until $V$ is minimized and stops changing value. The algorithm is applied to the measured extinction spectrum of $\alpha$-D-glucose-PE sample. The results of the iteration scheme are shown in Fig. 5.13. It can be seen that, as a result of strong penalization of the negative residuals at each iteration, the estimated data series $x$, obtained after the optimum number of iterations, closely matches the slowly varying spectrum background and hence serves as a reasonable estimate of the frequency dependent scattering contribution in the measured spectrum. It must be noted that the term "optimum number of iterations" is defined as the number of iterations after which the convergence condition given by Eq. 5.42 is met.

For the four samples, considered here, convergence was achieved after 4 iterations for the granular $\alpha$-D-glucose-PE sample, 3 iterations for the coarsely ground $\alpha$-D-glucose-PE sample, with $\lambda = 10$ for a third order ($r = 3$ in Eq. 5.36) Hodrick-Prescott filter, and 3 iterations for the $\alpha$-monohydrate lactose-PE (diameter 60-80 $\mu$m) sample, with $\lambda = 10$ for a second order Hodrick-Prescott filter, and 5 iterations for the $\alpha$-monohydrate lactose-PE (diameter 200-400 $\mu$m) sample with, with $\lambda = 15$ for a second order Hodrick-Prescott filter.

In conclusion, we present an iterative generalized Hodrick-Prescott filtering technique for estimating frequency dependent scattering loss of terahertz by composite granular materials with absorbing constituents. Similar algorithms have been proposed for providing baseline correction to chromatograms and Raman vibrational spectra using the Whittaker (1922) smoother (Zhang *et al.* 2010). However, these algorithms differ from the proposed algorithm as they use, (i) Whittaker smoother which is a first order derivative based smoother, (ii) different adaptive weights with some weights assigned a value of zero (which may cause stability issues), and (iii) a different convergence condition.

The proposed method is tested on four sample pellets, two comprised of $\alpha$-monohydrate lactose and PE (with different granularity), while the other two comprised of $\alpha$-D-glucose (with different granularity) and PE. From the comparison of the scattering corrected spectrum with the scattering free/limited spectrum obtained from well prepared samples, shown in Fig. 5.14 and 5.15, it is clear that the technique not only reasonably estimates general scattering attenuation profile but it also reduces the broadening of the absorption peak caused by the phenomenon of resonance light scattering

(Collings *et al.* 1999). For all the four cases, the algorithm converges much faster in comparison to the wavelet based method discussed in Section 5.4. It must also be noted that for the $\alpha$-monohydrate lactose + PE (diameter 200-400 $\mu$m) sample, this algorithm achieves much better reduction in the broadening of the absorption feature at 1.37 THz in comparison to the wavelet based method discussed in Section 5.4. The technique requires the material under study to exhibit sharp absorption features and uses no other *a priori* information of the physical characteristics of the sample or the material, which makes it potentially useful for material analysis in real-world applications such as in stand-off measurements and quality control.

## 5.6 Chapter summary

In this chapter we present signal processing based approaches for estimating and mitigating scattering effects in THz-TDS measurements for samples that exhibit sharp and sparse absorption features, without requiring any a priori information of its granularity, refractive index, and density. Two materials, $\alpha$-monohydrate lactose and $\alpha$-D-glucose, were considered for this study. Both materials are commonly found in many pharmaceutical tablets and food products and show distinctive and sharp absorption features in the THz spectral range, making them suitable for this study.

The first technique explores the relation between the change in spectral moments and time domain features of a THz pulse when it scatters during transmission through a inhomogeneous dielectric material sample. Using the Rayleigh distribution probability density function to represent the measured THz reference spectrum and modeling the scattering as a quadratic over the measurement frequency range, an expression for the unknown scattering coefficient is derived. The technique was applied to transmission measurements for two samples comprised of $\alpha$-monohydrate lactose powder and PE powder (different granularities for each sample) mixed in a 1:1 ratio and pressed to form a pellet. While the estimated scattering profile captured the overall frequency trend of the extinction spectrum, it overestimated the measurements between 0.7–1.1 THz introducing undesirable artifacts in the scattering reduced spectrum.

In order to avoid these errors and improve the reliability of the scattering reduced spectrum, instead of fitting probability distribution functions, an alternative technique of using detailed analytical expressions to describe the THz signals was used. An analytical model proposed by Xu *et al.* (2003) to represent the THz signal was used for this

study. Following the same procedure as described above the scattering baseline slope was calculated and subtracted for the measured spectrum for the two, $\alpha$-monohydrate lactose and PE, samples. The technique was found to reasonably estimates scattering loss profile for both the cases without using a priori information of the physical characteristics or the internal structure of the sample or the material. Following this, using the relation between the log magnitude spectrum of the reference and the sample measurements and an arbitrary frequency dependence of the scattering attenuation, a system of equations is formed that can be iteratively solved to result in a spectral function that is independent of the scattering attenuation and depends only on the absorption from the sample. This technique eliminates the need of relying on assumptions such as a quadratic frequency dependence of the scattering attenuation and an analytical expression to represent the THz spectrum. The technique was found to reasonably eliminate the samples scattering contribution from the transmission measurements for the $\alpha$-monohydrate lactose and PE samples described earlier.

The *generalized scattering mitigation* technique heavily relied on the availability of spectral regions where the measured spectrum shows no sharp absorption resonances. However, for materials exhibiting sharp resonances close to each other in the THz spectrum, extraction of baseline region can be difficult. In the next Section we present an iterative wavelet based technique, that does not require the sample spectrum to have sparse absorption features. The proposed technique is an iterative reconstruction technique using only the details sub-band to estimate the scattering baseline. The method was tested on four sample pellets, two comprising $\alpha$-monohydrate lactose and PE (with different granularity), while the other two comprising a-D-glucose (with different granularity) and PE. From the comparison of the scattering reduced spectrum with the scattering free/limited spectrum obtained from well prepared samples, it was found that the technique reasonably estimated most of the general scattering attenuation profile.

While the iterative wavelet reconstruction technique was successful in mitigating the scattering and other background effects in the THz measurements of the samples under study, its accuracy and success relies on the relation between the choice of mother wavelet and the order of the polynomial to be estimated. In the next section we presented a general approach using an iterative implementation of the Hodrick-Prescott filtering technique (Hodrick and Prescott 1997). The proposed method is essentially a minimization technique using regularized least square regression. The same samples

and convergence condition, as used in the iterative wavelet reconstruction technique, was used for this technique to enable comparison between the performance and efficiency of the two techniques. The Hodrick-Prescott filtering technique was able to achieve results with similar level of accuracy as that of the iterative wavelet reconstruction technique, however, the Hodrick-Prescott filtering technique was found to converge much faster in comparison to the iterative wavelet reconstruction technique.

In conclusion, in this chapter we have proposed several new signal processing algorithms that can mitigate the scattering contribution in the THz measurement of inhomogeneous dielectric media with absorbing constituents. Each technique has a certain advantage over the other and can be employed as per the needs and requirements of the measurement analysis.

In the next chapter, we review various experimental techniques developed for mitigating or reducing the effects of scattering and present some preliminary work on analysing multiple Fresnel echoes for estimating and mitigating scattering effects in THz-TDS measurements.

# Chapter 6

# Experimental techniques for mitigating scattering effects

IN the previous chapters, we have discussed various theoretical models and signal processing techniques to estimate and mitigate scattering contribution in the THz-TDS measurements. This chapter reviews some common experimental techniques such as milling the material of interest in to fine powder and time domain averaging spatially disjoint or multiple sample measurements, in order to reduce the presence of scattering features and effects in the THz-TDS measurements. Recognizing the invasive access and/or specialized measurement apparatus requirement for these techniques, we present an initial exploration into studying etalon echoes, produced during the transmission of a terahertz pulse through a dielectric sample, for estimating scattering contribution in the THz-TDS measurements of a sample material that exhibits sharp and strong absorption resonances. The analysis shows some interesting results and produces some open questions that are discussed at the end of this chapter.

## 6.1 Milling

The amplitude of scattered light depends on several factors such as angle of observation (the scattering pattern), wavelength of the incident radiation, concentration and particle size of the scatterers, and also on the ratio of the refractive indices of the scatterer to the medium in which it is embedded. Symbolically this can be represented as:

$$I_{sc} = I_{in}(\theta, \lambda, d, m), \tag{6.1}$$

where $I_{sc}$ represents the scattered intensity, $I_{in}$ is the incident intensity, $\theta$ represents the angle of observation, $\lambda$ is wavelength of the incident radiation, $d$ is the particle/scatterer diameter, and $m$ is the ratio of refractive index of the scatterer and the surrounding medium.

In 1906, Mie (1908) developed a complete mathematical-physical theory of the scattering of electromagnetic radiation by an isotropic spherical particles . The Mie theory predicts scattering intensity as a function of the angle at which light is scattered by a spherical object. Mie theory can be sub-divided into several approximations by placing constraints over the ratio of wavelength $\lambda$ to object size $d$ (defined by a parameter $x$ such that $x = 2\pi n_m/\lambda$, where $n_m$ represents the refractive index of the medium) and index of refraction of sphere to that of the medium $m$:

(i) Rayleigh scattering ($x \ll 1$ and $x|m-1| \ll 1$) : Scattering cross-section directly proportional to sixth power of the object's radius and inversely proportional to fourth power of wavelength.
(ii) Rayleigh-Gans-Debye approximation ($|m-1| \ll 1$ and $x|m-1| \ll 1$) : Defined for "optically soft" scatterers. Because the scatterer is "soft" ($|m-1| \ll 1$) there is very little reflection of the incident field. Also since ($x|m-1|$) $\ll 1$ there is very little phase shift inside the object. As a result of these two constraints, the internal field is approximately the same as the incident field in the absence of the object. Scattering cross-section is directly proportional to the sixth power of object's radius and inversely proportional to wavelength.
(iii) Anomalous Diffraction ($x \gg 1$ and $x|m-1| \ll 1$) : At very low refractive index, the particle transmits light almost without deflection, which then interferes with the diffracted light, producing anomalous diffraction. Scattering cross-section is directly proportional to the fourth power of object's radius and inversely proportional to wavelength (power between 1 to 2).
(iv) Fraunhofer diffraction ($x \gg 1$ and $|m-1| \gg 1$) : This well-known approximation

is valid for large obstacles and unpolarized light and scattering close to the forward direction. Scattering cross-section is directly proportional to the fourth power of object's radius and inversely proportional to the square of the wavelength.
(v) Geometrical optics ($x \gg 1$ and $x|m-1| \gg 1$) : Usually treated as a combination of Fraunhofer diffraction in the forward direction with reflection and refraction at larger angles.

This is also illustrated in Fig. 6.1. Thus, it can be seen that, for all Mie theory subdivisions, the value of the scattering cross-section and therefore the amplitude reduction in the intensity of the transmitted light is directly proportional to the diameter of the scattering particle. As described in the Section 4.2, for sparse (low concentration) media the total scattering cross-section can be obtained by scaling the scattering cross-section of a single particle by the total number of scatterers in the media. For dense media, multiple scattering effects becomes significant and inter-particle correlation must be considered. Many authors have addressed the problem of accounting for the inter-particle interferences by appending an additional structure factor ($S$) to the expression of the total scattering cross-section of a sparse medium (Holoubek 1999, Belanger *et al.* 1990, Hayter and Penfold 1981, Dunlap and Howe 1991)As the structure factor is a function of volume fraction, scatterer shape, and size distribution, its inclusion may effect the proportionality relation between the total scattering cross-section and the individual scatterer diameter. There is no simple relationship between the scattering cross-section of a dense multiply scattering medium and the physical size of the individual particles. However, many researchers have reported observations which show a reduction in the total scattering cross-section for a dense medium as a result of reduction in the individual scatterer size (Shen *et al.* 2008, Fischer 2005, Franz *et al.* 2008).

In this section, we demonstrate the results of a commonly used laboratory practice of milling granular material into fine powder to mitigate or reduce the effects of scattering. We test this technique for following samples:

(1) D-$\alpha$-Glucose + PE samples: Two different granularities of D-$\alpha$-Glucose are considered.
(2) $\alpha$-monohydrate lactose and PE samples: Two different granularities for PE considered (as the lactose powder was already very fine).
(3) D-tartaric acid + PE samples: Two different granularities of D-tartaric acid considered.

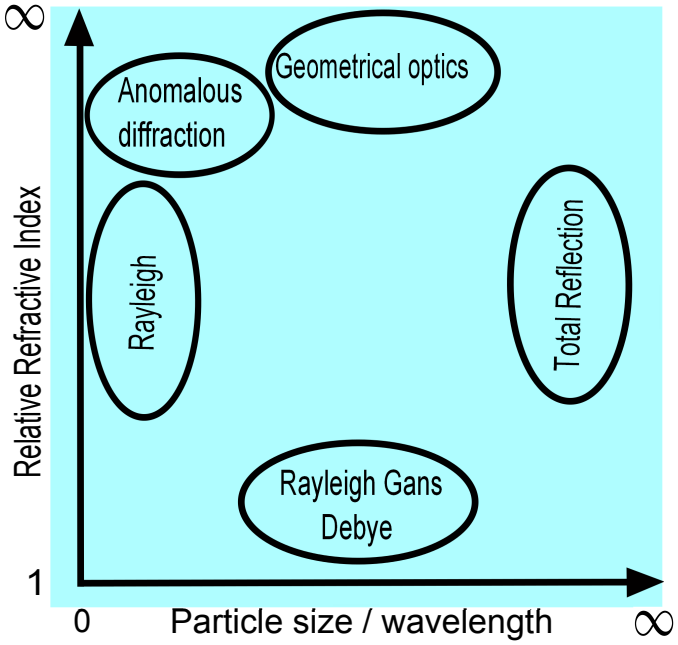


**Figure 6.1. The Mie theory sub-divisions.** Constrained subdivisions of Mie theory for which simplified mathematical expressions were derived by various researchers.

### 6.1.1 Sample preparation

The following describes the sample preparation methods:

(1) D-$\alpha$-Glucose + PE samples: Granular polycrystalline glucose was purchased from Sigma-Aldrich. One of the samples was directly mixed with fine polyethylene powder and pressed to a coplanar pellet, while for the other sample, the granular glucose was grounded into a fine powder and then mixed with fine polyethylene powder.
(2) $\alpha$-monohydrate lactose and PE samples: Granular PE powder was purchased from Inducos. One of the samples was formed by directly mixing the PE powder with fine $\alpha$-monohydrate lactose powder and pressed to a coplanar pellet, while for the other sample, the granular PE powder was milled into fine powder, then mixed with fine $\alpha$-monohydrate lactose powder and pressed to form a pellet.
(3) D-tartaric acid + PE samples: Granular D-tartaric acid was purchased from Sigma-Aldrich. One of the samples was directly mixed with fine polyethylene powder and pressed to a coplanar pellet, while for the other sample, the granular D-tartaric acid powder was grounded into a fine powder and then mixed with fine polyethylene powder.

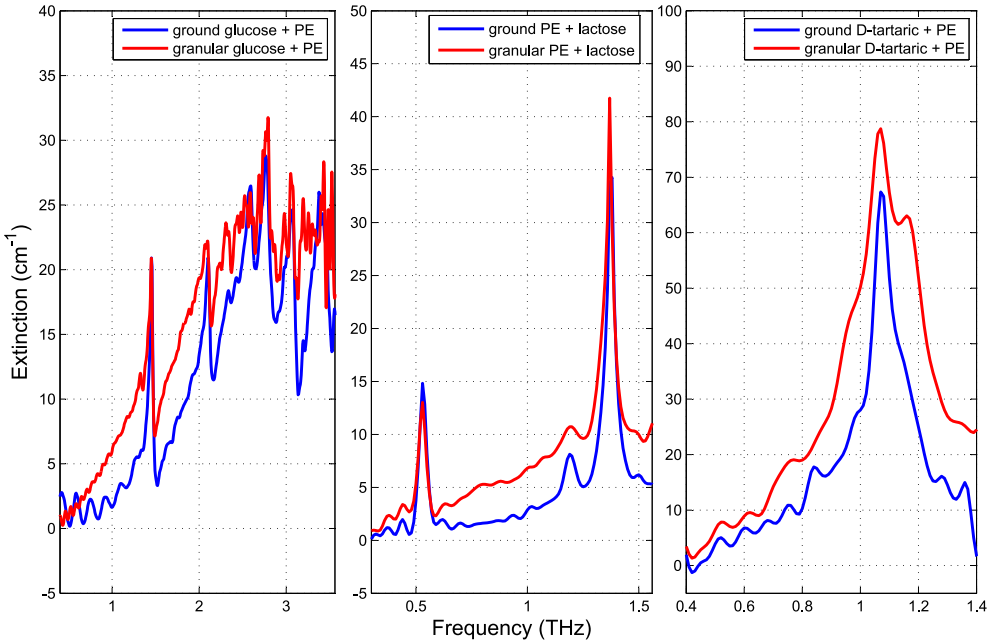


**Figure 6.2. Scattering reduction using the technique of milling.** (a) Extinction spectrum for ground and granular D-$\alpha$-glucose and PE sample, (b) Extinction spectrum for ground and granular PE and $\alpha$-monohydrate lactose sample, (c) Extinction spectrum for ground and granular D-tartaric acid and PE sample.

The mixing ratio (mass of material:mass of PE) was kept the same for each pair of fine powdered sample and granular sample.

Using the apparatus described in Fig. 2.6, we carried out transmission mode THz time domain spectroscopy of the, above mentioned, six samples. Using the procedure described in Section 2.3.3, the extinction coefficient was obtained for each samples. The results are plotted in Fig. 6.2.

It is clear from Fig. 6.2 that, for the D-$\alpha$-Glucose samples, the granular sample exhibits an increased baseline and significant broadening of the absorption peaks in the low frequency range. Milling the glucose into a finer powder not only reduces the baseline slope but also reduces the broadening of the absorption bands. Similar results can be seen for the D-tartaric and PE samples. For the $\alpha$-monohydrate lactose samples, while

the absorption band shapes were not significantly altered in presence of granular PE, a significant rise in the baseline slope can be observed. Again, for the milled PE sample, the baseline slope owing to the scattering has significantly reduced. In conclusion, it is confirmed that milling or grinding the materials significantly reduces the effects of scattering in the extinction spectrum.

One drawback of this approach is that it requires invasive access to the material. Unfortunately, in real-world applications like stand-off measurements it is often not possible to access the material, let alone the possibility of milling or grinding it.

## 6.2 Time domain averaging

### 6.2.1 Spatially disjoint measurements

One basic approach to reduce spectral artifact in the THz-TDS measurement, caused as a consequence of multiple scattering within the sample, was proposed by Shen *et al.* (2008). They used raw granulated sucrose with the coarse grain size up to 800 $\mu$m. As the average particle size for the sample is greater than the incident wavelength and the inter-particle distances, multiple scattering is dominant within the sample. In order to reduce spectral artifacts due to noise and scattering, they averaged multiple measurements taken over a large sample area at different disjoint locations instead of carrying out a single point measurement. For this they used a TPI imaga 1000 (Teraview, Ltd, UK), to map the sample over an area of $10\times10$ mm$^2$. They argued that by averaging over a large area, reliable terahertz spectrum can be obtained as the averaging process cancels out the contribution of random scattering events that are not in phase and vary across sample positions, while the sample contribution will be enhanced by the averaging process. As can be seen in Fig. 6.3, their results clearly showed improvement in noise and spectral artifact due to scattering for the parameters extracted from the time domain averaging of disjoint measurements over a larger area.

### 6.2.2 Multiple sample measurements

Motivated by the work of Shen *et al.* (2008), we have implemented the concept of time domain averaging for reducing the noise and spectral artifacts in THz-TDS measurements carried out using the setup illustrated by Fig. 2.6. However, instead of making

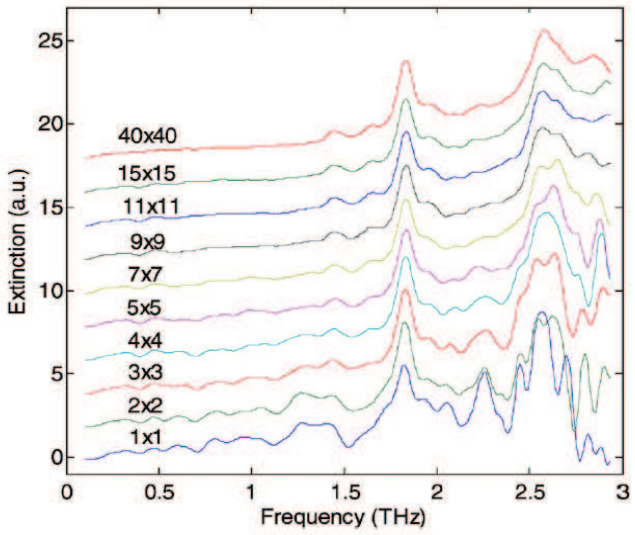


**Figure 6.3. Spatially disjoint measurements.** Extinction spectrum of THz-TDS measurements of raw sucrose powder carried out by Shen *et al.* (2008). The spectra are vertically offset for clarity. The number above each curve represents the number of pixels used for averaging. It is evident that with large number of measurements in the averaging process, better noise and spectral artifact removal is obtained. After Shen *et al.* (2008).

a big sample so that multiple spatially disjoint measurements can be carried out (THz beam-width (focused) in our setup is approximately 1 cm), we averaged the measurements taken from multiple samples (powdered form in a sample cell of diameter $\approx$ 12 mm) created from the same substance (or mixture of substances) using identical preparation procedure. As in each sample, the location (position) distribution, and orientation of the scattering centers will be random and different the contribution of the scattering events from each sample will also be random and out of phase. Thus, time domain averaging for measurements taken from multiple samples should also reduce or diminish the spectral artifacts arising due to THz scattering and noise.

In order to test this technique, we prepared 7 samples of thickness 5.3 mm from a mixture of $\alpha$-monohydrate lactose and PE powder (mixed in a ratio of 1:1) and carried out THz-TDS using the setup described by Fig. 2.6. Using the parameter extraction technique described in Section 2.3.4, the absorption coefficients obtained for the three samples and the time domain averaged signal is shown in Fig. 6.4. It can be seen that, while the time domain averaging has certainly reduced spurious spectral artifacts and the shape of the absorption feature at 0.53 THz, it does not have any effect on the scattering baseline slope.

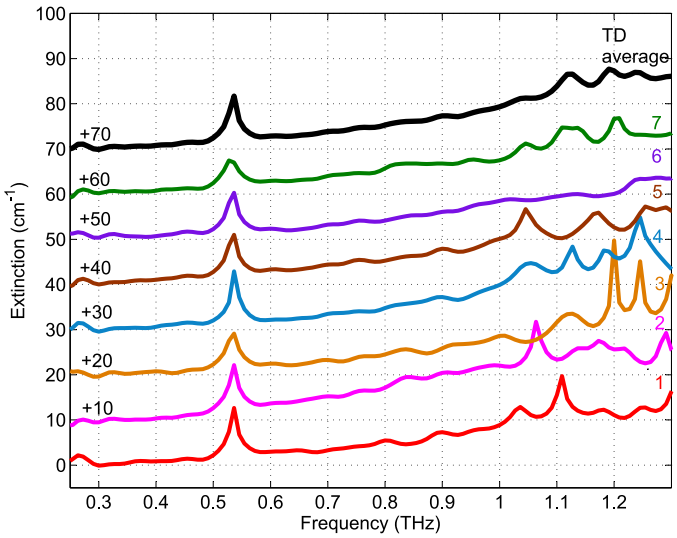


**Figure 6.4. Time domain averaging.** Extinction spectrum of 7 samples of $\alpha$-monohydrate lactose and PE powder made from the same mixture (colored plots) and the extinction spectrum obtained from the time domain averaged signal (black). The plots are vertically offset as given by the number on extreme left. The number on the extreme right denote the sample number. NOTE: Due to the dynamic range limitations of the measurement apparatus, measurements are valid only up to approximately 1 THz.

## 6.3 Harvesting Fresnel echoes for estimating and mitigating scattering

Here, we present THz time domain transmission measurements of $\alpha$-monohydrate lactose mixed with granular PE to study the etalon echoes produced at the sample interfaces for estimating and separating the scattering contribution from the sharp and strong absorption features in the samples extinction spectrum.

### 6.3.1 Background

As described in Section 3.2, when a plane wave of frequency $\omega$ propagating across the interface of a medium a into medium b with different refractive indices. A fraction of the wave energy is refracted into the second medium while some of it is reflected back in the first medium. If the second medium is a slab, the traversing refractive wave will encounter the other interface where again reflection and refraction will take place. This causes generation of Fresnel echoes and this process is known as the Fabry-Pérot effect. Fabry-Pérot effect effect can be represented mathematically as (Withayachumnankul

2009):

$$\begin{aligned} \mathrm{FP}(\omega) &= 1+\rho^2\exp\left[-j\hat{n}_\mathrm{b}(\omega)\right. \\ &\quad \left.\frac{\omega 2d}{c}\right]+\rho^4\exp\left[-j\hat{n}_\mathrm{b}(\omega)\frac{\omega 4d}{c}\right]+.... \end{aligned} \tag{6.3}$$

For thick samples the temporal curves of the detected electric field exhibit well separated echoes (see Fig. 3.4). As a result of this temporal windowing, it becomes possible to separate the directly transmitted pulse and the Fresnel echoes (Duvillaret *et al.* 1996). The basic idea of this analysis is to study the spectral properties of the Fresnel echoes in order to explore the possibility of estimating and subsequently mitigating the effects of scattering form the THz-TDS spectra of material exhibiting strong and sharp absorption features.

### Experiment Details

Using a standard setup, we carry out the transmission mode THz-TDS of samples made of a mixture of $\alpha$-monohydrate lactose and spectrometric grade granular PE powder, mixed in a ratio of 1:1 by weight, for our experiments. The powdered mixture was pressed at ($\approx$10 tons/cm$^2$) to form a pellet of thickness 4.5 mm, using a hydraulic press. The pellet was then sandwiched between two very thin intrinsic FZ silicon wafers (thickness $\approx$ 50 $\mu$m) to form a sample cell structure. For reference measurements, an identical empty sample cell structure was used. This can be seen in Fig. 2.9 as described in Section 2.3.4.

### Method

The basic idea of the method consists of time windowing at least two echoes of the terahertz pulse that are caused by multiple reflections in the sample and to carry out the extraction process for each of these echoes. However, materials with low refractive index such as polyethylene (PE), $\alpha$-monohydrate lactose, do not generate strong reflections at the sample boundaries. Thus, very feeble echoes are generated in the spectroscopy process. In order to generate strong echoes we modified our setup to include a sample holder made up of very thin (thickness $\approx$ 50 $\mu$m) Float Zone (FZ) silicon

wafers. Note that FZ silicon wafers have a much higher refractive index, and therefore produce stronger echoes that can be easily observed and extracted. At the same time these wafers have much low absorption and therefore do not contribute to the absorption characteristics of the sample. Fig. 2.9 illustrates the propagation of T-rays through the silicon sample cell during the measurements of the sample and reference data.

By analyzing the propagation geometry, the transfer function for this system can be expressed as (Withayachumnankul *et al.* 2006):

$$\begin{aligned} H(\omega) &= E_{\text{sam}}(\omega)/E_{\text{ref}}(\omega) \\ &= \frac{\tau_{\text{ws}}\tau_{\text{sw}}\text{FP}^2_{\text{aws}}(\omega)\text{FP}_{\text{wsw}}(\omega)}{\tau_{\text{wa}}\tau_{\text{aw}}\text{FP}^2_{\text{awa}}(\omega)\text{FP}_{\text{waw}}(\omega)} \exp\left[-j(\hat{n}_{\text{s}}-n_0)\frac{\omega d_{\text{s}}}{c}\right], \end{aligned} \tag{6.4}$$

where the subscripts a, s and w are for air, sample, and window, respectively, and $d_{\text{s}}$ is the thickness of the sample. Here, $\hat{n}_{\text{s}}$ is the complex refractive index of the sample and $n_0$ is the refractive index of free air. Here, $\text{FP}_{\text{aws}}$ is the Fabry-Pérot term for the reflections in the window, with air on one side and sample on the other side. Similarly, $\text{FP}_{\text{awa}}$ is the Fabry-Pérot term for the reflections in the window, with air on both the sides, while $\text{FP}_{\text{wsw}}$ and $\text{FP}_{\text{waw}}$ represents the Fabry-Pérot term for reflections in sample and air, with window on both sides, respectively.

As the sample in our experiments has a low refractive index, the values of the Fresnel reflection coefficients $\rho_{\text{ws}}$ and $\rho_{\text{wa}}$ are very similar and therefore, the terms $\text{FP}^2_{\text{aws}}/\text{FP}^2_{\text{awa}}$, in Eq. 6.4, can be approximated to 1. This can be seen in Fig. 6.5. Thus the transfer function of the sample simplifies to:

$$\begin{aligned} H(\omega) &= E_{\text{sam}}(\omega)/E_{\text{ref}}(\omega) \\ &= \frac{\tau_{\text{ws}}\tau_{\text{sw}}\text{FP}_{\text{wsw}}(\omega)}{\tau_{\text{wa}}\tau_{\text{aw}}\text{FP}_{\text{waw}}(\omega)} \exp\left[-j(\hat{n}_{\text{s}}-n_0)\frac{\omega d_{\text{s}}}{c}\right]. \end{aligned} \tag{6.5}$$

Typically, only the terahertz pulse transmitted directly through the sample is taken into account when determining the complex refractive index. However, any of the other transmitted terahertz pulses that have been subject to multiple reflections in the sample can be taken instead (Duvillaret *et al.* 1999). Using Equation 6.5, let us consider the extraction of the complex refractive index and hence the attenuation coefficient using the directly transmitted pulse (all reflections removed), the first transmitted echo (all other reflections and directly transmitted pulse removed), and the second transmitted echo (all other reflections and directly transmitted pulse removed). The procedure is tabulated in Table II.

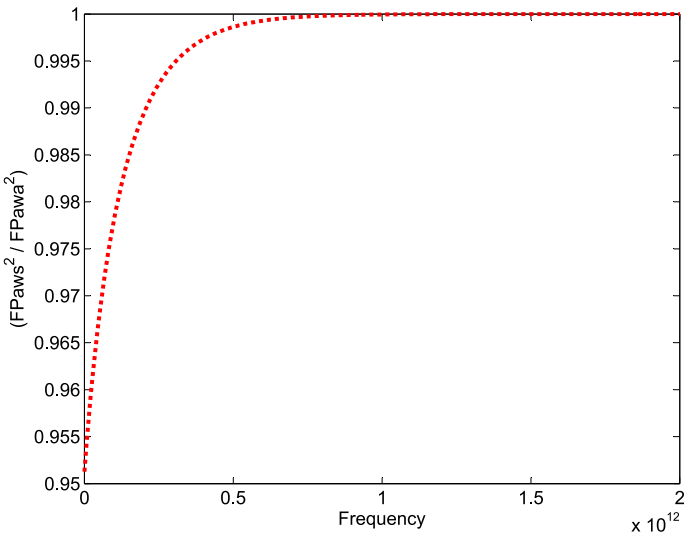


**Figure 6.5. Approximating the term $FP^2_{aws}/FP^2_{awa}$.** Frequency dependent value of the term $FP^2_{aws}/FP^2_{awa}$ for a sample pellet made of PE and $\alpha$-monohydrate lactose in the Float-Zone (FZ) silicon sample holder. The values for $FP_{aws}$ and $FP_{awa}$ were calculated using the measured refractive index of the lactose powder and assuming a refractive index of 3.15 for the FZ silicon wafer (from the datasheet).

As described earlier, the measured total attenuation suffered by the signal while propagating through the medium is the sum of absorption and scattering contributions from the sample (Shen *et al.* 2008). For resonant materials like $\alpha$-monohydrate lactose, absorption features are present as sharp spikes at distinct frequency bins specific to the material of the medium (Fischer *et al.* 2002). While, scattering loss gradually increases with the frequency and often contribute as the slowly varying background in the measured extinction spectrum and are often modeled as linear or quadratic functions over the given frequency range (Narayana and Ophir 1983, Bao *et al.* 2000, Martens and Stark 1991, Ophir *et al.* 1984).

The THz spectrum of $\alpha$-monohydrate lactose has been extensively studied, and several researches have identified its absorption *fingerprints* at 0.53, 1.2 and 1.37 THz (Zeitler *et al.* 2007b, Shen *et al.* 2005a, Brown *et al.* 2007, Walther *et al.* 2005). Due to bandwidth limitations of our measurement setup, we are only able to extract the extinction spectrum up to $\approx$ 0.6 THz, for the three signals. The results are plotted in Fig. 6.6. It can be clearly seen that, for each subsequent echo, the largest detectable signal ($\alpha_{max}$) reduces according to the following equation as given by Jepsen and Fischer

**Table 6.1. Extracting optical parameters from echoes.** Extracting complex R.I. attenuation coefficient.

| | Directly Transmitted Pulse | First Echo | Second Echo |
|---|---|---|---|
| Transfer Function | $H_{\text{sam,rr}}(\omega) = \frac{\tau_{\text{sw}}\tau_{\text{ws}}}{\tau_{\text{aw}}\tau_{\text{wa}}}$ $\exp(-j\hat{n}_{\text{s}}\frac{\omega d_{\text{s}}}{c})$ | $H_{\text{sam,e1}}(\omega) = \frac{\tau_{\text{sw}}\tau_{\text{ws}}\rho_{\text{sw}}\rho_{\text{ws}}}{\tau_{\text{aw}}\tau_{\text{wa}}\rho_{\text{aw}}\rho_{\text{wa}}}$ $\exp(-j\hat{n}_{\text{s}}\frac{\omega 3d_{\text{s}}}{c})$ | $H_{\text{sam,e2}}(\omega) = \frac{\tau_{\text{sw}}\tau_{\text{ws}}\rho_{\text{sw}}^2\rho_{\text{ws}}^2}{\tau_{\text{aw}}\tau_{\text{wa}}\rho_{\text{aw}}^2\rho_{\text{wa}}^2}$ $\exp(-j\hat{n}_{\text{s}}\frac{\omega 5d_{\text{s}}}{c})$ |
| Refractive Index | $j\hat{n}_{\text{s}} = \frac{c}{\omega d_{\text{s}}}\log(\frac{\tau_{\text{sw}}\tau_{\text{ws}}}{\tau_{\text{aw}}\tau_{\text{wa}}})$ $-\log(H_{\text{sam,rr}}(\omega))$ | $j\hat{n}_{\text{s}} = \frac{c}{\omega 3d_{\text{s}}}\log(\frac{\tau_{\text{sw}}\tau_{\text{ws}}\rho_{\text{sw}}\rho_{\text{ws}}}{\tau_{\text{aw}}\tau_{\text{wa}}\rho_{\text{aw}}\rho_{\text{wa}}})$ $-\log(H_{\text{sam,e1}}(\omega))$ | $j\hat{n}_{\text{s}} = \frac{c}{\omega 5d_{\text{s}}}\log(\frac{\tau_{\text{sw}}\tau_{\text{ws}}\rho_{\text{sw}}^2\rho_{\text{ws}}^2}{\tau_{\text{aw}}\tau_{\text{wa}}\rho_{\text{aw}}^2\rho_{\text{wa}}^2})$ $-\log(H_{\text{sam,e2}}(\omega))$ |
| Atten. Coeff. | $\alpha_{\text{s}}(\omega) = \frac{c}{\omega d_{\text{s}}}\log(\frac{\tau_{\text{sw}}\tau_{\text{ws}}}{\tau_{\text{aw}}\tau_{\text{wa}}})$ $-\log(\lvert H_{\text{sam,rr}}(\omega)\rvert)$ | $\alpha_{\text{s}}(\omega) = \frac{c}{\omega 3d_{\text{s}}}\log(\frac{\tau_{\text{sw}}\tau_{\text{ws}}\rho_{\text{sw}}\rho_{\text{ws}}}{\tau_{\text{aw}}\tau_{\text{wa}}\rho_{\text{aw}}\rho_{\text{wa}}})$ $-\log(\lvert H_{\text{sam,e1}}(\omega)\rvert)$ | $\alpha_{\text{s}}(\omega) = \frac{c}{\omega 5d_{\text{s}}}\log(\frac{\tau_{\text{sw}}\tau_{\text{ws}}\rho_{\text{sw}}^2\rho_{\text{ws}}^2}{\tau_{\text{aw}}\tau_{\text{wa}}\rho_{\text{aw}}^2\rho_{\text{wa}}^2})$ $-\log(\lvert H_{\text{sam,e2}}(\omega)\rvert)$ |

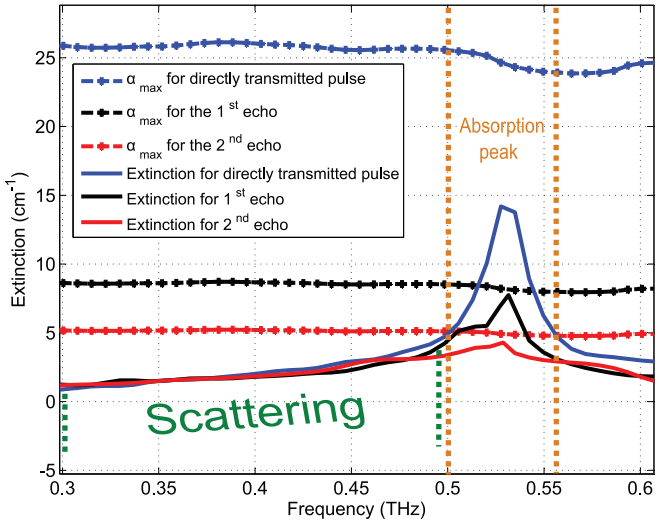


**Figure 6.6. Extinction spectrum—main pulse and echoes.** Extinction spectrum plot calculated for the directly transmitted pulse (Black), the first transmitted Fresnel echo (Red), and the second transmitted Fresnel echo (Blue): While scattering loss are similar for all the three cases (in frequency range 0 - 0.5 THz), the absorption peak at 0.53 THz is significantly different.

(2005):

$$\alpha_{\max}(\omega) = \frac{2}{d} \ln \left\{ \eta_{\mathrm{DR}} \frac{4n(\omega)}{(n(\omega)+1)^2} \right\}, \tag{6.6}$$

where $\eta_{\mathrm{DR}}$ represents the dynamic range of the setup. As a results, there is an apparent reduction in the amplitude of the absorption feature in the extinction spectrum of the first and second echo. Particularly in the extinction spectrum of second echo, the contribution of the absorption peak is negligible. On the other hand, for the given sample, the scattering loss profile over the frequency range of the measurement (up to 0.6 THz) is well within the limit of the largest detectable signal ($\alpha_{\max}$), and therefore remains unaffected. In other words, we can say that detectable signal in the extinction spectrum of the second echo is mostly due to scattering with negligible absorption features and therefore can be used as an estimate of the scattering response of the sample medium.

### Limitations and open questions

- It must be noted that with the reducing maximum detectable signal the measurement bandwidth also reduces and thus the method is only able to provide scattering estimation in the low frequency range. The method is highly dependent on the dynamic range of the measurement setup. The number of echoes required before a successful scattering estimate extraction will vary with the sample material and the dynamic range of the measurement setup. To add to the high dynamic range requirements of this method, the sample under study needs to be optically thick in order to produce Fresnel echoes that can be resolved and separated in time.

- The method also requires the sample to exhibit strong and sharp absorption features. Consider a sample that has first a sharp and strong absorption feature immediately followed by a much weaker absorption feature, while, the strong feature would get attenuated much faster with every echo, the weaker one will still remain. Clearly in this scenario the method fails to separate scattering from the absorption features. However, for applications such as material identification and characterization only strong and sharp features form the basis for robust spectral fingerprint and hence this limitation is rather forgiving.

- One advantage of this technique is that no additional signal processing other than the usual parameter extraction process is required. One can simply calculate the extinction spectra of a later echo and can use it as an estimate of the scattering

baseline and this can be easily automated for implementation in commercial systems. Thus, while in it current form the method is not very useful but it definitely has produced some interesting results and demands to be looked in to for further analysis and improvement.

## 6.4 Chapter summary

In sync with the main theme of this thesis, this chapter discusses various experimental techniques to characterize and/or mitigate scattering effects in the THz-TDS measurements. First the common technique of milling the material of interest into fine powder to reduce the scattering contribution is discussed. In order to better understand the relation between scattering cross-section, the particle size and refractive index of the constituents of a sample, a brief review of the sub-divisions of the Mie theory proposed by Mie (1908) is presented. To demonstrate the technique, THz-TDS measurements of six samples, first made up of granular D-$\alpha$-Glucose and fine PE powder, second made of fine D-$\alpha$-Glucose and fine PE powder, third made of fine $\alpha$-lactose and fine PE powder, fourth made of fine $\alpha$-lactose and granular PE powder, fifth made of granular D-tartaric acid and fine PE powder, and the sixth sample made of fine D-tartaric acid and fine PE powder, were taken. The results confirmed that milling/grinding the material of interest in to a fine powder significantly reduces the scattering effects such as increased baseline slope and absorption peak broadening in the THz-TDS measurements. However, as this technique requires invasive access to the sample material it fails to be of much use for real-world applications such as stand-off measurements and security screening.

The second technique discussed here is averaging multiple spatially disjoint measurements proposed by Shen *et al.* (2008). They argued that by averaging over a large area, reliable terahertz spectrum can be obtained as the averaging process cancels out the contribution of random scattering events that are not in phase and vary across sample positions, while the sample contribution will be enhanced by the averaging process. Their results clearly showed improvement in noise and spectral artifact due to scattering for the parameters extracted from the time domain averaging of disjoint measurements over a larger area. However, their results showed no improvements or reduction in the scattering baseline slope of the measured spectrum. Motivated by the work of Shen *et al.* (2008), we carried out time domain averaging of THz-TDS measurements

of multiple samples of the same material instead of averaging measurements taken at multiple spatially disjoint locations on the same sample which requires special apparatus for changing the focus point of the THz beam. As in each sample, the location (position) distribution, and orientation of the scattering centers will be random and different the contribution of the scattering events from each sample will also be random and out of phase. Thus, time domain averaging for measurements taken from multiple samples should also reduce or diminish the spectral artifacts arising due to THz scattering and noise. The technique was applied to seven samples made from the same mixture of $\alpha$-monohydrate lactose (mixed in a ratio of 1:1). Upon averaging the transmitted time domain signal of the seven samples it was found that, while the time domain averaging certainly reduced spurious spectral artifacts and the shape of the absorption feature at 0.53 THz, it did not have any effect on the scattering baseline slope.

Finally, we present an initial exploration in to analysing multiple echoes, that are usually produced in a transmission mode setup, to provide scattering estimation and corrections in the THz-TDS measurements of optically thick samples that exhibit sharp and strong absorption features. The method shows some promising results but is not very useful in its current form and requires further analysis.

# Chapter 7

# Thesis Summary and Future Work

This chapter concludes the thesis. The first three chapters of the thesis provide an introduction to T-rays and their applications followed by a detailed review of the underlying mechanisms behind the generation and detection of T-rays, basic principles, operation and variants of THz-TDS, data acquisition, material characterization theory, common signal processing techniques used in THz-TDS and the basic concepts and theories of terahertz interaction with materials and propagation in dielectric materials. Chapters 4 to 6 contain the original contributions, divided into three main sections under the common theme of scattering estimation and mitigation, (i) theoretical modeling, (ii) signal processing techniques, and (iii) experimental techniques. This chapter provides a brief summary of all the main sections and the original contributions of this thesis.

## 7.1 Section I—theoretical modeling

### 7.1.1 Scattering estimation—theoretical modeling

- **Background**: This chapter reviews various theoretical models developed for estimating and approximating the scattering cross-section, when an electromagnetic wave interacts with a random medium with characteristic particle dimensions comparable to the wavelength of the incident radiation. We compare the discussed theories with transmission mode THz-TDS measurements of various material samples to validate their applicability.

- **Methodology and results**: First the case of scattering through a sparse or low particle density media is considered. Here, a comparison between the widely used independent scattering approximation and Foldys approximation to calculate the scattering cross-section is carried out. Foldys approximation, was found to be in good agreement with the measurements while the independent scattering approximation failed to explain the measurements. Then we consider the case of THz scattering from dense media. Several existing theories for estimating scattering response of a dense media are discussed. First, we propose a parameterized model based on the effective medium theory given by Chýlek and Srivastava (1983), which estimates the empirical measurements to good accuracy. Thereafter, we propose an iterative algorithm that builds on the effective field theory proposed by Waterman and Truell (1961) and offers a rather simple and computationally efficient method for accurately explaining the multiple scattering response of a medium. Finally, we present a numerical approach to allay the scattering contribution in THz-TDS measurements, provided the samples refractive index is known, and reveal the true absorption spectra for a given sample.

- **Original contributions**: - For the first time, a parameterized model using the effective medium theory proposed by Chýlek *et al.* (1988) is applied to estimate the frequency dependent scattering loss for transmission mode THz-TDS measurements (Kaushik *et al.* 2012a).

  - A new iterative algorithmusing themultiple scattering theory of Waterman and Truell (1961) and the self consistency condition of Chýlek and Srivastava (1983) for estimating scattering response of dense media is proposed and investigated (Kaushik *et al.* 2012d).

- A novel numerical approach based on the modified Rayleigh-Gans-Debye approximation to reduce the scattering contribution in transmission mode THz-TDS measurements of two phased media with absorbing constituents (Kaushik *et al.* 2012e).

## 7.2 Section II—signal processing techniques

### 7.2.1 Scattering estimation and mitigation—signal processing techniques

- **Background**: Here we present signal processing based approaches for estimating and mitigating scattering effects in THz-TDS measurements for samples that exhibit sharp and sparse absorption features, without requiring *a priori* information of their granularity, refractive index, and density. We selected two materials for this study: $\alpha$-monohydrate lactose and $\alpha$-D-glucose. Both materials are commonly found in many pharmaceutical tablets and food products and show distinctive and sharp absorption features in the THz spectral range, making them suitable for this study.

- **Methodology and results**: The first technique explores the relation between the change in spectral moments and time domain features of a THz pulse as it propagates through a dielectric material sample. Assuming a standard representation for the reference spectrum and modeling the scattering as a quadratic function over the measured frequency range, an expression for the unknown scattering coefficient is derived. Thereafter, we describe a technique that uses the relation between the log magnitude spectrum of the reference and the sample measurements, to form a system of equations that can be iteratively solved to result in a spectral function that is independent of the scattering attenuation and depends only on absorption from the sample. Following this, we present an iterative wavelet based technique, that does not rely on assumptions used on the earlier techniques and helps in cleaning the measurements for scattering contribution as well as other background contributions such as systematic errors due to laser drift to enable direct comparison with spectra of pure samples in a spectral data base for automated recognition. Finally, we present a general approach using an iterative implementation of the Hodrick-Prescott filtering technique (Hodrick

and Prescott 1997) to achieve results with similar level of accuracy, however, converging much faster than the iterative wavelet reconstruction technique.

- **Original contributions**: - For the first time, a technique utilizing the analytical description of the THz signal proposed by Xu *et al.* (2003) is developed, to estimate the scattering contribution in THz-TDS measurements by exploring the relation between the change in spectral and temporal moments of a THz pulse as it propagates in a random media is introduced (Kaushik *et al.* 2012b).

  - A new technique that forms a system of equations that result in a spectral function that is independent of scattering and only depends on the absorption coefficient is proposed (Kaushik *et al.* 2011).

  - A new iterative multilevel discrete wavelet transform based algorithm for estimating frequency dependent scattering baseline for transmission mode THz-TDS measurements is also presented in the section (Kaushik *et al.* 2012c).

## 7.3 Section III—experimental techniques

### 7.3.1 Experimental techniques for mitigating scattering effects

- **Background**: This section reviews some common experimental techniques such as milling the material of interest into fine powder and time domain averaging spatially disjoint or multiple sample measurements, in order to reduce the presence of scattering features and effects in the THz-TDS measurements. We also present an initial exploration in analysing Fresnel echoes for estimating scattering contribution in THz-TDS measurements. The technique shows interesting results and demands further exploration.

- **Methodology and results**: First the common technique of milling the material of interest into fine powder to reduce the scattering contribution is discussed. To provide context to this technique a brief review of the sub-divisions of the Mie theory proposed by Mie (1908) is presented. Milling was found to significantly reduces the scattering effects. However, being invasive in nature access the technique fails to be of much use for real-world applications such as stand-off measurements and security screening. Motivated by the technique of averaging multiple spatially disjoint measurements proposed by Shen *et al.* (2008), we investigated averaging of THz-TDS measurements of multiple samples of the same

material to provide scattering mitigation. While, the technique was helpful in reducing spurious spectral artifacts in the measured spectrum, it did not have any effect on the scattering baseline slope. Finally, we present an initial exploration in to analysing multiple Fresnel echoes for estimating scattering contribution in THz-TDS measurements. The observations look promising and suggest further investigation.

## 7.4 Future work and extensions

Here, we present our recommendations for extensions and future directions for the work presented in this thesis. The recommendations are classified in terms of materials to be studied, extensions to existing algorithms and new techniques, and new scenarios to be explored.

- **Materials to be studied**: In this thesis, all the materials that we have considered are mostly ingredients of common pharmaceutical tablets. While the crystalline nature and the overall dielectric properties of these materials make them suitable candidates for studying THz scattering, they all have low refractive indices in the range of 1.4 - 2 and hence provide with samples that posses low refractive index mismatch between the host and the embedded medium. As the refractive index mismatch between the host and the embedded medium increases, assuming that the sample density remains constant, higher orders of multiple scattering must be observed when a THz pulse passes through it. Hence in order to study and analyze higher orders of THz multiple scattering using the algorithms discussed in this thesis we would like to investigate materials such as crystalline quartz, sapphire, silicon ...etc that exhibit high refractive index.

- **Extensions to existing algorithms and new techniques**:

  Extensions:

  - The numerical approach is based on the modified Rayleigh-Debye-Gans (RGD) approximation proposed by Shimizu (1983), as discussed in Section 4.5. Ordinary RGD approximation is only valid if the relative refractive index of the embedded particle is close to unity, and its size satisfies the condition $kd\,|m-1| < 1$, where $m = n_{\mathrm{p}}/n_{\mathrm{m}}$, $d$ is the particle diameter and $k$ is the propagation constant of the incident radiation (Elimelech *et al.* 1998). Modifications proposed by Shimizu

(1983) pushed the validity of the RGD approximation up to $kd\,|m-1| \gg 1$ (2.65 and 5.5 for their experiments) thus making their approximation applicable to a wide variety of materials. In order to develop a general model that relates the scattering attenuation of random two phased media with the refractive indices of its constituents, one can investigate Mie's theoretical description of light scattering to develop an expression for scattering attenuation through a distribution of particles with varying sizes using the approximation of scattering efficiency given by Fournier and Forand (1994).

New techniques:

- When THz radiation passes through a random media multiply scattered (diffused) photons acquire a complicated distribution of phases due to the various different path lengths traveled from source to detector. As the detector integrates over this distribution (assuming an integrating sphere detector system), interference affects average to a much lower value than would be obtained if all the photons were minimally scattered. The most useful characteristic of the majority of the distribution of photons (their coherence) is effectively negated. The complexity of the light scattering process poses a potential problem at this point. The number of degrees of freedom of the interaction between a scattering medium and a large number of incident photons prevents an analytical solution for the required compensating phase. The internal structure of the examined material is by definition not *a priori* known. A small fraction of the incident photons are transmitted with well defined coherence and are detectable. The phase of the input pulse can be adjusted using a pulse shaper or a spatial light modulator in order to improve some characteristic of the detected signal. The subsequent iteration of the applied phase toward a profile that optimally shapes the incident pulses can be computer controlled. With increasing researchers reporting on new spatial light modulators for terahertz radiation (Chan *et al.* 2009, Chen *et al.* 2011b), this new idea may potentially be very useful for scattering mitigation in real world applications such as standoff detection, food, and chemical quality control.

- **New scenarios to be explored**:

  Biomedical analysis:

  Understanding scattering is crucial in many THz biomedical sensing applications such as *in vivo* skin cancer detection, and tissue analysis. Recently, Png

(2010) reported preliminary work on detection of Alzheimer's disease by sensing the protein plaques in brain tissue using THz. One of the major challenges in Alzheimer's disease detection using THz is understanding how terahertz radiation interacts and gets scattered by the granular media around the protein plaques in the brain tissue. Png (2010) also reported some analytical models and a full-wave electromagnetic (EM) field numerical solver to address the issue of THZ scattering. However, Png (2010) achieved only limited success in explaining the THz measurements with the analytical models considered. Also the full-wave EM field solver required full *a priori* information about the sample medium and hence is not suitable for real world application.

A spectrum of algorithms that enable scattering estimation and mitigation are reported in this thesis and hence may be useful in investigating the problem described above.

Security/defence applications:

As THz radiation is non-ionizing and can penetrate most everyday dry non-metallic materials, it has found increasing attention in security and defence applications such as illicit drugs, explosives, and weapons detection (Appleby and Wallace 2007, Wang *et al.* 2002a, Zandonella 2003, Morita *et al.* 2005, Jördens and Koch 2008). As generally such materials of interest are hidden under layers of other common everyday materials, scattering plays an important role when investigating such scenarios. A further area of exploration is to use the algorithms described in this thesis and develop new methods/algorithms to investigate application of THz for security/defence applications.

# Appendix A

# Matlab source code

THIS Appendix provides a summary of the Matlab source code used to implement the algorithms and generate results in Chapters 4-6 of this thesis. The names of the source code files, their functions, and the related chapters are listed. The full source code is available in enclosed CD-ROM. For most of the original contributions, extracts of the full source code are presented here to highlight the main steps.

## A.1 Initial data processing of the measured datasets

In this thesis all the measured datasets were processed by a common set of data processing algorithms before any meaningful interpretation or further analysis can be carried out. The following flow chart describes the common data processing algorithm:

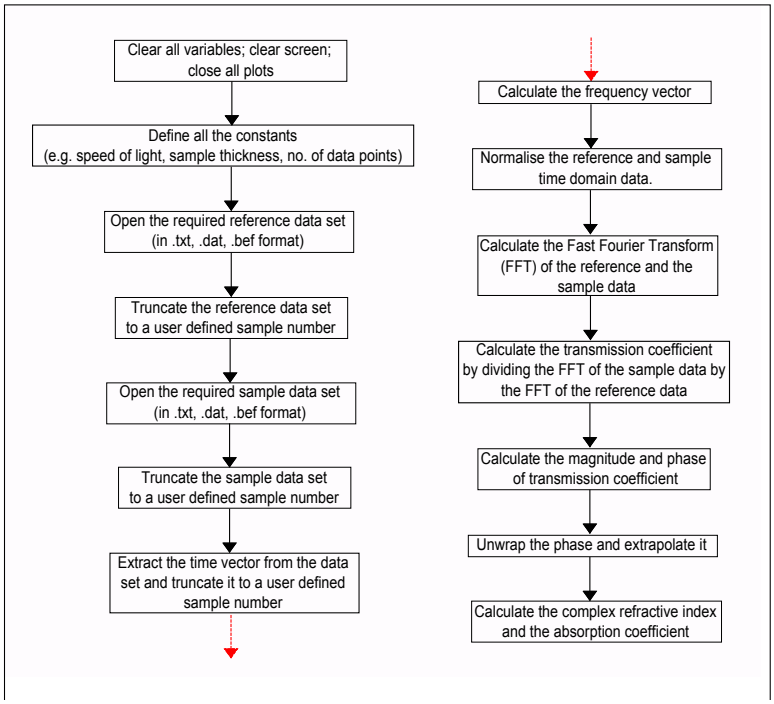


**Figure A.1. Flow chart of common data processing techniques.** First the raw data is fetched from the THz measurement files that are recorded in .txt or .dat or .dat format. Then we use the built-in Matlab function for calculating Fast Fourier Transform (FFT) to transform the data from time domain to the frequency domain. Then the optical parameters are extracted as shown above.

## A.2 List of source code files and related chapters

Table A.1 lists the names of the Matlab codes along with their functions and the related chapter/section, used in this thesis.

## A.3 Source code

This section consists of the Matlab codes as listed in Table A.1. Full source code along with the data sets is also available in the enclosed CD-ROM.

**Table A.1. List of source code files.** A list of Matlab files used for implementing the algorithms and generating the results described in this thesis along with the related chapters.

| Name of Matlab File | Function | Related Chapters |
|---|---|---|
| weakscatteringlimit.m | Sparse medium limit analysis using independent scattering and Foldy's EFA algorithm | Chapter-4 Section-4.2 |
| effectivemedium.m | Dense medium scattering analysis using the model of Chýlek and Srivastava (1983) | Chapter-4 Section-4.3.2 |
| densemediamodel.m | Dense medium model scattering analysis based on the model of Waterman and Truell (1961) | Chapter-4 Section-4.4 |
| modifiedRGDmodel.m | Numerical algorithm using the modified RGD model for scattering reduction | Chapter-4 Section-4.5 |
| specmomentsmethod1.m | Scattering mitigation from spectral and temporal moments (Rayleigh distribution model) | Chapter-5 Section-5.2 |
| specmomentsmethod2.m | Scattering mitigation from spectral and temporal moments (analytical signal model) | Chapter-5 Section-5.2 |
| robustscatter.m | Iterative scattering mitigation using log spectral magnitude | Chapter-5 Section-5.3 |
| waveletbasedmethod.m | Wavelet based method for scattering estimation and correction | Chapter-5 Section-5.4 |
| HPfilter.m | Generalized Hodrick Prescott filtering for scattering estimation and mitigation | Chapter-5 Section-5.5 |

### A.3.1 weakscatteringlimit.m

```
% weakscatteringlimit.m
%
% This program carries out the sparse medium limit analysis using
% independent scattering model, Foldy s EFA algorithm and Stroud and Pan s
% self consistent effective medium theory.
%
% Author: Mayank Kaushik, 2011


% weakscatteringlimit.m
%
% This program carries out the sparse medium limit analysis using
```

```
% independent scattering model, Foldy s EFA algorithm and Stroud and Pan s
% self consistent effective medium theory.
%
% Author: Mayank kaushik


clear all; clc;
%close all;

% value from experiments
c = 299792458;                                  % Speed of light
N = 1024;                                       % Number of data points
                                                % in one scan
d = 360e-6;                                     % Sample thickness in m
Nfft = 1024;                                    % Number of point to
                                                % calculate FFT
scans = 8;                                      % Number of scans
                                                % carried out

Particle_Radius = 180e-6;                       % Particle radius in m

%%%%%%%%% Reading data from experiment into a Matlab variable %%%%%%%%%%%%%

%%%%%%%%%%%%%%%%%% Reference %%%%%%%%%%%%%%%%%%%%%

for ii= 1 :scans
    fn = sprintf( ref_pe_200_400_powder_sparse_tape%01d.dat ,ii);
    fid = fopen(fn, r );
    ln1 = fgetl(fid);                           % skip first comment
                                                % line
    ln2 = fgetl(fid);                           % skip second comment
                                                % line
    jj = 1;
    while feof(fid) == 0
        ln = fgetl(fid);
        C = textscan(ln,  %f %f ,1);
        t(jj) = C{1};
        r(ii,jj) = C{2};
        jj = jj+1;
    end;
    r(ii,:) = r(ii,:)-mean(r(ii,:));            % remove DC
    fclose(fid);
```

```
end;

r = mean(r(1:scans,:));

%%%
```

```
t1 = t*1e-12;                                   % scaling the time
                                                % vector

Ts = mean(diff(t1));
fs = 1/Ts;
ff = (0:Nfft-1)/Nfft*fs;                        % frequency vector
f = fs/2*linspace(0,1,Nfft/2+1);
dw = 1/N/Ts*2*pi;
w = (-1*N/2:1:N/2-1).*dw;                       % angular frequency
                                                % vector


r_max = max(max(r));                            % normalise the
                                                % reference and the
                                                % sample signal
r = r./r_max;
ss = ss./r_max;

As = fft(ss,Nfft,2);
Ar = fft(r,Nfft,2);

T = (As)./(Ar);                                 % complex transmission
                                                % function/vector
A = abs(T);                                     % amplitude of the
                                                % transmission function


phi_unwrap = unwrapsp2(angle(T),20,120,ff);     % phase of the
                                                % tranmission fuction


for i=1:size(phi_unwrap,1)
    n(i,:) = (1-c/d/2/pi*(phi_unwrap(i,:)./ff));
end

n_mean = mean(n,1);                             % refractive index
                                                % estimate


n_samp = 1.46;                                  % bulk refractive
                                                % index of PE
tau_as = 2/(1+1.46);                            % transmission
                                                % coefficients
tau_sw = (2*1.46)/(1.46+1.5);
tau_aw = 2/(1+1.5);
```

```
rho_aw_wa =   (1-1.5/1+1.5) * (1.5-1/1.5+1);
%((1-nwindow)./(1+nwindow))*((nwindow-1)./(nwindow+1));
rho_sw_wa =   ((1.46-1.5)./(1.46+1.5)).*((1.5-1)./(1.5+1));
%((n_mean-nwindow)./(n_mean+nwindow)).*((nwindow-n_mean)./(nwindow+n_mean));
rho_as_sw =   ((1-1.46)./(1+1.46)).*((1.46-1.5)./(1.5+1.46));

FPasw = [1 + rho_as_sw.*exp(-2*i*1.5*2*pi*ff*(500e-6)/c)].^-1;
FPswa = [1 + rho_sw_wa.*exp(-2*i*1.5*2*pi*ff*(500e-6)/c)].^-1;
FPawa = [1 + rho_aw_wa.*exp(-2*i*1.5*2*pi*ff*(500e-6)/c)].^-1;

alpha_samp = -(2/d).*(log(A) +...
    ..log((tau_as.*tau_sw.*FPasw.*FPswa)./(FPawa.*tau_aw)));
% extinction coefficient estimate

ff(1) = ff(2);                                  % replace the first point
                                                % of the frequency vector
                                                % with the second
                                                % to avoid divide by zero
                                                % when calculating lambda
lambda = c./ff;                                 % wavelength vector - lambda

for i = 1:length(lambda)

    x(i) = 2*pi*Particle_Radius./lambda(i);
    qextm(i)  = ((x(i).^2)/2) * mie(1.46,x(i));
    S1(i) = mie_S12(1.46, x(i), 1);
end;

%%%%%%%%%%%%%%%%%%%%%%% Independent scattering model %%%%%%%%%%%%%%%%%%%%%%%
alp_ind = (1)*(0.08)*(3./(4*pi*(Particle_Radius)^3))...
    .. .*qextm * pi * Particle_Radius^2 .* (2./(x.^2)) ;
alp_bando = (0.08)*(3./(4*pi*(Particle_Radius)^3))...
    .. .* ((c^2)./(2*pi.*(ff).^2)) .*qextm;
k = 2*pi./lambda;

%%%%%%%%%%%%%%%%%%%%%%% Foldy s EFA model %%%%%%%%%%%%%%%%%%%%%%%%%%%%%%%%%%
Fsa = S1.*(1i./k); %formula from ishamaru book single scattering page 34
K = sqrt( k.^(2) + (4*pi) * (0.08) * ...
    .. (3./(4*pi*(Particle_Radius)^3)) .* Fsa );
alp_foldy = imag(K);
```

```
%%%%%%%%%%%%%%%%%%%%%%%% Stroud and Pan EMA model %%%%%%%%%%%%%%%%%%%%%%%%
e_eff = 1 + ((4*pi*1i* (0.08) * (3./(4*pi*(Particle_Radius)^3)))...
    .. ./((2*pi.*ff/c).^3)).*S1;
K_eff = sqrt(e_eff).*2*pi.*ff/c;
alp_stroud = imag(K_eff);


%%% Comment: we noted that alp_ind = alp_bando, alp_foldy_efa = alp_stroud %%%

%%%%%%%%%%%%%%%%%%%%%%%%%%%%%%%% Plot the results %%%%%%%%%%%%%%%%%%%%%%%%

 figure(1);
 plot(ff(1:end)*1e-12,alpha_samp/100 , b , linewidth , 2);hold on;
 plot(ff*1e-12,alp_foldy/100, m , linewidth , 2);
 plot(ff*1e-12,alp_bando/100, r , linewidth , 2);
 plot(ff*1e-12,alp_stroud/100, g , linewidth , 2);
 grid on;A11=gca;A12=gca; hold on;
 xlabel( Frequency (THz) );ylabel( Extinction Loss (cm^{-1}) )
 set([A11 A12], XLim ,[0.2 1.2], YLim ,[-5 20]);

 %%%%%%%%%%%%%%%%%%%%%%%%%%%%%%%%%%%%%%%%%%%%%%%%%%%%%%%%%%%%%%%%%%%%%%%%%%
```

## A.3.2 effectivemedium.m

```
% effectivemedium.m
%
% This program carries out the Dense medium model scattering analysis based
% on the model of Chylek and Shrivastava (1983).
%
% Author: Mayank Kaushik, 2011


clear all; clc;
close all;


% values from experiments
c = 299792458;                                      % Speed of light
N = 1022;                                           % Number of data points
                                                    % in one scan
```

```
d = 0.5;                                        % Sample thickness in cm
Nfft = 1022;                                    % Number of point to
                                                % calculate FFT
scans = 8;                                      % Number of scans carried out
Particle_Radius = 25e-6;                        % Scatterer radius
                                                % (air voids in this case)


%%%%%%%%%%% Reading data from experiment into a Matlab variable %%%%%%%%%

%%%%%%%%%%%%%%%%%% Reference %%%%%%%%%%%%%%%%%%%%

for ii= 1 :scans
    fn = sprintf( ref_pe_0_80_nitro_0%01d.dat ,ii);
    fid = fopen(fn, r );
    ln1 = fgetl(fid);                           % skip first comment line
    ln2 = fgetl(fid);                           % skip second comment line
    jj = 1;
    while feof(fid) == 0
        ln = fgetl(fid);
        C = textscan(ln,  %f %f ,1);
        t(jj) = C{1};
        r(ii,jj) = C{2};
        jj = jj+1;
    end;
    r(ii,:) = r(ii,:)-mean(r(ii,:));            % remove DC
    fclose(fid);
end;

r = mean(r(1:scans,:));

%%%%%%%%%%%%%%%%%%%%%%%%%%%%%%%%%%%%%%%%%%%%%%%%%%%%%%%%%%%%%%%%%%%%%%%

%%%%%%%%%%%%%%%%%%% Sample %%%%%%%%%%%%%%%%%%%%%%

for ii= 1 :scans
    fn = sprintf( pe_0_80_nitro_0%01d.dat ,ii);
    fid = fopen(fn, r );
    ln1 = fgetl(fid);                           % skip first comment line
    ln2 = fgetl(fid);                           % skip second comment line
    jj = 1;
    while feof(fid) == 0
```

```
        ln = fgetl(fid);
        C = textscan(ln,  %f %f ,1);
        t(jj) = C{1};
        ss(ii,jj) = C{2};
        jj = jj+1;
    end;
    ss(ii,:) = ss(ii,:)-mean(ss(ii,:));            % remove DC
    fclose(fid);
end;

ss = mean(ss(1:scans,:));

%%%%%%%%%%%%%%%%%%%%%%%%%%%%%%%%%%%%%%%%%%%%%%%%%%%%%%%%%%%%%%%%%%%%%%%%%%%%%%%
%%%%%%%%%%%%%%%%%%%%%%%%%%%%%%%%%%%%%%%%%%%%%%%%%%%%%%%%%%%%%%%%%%%%%%%%%%%%%%%

r = (r(1:N));                                      % discard redundent
                                                   % data points from
                                                   % the reference data
ss = (ss(1:N));                                    % discard redundent
                                                   % data points from the
                                                   % sample data
t = t(1:N);                                        % discard redundent
                                                   % data points from
                                                   % the time vector

t1 = t*1e-12;                                      % scaling the time vector
Ts = mean(diff(t1));
fs = 1/Ts;
ff = (0:Nfft-1)/Nfft*fs;                           % frequency vector
f = fs/2*linspace(0,1,Nfft/2+1);
dw = 1/N/Ts*2*pi;
w = (-1*N/2:1:N/2-1).*dw;                          % angular frequency vector


r_max = max(max(r));                               % normalise the reference
                                                   % and the sample signal
r = r./r_max;
ss = ss./r_max;

As = fft(ss,Nfft,2);
Ar = fft(r,Nfft,2);
```

```
T = (As)./(Ar);                                    % complex transmission
                                                   % function
A = abs(T);                                        % amplitude of the
                                                   % transmission function

tau_sw = (2*1.46)/(1.46+1.6);                      % Fresnel transmission
                                                   % coefficients PE– 1.46
                                                   % and Teflon window – 1.6
tau_ws = (2*1.6)/(1.46+1.6);
tau_aw = 2/(1+1.6);
tau_wa = (2*1.6)/(1+1.6);

alpha_mean = (2/d).*(log((tau_sw*tau_ws)/(tau_aw*tau_wa)) – log(A));
% extinction coefficient estimate

ff = [ff(2) ff(2:end)];                            % replace the first point
                                                   % of the frequency
                                                   % vector with the
                                                   % second to avoid divide
                                                   % by zero when
                                                   % calculating lambda
lambda = c./ff;                                    % wavelength vector

e1 = 1;                                            % permittivity of the
                                                   % air void (scatterer)
e2 = (1.46).^2;                                    % permittivity of the
                                                   % PE particles
                                                   % (surrounding medium)
m2 = sqrt(e2);                                     % refractive index of
                                                   % the PE particles
                                                   % (surrounding medium)
vol_frac = 0.76;                                   % volume fraction of
                                                   % the PE particles
                                                   % (surrounding medium)

%%%%%%%%%%%%%%%Simple Bruggeman Model%%%%%%%%%%%%%%%%%%%%%%%%%%%%%%%%%%%
g = 1/3;
cc = (g – 0.24)*e1 + (g – vol_frac).*e2;

[xx] = solve( (0.24)*((1^2 – xx^2)/(1^2 + 2*xx^2)) +...
...(0.76)*((1.46^2 – xx^2)/(1.46^2 + 2*xx^2)) = 0 );
% solution to the Bruggeman equation
```

```
vv = double(xx);
e_eff_in = vv(4)^2;                                    % initial estimate
                                                       % of the effective
                                                       % permittivity of the
                                                       % composite medium
m_eff_in = vv(4)*ones(1,length(lambda));               % initial estimate of
                                                       % the effective
                                                       % refractive index of
                                                       % the composite medium
%%%%%%%%%%%%%%%%%%%%%%%%%%%%%%%%%%%%%%%%%%%%%%%%%%%%%%%%%%%%%%%%%%%%%%%%%%%%

%%%%%%%%%%%%%%%%%%%% petr chylek & vandana theory%%%%%%%%%%%%%%%%%%%

    for mm = 1:2                                       % number of iterations
                                                       % for the algorithm
                                                       % (correct value
                                                       % determined using the
                                                       % convergence criteria)
        m = m_eff_in;

        for jj = 1:length(lambda)

            Aeff(jj) = 1i*12*(pi.^2).*(m(jj)^3)./(lambda(jj).^3);
            x(jj) = 2*pi.*1.46*Particle_Radius./lambda(jj);
            qextm(jj)  = mie_chylek(1./m(jj),x(jj));
            Beff(jj) = (1-vol_frac)*(3./(4*pi*(Particle_Radius)^3)).* ...
                       .. ((x(jj).^2)/2).*qextm(jj);

        end;

        e_eff_fin = e2.*(Aeff*(vol_frac) + Beff)./(Aeff*(vol_frac) - 2.*Beff);
        convergence(mm) = mean(sqrt(abs(e_eff_fin)) - (abs(m_eff_in)));
        m_eff_in = sqrt(e_eff_fin);
    end;
%%%%%%%%%%%%%%%%%%%%%%%%%%%%%%%%%%%%%%%%%%%%%%%%%%%%%%%%%%%%%%%%%%%%%%%%%%%%

K_eff = ((2*pi.*ff)/c).*m_eff_in;                      % final estimate of the
                                                       % effective propagation
                                                       % constant
alp = imag(K_eff);                                     % final estimate of the
                                                       % effective
                                                       % extinction coefficient
```

```
%%%%%%%%%%%%%%%%%%%%%%%%%%%%%%%%%% Plot the results %%%%%%%%%%%%%%%%%%%%%%%%

figure(1);
%subplot(1,2,1);
plot(ff(1:end)*1e-12,alpha_mean(1:end), 'b' , 'linewidth' , 2); hold on;
plot(ff(1:end)*1e-12,-imag(K_eff(1:end))/100, 'r^' , 'linewidth' , 2);
grid on;A11=gca;title( 'n' );A12=gca;
title( 'Measured Extinction Loss Vs. Chylek et al model' ); hold on;
xlabel( 'Frequency(THz)' );ylabel( 'Extinction Loss (cm-1)' );
set([A11 A12], 'XLim' ,[0.13 1.5]);

%%%%%%%%%%%%%%%%%%%%%%%%%%%%%%%%%%%%%%%%%%%%%%%%%%%%%%%%%%%%%%%%%%%%%%%%%%%
```

### A.3.3 densemediamodel.m

```
% densemediamodel.m
%
% This program carries out the Dense medium model scattering analysis based
% on the model of Waterman and Truell (1961) and the self consistency
% conditon of Chylek and Shrivastava (1988).
%
% Author: Mayank kaushik

clear all; clc;
%close all;


% values from experiments
c = 299792458;                                  % Speed of light
N = 1022;                                       % Number of data points
                                                % in one scan
d = 0.5;                                        % Sample thickness in cm
Nfft = 1022;                                    % Number of point to
                                                % calculate FFT
scans = 8;                                      % Number of scans
                                                % carried out
Particle_Radius = 90e-6;                        % Scatterer radius
                                                %(air voids in this case)
```

```
%%%%%%%%% Reading data from experiment into a Matlab variable %%%%%%%%%%%%%

%%%%%%%%%%%%%%%%% Reference %%%%%%%%%%%%%%%%%%%%

for ii= 1 :scans
    fn = sprintf( ref_pe_200_400_nitro_0%01d.dat ,ii);
    fid = fopen(fn, r );
    ln1 = fgetl(fid);                                   % skip first comment
                                                        %line
    ln2 = fgetl(fid);                                   % skip second comment
                                                        % line
    jj = 1;
    while feof(fid) == 0
        ln = fgetl(fid);
        C = textscan(ln,  %f %f ,1);
        t(jj) = C{1};
        rr(ii,jj) = C{2};
        jj = jj+1;
    end;
    rr(ii,:) = rr(ii,:)-mean(rr(ii,:));                 % remove DC
    fclose(fid);
end;

r = mean(rr(1:scans,:));

%%%%%%%%%%%%%%%%%%%%%%%%%%%%%%%%%%%%%%%%%%%%%%%%%%%%%%%%%%%%%%%%%%%%%%%

%%%%%%%%%%%%%%%%% Sample %%%%%%%%%%%%%%%%%%%%

for ii= 1 :scans
    fn = sprintf( pe_200_400_nitro_0%01d.dat ,ii);
    fid = fopen(fn, r );
    ln1 = fgetl(fid);                               % skip first comment line
    ln2 = fgetl(fid);                               % skip second comment line
    jj = 1;
    while feof(fid) == 0
        ln = fgetl(fid);
        C = textscan(ln,  %f %f ,1);
        t(jj) = C{1};
        ss(ii,jj) = C{2};
        jj = jj+1;
```

```
    end;
    ss(ii,:) = ss(ii,:)-mean(ss(ii,:));            % remove DC
    fclose(fid);
end;

ss = mean(ss(1:scans,:));

%%%
```

```
alpha_mean = (2/d).*(log((tau_sw*tau_ws)/(tau_aw*tau_wa)) - log(A));
                                    % extinction coefficient estimate


ff = [ff(2) ff(2:end)];                 % replace the first point
                                        % of the frequency vector
                                        % with the second to avoid
                                        % divide by zero when
                                        % calculating lambda
lambda = c./ff;                         % wavelength vector - lambda

Ps = 70;                                % index number for end
                                        % of valid data range
                                        % calculated based on the
                                        % dynamic range of the
                                        % measurment setup (will vary
                                        % from sample to sample)

e0 = (1.46).^2;                       % Permittivity of the PE particles
                                      % (surrounding medium)
n_air = 1;
n0 = sqrt(e0);                        % refractive index of the PE
                                      % particles (surrounding medium)

k0 = 2*pi.*n0./lambda(1:Ps);          % propagation constant in the
                                      % surrounding medium
cw =  c./(2*pi.*ff(1:length(lambda(1:Ps))));
                                       % speed of the T-ray * angular
                                       % frequency (single variable formed
                                       % for ease of representaion later on)
vol_frac = 0.45;                       % volume fraction of the
                                       % scatterers (air voids)
n_in = vol_frac*n_air + (1-vol_frac)*n0;    % initial estimate - basic
                                       % dielectric mixing rule
                                       % (Maxwell Garnett)
n = n_in*ones(1,length(lambda(1:Ps)));
K = k0(1:length(lambda(1:Ps)));

for i = 1:3                            % number of iterations
                                       % for the algorithm (correct
                                       % value determined using
```

```
                                        % the convergence criteria)

%%%%%% calculation of the forward and backward scattering amlitudes %%%%%%%
for j = 1:Ps

    x(j) = 2*pi*n(j)*Particle_Radius./lambda(j);
    S1(j) = mie_S12(1/(n(j)), x(j), 1);
    S2(j) = mie_S12(1/(n(j)), x(j), -1);

    S11(j) = mie_S12(1/(n(j)), x(j), 1);
    S12(j) = mie_S12(1.46/(n(j)), x(j), 1);

    S11b(j) = mie_S12(1/(n(j)), x(j), -1);
    S12b(j) = mie_S12(1.46/(n(j)), x(j), -1);
end;
f_0 = S1.*(1i./K);
f_pi = S2.*(1i./K);

%%%%%%%%%%%%%%%%%%%%%%%%%%%%%%%%%%%%%%%%%%%%%%%%%%%%%%%%%%%%%%%%%%%%%%%%%%%

%%%%%%% calculation of the convergence condition for the algorthim %%%%%%%%
f_1(:,i) = S11.*(1i./K);
f_2(:,i) = S12.*(1i./K);
f_1b(:,i) = S11b.*(1i./K);
f_2b(:,i) = S12b.*(1i./K);
adif(:,i) = sum(abs(f_1(:,i) + f_2(:,i)));
adifb(:,i) = sum(abs(f_1b(:,i) + f_2b(:,i)));
converge(:,i) = adif(:,i) + adifb(:,i);
%%%%%%%%%%%%%%%%%%%%%%%%%%%%%%%%%%%%%%%%%%%%%%%%%%%%%%%%%%%%%%%%%%%%%%%%%%%


%%%%%%%%%%% WATERMANN TRUELL  formula %%%%%%%%%%%%%%%%%%%%%%%
N = (vol_frac)*(3./(4*pi*(Particle_Radius)^3));
A = (1 + (2*pi*N.*f_0./((K).^2))).^2;
B = (2*pi*N.*f_pi./((K).^2)).^2;

K2 = (K.^2).*(A-B);
K = sqrt(K2);
n = (cw.*K);
alp_water = imag(K);
%%%%%%%%%%%%%%%%%%%%%%%%%%%%%%%%%%%%%%%%%%%%%%%%%%%%%%%%%%%%%%%%%%%%%%%%%%%
```

```
end;

nf = n0*ones(1,length(lambda));
Kf = k0;
for i = 1:2                                          % number of iteration for
                                                     % the algorithm proposed by
                                                     % Guisto et al. 2003

%%%%%%%%%% Foldy s EFA formuls %%%%%%%%%%%%%%%%%%%%%%%%%%%%
for jj = 1:Ps
    xf(jj) = 2*pi*nf(jj)*Particle_Radius./lambda(jj);
    S1f(jj) = mie_S12(1/nf(jj), xf(jj), 1);
end;

    Fsa = S1f.*(1i./Kf);                             % formula from ishamaru
                                                     % book single scattering page
                                                     % 34
    Kf = sqrt( Kf.^(2) + (4*pi) * (vol_frac) *...
        .. (3./(4*pi*(Particle_Radius)^3)) .* Fsa );
    alp_foldy = imag(Kf);
    nf = (cw.*Kf);
end;

%%%%%%%%%%%%%%%%%%%%%%%%%%%%%%%%%%%%%%%%%%%%%%%%%%%%%%%%%%%%%%%%%%%%%%%

%%%%%%%%%%%%%%%%%%%%%%%%%%%% Plot the results %%%%%%%%%%%%%%%%%%%%%%%%%%%%
figure(100);
plot(ff(1:Ps)*1e-12,alpha_mean(1:Ps), b , linewidth , 2); hold on;
plot(ff(1:Ps)*1e-12,(alp_water/100), g , linewidth , 2);
                                                       % divide by 100 to
                                                       % express results in cm^{-1}
plot(ff(1:Ps)*1e-12,(alp_foldy/100), r , linewidth , 2);
                                                        % divide by 100 to
                                                        % express results in cm^{-1}
grid on;A11=gca;title( n );A12=gca;title(  ); hold on;
xlabel( Frequency(THz) );ylabel( Extinction (cm-1) );
set([A11 A12], XLim ,[0.2 1.5]);
%%%%%%%%%%%%%%%%%%%
```

```
% modifiedRGDmodel.m
%
% This program implements a numerical algorithm that uses the modified RGD
% model for providing scattering reduction/correction to THz-TDS
% measurements
%
% Author: Mayank Kaushik, 2012


clear all; clc;


% txta from experiments
c = 299792458;
N = 360;
d = 2.1*(10^-3);
Nfft = 360;
scans = 3;


%%%%%%%% Reading data from experiment into a Matlab variable %%%%%%%%%%%%%%

%%%%%%%%%%%%%%%%%% Reference %%%%%%%%%%%%%%%%%%%%%

for ii= 1 :scans
    fn = sprintf( ref_lpp_%01d.dat ,ii);
    fid = fopen(fn, r );
    ln1 = fgetl(fid);                                % skip first comment line
    ln2 = fgetl(fid);                                % skip second comment line
    jj = 1;
    while feof(fid) == 0
        ln = fgetl(fid);
        C = textscan(ln,  %f %f ,1);
        t(jj) = C{1};
        r(ii,jj) = C{2};
        jj = jj+1;
    end;
    r(ii,:) = r(ii,:)-mean(r(ii,:));                 % remove DC
    fclose(fid);
end;
```

```
r = mean(r(1:scans,:));

%%%%%%%%%%%%%%%%%%%%%%%%%%%%%%%%%%%%%%%%%%%%%%%%%%%%%%%%%%%%

%%%%%%%%%%%%%%%%%%%% Sample %%%%%%%%%%%%%%%%%%%%%%

for ii= 1 :scans
    fn = sprintf( lactose_200_400_pe_2.1mm_%01d.dat ,ii);
    fid = fopen(fn, r );
    ln1 = fgetl(fid);                                   % skip first comment line
    ln2 = fgetl(fid);                                   % skip second comment line
    jj = 1;
    while feof(fid) == 0
        ln = fgetl(fid);
        C = textscan(ln,  %f %f ,1);
        t(jj) = C{1};
        ss(ii,jj) = C{2};
        jj = jj+1;
    end;
    ss(ii,:) = ss(ii,:)-mean(ss(ii,:));                 % remove DC
    fclose(fid);
end;

ss = mean(ss(1:scans,:));

%%%%%%%%%%%%%%%%%%%%%%%%%%%%%%%%%%%%%%%%%%%%%%%%%%%%%%%%%%%%
%%%%%%%%%%%%%%%%%%%
```

```
fpnt = fpnt*5;
fpnt2 = fpnt/2;
df = fs/fpnt;
fscale = [0:df:fs/2-df];                    % frequency scale,
                                            % max freq is half of
                                            % sampling freq

wscale = 2.*pi.*fscale;

r_max = max(max(r));                        % normalise the reference
                                            % and the sample signal

r = r./r_max;
ss = ss./r_max;
ss = 1*ss;

Ar = fft(r, fpnt);
As = fft(ss, fpnt);
Ar = Ar(1:end/2);
As = As(1:end/2);

T = As./Ar;                                 % complex transmission
                                            % function/vector
A = abs(T);                                 % amplitude of the
                                            % transmission function



                                            % do an average phase
                                            % between 0.25->0.5 THz
                                            % and perform linear fit
                                            % to estimate the DC
                                            % phase error
fmin = 0.2e12; fmax = 1e12;
fminp = round(fmin/df);
fmaxp = round(fmax/df);

lnT = log(abs(T));
argT = unwrapsp2(angle(T(1:fpnt2)), fminp, fmaxp, fscale(1:fpnt2));
                                            % phase of the tranmission
                                            % fuction

wLc = wscale.*d./c;
```

```
nn = 1 - argT./wLc;                                % sample s frequency
                                                   % dependent referactive
                                                   % index
nn(1) = nn(2);

tau = 4*nn./(nn+1).^2;
kk = (log(abs(tau)) - lnT)./wLc;                   % propagation Constant
kk(1) = kk(2);

aa = 2.*wscale.*kk./(c.*100);                      % frequency dependent
                                                   % extinction coefficient

npe = 1.46*ones(1,length(fscale));                 % refractive index of PE
                                                   % (assumed to be same
                                                   % throughout the frequency
                                                   % range)
m_tol = 0.3;                                       % total mass of the sample
                                                   % in grams
V_tol = (pi*(7.5^2)*2.1)/1000;                     % volume of a cylinder
                                                   % pi*r^2*h: r = 7.5 mm
                                                   % and h = 2.1 mm. divide
                                                   % by 1000 to express in cm^3
m_pe = 0.2;                                        % mass of PE in grams
density_pe = 0.948                                 % g/cm^3 as provided by
                                                   % the supplier
Vpe = m_pe/density_pe;                             % volume of PE in the
                                                   % sample (in cm^3)
Vlac = V_tol - Vpe;                                % volume of lactose in
                                                   % the sample (in cm^3)

Vfpe = Vpe/V_tol;                                  % volume fraction of PE
Vflac = Vlac/V_tol;                                % volume fraction of lactose

nlac = (nn - npe*Vfpe)/Vflac;                      % refractive index of lactose

wc = (2*pi.*fscale)/c;
a_RGD = (12)*(pi^2).*(wc.^2).*((npe.^2)./(nlac.^2)).*((nlac - npe).^2);
                                                   % estimate of the effective
                                                   % extinction coefficent
                                                   % before performing least
                                                   % squares fitting with the
```

```
                                                    % measurements to estimate
                                                    % the unknown parameter
valid_range = 1:255;                                % valid data range selected
                                                    % based on the dynamic range
                                                    % of the system

%%%%%%%%%%%%%%%%%%%% least square curve fitting %%%%%%%%%%%%%%%%%%%%%%%%%

xdata = a_RGD(valid_range);
ydata = aa(valid_range);
f = @(x,xdata)x*xdata;
init_sol = 0.1;
x = lsqcurvefit(f,init_sol,xdata,ydata);

%%%%%%%%%%%%%%%%%%%%%%%%%%%%%%%%%%%%%%%%%%%%%%%%%%%%%%%%%%%%%%%%%%%%%%%%%%%

a_RGD = a_RGD*x;                                    % final estimate of the
                                                    % effective extinction
                                                    % coefficent

%%%%%%%%%%%%%%%%%%%%%%%%%%%%%%%% Plot the results%%%%%%%%%%%%%%%%%%%%%%%%%

figure(1);
subplot(2,1,1);plot(fscale*1e-12,nn); hold on;
plot(fscale*1e-12,1.46*ones(1,length(fscale)), r );
grid on;A11=gca;title( n );xlabel( f (THz) );
subplot(2,1,2);plot(fscale*1e-12,aa); hold on;
grid on;A12=gca;title( absorp );
xlabel( f (THz) );ylabel( cm^{-1} );
set([A11 A12], XLim ,[0.2 2.5]);


 figure(2);
 plot(fscale(1:end)*1e-12,aa, b , linewidth , 2);hold on;
 plot(fscale*1e-12,a_RGD, m. , linewidth , 0.5);
 plot(fscale*1e-12,(aa - a_RGD), k-- , linewidth , 2);
 grid on;A11=gca;title( n );A12=gca;
 title( Extinction Loss for alpha-glucose mixed with P.E ); hold on;
 xlabel( Frequency (THz) );ylabel( Extinction (cm^{-1}) )
 set([A11 A12], XLim ,[0.25 1.56], YLim ,[-5 40]);

%%%%%%%%%%%%%%%%%%%%%%%%%%%%%%%%%%%%%%%%%%%%%%%%%%%%%%%%%%%%%%%%%%%%%%%%%%%
```

### A.3.5 specmomentsmethod1.m

```
% specmomentsmethod1.m
%
% This program implements the a scattering mitigation algorithm that uses
% the spectral and temporal moments of the measured reference and sample
% data. Assumptions: Rayleigh distribution model for representing THz
% signal and a quadratic scattering loss profile.
%
% Author: Mayank Kaushik, 2009



clear all; clc;
close all;

% values from experiments
c = 299792458;                                          % Speed of light
N = 1020;                                               % Number of data points
                                                        % in one scan
d = 0.45;                                               % Sample thickness in cm
Nfft = 1020;                                            % Number of point to
                                                        % calculate FFT
scans = 8;                                              % Number of scans carried
                                                        % out


%%%%%%%%%%% Reading data from experiment into a Matlab variable %%%%%%%%%%

%%%%%%%%%%%%%%%%%% Reference %%%%%%%%%%%%%%%%%%%%

for ii= 1 :scans
    fn = sprintf( ref_lp_0%01d.dat ,ii);
    fid = fopen(fn, r );
    ln1 = fgetl(fid);                                    % skip first comment line
    ln2 = fgetl(fid);                                    % skip second comment line
    jj = 1;
    while feof(fid) == 0
        ln = fgetl(fid);
```

```
        C = textscan(ln,  %f %f ,1);
        t(jj) = C{1};
        r(ii,jj) = C{2};
        jj = jj+1;
    end;
    r(ii,:) = r(ii,:)-mean(r(ii,:));                    % remove DC
    fclose(fid);
end;

r = mean(r(1:scans,:));

%%%%%%%%%%%%%%%%%%%%%%%%%%%%%%%%%%%%%%%%%%%%%%%%%%%%%%%%%%%%

%%%%%%%%%%%%%%%%%%%% Sample %%%%%%%%%%%%%%%%%%%%%%
for ii= 1 :scans
    fn = sprintf( lp_0_80_0%01d.dat ,ii);
    fid = fopen(fn, r );
    ln1 = fgetl(fid);                                    % skip first comment line
    ln2 = fgetl(fid);                                    % skip second comment line
    jj = 1;
    while feof(fid) == 0
        ln = fgetl(fid);
        C = textscan(ln,  %f %f ,1);
        t(jj) = C{1};
        ss(ii,jj) = C{2};
        jj = jj+1;
    end;
    ss(ii,:) = ss(ii,:)-mean(ss(ii,:));                  % remove DC
    fclose(fid);
end;

ss = mean(ss(1:scans,:));

%%%%%%%%%%%%%%%%%%%%%%%%%%%%%%%%%%%%%%%%%%%%%%%%%%%%%%%%%%%%
%%%%%%%%%%%%%%%%%%%
```

```
t1 = t*1e-12;                                          % scaling the time vector
Ts = mean(diff(t1));
fs = 1/Ts;
ff = (0:Nfft-1)/Nfft*fs;                               % frequency vector
f = fs/2*linspace(0,1,Nfft/2+1);
dw = 1/N/Ts*2*pi;
w = (-1*N/2:1:N/2-1).*dw;                              % angular frequency vector

spec_r = singlesidedfourier1(r,fs,Nfft,256,0);         % signle sided reference
                                                       % spectrum for centroid
                                                       % calculation
spec_ss = singlesidedfourier1(ss,fs,Nfft,256,0);       % single sided spectrum
                                                       % for centroid calculation

tau_r = fwhm(t,r) *10^-12;                             % full width half mean
                                                       % duration of the reference
                                                       % signal
tau_s = fwhm(t,ss) *10^-12;                            % full width half mean
                                                       % duration of the sample
                                                       % signal
ww = 2*pi.*ff;

r_mod = ((ww.*tau_r)/sqrt(2)).*exp(-(ww.^2).*(tau_r^2)/4);  % Xu et al. 2003 model
                                                            % representaion for
                                                            % the reference signal
s_mod = ((ww.*tau_s)/sqrt(2)).*exp(-(ww.^2).*(tau_s^2)/4);  % Xu et al. 2003 model
                                                            % representaion for
                                                            % the sample signal

valid_data_range = 4:200;                              % valid data range
                                                       % selected based on
                                                       % the dynamic range
                                                       % of the system
                                                       % starting point selected
                                                       % based on the spectral
                                                       % coverage of the coverage
                                                       % of the single sided
                                                       % spectra -  spec_r
                                                       % and spec_ss

x_vec = 1:200-1;                                       % sample number vector
```

```
                                                    % for the valid data range
mom_r =  (trapz(x_vec, (x_vec.^1).*spec_r(valid_data_range))...
          /trapz(x_vec, spec_r(valid_data_range))) ;
                                                    % reference spectrum
                                                    % first order moment
mom_s = (trapz(x_vec, (x_vec.^1).*spec_ss(valid_data_range))...
         /trapz(x_vec, spec_ss(valid_data_range))) ;
                                                    % sample spectrum
                                                    % first order moment

sig_r = mom_r/1.253;
sig_s = mom_s/1.253;

alpd  = (sig_s^2 - sig_r^2)/(2*(sig_r^2)*(sig_s^2));    % estimated extinction
                                                    % coefficient
scat_slope  = -alpd.*((1:512).^2)/d;                % estimated scattering
                                                    % loss profile


As = fft(ss,Nfft,2);                                % FFT of the sample
                                                    % signal
Ar = fft(r,Nfft,2);                                 % FFT of the reference
                                                    % signal

T = As./Ar;                                         % complex transmission
                                                    % function
A = abs(T);                                         % amplitude of the
                                                    % transmission function

phi_unwrap = unwrapsp2(angle(T),20,120,ff);         % phase of the
                                                    % tranmission fuction

                                                    % do an average phase
                                                    % between 0.25->0.5 THz
                                                    % and perform linear fit
                                                    % to estimate the DC phase
                                                    % error
for ii=1:size(phi_unwrap,1)
    n(ii,:) = (1-c/d/2/pi*(phi_unwrap(ii,:)./ff));
    alpha(ii,:) = -2/d.*log((n(ii,:)+1).^2./4./n(ii,:).*A(ii,:));
end
```

```
n_mean = mean(n,1);                                    % refractive index
                                                       % estimate
alpha_mean = mean(alpha,1) ;                           % extinction coefficient
                                                       % estimate

%%%%%%%%%%%%%%%%%%%%%%%%%%%%%%%% Plot the results %%%%%%%%%%%%%%%%%%%%%%%%
figure(1);
plot(ff(1:512)*1e-12,(alpha_mean(1:512) ), m , linewidth ,2); hold on;
plot(ff(1:512)*1e-12, scat_slope(1:512), g , linewidth ,2);
plot(ff(1:512)*1e-12,((alpha_mean(1:512)) - scat_slope(1:512)), b , linewidth ,2);
grid on;A11=gca;title( n );A12=gca;title( Extinction Loss for sample ); hold on;
xlabel( Frequency (THz) );ylabel( Extinction Loss(cm^-^1) )
set([A11 A12], XLim ,[0.15 1.5]);
%%%%%%%%%%%%%%%%%%%%%%%%%%%%%%%%%%%%%%%%%%%%%%%%%%%%%%%%%%%%%%%%%%%%%%%%%%%
```

## A.3.6 specmomentsmethod2.m

```
% specmomentsmethod2.m
%
% This program implements the a scattering mitigation algorithm that uses
% the spectral and temporal moments of the measured reference and sample
% data. Assumptions: Analytical model of Xu et al.(2003) for representing THz
% signal and a quadratic scattering loss profile.
%
% Author: Mayank Kaushik, 2010

clear all; clc;
%close all;

% values from experiments
c = 299792458;                                         % Speed of light
N = 1020;                                              % Number of data points
                                                       % in one scan
d = 0.45;                                              % Sample thickness in cm
Nfft = 1020;                                           % Number of point to
                                                       % calculate FFT
scans = 8;                                             % Number of scans carried
                                                       % out
```

```
%%%%%%%%% Reading data from experiment into a Matlab variable %%%%%%%%%%%%

%%%%%%%%%%%%%%%%%% Reference %%%%%%%%%%%%%%%%%%%%

for ii= 1 :scans
    fn = sprintf( ref_lp_0%01d.dat ,ii);
    fid = fopen(fn, r );
    ln1 = fgetl(fid);                                   % skip first comment
                                                        % line
    ln2 = fgetl(fid);                                   % skip second comment
                                                        % line
    jj = 1;
    while feof(fid) == 0
        ln = fgetl(fid);
        C = textscan(ln,  %f %f ,1);
        t(jj) = C{1};
        r(ii,jj) = C{2};
        jj = jj+1;
    end;
    r(ii,:) = r(ii,:)-mean(r(ii,:));                    % remove DC
    fclose(fid);
end;

r = mean(r(1:scans,:));

%%%%%%%%%%%%%%%%%%%%%%%%%%%%%%%%%%%%%%%%%%%%%%%%%%%%%%%%

%%%%%%%%%%%%%%%%%% Sample %%%%%%%%%%%%%%%%%%%%%%
for ii= 1 :scans
    fn = sprintf( lp_0_80_0%01d.dat ,ii);
    fid = fopen(fn, r );
    ln1 = fgetl(fid);                                % skip first comment line
    ln2 = fgetl(fid);                                % skip second comment line
    jj = 1;
    while feof(fid) == 0
        ln = fgetl(fid);
        C = textscan(ln,  %f %f ,1);
        t(jj) = C{1};
        ss(ii,jj) = C{2};
        jj = jj+1;
    end;
```

```
    ss(ii,:) = ss(ii,:)-mean(ss(ii,:));                % remove DC
    fclose(fid);
end;

ss = mean(ss(1:scans,:));

%%%
```

```
                                                % for the
                                                % SAMPLE signal


alpha_fwhm = (tau_s^2 - tau_r^2)/4;             % frequency dependent
                                                % attenuation coefficient
                                                % calculated using
                                                % FWHM method
xx = 2*pi*(1:512);                              % frequency vector for
                                                % the centroid method
                                                % on all data points

scat_slope_fwhm = ((alpha_fwhm) .*ww.^2)/d;     % scattering attenuation
                                                % profile calculated
                                                % using FWHM method

As = fft(ss,Nfft,2);                            % FFT of the sample
                                                % signal
Ar = fft(r,Nfft,2);                             % FFT of the reference
                                                % signal
T = As./Ar;                                     % complex transmission
                                                % function/vector
A = abs(T);                                     % amplitude of the
                                                % transmission function

phi_unwrap = unwrapsp2(angle(T),20,120,ff);     % phase of the tranmission
                                                % function
                                                % do an average phase
                                                % between 0.25->0.5 THz
                                                % and perform linear fit
                                                % to estimate the DC
                                                % phase error
for ii=1:size(phi_unwrap,1)
    n(ii,:) = (1-c/d/2/pi*(phi_unwrap(ii,:)./ff));
    alpha(ii,:) = -2/d.*log((n(ii,:)+1).^2./4./n(ii,:).*A(ii,:));
end

n_mean = mean(n,1);                             % refractive index
                                                % estimate
alpha_mean = mean(alpha,1) ;                    % extinction coefficient
                                                % estimate
```

```
%%%%%%%%%%%%%%%%%%%%%%%%%%%%%%%%% Plot the results %%%%%%%%%%%%%%%%%%%%%%%
figure(1);
plot(ff(1:512)*1e-12,(alpha_mean(1:512) ), m , linewidth ,2); hold on;
plot(ff(1:512)*1e-12, scat_slope_fwhm(1:512), k , linewidth ,2);
plot(ff(1:512)*1e-12,((alpha_mean(1:512))-scat_slope_fwhm(1:512)), b , linewidth ,2);
grid on;A11=gca;title( n );A12=gca;title( Extinction Loss for sample ); hold on;
xlabel( Frequency (THz) );ylabel( Extinction Loss(cm^-^1) )
set([A11 A12], XLim ,[0.15 1.5]);
%%%%%%%%%%%%%%%%%%%%%%%%%%%%%%%%%%%%%%%%%%%%%%%%%%%%%%%%%%%%%%%%%%%%%%%%%%%
```

### A.3.7 robustscatter.m

```
% robustscatter.m
%
% This program implements the generalized iterative scattering mitigation
% algorithm that using log spectral magnitude of the reference and the
% sample data to produces features that are robust against various
% scattering conditions.
%
% Author: Mayank Kaushik, 2011




clear all; clc;
close all;

% values from experiments
c = 299792458;                                          % Speed of light
N = 1020;                                               % Number of data points
                                                        % in one scan
d = 0.45;                                               % Sample thickness in cm
Nfft = 1020;                                            % Number of point to
                                                        % calculate FFT
scans = 8;                                              % Number of scans carried
                                                        % out


%%%%%%%%%%% Reading data from experiment into a Matlab variable %%%%%%%%%%
```

```
%%%%%%%%%%%%%%%%%% Reference %%%%%%%%%%%%%%%%%%%%

for ii= 1 :scans
    fn = sprintf( ref_lp_0%01d.dat ,ii);
    fid = fopen(fn, r );
    ln1 = fgetl(fid);                                   % skip first comment line
    ln2 = fgetl(fid);                                   % skip second comment line
    jj = 1;
    while feof(fid) == 0
        ln = fgetl(fid);
        C = textscan(ln,  %f %f ,1);
        t(jj) = C{1};
        r(ii,jj) = C{2};
        jj = jj+1;
    end;
    r(ii,:) = r(ii,:)-mean(r(ii,:));                    % remove DC
    fclose(fid);
end;

r = mean(r(1:scans,:));

%%%%%%%%%%%%%%%%%%%%%%%%%%%%%%%%%%%%%%%%%%%%%%%%%%%%

%%%%%%%%%%%%%%%%%% Sample %%%%%%%%%%%%%%%%%%%%
for ii= 1 :scans
    fn = sprintf( lp_0_80_0%01d.dat ,ii);
    fid = fopen(fn, r );
    ln1 = fgetl(fid);                                    % skip first comment line
    ln2 = fgetl(fid);                                    % skip second comment line
    jj = 1;
    while feof(fid) == 0
        ln = fgetl(fid);
        C = textscan(ln,  %f %f ,1);
        t(jj) = C{1};
        ss(ii,jj) = C{2};
        jj = jj+1;
    end;
    ss(ii,:) = ss(ii,:)-mean(ss(ii,:));                  % remove DC
    fclose(fid);
end;
```

```
ss = mean(ss(1:scans,:));

%%%
```

```
end

n_mean1 = mean(n1,1);                                   % refractive index
                                                        % estimate
alpha_mean1 = mean(alpha1,1) ;                          % extinction coefficient
                                                        % estimate


valid_data_range = 1:120;                               % valid data range
                                                        % selected based on
                                                        % the dynamic range
                                                        % of the system
pp = peakdet(alpha_mean1(valid_data_range),3);          % peak detection algorithm
diff_pp = diff(pp(:,1));                                % differentiate the
                                                        % peak location vector
max_diff_loc = find(diff_pp == max(diff_pp));           % find the maximum
                                                        % value of the
                                                        % differentiated peak
                                                        % loaction vector
                                                        % use the maximum
                                                        % value of the
                                                        % differentiated peak
                                                        % location vector to
                                                        % find the biggest
                                                        % scattering only range
                                                        % in the given data set
idx1 = pp(max_diff_loc);
idx2 = pp(max_diff_loc + 1);
scatter_only_range = (idx1+2):(idx2-2);

len = length(valid_data_range);

for a  = 0.1:0.005:1                                    % iterative algorithm
                                                        % - for details refer
                                                        % to Chapter-5 Section-5.3
    ind = ((a-0.1)/0.005) + 1;
    lv = (1:len).^a;
    l_As = log(abs(As(1:len)))./(lv);
    l_Ar = log(abs(Ar(1:len)))./(lv);
    l2_As(:,:,round(ind)) = (lv).*(l_As - mean(l_As));
    m_err(round(ind)) = abs(mean(l2_As(:,scatter_only_range,round(ind))...
                        - log(abs(Ar(scatter_only_range)))));
```

```
end;

a_ind = find(abs(m_err) == min(abs(m_err)));
aa  = 0.1:0.005:1;
aa(a_ind)
ml_As = l2_As(:,:,a_ind);

rmod_ss = ((ifft(exp(ml_As(1:end)))));                  % reconstructed time
                                                        % domain signal
                                                        % (scattering reduced)

Ams = abs(fft(rmod_ss));
As = As(1:len);
Ar = Ar(1:len);
Ams = (Ams/max(Ams)).*max(abs(As));                     % scale the reconstructed
                                                        % spectrum to match the
                                                        % measured sample spectrum
                                                        % amplitude

T2 = (Ams)./(Ar);                                       % transmission coefficent
                                                        % for the reconstructed
                                                        % signal
A2 = abs(T2);

phi_unwrap1 = unwrapsp2(angle(T2),20,120,ff);           % phase of the
                                                        % tranmission fuction

for ii=1:size(phi_unwrap1,1)
    n(ii,:) = (1-c/d/2/pi*(phi_unwrap1(ii,:)./ff(valid_data_range)));
    alpha(ii,:) = -2/d.*log((n(ii,:)+1).^2./4./n(ii,:).*A2(ii,:));
end

n_mean = mean(n,1);                                     % refractive index
                                                        % estimate using the
                                                        % reconstructed signal
alpha_mean = mean(alpha,1) ;                            % extinction
                                                        % coefficient estimate
                                                        % using the reconstructed
                                                        % signal


%%%%%%%%%%%%%%%%%%%%%%%%%%%%%%%%% Plot the results %%%%%%%%%%%%%%%%%%%%%%%
```

```
figure(1);
plot(ff(valid_data_range)*1e-12,alpha_mean , r , linewidth , 3);hold on;
plot(ff(valid_data_range)*1e-12,alpha_mean1(valid_data_range), k , linewidth , 3);
grid on;A11=gca;title( n );A12=gca;
title( Extinction Loss for alpha-Lactose monohydrate mixed with P.E );
xlabel( Frequency(THz) );
ylabel( Extinction Loss (cm-1) )
set([A11 A12], XLim ,[0.2 1.6]);
%%%%%%%%%%%%%%%%%%%%%%%%%%%%%%%%%%%%%%%%%%%%%%%%%%%%%%%%%%%%%%%%%%%%%%%%%%%%%%%
```

### A.3.8 waveletbasedmethod.m

```
% waveletbasedmethod.m
%
% This program implements an Iterative wavelet based reconstruction algorithm
% for estimating and mitigating scattering contribution in THz-TDS
% measurements.
%
% Author: Mayank Kaushik, 2011


clear all; clc;
close all;


% values from experiments
c = 299792458;                                  % Speed of light
N = 1020;                                       % Number of data points
                                                % in one scan
d = 0.35;                                       % Sample thickness in cm
Nfft = 1020;                                    % Number of point to
                                                % calculate FFT
scans = 9;                                      % Number of scans carried
                                                % out

%%%%%%%%%%%%% Reading data from experiment into a Matlab variable %%%%%%%%%

%%%%%%%%%%%%%%%%%% Reference %%%%%%%%%%%%%%%%%%%%%

for ii= 1 :scans
```

```
    fn = sprintf( glu5r%01d.bef ,ii);
    fid = fopen(fn, r );
    ln1 = fgetl(fid);                                % skip first comment line
    ln2 = fgetl(fid);                                % skip second comment line
    jj = 1;
    while feof(fid) == 0
        ln = fgetl(fid);
        C = textscan(ln,  %f %f ,1);
        t(jj) = C{1};
        r(ii,jj) = C{2};
        jj = jj+1;
    end;
    r(ii,:) = r(ii,:)-mean(r(ii,:));                 % remove DC
    fclose(fid);
end;

r = mean(r(1:scans,:));

%%%%%%%%%%%%%%%%%%%%%%%%%%%%%%%%%%%%%%%%%%%%%%%%%%%%%%%%%%%%

%%%%%%%%%%%%%%%%%%% Sample %%%%%%%%%%%%%%%%%%%%%%

for ii= 1 :scans
    fn = sprintf( glu5s%01d.bef ,ii);
    fid = fopen(fn, r );
    ln1 = fgetl(fid);                                % skip first comment line
    ln2 = fgetl(fid);                                % skip second comment line
    jj = 1;
    while feof(fid) == 0
        ln = fgetl(fid);
        C = textscan(ln,  %f %f ,1);
        t(jj) = C{1};
        ss(ii,jj) = C{2};
        jj = jj+1;
    end;
    ss(ii,:) = ss(ii,:)-mean(ss(ii,:));              % remove DC
    fclose(fid);
end;

ss = mean(ss(1:scans,:));

%%%%%%%%%%%%%%%%%%%%%%%%%%%%%%%%%%%%%%%%%%%%%%%%%%%%%%%%%%%%
```

```
%%%%%%%%%%%%%%%%%%%%%%%%%%%%%%%%%%%%%%%%%%%%%%%%%%%%%%%%%%%%%%%%%%%%%%%%%%%%%%%%

r = (r(1:N));                                   % discard redundent data
                                                % points from the reference
                                                % data
ss = (ss(1:N));                                 % discard redundent data
                                                % points from the sample
                                                % data
t = t(1:N);                                     % discard redundent data
                                                % points from the time
                                                % vector


t1 = t*1e-12;                                   % scaling the time vector
Ts = mean(diff(t1));
fs = 1/Ts;
ff = (0:Nfft-1)/Nfft*fs;                        % frequency vector
f = fs/2*linspace(0,1,Nfft/2+1);
dw = 1/N/Ts*2*pi;
w = (-1*N/2:1:N/2-1).*dw;                       % angular frequency vector


r_max = max(max(r));                            % normalise the reference
                                                % and the sample signal
r = r./r_max;
ss = ss./r_max;

As = fft(ss,Nfft,2);
Ar = fft(r,Nfft,2);

T = (As)./(Ar);                                 % complex transmission
                                                % function
A = abs(T);                                     % amplitude of the
                                                % transmission function


phi_unwrap = unwrapsp2(angle(T),20,120,ff);     % phase of the tranmission
                                                % function
                                                % do an average phase
                                                % between 0.25->0.5 THz
                                                % and perform linear fit
                                                % to estimate the DC phase
                                                % error
```

```
for i=1:size(phi_unwrap,1)
    n(i,:) = (1-c/d/2/pi*(phi_unwrap(i,:)./ff));
    alpha(i,:) = -(2./(d)).*log((n(i,:)+1).^2./4./n(i,:).*A(i,:));
end

n_mean = mean(n,1);                                 % refractive index
                                                    % estimate
alpha_mean = mean(alpha,1) ;                        % extinction coefficient
                                                    % estimate


valid_data_range= 10:205;                           % valid data range selected
                                                    % based on the dynamic range
                                                    % of the system
alp1 = alpha_mean(valid_data_range);                % extinction coefficient
                                                    % in valid data range
alp = alp1;                                         % initialize the scattering
                                                    % reduced coefficient with
                                                    % the measured value

minval = 0.0001*sum(abs(alp1).^2);                  % threshold error energy

for i = 1:14                                        % number of iterations
                                                    % for the algorithm
                                                    % (correct value determined
                                                    % using the convergence
                                                    % criteria: err_n)
    [C,L] = wavedec(alp,4, db4 );                   % for details on algorithm
                                                    % refer to Chapter-5
                                                    % Section-5.4
    [dd1,dd2,dd3,dd4] = detcoef(C,L,[1,2,3,4]);
    aa = appcoef(C,L, db4 );
    d_est = waverec([zeros(1,length(aa)) dd4 dd3 dd2 dd1], L,  db4 );
    a_est = waverec([aa zeros(1,length([dd4 dd3 dd2 dd1]))], L,  db4 );
    alp2 = (d_est) ;
    for k = 1:length(alp)
        if alp2(k) < 0
            alp2(k) = 0;
        else
            alp2(k) = alp2(k);
        end;
    end;
```

```
    alp =  alp - alp2;

    infd = find(d_est < 0);
    err_n(i) = sum(abs(d_est(infd)).^2);

 end;

%%%%%%%%%%%%%%%%%%%%%%%%%%%%%%%%% Plot the results%%%%%%%%%%%%%%%%%%%%%%%%%

figure(1);
plot((err_n), b , linewidth ,2); hold on; grid on;
plot(minval.*ones(1,length(err_n)), r , linewidth ,2);
title( Convergence croteria: error energy (err_n) falls elaw the threshold );

figure(2);
plot(ff(valid_data_range)*1e-12,alp1, b , linewidth ,2); hold on;
plot(ff(valid_data_range)*1e-12,alp, r , linewidth ,2);
plot(ff(valid_data_range)*1e-12,(alp1 - alp), k , linewidth ,2);
grid on;A11=gca;title( n );A12=gca;
title( Measured Extinction Loss and Scattering Removed Extinction ); hold on;
xlabel( Frequency(THz) );ylabel( Extinction Loss (cm-1) );
set([A11 A12], XLim ,[0.2 3]);

%%%%%%%%%%%%%%%%%%%%%%%%%%%%%%%%%%%%%%%%%%%%%%%%%%%%%%%%%%%%%%%%%%%%%%%%%%%%
```

### A.3.9 HPfilter.m

```
% HPfilter.m
%
% This program implements the generalized Hodrick Prescott filter based
% adaptive algorithm for estimating and mitigating scattering contribution
% in THz-TDS measurements.
%
% Author: Mayank Kaushik, 2012


clear all; clc;
close all;

% values from experiments
```

```
c = 299792458;                                  % Speed of light
N = 1020;                                       % Number of data points
                                                % in one scan
d = 0.17;                                       % Sample thickness in cm
Nfft = 1020;                                    % Number of point to
                                                % calculate FFT
scans = 16;                                     % Number of scans carried
                                                % out

%%%%%%%%%% Reading data from experiment into a Matlab variable %%%%%%%%%%

%%%%%%%%%%%%%%%%% Reference %%%%%%%%%%%%%%%%%%%%

for ii= 9 :scans
    fn = sprintf( a_glu_ref_%01d.txt ,ii);
    fid = fopen(fn, r );
    ln1 = fgetl(fid);                           % skip first comment line
    ln2 = fgetl(fid);                           % skip second comment line
    jj = 1;
    while feof(fid) == 0
        ln = fgetl(fid);
        C = textscan(ln,  %f %f ,1);
        t(jj) = C{1};
        r(ii,jj) = C{2};
        jj = jj+1;
    end;
    r(ii,:) = r(ii,:)-mean(r(ii,:));            % remove DC
    fclose(fid);
end;

r = mean(r(1:scans,:));

%%%%%%%%%%%%%%%%%%%%%%%%%%%%%%%%%%%%%%%%%%%%%%%%%%%%

%%%%%%%%%%%%%%%%%% Sample %%%%%%%%%%%%%%%%%%%%%%

for ii= 9 :scans
    fn = sprintf( a_glu_sam_%01d.txt ,ii);
    fid = fopen(fn, r );
    ln1 = fgetl(fid);                           % skip first comment line
    ln2 = fgetl(fid);                           % skip second comment line
    jj = 1;
```

```
    while feof(fid) == 0
        ln = fgetl(fid);
        C = textscan(ln,  %f %f ,1);
        t(jj) = C{1};
        ss(ii,jj) = C{2};
        jj = jj+1;
    end;
    ss(ii,:) = ss(ii,:)-mean(ss(ii,:));            % remove DC
    fclose(fid);
end;

ss = mean(ss(1:scans,:));

%%%
```

```
T = (As)./(Ar);                                    % complex transmission
                                                   % function
A = abs(T);                                        % amplitude of the
                                                   % transmission function

phi_unwrap = unwrapsp2(angle(T),20,120,ff);        % phase of the tranmission
                                                   % fuction
                                                   % do an average phase
                                                   % between 0.25->0.5 THz
                                                   % and perform linear fit
                                                   % to estimate the DC phase
                                                   % error

for i=1:size(phi_unwrap,1)
    n(i,:) = (1-c/d/2/pi*(phi_unwrap(i,:)./ff));
    alpha(i,:) = -(2./(d)).*log((n(i,:)+1).^2./4./n(i,:).*A(i,:));
end

n_mean = mean(n,1);                                % refractive index
                                                   % estimate
alpha_mean = mean(alpha,1) ;                       % extinction coefficient
                                                   % estimate


valid_data_range = 5:215;                          % valid data range
                                                   % selected based on the
                                                   % dynamic range of the system
y = alpha_mean(valid_data_range) ;                 % extinction coefficient
                                                   % in valid data range
lambda = 10;                                       % smoothness parameter
                                                   % for the HOdrick Prescott
                                                   % filtering
m = length(y);
w = 1*ones(m,1);
D = diff(speye(m),3);
I = speye(m);

%%%%%%%%%%%%%%%%%%%%%% Hodrick Prescott Filtering %%%%%%%%%%%%%%%%%%%%%%%%
%%% For details refer to chapter 5 section 5.5 of the thesis %%%
for it = 1:3
  W = spdiags(w,0,m,m);
  z = (((W)+ lambda*D * D)^-1)*(W)*(y);
```

```
  w = (max((z-y), 0.001));
  ymz = y-z;
  infd = find(ymz < 0);
  err_n(it) = sum(abs(ymz(infd)).^2);
end;

%%%%%%%%%%%%%%%%%%%%%%%%%%%%%%%%%%%%%%%%%%%%%%%%%%%%%%%%%%%%%%%%%%%%%%%%%%%%%%%
minval = 0.0001*sum(abs(y).^2);                    % threshold error energy

%%%%%%%%%%%%%%%%%%%%%%%%%%%%%%%% Plot the results%%%%%%%%%%%%%%%%%%%%%%%%%%

figure(1);
plot((err_n), b , linewidth ,2); hold on; grid on;
plot(minval.*ones(1,length(err_n)), r , linewidth ,2)

figure(2);
plot(ff(10:length(z)+9)*1e-12,y, b , linewidth , 2); hold on;
plot(ff(10:length(z)+9)*1e-12,z, r , linewidth , 2);
plot(ff(10:length(z)+9)*1e-12,y-z, m , linewidth , 2);
grid on;A11=gca;title( n );A12=gca;
title( Extinction Loss for alpha-glucose mixed with P.E ); hold on;
xlabel( Freq(THz) );ylabel( Extinction Efficiency (a.u.) )
set([A11 A12], XLim ,[0.1 3.2]);

%%%%%%%%%%%%%%%%%%%%%%%%%%%%%%%%%%%%%%%%%%%%%%%%%%%%%%%%%%%%%%%%%%%%%%%%%%%%%%%
```

# Appendix B

# Analytical models for T-Ray signals

THIS Appendix briefly describes the details of the analytical models for T-ray signals used for simulations in this thesis. The T-ray generation and detection setup used in this thesis employed PCA antenna. Here we have discussed two PCA antenna based T-ray signal and spectrum models. The first and the original model was reported by Duvillaret *et al.* (2001), while the second model was reported by Xu *et al.* (2003).

## B.1 Analytical model by Duvillaret et al. (2001)

First consider the terahertz generation process using a photo-conductive emitting antenna (PCA) . The time-dependent photo current density $J_{em}(t)$ in the emitter can be expressed as the convolution of the impulse response of the PCA and the optical laser pulse (Duvillaret *et al.* 2001):

$$J_{em}(t) = P_{opt}(t)[n_{em}(t)qv_{em}(t)], \tag{B.1}$$

where, $P_{opt}(t)$ is the incident optical pump pulse (assuming a Gaussian temporal profile), $q$ is the carrier charge, equal to 1.602 $\times 10^{-19} C$, $n_{em}(t)$ is the free-carrier density, and $v_{em}(t)$ is the free-carrier average velocity. The subscript 'em' represents the emitter.

The density of the free-carriers generated from the photo-excitation process, decay exponentially as a results of carrier recombination and trapping. The carrier density can be expressed as:

$$n_{em}(t) \propto \exp\left(-\frac{t}{\tau_{em}}\right), \tag{B.2}$$

where $\tau_{em}$ is the carrier recombination time. The average carrier velocity, $v_{em}(t)$, depends on the applied electric field, $E_{DC}$, as:

$$\frac{dv_{em}(t)}{dt} = -\frac{v_{em}(t)}{\delta\tau_{em}} + \frac{q}{m^*}E_{DC}, \tag{B.3}$$

where $\delta\tau_{em}$ is the carrier collision time and $m^*$ is the carrier effective mass.

A rapid change in the current density, $J_{em}(t)$, in the emitter causes generation of the terahertz radiation from the transmitting antenna. In the far-field the terahertz electric field is found to be proportional to the first derivative of the photo-current density, or mathematically:

$$E_{THz}(t) \propto \frac{dJ_{em}(t)}{dt}, \tag{B.4}$$

which can also be expressed in terms of spectrum by first expanding the above equation in terms of $P_{opt}(t)$, $n_{em}(t)$, and $v_{em}(t)$ and the taking a Fourier transform:

$$E_{THz}(\omega) \propto \frac{P_{em}E_{DC}\delta\tau_{em}(\tau_{em} - \tilde{\tau}_{em})}{2\pi m^*_{em}} \times \frac{\omega \exp(-\omega^2\tilde{\tau}^2_{las}/4)}{(1 - j\omega\tau_{em})(1 - j\omega\tilde{\tau}_{em})}, \tag{B.5}$$

where, $P_{em}$ is the average laser power and $\tau_{las}$ is the duration of the Gaussian temporal profile of the optical pump pulse. On the receiver end, the antenna is gated by the optical probe pulse and the photo-current density in the receiving PCA antenna

can be expressed as the convolution between the optical probe pulse and the PCA impulse response. The expression is similar to that of emitter photo-current density $J_{\mathrm{em}}(t)$ with equivalent expression for the $P_{\mathrm{opt}}(t)$ and free-carrier density, $n_{\mathrm{rec}}(t)$, where 'rec' represents the receiver. However, the current density in the receiver is a function of the delay $\Delta t$ between the pump and probe pulses, as the average carrier velocity in the receiver, $v_{\mathrm{rec}}(t)$, depends on the incoming terahertz electric field $E_{\mathrm{THz}}(t+\Delta t)$ (Duvillaret *et al.* 2001):

$$\begin{aligned} J_{\mathrm{rec}}(t;\Delta t) &= P_{\mathrm{opt}}(t)[n_{\mathrm{rec}} q v_{\mathrm{rec}}(t;\Delta t)], \\ \frac{dv_{\mathrm{rec}}(t;\Delta t)}{dt} &= -\frac{v_{\mathrm{rec}}(t;\Delta t)}{\delta\tau_{\mathrm{rec}}} + \frac{q}{m^*_{\mathrm{rec}}} E_{\mathrm{THz}}(t+\Delta t). \end{aligned} \tag{B.6}$$

The measurable current at the output of the receiving antenna is proportional to the average of the photo-current $J_{\mathrm{rec}}(\Delta t)$ (Duvillaret *et al.* 2001). Taking the Fourier transform of the average current, $\bar{J}_{\mathrm{rec}}(\Delta t)$, we get:

$$\bar{J}_{\mathrm{rec}}(\omega) \propto \frac{P_{\mathrm{em}} P_{\mathrm{rec}} E_{\mathrm{DC}} \tau_{\mathrm{em}} \tau_{\mathrm{rec}} \tilde{\tau}_{\mathrm{em}} \tilde{\tau}_{\mathrm{rec}}}{2\pi m^*_{\mathrm{em}} m^*_{\mathrm{rec}}} \times \frac{\omega \exp(-\omega^2 \tilde{\tau}^2_{\mathrm{las}}/2)}{(1-j\omega\tau_{\mathrm{em}})(1-j\omega\tilde{\tau}_{\mathrm{em}})(1-j\omega\tau_{\mathrm{rec}})}. \tag{B.7}$$

In Section 5.2 of this thesis, we have explored the use of analytical expression to represent the measured THz signal in order to establish relation between the scattering attenuation and the change in the spectral and temporal moments of a THz pulse when it passes through a dielectric material. In order to do so we need to calculate the spectral moments using the following general formula:

$$m_{\mathrm{n}} = \frac{\int_0^\infty \omega^n S(\omega) \mathrm{d}\omega}{\int_0^\infty S(\omega) \mathrm{d}\omega}, \tag{B.8}$$

where $n$ is the order of the moment and $S(\omega)$ is the signal under consideration. Unfortunately, the analytical model given by Duvillaret *et al.* (2001) does not have a closed form solution for calculating the spectral moments. Thus, we consider another analytical expression for modeling the THz spectrum as given by Xu *et al.* (2003).

## B.2 Analytical model by Xu et al. (2003)

According to Xu *et al.* (2003), the temporal waveform of the terahertz pulse depends mainly on the generation and detection mechanism and varies from one terahertz spectrometer to another. The temporal waveform of the T-ray pulse generated by a photoconductive antenna may be described as either bipolar (with an outer electrical field) or as unipolar (with an inner electrical field). These waveforms may be simulated using several simple formulas. Xu *et al.* (2003) gave simple models to represent the temporal profile of the THz signal generated by (i) a Photo-Conductive Antenna (PCA), which has a bi-polar waveform; (ii) an unbiased semiconductor and Surface Current Generation (SCG), which has a unipolar waveform; and (iii) Optical Rectification (OR), which has a decaying oscillation. Their model for the PCA is as follows:

$$E_{\mathrm{T}}(t) = 2A\frac{1}{\tau^2}\exp\left(-t^2/\tau^2\right), \tag{B.9}$$

where $A$ represents the maximum amplitude of the terahertz field, and $\tau$ represents the pulse duration in seconds. In terms of spectrum:

$$E_{\mathrm{T}}(t) = A\frac{\omega\tau}{\sqrt{2}}\exp\left(-\omega^2\tau^2/4\right). \tag{B.10}$$

In contrast to the previous model, this analytical expression is much simpler and does not provide any details of the physical processes that cause the generation or detection of the terahertz signal. However, this model has a definite solution for the calculation of moments using Eq. B.8.

# Bibliography


ABBOTT-D., AND ZHANG-X.-C. (2007). Special issue on T-ray imaging, sensing, and retection, *Proceedings of the IEEE*, **95**(8), pp. 1509–1513.

APPLEBY-R., AND WALLACE-H. (2007). Standoff detection of weapons and contraband in the 100 GHz to 1 THz region, *IEEE Transactions onAntennas and Propagation*, **55**(11), pp. 2944–2956.

ARAUJO-F., AREOSA-M. B. M., AND NETO-J. A. R. (2003). r-filters: a Hodrick-Prescott filter generalization, *Working Papers Series 69*, Central Bank of Brazil, Research Department.

ARBAB-M. . H., WINEBRENNER-D. P., THORSOS-E. I., AND CHEN-A. (2010). Retrieval of terahertz spectroscopic signatures in the presence of rough surface scattering using wavelet methods, *Applied Physics Letters*, **97**(18), article number 181903.

ASHWORTH-P. C., MACPHERSON-E. P., PROVENZANO-E., PINDER-S. E., PURUSHOTHAM-A. D., PEPPER-M., AND WALLACE-V. P. (2009). Terahertz pulsed spectroscopy of freshly excised human breast cancer, *Opt. Express*, **17**(15), pp. 12444–12454.

AUSTON-D. H., AND CHEUNG-K. P. (1985). Coherent time-domain far-infrared spectroscopy, *J. Opt. Soc. Am. B*, **2**(4), pp. 606–612.

BANDYOPADHYAY-A., SENGUPTA-A., BARAT-R., GARY-D., FEDERICI-J., CHEN-M., AND TANNER-D. (2007). Effects of scattering on THz spectra of granular solids, *International Journal of Infrared and Millimeter Waves*, **28**, pp. 969–978. 10.1007/s10762-007-9276-y.

BAO-S.-X., LIU-J.-S., RONG-L.-M., WANG-Z.-H., AND GUO-J. (2000). Quadratic polynomial technique for absorption correction in X-ray fluorescence spectrometry using continuous scattered background, *Spectrochimica Acta Part B: Atomic Spectroscopy*, **55**(4), pp. 379–382.

BARNES-R., BENEDICT-W., AND LEWIS-C. (1935). The far infrared spectrum of H2O, *Phys. Rev.*, **47**, pp. 918–921.

BELANGER-C., CIELO-P., FAVIS-B. D., AND PATTERSON-W. I. (1990). Analysis of polymer blend morphology by transmission and reflection light scattering techniques, *Polymer Engineering & Science*, **30**(17), pp. 1090–1097.

BORN-M., AND WOLF-E. (1999). *Principles of Optics*, 7 edn, Cambridge.

BROWN-E. R., BJARNASON-J. E., FEDOR-A. M., AND KORTER-T. M. (2007). On the strong and narrow absorption signature in lactose at 0.53 THz, *Applied Physics Letters*, **90**(6), article number 061908.

BROWN-E. R., SMITH-F. W., AND MCINTOSH-K. A. (1993). Coherent millimeter wave generation by heterodyne conversion in low temperature grown GaAs photoconductors, *Journal of Applied Physics*, **73**(3), pp. 1480–1484.

BRUGGEMAN-D. A. G. (1935). Calculation of various physics constants in heterogenous substances I dielectricity constants and conductivity of mixed bodies from isotropic substances, *Annalen der Physik*, **24**(7), pp. 636–664.

CHAIX-J.-F., GARNIER-V., AND CORNELOUP-G. (2006). Ultrasonic wave propagation in heterogeneous solid media: Theoretical analysis and experimental validation, *Ultrasonics*, **44**(2), pp. 200–210.

CHAN-W. L., CHEN-H.-T., TAYLOR-A. J., BRENER-I., CICH-M. J., AND MITTLEMAN-D. M. (2009). A spatial light modulator for terahertz beams, *Applied Physics Letters*, **94**(21), article number 213511.

CHEN-H.-T., KERSTING-R., AND CHO-G. C. (2003). Terahertz imaging with nanometer resolution, *Applied Physics Letters*, **83**(15), pp. 3009–3011.

CHEN-H.-T., O'HARA-J., AZAD-A., AND TAYLOR-A. (2011a). Manipulation of terahertz radiation using metamaterials, *Laser Photonics Reviews*, **5**(4), pp. 513–533.

CHEN-H.-T., O'HARA-J., AZAD-A., AND TAYLOR-A. (2011b). Manipulation of terahertz radiation using metamaterials, *Laser Photonics Reviews*, **5**(4), pp. 513–533.

CHEN-H.-T., WILLIE-J. P., ZIDE-J. M. O., GOSSARD-A. C., TAYLOR-A. J., AND AVERITT-R. D. (2006). Active terahertz metamaterial devices, , **444**(7119), pp. 597–600.

CHEN-Q., JIANG-Z., XU-G. X., AND ZHANG-X.-C. (2000). Near-field terahertz imaging with a dynamic aperture, *Opt. Lett.*, **25**(15), pp. 1122–1124.

CHEN-Y., PETER-J., SEMMLER-W., AND SCHULZ-R. (2008). On the transition from ballistic to diffusive transport in highly scattering turbid slabs as observed in the angular spectrum: Monte carlo simulations, *Biomedical Optics*, Optical Society of America.

CHOI-M. K., BETTERMANN-A., AND WEIDE-D. W. (2004). Potential for detection of explosive and biological hazards with electronic terahertz systems, *Philosophical Transactions: Mathematical, Physical and Engineering Sciences*, **362**(1815), pp. 337–349.

CHÝLEK-P., AND SRIVASTAVA-V. (1983). Dielectric constant of a composite inhomogeneous medium, *Phys. Rev. B*, **27**(8), pp. 5098–5106.

CHÝLEK-P., SRIVASTAVA-V., PINNICK-R. G., AND WANG-R. T. (1988). Scattering of electromagnetic waves by composite spherical particles: experiment and effective medium approximations, *Appl. Opt.*, **27**(12), pp. 2396–2404.

COGDILL-R., FORCHT-R., SHEN-Y., TADAY-P., CREEKMORE-J., ANDERSON-C., AND DRENNEN-J. (2007). Comparison of terahertz pulse imaging and near-infrared spectroscopy for rapid, non-destructive analysis of tablet coating thickness and uniformity, *Journal of Pharmaceutical Innovation*, **2**, pp. 29–36. 10.1007/s12247-007-9004-0.

COLLINGS-P. J., GIBBS-E. J., STARR-T. E., VAFEK-O., YEE-C., POMERANCE-L. A., AND PASTERNACK-R. (1999). Resonance light scattering and its application in determining the size, shape, and aggregation number for supramolecular assemblies of chromophores, *The Journal of Physical Chemistry B*, **103**(40), pp. 8474–8481.

CRAWLEY-D., LONGBOTTOM-C., WALLACE-V. P., COLE-B., ARNONE-D., AND PEPPER-M. (2003). Three-dimensional terahertz pulse imaging of dental tissue, *Journal of Biomedical Optics*, **8**(2), pp. 303–307.

DARROW-J., ZHANG-X.-C., AUSTON-D., AND MORSE-J. (1992). Saturation properties of large-aperture photoconducting antennas, *IEEE Journal of Quantum Electronics*, **28**(6), pp. 1607–1616.

DAS-B., LIU-F., AND ALFANO-R. (1997). Time-resolved fluorescence and photon migration studies in biomedical and model random media, *Reports on Progress in Physics*, **60**(2), pp. 227–292.

DAVIES-A. G., BURNETT-A. D., FAN-W., LINFIELD-E. H., AND CUNNINGHAM-J. E. (2008). Terahertz spectroscopy of explosives and drugs, *Materials Today*, **11**(3), pp. 18–26.

DEXHEIMER-S. (2007). *Terahertz Spectroscopy: Principles and Applications*, Optical Science and Engineering, CRC Press.

DINES-K. A., AND KAK-A. C. (1979). Ultrasonic attenuation tomography of soft tissues, *Ultrasonic Imaging*, **1**(1), pp. 16–33.

DING-K.-H., AND TSANG-L. (1991). Effective propagation constants and attenuation rates in media of densely distributed coated dielectric particles with size distributions, *Journal of Electromagnetic Waves and Applications*, **5**(2), pp. 117–142.

DOBROIU-A., OTANI-C., AND KAWASE-K. (2006). Terahertz-wave sources and imaging applications, *Measurement Science and Technology*, **17**(11), article number R161.

DOBROIU-A., YAMASHITA-M., OHSHIMA-Y. N., MORITA-Y., OTANI-C., AND KAWASE-K. (2004). Terahertz imaging system based on a backward-wave oscillator, *Appl. Opt.*, **43**(30), pp. 5637–5646.

DORNEY-T. D., BARANIUK-R. G., AND MITTLEMAN-D. M. (2001). Material parameter estimation with terahertz time-domain spectroscopy, *J. Opt. Soc. Am. A*, **18**(7), pp. 1562–1571.

DOYLE-W. T. (1989). Optical properties of a suspension of metal spheres, *Phys. Rev. B*, **39**(14), pp. 9852–9858.

DUNLAP-P. N., AND HOWE-S. E. (1991). Design of particulate composites for optical applications, *Polymer Composites*, **12**(1), pp. 39–47.

DUVILLARET-L., GARET-F., AND COUTAZ-J.-L. (1996). A reliable method for extraction of material parameters in terahertz time-domain spectroscopy, *Selected Topics in Quantum Electronics, IEEE Journal of*, **2**(3), pp. 739–746.

DUVILLARET-L., GARET-F., AND COUTAZ-J.-L. (1999). Highly precise determination of optical constants and sample thickness in terahertz time-domain spectroscopy, *Appl. Opt.*, **38**(2), pp. 409–415.

DUVILLARET-L., GARET-F., ROUX-J.-F., AND COUTAZ-J.-L. (2001). Analytical modeling and optimization of terahertz time-domain spectroscopy experiments, using photoswitches as antennas, *IEEE Journal of Selected Topics in Quantum Electronics*, **7**(4), pp. 615–623.

ELIMELECH-M., GREGORY-J., JIA-X., AND WILLIAMS-R. (1998). *Particle Deposition and Aggregation: Measurement, Modelling and Simulation*, Colloid and Surface Engineering Series.

EXTER-M. V., FATTINGER-C., AND GRISCHKOWSKY-D. (1989). Terahertz time-domain spectroscopy of water vapor, *Opt. Lett.*, **14**(20), pp. 1128–1130.

FARIAS-T. L., KÖYLÜ-U. O., AND CARVALHO-M. G. (1996). Range of validity of the Rayleigh—Debye—Gans theory for optics of fractal aggregates, *Appl. Opt.*, **35**(33), pp. 6560–6567.

FATTINGER-C., AND GRISCHKOWSKY-D. (1988). Point source terahertz optics, *Applied Physics Letters*, **53**(16), pp. 1480–1482.

FATTINGER-C., AND GRISCHKOWSKY-D. (1989). Terahertz beams, *Applied Physics Letters*, **54**(6), pp. 490–492.

FEDERICI-J. F., GARY-D., SCHULKIN-B., HUANG-F., ALTAN-H., BARAT-R., AND ZIMDARS-D. (2003). Terahertz imaging using an interferometric array, *Applied Physics Letters*, **83**(12), pp. 2477–2479.

FERGUSON-B., AND ABBOTT-D. (2001a). De-noising techniques for terahertz responses of biological samples, *Microelectronics Journal*, **32**(12), pp. 943–953.

FERGUSON-B., AND ABBOTT-D. (2001b). Wavelet de-noising of optical terahertz pulse imaging data, *Fluctuation and Noise Letters*, **1**(02), pp. 65–69.

FERGUSON-B., AND ZHANG-X.-C. (2002). Materials for terahertz science and technology, *Nature Materials*, **1**, pp. 26–33.

FERGUSON-B., WANG-S., GRAY-D., ABBOTT-D., AND ZHANG-X.-C. (2002). T-ray computed tomography, *Opt. Lett.*, **27**(15), pp. 1312–1314.

FISCHER-B. M. (2005). *Broadband THz Time Domain Spectroscopy of Biomolecules— A Comprehensive Study of The Dielectric Properties of Biomolecules in The Far-Infrared*, PhD thesis. Freiburg University, Germany.

FISCHER-B. M., HOFFMANN-M., HELM-H., MODJESCH-G., AND JEPSEN-P. U. (2005). Chemical recognition in terahertz time-domain spectroscopy and imaging, *Semiconductor Science and Technology*, **20**(7), article number S246.

FISCHER-B. M., WALTHER-M., AND JEPSEN-P. U. (2002). Far-infrared vibrational modes of DNA components studied by terahertz time-domain spectroscopy, *Physics in Medicine and Biology*, **47**(21), pp. 3807–3814.

FITCH-M. J., AND OSIANDER-R. (2004). Terahertz waves for communications and sensing, , **25**(4), pp. 348–355.

FITZGERALD-A., BERRY-E., ZINOVEV-N., WALKER-G., SMITH-M., AND CHAMBERLAIN-J. (2002). An introduction to medical imaging with coherent terahertz frequency radiation, *Physics in Medicine and Biology*, **47**(7), pp. R67–R84.

FITZGERALD-A., COLE-B., AND TADAY-P. (2005). Nondestructive analysis of tablet coating thicknesses using terahertz pulsed imaging, *Journal of Pharmaceutical Sciences*, **94**(1), pp. 177–183.

FLAX-S. W., PELC-N. J., GLOVER-G. H., GUTMANN-F. D., AND MCLACHLAN-M. (1983). Spectral characterization and attenuation measurements in ultrasound, *Ultrasonic Imaging*, **5**(2), pp. 95–116.

FOLDY-L. L. (1945). The Multiple Scattering of Waves. I. General Theory of Isotropic Scattering by Randomly Distributed Scatterers, *Phys. Rev.*, **67**, pp. 107–119.

FOSS-C. A., HORNYAK-G. L., STOCKERT-J. A., AND MARTIN-C. R. (1994). Template-synthesized nanoscopic gold particles: Optical spectra and the effects of particle size and shape, *The Journal of Physical Chemistry*, **98**(11), pp. 2963–2971.

FOURNIER-G., AND FORAND-J. (1994). Analytic phase function for ocean water, *in* J. S. Jaffe. (ed.), *Proceedings of the SPIE*, Vol. 2258, pp. 194–201.

FOX-M., AND BERTSCH-G. F. (2002). Optical properties of solids, *American Journal of Physics*, **70**(12), pp. 1269–1270.

FRANZ-M., FISCHER-B. M., AND WALTHER-M. (2008). The Christiansen effect in terahertz time-domain spectra of coarse-grained powders, *Applied Physics Letters*, **92**(2), article number 021107.

GIUSTO-A., SAIJA-R., IATÌ-M. A., DENTI-P., BORGHESE-F., AND SINDONI-O. I. (2003). Optical properties of high-density dispersions of particles: Application to intralipid solutions, *Appl. Opt.*, **42**(21), pp. 4375–4380.

GORENFLO-S. (2006). *A Comprehensive Study of Macromolecules in Composites using Broadband THz Sspectroscopy*, PhD thesis. Universitat Freiburg.

GROSS-E. P. (1955). Shape of collision-broadened spectral lines, *Phys. Rev.*, **97**, pp. 395–403.

GRZEGORCZYK-T. M., AND KONG-J. A. (2006). Review of left-handed metamaterials: Evolution from theoretical and numerical studies to potential applications, *Journal of Electromagnetic Waves and Applications*, **20**(14), pp. 2053–2064.

GÜRTLER-A., WINNEWISSER-C., HELM-H., AND JEPSEN-P. U. (2000). Terahertz pulse propagation in the near field and the far field, *J. Opt. Soc. Am. A*, **17**(1), pp. 74–83.

HAYTER-J. B., AND PENFOLD-J. (1981). An analytic structure factor for macroion solutions, *Molecular Physics*, **42**(1), pp. 109–118.

HIRATA-A., HARADA-M., AND NAGATSUMA-T. (2003). 120-GHz wireless link using photonic techniques for generation, modulation, and emission of millimeter-wave signals, *J. Lightwave Technol.*, **21**(10), pp. 2145–2153.

HIRATA-A., NAGATSUMA-T., KOSUGI-T., TAKAHASHI-H., YAMAGUCHI-R., SHIMIZU-N., KUKUTSU-N., MURATA-K., KADO-Y., IKEGAWA-H., NISHIKAWA-H., AND NAKAYAMA-T. (2007). 10-Gbit/s wireless communications technology using sub-terahertz waves, Vol. 6772, *Proceedings of the SPIE*.

HIRSCH-O., ALEXANDER-P., AND GLADDEN-L. F. (2008). Techniques for cancellation of interfering multiple reflections in terahertz time-domain measurements, *Microelectronics Journal*, **39**(5), pp. 841–848.

HODRICK-R. J., AND PRESCOTT-E. C. (1997). Postwar U.S. business cycles: An empirical investigation, *Journal of Money, Credit and Banking*, **29**(1), pp. 1–16.

HO-L., MULLER-R., GORDON-K. C., KLEINEBUDDE-P., PEPPE-M., RADES-T., SHEN-Y., TADAY-P. F., AND ZEITLER-J. A. (2008). Applications of terahertz pulsed imaging to sustained-release tablet film coating quality assessment and dissolution performance, *Journal of Controlled Release*, **127**(1), pp. 79–87.

HO-L., MULLER-R., ROMER-M., GORDON-K. C., HEINMKI-J., KLEINEBUDDE-P., PEPPER-M., RADES-T., SHEN-Y. C., STRACHAN-C., TADAY-P., AND ZEITLER-J. (2007). Analysis of sustained-release tablet film coats using terahertz pulsed imaging, *Journal of Controlled Release*, **119**(3), pp. 253–261.

HOLOUBEK-J. (1999). Light scattering methods and characterization of polymer systems and processes, Vol. 3726, *Proceedings of the SPIE*, pp. 438–449.

HU-B. B., AND NUSS-M. C. (1995). Imaging with terahertz waves, *Opt. Lett.*, **20**(16), pp. 1716–1718.

HULST-H. (1957). *Light Scattering by Small Particles*, Structure of matter series, Dover Publications.

HUNSCHE-S., KOCH-M., BRENER-I., AND NUSS-M. C. (1998). THz near-field imaging, *Optics Communications*, **150**(1-6), pp. 22–26.

INGRAM-D. J. (1967). *Spectroscopy at Radio and Microwave Frequencies*, Vol. 2nd edition, Plenum Press (New York).

ISHIMARU-A. (1999). *Wave Propagation and Scattering in Random Media*, IEEE Press Series on Electromagnetic Wave Theory, IEEE Press.

ISHIMARU-A., AND KUGA-Y. (1982). Attenuation constant of a coherent field in a dense distribution of particles, *J. Opt. Soc. Am.*, **72**(10), pp. 1317–1320.

IZATT-J. R., BOULAY-R., GAGNON-R., AND DROUIN-B. (1988). Simultaneous measurement of moisture content and basis weight of paper sheet with a submillimeter laser. US Patent 4,755,678.

JACKSON-J. B., MOUROU-M., WHITAKER-J. F., DULING III-I. N., WILLIAMSON-S. L., MENU-M., AND MOUROU-G. A. (2008). Terahertz imaging for non-destructive evaluation of mural paintings, *Optics Communications*, **281**(4), pp. 527–532.

JEPSEN-P. U., AND FISCHER-B. M. (2005). Dynamic range in terahertz time-domain transmission and reflectionspectroscopy, *Opt. Lett.*, **30**(1), pp. 29–31.

JEPSEN-P. U., AND KEIDING-S. R. (1995). Radiation patterns from lens-coupled terahertz antennas, *Opt. Lett.*, **20**(8), pp. 807–809.

JEPSEN-P. U., JACOBSEN-R. H., AND KEIDING-S. R. (1996). Generation and detection of terahertz pulses from biased semiconductor antennas, *J. Opt. Soc. Am. B*, **13**(11), pp. 2424–2436.

JIANG-Z., AND ZHANG-X.-C. (1998). Single-shot spatiotemporal terahertz field imaging, *Opt. Lett.*, **23**(14), pp. 1114–1116.

JIANG-Z., XU-X. G., AND ZHANG-X.-C. (2000). Improvement of terahertz imaging with a dynamic subtraction technique, *Appl. Opt.*, **39**(17), pp. 2982–2987.

JONASZ-M., AND FOURNIER-G. (2007). *Light Scattering by Particles in Water: Theoretical and Experimental Foundations*, Academic Press.

JÖRDENS-C., AND KOCH-M. (2008). Detection of foreign bodies in chocolate with pulsed terahertz spectroscopy, *Optical Engineering*, **47**(3), article number 037003.

KANNO-S., AND HAMADA-T. (1975). Theory of thomson scattering in a strong magnetic field. iii, *Publications of the Astronomical Society of Japan*, **27**, pp. 545–552.

KAUSHIK-M., NG-B., FISCHER-B., AND ABBOTT-D. (2012a). Terahertz scattering by granular composite materials: An effective medium theory, *Applied Physics Letters*, **100**(1), article number 011107.

KAUSHIK-M., NG-B.-H., FISCHER-B., AND ABBOTT-D. (2012b). Reduction of scattering effects in THz-TDS signals, *IEEE Photonics Technology Letters*, **24**(2), pp. 155–157.

KAUSHIK-M., NG-B. W.-H., FISCHER-B., AND ABBOTT-D. (2011). Scattering robust features for classification of materials using terahertz, *Seventh International Conference on Intelligent Sensors, Sensor Networks and Information Processing (ISSNIP)*, pp. 33–36.

KAUSHIK-M., NG-B. W.-H., FISCHER-B. M., AND ABBOTT-D. (2012c). Terahertz fingerprinting in presence of quasi-ballistic scattering, *Applied Physics Letters*, **101**(6), article number 061108.

KAUSHIK-M., NG-B. W.-H., FISCHER-B. M., AND ABBOTT-D. (2012d). Terahertz scattering by dense media, *Applied Physics Letters*, **100**(24), article number 241110.

KAUSHIK-M., NG-B. W.-H., FISCHER-B. M., AND ABBOTT-D. (2012e). Terahertz scattering by two phased media with optically soft scatterers, *Journal of Applied Physics*, **112**(11), article number 113112.

KAWASE-K., OGAWA-Y., WATANABE-Y., AND INOUE-H. (2003). Non-destructive terahertz imaging of illicit drugs using spectral fingerprints, *Opt. Express*, **11**(20), pp. 2549–2554.

KERSTING-R., BUERSGENS-F., ACUNA-G., AND CHO-G. (2008). Terahertz near-field microscopy, *in* R. Haug. (ed.), *Advances in Solid State Physics*, Vol. 47 of *Advances in Solid State Physics*, Springer Berlin / Heidelberg, pp. 203–222.

KLAR-T., KILDISHEV-A., DRACHEV-V., AND SHALAEV-V. (2006). Negative-index metamaterials: Going optical, *IEEE Journal of Selected Topics in Quantum Electronics*, **12**(6), pp. 1106–1115.

KNOBLOCH-P., SCHILDKNECHT-C., OSTMANN-T. K., KOCH-M., HOFFMANN-S., HOFMANN-M., REHBERG-E., SPERLING-M., DONHUIJSEN-K., HEIN-G., AND PIERZ-K. (2002). Medical THz imaging: an investigation of histo-pathological samples, *Physics in Medicine and Biology*, **47**(21), article number 3875.

KOSCHNY-T., ZHANG-L., AND SOUKOULIS-C. M. (2005). Isotropic three-dimensional left-handed metamaterials, *Phys. Rev. B*, **71**, article number 121103.

KUGA-Y., RICE-D., AND WEST-R. (1996). Propagation constant and the velocity of the coherent wave in a dense strongly scattering medium, *IEEE Transactions on Antennas and Propagation*, **44**(3), pp. 326–332.

LAKHTAKIA-A. (1992). Size-dependent Maxwell-Garnett formula from an integral equation formalism, *Optik*, **91**(3), pp. 134–137.

LAX-M. (1951). Multiple scattering of waves, *Rev. Mod. Phys.*, **23**, pp. 287–310.

LEAHY-HOPPA-M., MIRAGLIOTTA-J., OSIANDER-R., BURNETT-J., DIKMELIK-Y., MCENNIS-C., AND SPICER-J. (2010). Ultrafast laser-based spectroscopy and sensing: Applications in libs, cars, and thz spectroscopy, *Sensors*, **10**(5), pp. 4342–4372.

LEISAWITZ-D., DANCHI-W., DIPIRRO-M., FEINBERG-L., GEZARI-D., HAGOPIAN-M., LANGER-W., MATHER-J., MOSELEY-S. J., SHAO-M., SILVERBERG-R., STAGUHN-J., SWAIN-M., YORKE-H., AND ZHANG-X. (2000). Scientific motivation and technology requirements for the spirit and specs far-infrared/submillimeter space interferometers, Vol. 4013, *Proceeding of SPIE*, pp. 36–46.

LEUNG TSANG-K. J. A. (2002). *Scattering of Electromagnetic Waves: Advanced Topics*, John Wiley and Sons, Inc.

LIN-H., FUMEAUX-C., UNG-B.-Y., AND ABBOTT-D. (2011). Comprehensive modeling of THz microscope with a sub-wavelength source, *Opt. Express*, **19**(6), pp. 5327–5338.

LORENTZ-H. A. (1905). The absoption and emission lines of gaseous bodies, *Koninklijke Nederlandse Akademie van Weteschappen Proceedings Series B Physical Sciences*, **8**, pp. 591–611.

MALLAT-S. G. (1988). *Multiresolution Representations and Wavelets*, PhD thesis.

MANDT-C. E., KUGA-Y., TSANG-L., AND ISHIMARU-A. (1992). Microwave propagation and scattering in a dense distribution of non-tenuous spheres: experiment and theory, *Waves in Random Media*, **2**(3), pp. 225–234.

MARKELZ-A., ROITBERG-A., AND HEILWEIL-E. (2000). Pulsed terahertz spectroscopy of DNA, bovine serum albumin and collagen between 0.1 and 2.0 THz, *Chemical Physics Letters*, **320**(1-2), pp. 42–48.

MARTENS-H., AND STARK-E. (1991). Extended multiplicative signal correction and spectral interference subtraction: New preprocessing methods for near infrared spectroscopy, *Journal of Pharmaceutical and Biomedical Analysis*, **9**(8), pp. 625–635.

MAURER-L., AND LEUENBERGER-H. (2009). Terahertz pulsed imaging and near infrared imaging to monitor the coating process of pharmaceutical tablets, *International Journal of Pharmaceutics*, **370**(1-2), pp. 8–16.

MAXWELL GARNETT-J. C. (1904). Colours in metal glasses and in metallic films., *Royal Society of London Proceedings Series I*, **73**, pp. 443–445.

MIE-G. (1908). Beitrge zur Optik trber Medien, speziell kolloidaler Metallsungen, *Annalen der Physik*, **330**(3), pp. 377–445.

MISHCHENKO-M., TRAVIS-L., AND LACIS-A. (2002). *Scattering, Absorption, and Emission of Light by Small Particles*, Cambridge University Press.

MITROFANOV-O., BRENER-I., HAREL-R., WYNN-J., PFEIFFER-L., WEST-K., AND FEDERICI-J. (2000). Terahertz near-field microscopy based on a collection mode detector, *Applied Physics Letters*, **77**(22), pp. 3496–3498.

MITTLEMAN-D., AND NUSS-M. C. (2000). Method and apparatus for terahertz tomographic imaging.

MITTLEMAN-D., GUPTA-M., NEELAMANI-R., BARANIUK-R., RUDD-J., AND KOCH-M. (1999). Recent advances in terahertz imaging, *Applied Physics B: Lasers and Optics*, **68**, pp. 1085–1094. 10.1007/s003400050750.

MITTLEMAN-D., JACOBSEN-R., AND NUSS-M. (1996). T-ray imaging, *Selected Topics in Quantum Electronics, IEEE Journal of*, **2**(3), pp. 679–692.

MITTLEMAN-D., JACOBSEN-R., NEELAMANI-R., BARANIUK-R., AND NUSS-M. (1998). Gas sensing using terahertz time-domain spectroscopy, *Applied Physics B: Lasers and Optics*, **67**, pp. 379–390.

MOHR-P. J., AND TAYLOR-B. N. (2005). Codata recommended values of the fundamental physical constants: 2002, *Rev. Mod. Phys.*, **77**, pp. 1–107.

MORITA-Y., DOBROIU-A., KAWASE-K., AND OTANI-C. (2005). Terahertz technique for detection of microleaks in the seal of flexible plastic packages, *Optical Engineering*, **44**(1), article number 019001.

MUJUMDAR-S., DICE-G., AND ELEZZABI-A. (2005). Few-cycle pulse propagation in multiple scattering media, *Optics Communications*, **247**(13), pp. 19–27.

NAFTALY-M., AND MILES-R. (2007). A method for removing etalon oscillations from THz time-domain spectra, *Optics Communications*, **280**(2), pp. 291–295.

NAFTALY-M., DUDLEY-R., AND FLETCHER-J. (2010). An etalon-based method for frequency calibration of terahertz time-domain spectrometers, *Optics Communications*, **283**(9), pp. 1849–1853.

NAM-K., ZURK-L., AND S.-S. (2012). Modeling terahertz diffuse scattering from granular media using radiative transfer theory, *Progress in Electromagnetics Research B*, **38**, pp. 205–223.

NARAYANA-P., AND OPHIR-J. (1983). A closed form method for the measurement of attenuation in nonlinearly dispersive media, *Ultrasonic Imaging*, **5**(1), pp. 17–21.

NEWTON-R. (2002). *Scattering Theory of Waves and Particles*, Dover Publications.

NGUYEN-K., JOHNS-M., GLADDEN-L., WORRALL-C., ALEXANDER-P., BARBIERI-S., BEERE-H., RITCHIE-D., AND LINFIELD-E. (2005). Three-dimensional imaging with a terahertz quantum cascade laser, *High Frequency Postgraduate Student Colloquium, 2005*, pp. 101–104.

NING-L., SHEN-J., JINHAI-S., LAISHUN-L., XU-X., LU-M., AND YAN-J. (2005). Study on the THz spectrum of methamphetamine, *Opt. Express*, **13**(18), pp. 6750–6755.

O'HARA-J., AND GRISCHKOWSKY-D. (2002). Synthetic phased-array terahertz imaging, *Opt. Lett.*, **27**(12), pp. 1070–1072.

O'HARA-J., AND GRISCHKOWSKY-D. (2004). Quasi-optic synthetic phased-array terahertz imaging, *J. Opt. Soc. Am. B*, **21**(6), pp. 1178–1191.

OH-S., KANG-J., MAENG-I., SUH-J.-S., HUH-Y.-M., HAAM-S., AND SON-J.-H. (2009). Nanoparticle-enabled terahertz imaging for cancer diagnosis, *Opt. Express*, **17**(5), pp. 3469–3475.

OPHIR-J., SHAWKER-T., MAKLAD-N., MILLER-J., FLAX-S., NARAYANA-P., AND JONESS-J. (1984). Attenuation estimation in reflection: Progress and prospects, *Ultrasonic Imaging*, **6**(4), pp. 349–395.

PADILLA-W. J., ARONSSON-M. T., HIGHSTRETE-C., LEE-M., TAYLOR-A. J., AND AVERITT-R. D. (2007). Electrically resonant terahertz metamaterials: Theoretical and experimental investigations, *Phys. Rev. B*, **75**, article number 041102.

PADILLA-W. J., TAYLOR-A. J., HIGHSTRETE-C., LEE-M., AND AVERITT-R. D. (2006). Dynamical electric and magnetic metamaterial response at terahertz frequencies, *Phys. Rev. Lett.*, **96**, p. 107401.

PEARCE-J., AND MITTLEMAN-D. (2001). Propagation of single-cycle terahertz pulses in random media, *Opt. Lett.*, **26**(24), pp. 2002–2004.

PEARCE-J., AND MITTLEMAN-D. M. (2002). Scale model experimentation: using terahertz pulses to study light scattering, *Phys. Med. Biol.*, **47**, pp. 3823–3830.

PEARCE-J., CHOI-H., MITTLEMAN-D., WHITE-J., AND ZIMDARS-D. (2005). Terahertz wide aperture reflection tomography, *Opt. Lett.*, **30**(13), pp. 1653–1655.

PEARCE-J., JIAN-Z., AND MITTLEMAN-D. M. (2003). Statistics of multiply scattered broadband terahertz pulses, *Phys. Rev. Lett.*, **91**, article number 043903.

PENDRY-J., AND SMITH-D. (2004). Reversing light with negative refraction, *Physics Today*, **57**(6), pp. 37–43.

PHILLIPS-T., AND KEENE-J. (1992). Submillimeter astronomy [heterodyne spectroscopy], *Proceedings of the IEEE*, **80**(11), pp. 1662–1678.

PIESIEWICZ-R., JEMAI-J., KOCH-M., AND KURNER-T. (2005). THz channel characterization for future wireless gigabit indoor communication systems, Vol. 5727, *Proceeding of SPIE*, pp. 166–176.

PIESIEWICZ-R., KLEINE-OSTMANN-T., KRUMBHOLZ-N., MITTLEMAN-D., KOCH-M., SCHOEBEL-J., AND KURNER-T. (2007). Short-range ultra-broadband terahertz communications: Concepts and perspectives, *IEEE Antennas and Propagation Magazine*, **49**(6), pp. 24–39.

PLANKEN-P., RIJMENAM-C., AND VALK-N. (2005). Terahertz near-field microscopy, *Conference on Lasers and Electro-Optics/Quantum Electronics and Laser Science and Photonic Applications Systems Technologies*, Optical Society of America.

PNG-G. (2010). *Terahertz Spectroscopy and Modelling of Biotissue*, PhD thesis. The University of Adelaide, Australia.

PRYCE-I. M., AYDIN-K., KELAITA-Y. A., BRIGGS-R. M., AND ATWATER-H. A. (2010). Highly strained compliant optical metamaterials with large frequency tunability, *Nano Letters*, **10**(10), pp. 4222–4227.

PUPEZA-I., WILK-R., AND KOCH-M. (2007). Highly accurate optical material parameter determination with thz time-domain spectroscopy, *Opt. Express*, **15**(7), pp. 4335–4350.

RAMAN-C. (1949). The theory of the christiansen experiment, *Proceedings Mathematical Sciences*, **29**, pp. 381–390. 10.1007/BF03036872.

RAWASHDEH-A., NATHIR-A. F., SANDROCK-M. L., SEUGLING-C. J., AND FOSS-C. A. (1998). Visible region polarization spectroscopic studies of template-synthesized gold nanoparticles oriented in polyethylene, *The Journal of Physical Chemistry B*, **102**(2), pp. 361–371.

ROSTAMI-A., RASOOLI-H., AND BAGHBAN-H. (2010). *Terahertz Technology: Fundamentals and Applications*, Lecture Notes in Electrical Engineering, Springer.

RUDD-J., AND MITTLEMAN-D. (2002). Influence of substrate-lens design in terahertz time-domain spectroscopy, *J. Opt. Soc. Am. B*, **19**(2), pp. 319–329.

RUDD-J., ZIMDARS-D., AND WARMUTH-M. (2000). Compact fiber-pigtailed terahertz imaging system, Vol. 3934, *Proceedings of SPIE*, pp. 27–35.

SALEH-B. E. A., AND TEICH-M. C. (2001). *Fundamentals of Photonics*, John Wiley and Sons, Inc.

SCHERGER-B., SCHELLER-M., VIEWEG-N., CUNDIFF-S., AND KOCH-M. (2011). Paper terahertz wave plates, *Opt. Express*, **19**(25), pp. 24884–24889.

SCHURIG-D., MOCK-J. J., AND SMITH-D. R. (2006). Electric-field-coupled resonators for negative permittivity metamaterials, *Applied Physics Letters*, **88**(4), article number 041109.

SENITZKY-B., AND OLINER-A. (1970). Submillimeter waves—a transition region, *Proceedings of the Symposium on Submillimeter Waves*, **20**.

SHALAEV-V. (2007). Optical negative-index metamaterials, *Nature photonics*, **1**(1), pp. 41–48.

SHANKER-B., AND LAKHTAKIA-A. (1993). Extended Maxwell Garnett formalism for composite adhesives for microwave-assisted adhesion of polymer surfaces, *Journal of Composite Materials*, **27**(12), pp. 1203–1213.

SHEN-Y. (1976). Far-infrared generation by optical mixing, *Progress in Quantum Electronics*, **4**, pp. 207–232.

SHEN-Y., AND TADAY-P. (2008). Development and application of terahertz pulsed imaging for nondestructive inspection of pharmaceutical tablet, *IEEE Journal of Selected Topics in Quantum Electronics*, **14**(2), pp. 407–415.

SHEN-Y. C., UPADHYA-P. C., BEERE-H. E., LINFIELD-E. H., DAVIES-A. G., GREGORY-I. S., BAKER-C., TRIBE-W. R., AND EVANS-M. J. (2004). Generation and detection of ultrabroadband terahertz radiation using photoconductive emitters and receivers, *Applied Physics Letters*, **85**(2), pp. 164–166.

SHEN-Y., TADAY-P., AND PEPPER-M. (2008). Elimination of scattering effects in spectral measurement of granulated materials using terahertz pulsed spectroscopy, *Applied Physics Letters*, **92**(5), article number 051103.

SHEN-Y., TADAY-P., NEWNHAM-D., AND PEPPER-M. (2005a). Chemical mapping using reflection terahertz pulsed imaging, *Semiconductor Science and Technology*, **20**(7), article number S254.

SHEN-Y., TADAY-P., NEWNHAM-D., KEMP-M., AND PEPPER-M. (2005b). 3D chemical mapping using terahertz pulsed imaging, Vol. 5727, *Proceedings of SPIE*, pp. 24–31.

SHIMIZU-K. (1983). Modification of the Rayleigh-Debye approximation, *J. Opt. Soc. Am.*, **73**(4), pp. 504–507.

SIEBERT-K., QUAST-H., LEONHARDT-R., LOFFLER-T., THOMSON-M., BAUER-T., ROSKOS-H., AND CZASCH-S. (2002). Continuous-wave all-optoelectronic terahertz imaging, *Applied Physics Letters*, **80**(16), pp. 3003–3005.

SIEGEL-P. (2002). Terahertz technology, *IEEE Transactions on Microwave Theory and Techniques*, **50**(3), pp. 910–928.

SIEGEL-P. (2004). Terahertz technology in biology and medicine, *IEEE Transactions on Microwave Theory and Techniques*, **52**(10), pp. 2438–2447.

SINGH-R., PLUM-E., MENZEL-C., ROCKSTUHL-C., AZAD-A. K., CHEVILLE-R. A., LEDERER-F., ZHANG-W., AND ZHELUDEV-N. I. (2009). Terahertz metamaterial with asymmetric transmission, *Phys. Rev. B*, **80**, article number 153104.

SINYUKOV-A., AND HAYDEN-L. (2002). Generation and detection of terahertz radiation with multilayered electro-optic polymer films, *Opt. Lett.*, **27**(1), pp. 55–57.

SMITH-P., AUSTON-D., AND NUSS-M. (1988). Subpicosecond photoconducting dipole antennas, *Quantum Electronics, IEEE Journal of*, **24**(2), pp. 255–260.

SMYE-S., CHAMBERLAIN-J., -A., AND BERRY-E. (2001). The interaction between terahertz radiation and biological tissue, *Physics in Medicine and Biology*, **46**(9), article number R101.

SORENSEN-C. M. (2001). Light scattering by fractal aggregates: A review, *Aerosol Science and Technology*, **35**(2), pp. 648–687.

SOUKOULIS-C. M., LINDEN-S., AND WEGENER-M. (2007). Negative refractive index at optical wavelengths, *Science*, **315**(5808), pp. 47–49.

SPENCER-J. A., GAO-Z., MOORE-T., BUHSE-L. F., TADAY-P. F., NEWNHAM-D. A., SHEN-Y., PORTIERI-A., AND HUSAIN-A. (2008). Delayed release tablet dissolution related to coating thickness by terahertz pulsed image mapping, *Journal of Pharmaceutical Sciences*, **97**(4), pp. 1543–1550.

STRACHAN-C., RADES-T., NEWNHAM-D., GORDON-K., PEPPE-M., AND TADAY-P. (2004). Using terahertz pulsed spectroscopy to study crystallinity of pharmaceutical materials, *Chemical Physics Letters*, **390**(1-3), pp. 20–24.

STROUD-D., AND PAN-F. P. (1978). Self-consistent approach to electromagnetic wave propagation in composite media: Application to model granular metals, *Phys. Rev. B*, **17**(4), pp. 1602–1610.

SUDIARTA-I., AND CHYLEK-P. (2001). Mie-scattering formalism for spherical particles embedded in an absorbing medium, *J. Opt. Soc. Am. A*, **18**(6), pp. 1275–1278.

SUNAGUCHI-N., SASAKI-Y., MAIKUSA-N., KAWAI-M., YUASA-T., AND OTANI-C. (2009). Depth-resolving THz imaging with tomosynthesis, *Opt. Express*, **17**(12), pp. 9558–9570.

TADAY-P., BRADLEY-I., ARNONE-D., AND PEPPER-M. (2003). Using terahertz pulse spectroscopy to study the crystalline structure of a drug: A case study of the polymorphs of ranitidine hydrochloride, *Journal of Pharmaceutical Sciences*, **92**(4), pp. 831–838.

TAKASHI., TAKESHI-Y., TSUTOMU-A., AND EMMANUEL-A. (2006). Real-time two-dimensional terahertz tomography of moving objects, *Optics Communications*, **267**(1), pp. 128–136.

TONOUCHI-M. (2007). Cutting-edge terahertz technology, *Nature Photonics*, **1**, pp. 97–105.

TWERSKY-V. (1978). Acoustic bulk parameters in distributions of pair-correlated scatterers, *The Journal of the Acoustical Society of America*, **64**(6), pp. 1710–1719.

UNG-B.-Y., FUMEAUX-C., LIN-H., FISCHER-B., NG-B.-H., AND ABBOTT-D. (2012). Low-cost ultra-thin broadband terahertz beam-splitter, *Opt. Express*, **20**(5), pp. 4968–4978.

UPADHYA-P., SHEN-Y., DAVIES-A., AND LINFIELD-E. (2003). Terahertz time-domain spectroscopy of glucose and uric acid, *Journal of Biological Physics*, **29**, pp. 117–121. 10.1023/A:1024476322147.

UPADHYA-P., SHEN-Y., DAVIES-A., AND LINFIELD-E. (2004). Far-infrared vibrational modes of polycrystalline saccharides, *Vibrational Spectroscopy*, **35**(12), pp. 139–143.

USAMI-M., IWAMOTO-T., FUKASAWA-R., TANI-M., WATANABE-M., AND SAKAI-K. (2002). Development of a THz spectroscopic imaging system, *Physics in Medicine and Biology*, **47**(21), pp. 3749–3753.

VAN VLECK-J. H., AND WEISSKOPF-V. F. (1945). On the shape of collision-broadened lines, *Rev. Mod. Phys.*, **17**, pp. 227–236.

WALLACE-V., ARNONE-D., WOODWARD-R., AND PYE-R. (2002). Biomedical applications of terahertz pulse imaging, Vol. 3, pp. 2333–2334.

WALSH-K., SCHULKIN-B., GARY-D., FEDERICI-J., BARAT-R., AND ZIMDARS-D. (2004). Terahertz near-field interferometric and synthetic aperture imaging, Vol. 5411, *Proceedings of the SPIE*, pp. 9–17.

WALTHER-M., FISCHER-B., AND JEPSEN-P. U. (2003). Noncovalent intermolecular forces in polycrystalline and amorphous saccharides in the far infrared, *Chemical Physics*, **288**(2), pp. 261–268.

WALTHER-M., FREEMAN-M., AND HEGMANN-F. (2005). Metal-wire terahertz time-domain spectroscopy, *Applied Physics Letters*, **87**(26), article number 261107.

WALTHER-M., PLOCHOCKA-P., FISCHER-B., HELM-H., AND UHD JEPSEN-P. (2002). Collective vibrational modes in biological molecules investigated by terahertz time-domain spectroscopy, *Biopolymers*, **67**(4-5), pp. 310–313.

WANG-G., AND SORENSEN-C. (2002). Experimental test of the Rayleigh–Debye–Gans theory for light scattering by fractal aggregates, *Appl. Opt.*, **41**(22), pp. 4645–4651.

WANG-S., AND ZHANG-X.-C. (2004). Pulsed terahertz tomography, *Journal of Physics D: Applied Physics*, **37**(4), pp. R1–R36.

WANG-S., FERGUSON-B., MANNELLA-C., ABBOTT-D., AND ZHANG-X.-C. (2002a). Powder detection using thz imaging, *Quantum Electronics and Laser Science Conference, 2002. QELS '02. Technical Digest.*, p. 44.

WANG-S., ZHANG-X.-C., MALEY-M. P., HUNDLEY-M. F., BULAEVSKII-L. N., KOSHELEV-A., AND TAYLOR-A. J. (2002b). Terahertz technology: Terahertz tomographicimaging with a Fresnel lens, *Opt. Photon. News*, **13**(12), pp. 58–58.

WATERMAN-P., AND TRUELL-R. (1961). Multiple scattering of waves, *Journal of Mathematical Physics*, **2**(4), pp. 512–537.

WATERS-J. (1992). Submillimeter-wavelength heterodyne spectroscopy and remote sensing of the upper atmosphere, *Proceedings of the IEEE*, **80**(11), pp. 1679–1701.

WHEATCROFT-J. (2012). *Terahertz Time-domain Spectroscopy and Fresnel Coefficient Based Predictive Model*, PhD thesis. Wright State University.

WHITTAKER-E. T. (1922). On a new method of graduation, *Proceedings of the Edinburgh Mathematical Society*, **41**, pp. 63–75.

WITHAYACHUMNANKUL-W. (2009). *Engineering Aspects of Terahertz Time-Domain Spectroscopy*, PhD thesis. The University of Adelaide, Australia.

WITHAYACHUMNANKUL-W., AND ABBOTT-D. (2009). Metamaterials in the terahertz regime, *IEEE Photonics Journal*, **1**(2), pp. 99–118.

WITHAYACHUMNANKUL-W., FERGUSON-B., RAINSFORD-T., MICKAN-S., AND ABBOTT-D. (2006). Direct fabry-pérot effect removal, *Fluctuation and Noise Letters*, **6**(02), pp. 227–239.

WITHAYACHUMNANKUL-W., PNG-G., YIN-X., ATAKARAMIANS-S., JONES-I., LIN-H., UNG-B. S.-Y., BALAKRISHNAN-J., NG-B. W.-H., FERGUSON-B., MICKAN-S. P., FISCHER-B., AND ABBOTT-D. (2007). T-ray sensing and imaging, *Proceedings of the IEEE*, **95**(8), pp. 1528–1558.

WOODWARD-R., WALLACE-V., ARNONE-D., LINFIELD-E., AND PEPPER-M. (2003). Terahertz pulsed imaging of skin cancer in the time and frequency domain, *Journal of Biological Physics*, **29**, pp. 257–259. 10.1023/A:1024409329416.

WU-Q., AND ZHANG-X.-C. (1995). Free-space electro-optic sampling of terahertz beams, *Applied Physics Letters*, **67**(24), pp. 3523–3525.

WU-Q., AND ZHANG-X.-C. (1997). 7 terahertz broadband GaP electro-optic sensor, *Applied Physics Letters*, **70**(14), pp. 1784–1786.

WU-Q., HEWITT-T., AND ZHANG-X.-C. (1996). Two-dimensional electro-optic imaging of THz beams, *Applied Physics Letters*, **69**(8), pp. 1026–1028.

XU-J., YUAN-T., MICKAN-S., AND ZHANG-X.-C. (2003). Limit of spectral resolution in terahertz time-domain spectroscopy, *Chinese Physics Letters*, **20**(8), pp. 1266–1268.

YANG-K. H., RICHARDS-P. L., AND SHEN-Y. R. (1971). Generation of far-infrared radiation by picosecond light pulses in $LiNbO_3$, *Applied Physics Letters*, **19**(9), pp. 320–323.

YOO-K. M., AND ALFANO-R. R. (1990). Time-resolved coherent and incoherent components of forward light scattering in random media, *Opt. Lett.*, **15**(6), pp. 320–322.

ZANDONELLA-C. (2003). Terahertz imaging: T-ray specs, *Nature*, **424**, pp. 721–722.

ZEITLER-J. A., SHEN-Y., BAKER-C., TADAY-P. F., PEPPER-M., AND RADES-T. (2007a). Analysis of coating structures and interfaces in solid oral dosage forms by three dimensional terahertz pulsed imaging, *Journal of Pharmaceutical Sciences*, **96**(2), pp. 330–340.

ZEITLER-J. A., TADAY-P. F., NEWNHAM-D. A., PEPPER-M., GORDON-K. C., AND RADES-T. (2007b). Terahertz pulsed spectroscopy and imaging in the pharmaceutical setting - a review, *Journal of Pharmacy and Pharmacology*, **59**(2), pp. 209–223.

ZHANG-S., PARK-Y., LI-J., LU-X., ZHANG-W., AND ZHANG-X. (2009). Negative refractive index in chiral metamaterials, *Physical review letters*, **102**(2), article number 23901.

ZHANG-X., AND XU-J. (2009). *Introduction to THz Wave Photonics*, Springer.

ZHANG-X.-C. (2002). Terahertz wave imaging: horizons and hurdles, *Physics in Medicine and Biology*, **47**(21), pp. 3667–3677.

ZHANG-X.-C. (2004). Three-dimensional terahertz wave imaging, *Philosophical Transactions: Mathematical, Physical and Engineering Sciences*, **362**(1815), pp. 283–299.

ZHANG-Z.-M., CHEN-S., AND LIANG-Y.-Z. (2010). Baseline correction using adaptive iteratively reweighted penalized least squares, *Analyst*, **135**, pp. 1138–1146.

ZHU-S., NG-B.-H., FISCHER-B., AND ABBOTT-D. (2009). THz signal denoising via redundant representation, *34th International Conference on Infrared, Millimeter, and Terahertz Waves, 2009, Busan (Korea)*, pp. 1–2.

ZURK-L., ORLOWSKI-B., WINEBRENNER-D., THORSOS-E., LEAHY-HOPPA-M., AND HAYDEN-L. (2007). Terahertz scattering from granular material, *J. Opt. Soc. Am. B*, **24**(9), pp. 2238–2243.

# Glossary

The physical used in this thesis are given below. All the values are according to the recommendation of the committee on Data for Science and Technology (Mohr and Taylor 2005).

**Table B.1.** Physical constants used in this thesis

| Quantity | Symbol | Value |
|---|---|---|
| Avagadro constant | $N_A$ | $6.0221415(10) \times 10^{23}$ mol$^{-1}$ |
| Boltzmann constant | $k_B$ | $1.3806505(24) \times 10^{-23}$ J/K |
| | | $8.617343(15) \times 10^{-5}$ eV/K |
| electron volt | eV | $1.60217653(14) \times 10^{-19}$J |
| Planck constant | h | $6.6260693(11) \times 10^{-34}$J · s |
| | | $4.13566743(35) \times 10^{-15}$ eV · s |
| speed of light in vacuum | c, $c_0$ | 299792458 m/s |
| vacuum permittivity | $\mu_0$ | $4\pi \times 10^{-7}$ N/A$^2$ |
| vacuum permeability | $\epsilon_0$ | $8.854187817... \times 10^{-12}$ F/m |

# Acronyms

**Table B.2.** Acronyms used in this thesis

| | |
|---|---|
| CC | correlation coefficient, 113 |
| COC | cyclic olefin copolymer, 92 |
| CMOS | complementary metal oxide semiconductor, 8 |
| DEMA | dynamic effective medium approximation, 88 |
| EO | electrooptic, 35 |
| EFA | effective field approximation, 79 |
| FEL | free-electron laser, 64 |
| FIR | far infrared, 2 |
| FTS | Fourier transform spectroscopy, 28 |
| FWHM | full width half maximum, 118 |
| PCA | photoconductive antenna, 29 |
| PVC | polyvinyl chloride, 42 |
| PE | polyethylene, 18 |
| QCA | quasi crystalline approximation, 18 |
| SEM | scanning electron microscope, 80 |
| SNR | signal to noise ratio, 48 |
| SOS | silicon on sapphire, 33 |
| SVMAF | spatially moving average filter, 49 |
| TE | transverse electric, 56 |
| THz-TDS | terahertz time-domain spectroscopy, 1 |
| TIR | total internal reflection, 58 |
| TM | transverse magnetic, 56 |

# Index

# Biography

Mayank Kaushik was born in Gujarat, India in 1983. From 2001-2005, he was educated at the NRI Institute of Information Science and Technology at Bhopal, India, where he obtained a Bachelor's Degree in Electronic & Telecommunication Engineering with honours. During his Bachelor Degree, as a part of his major project, he worked as a trainee at the Space Applications Centre (Ahmedabad), Indian Space Research Organisation, in the Microwave Remote Sensing Area (MRSA) and Microwave Sensors Data Acquisition and Processor Division (MSDAPD), under the supervision of Mr Nilesh M. Desai, on the topic of "Matlab simulation of digital pulse compression and its implementation on Xilinx FPGA device" and successfully designed a Synthetic Aperture Radar range compression chip.

In 2006, he came to Australia to pursue higher education and received his Master's Degree in Electronic and Telecommunication Engineering (Adv. - coursework), from the University of Adelaide in December 2007. For his Master's Degree major project, Mr Mayank Kaushik successfully designed, developed and implemented (PCB based design) new/modified technique for Radio Frequency stabilization using simple and robust model with highly reduced phase noise, under the supervision of Assoc. Prof. Christopher Coleman. Soon after that he was appointed as a research assistant at the University of South Australia (and later at the University of Adelaide) to work on various audio signal processing related projects for the Defence Science and Technology Organisation (DSTO). In August 2009, he was granted the University of Adelaide Divisional Scholarship to study towards his PhD under the supervision of Dr Brian W.-H. Ng, Dr Bernd M. Fischer, and Prof. Derek Abbott. During his candidature, Mr Mayank Kaushik was successful in publishing his research work in a number of high impact journals and also received two IEEE South Australia Section travel scholarship awards and the Walter & Dorothy Duncan Trust Grant to present his research work at the $35^{th}$ and the $36^{th}$ International Conference on Infrared Millimeter and Terahertz wave, held in Rome in 2010 and in Houston, TX, in 2011, respectively. On March

2012, he took up an appointment at the Defence Science and Technology Organisation, Edinburgh, as a Radar research scientist.

Mayank Kaushik
mayank@eleceng.adelaide.edu.au

# Scientific Genealogy of **Mayank Kaushik**